University of Alberta

Terahertz Electromagnetic Wave Interaction with Mesoscopic Media

by

Kenneth Chau ©

A thesis submitted to the Faculty of Graduate Studies and Research
in partial fulfillment of the requirements for the degree of

Doctor of Philosophy

Department of Electrical and Computer Engineering

Edmonton, Alberta
Spring, 2008

Library and
Archives Canada

Published Heritage
Branch

395 Wellington Street
Ottawa ON K1A 0N4
Canada

Bibliothèque et
Archives Canada

Direction du
Patrimoine de l'édition

395, rue Wellington
Ottawa ON K1A 0N4
Canada

Your file Votre référence
ISBN: 978-0-494-45404-6
Our file Notre référence
ISBN: 978-0-494-45404-6

NOTICE:
The author has granted a non-exclusive license allowing Library and Archives Canada to reproduce, publish, archive, preserve, conserve, communicate to the public by telecommunication or on the Internet, loan, distribute and sell theses worldwide, for commercial or non-commercial purposes, in microform, paper, electronic and/or any other formats.

The author retains copyright ownership and moral rights in this thesis. Neither the thesis nor substantial extracts from it may be printed or otherwise reproduced without the author's permission.

AVIS:
L'auteur a accordé une licence non exclusive permettant à la Bibliothèque et Archives Canada de reproduire, publier, archiver, sauvegarder, conserver, transmettre au public par télécommunication ou par l'Internet, prêter, distribuer et vendre des thèses partout dans le monde, à des fins commerciales ou autres, sur support microforme, papier, électronique et/ou autres formats.

L'auteur conserve la propriété du droit d'auteur et des droits moraux qui protège cette thèse. Ni la thèse ni des extraits substantiels de celle-ci ne doivent être imprimés ou autrement reproduits sans son autorisation.

In compliance with the Canadian Privacy Act some supporting forms may have been removed from this thesis.

While these forms may be included in the document page count, their removal does not represent any loss of content from the thesis.

Conformément à la loi canadienne sur la protection de la vie privée, quelques formulaires secondaires ont été enlevés de cette thèse.

Bien que ces formulaires aient inclus dans la pagination, il n'y aura aucun contenu manquant.

Canada

To my family and my wife, for their love and support

Abstract

This thesis presents experimental work and calculations on the interaction of terahertz (THz) electromagnetic waves with subwavelength scale dielectric and metallic media and chiral materials in the context of classical optics, electromagnetic theory, and solid state theory.

The propagation of THz electromagnetic waves within heterogeneous dielectric media is explored in Chapter 2 using the concepts of effective medium theory and photon transport. It is found that effective medium descriptions of heterogeneous dielectric media are inadequate when the size scale of the heterogeneity approaches the wavelength of the electromagnetic wave.

In Chapter 3, this thesis explores THz non-resonant particle plasmon interaction with a single subwavelength metallic particle and ensembles of subwavelength metallic particles. For an ensemble of particles, coherent near-field coupling between nearest neighbor particles leads to enhanced, polarized THz electric field transmission through the ensemble. The influences of particle size, particle shape, and metal conductivity on the enhanced THz electric field transmission phenomenon are studied. It is further revealed that ensembles of metallic particles coated with nano-layers of a different metal show diminished THz electric field transmission due to resistive loss at the bimetallic interface. Since this resistive loss is highly sensitive to the electromagnetically induced current density crossing the interface, the interface resistance effect can provide a spatially localized probe of electromagnetically driven charge motion. Using ensembles of multi-layered bimetallic particles, the interface resistance effect is exploited to map out the sub-

surface charge motion induced by the incident THz electromagnetic wave on metallic particles.

Chapter 4 demonstrates the application of THz time-domain spectroscopy as a non-invasive, spectroscopic probe of phase transition phenomena in metallic media composed of subwavelength sized particles. The experimental results reveal marked phase modulation of the THz electromagnetic wave transmission through the metallic medium at the melting point temperature, indicating the onset of solid-liquid phase transformation.

Chapter 5 introduces methods to modulate the THz plasmonic properties of metallic particle ensembles via electron-spin-dependent phenomena. In particular, it is shown that anisotropic magnetoresistance inherent to ferromagnetic media causes magnetically anisotropic THz electric field transmission through ferromagnetic particle ensembles. Interestingly, coating the ferromagnetic particles with a nano-scale nonmagnetic metallic layer enhances their magnetic response. The enhancement in the coated ferromagnetic particles is shown to arise from the dynamic, electromagnetically driven accumulation of spin-polarized electrons from the ferromagnetic particle into the nonmagnetic layer.

Electromagnetic interaction with a subwavelength sized particle that is asymmetric, or chiral, may lead to an electromagnetic effect known as optical activity. Chapter 6 explores the interaction between THz electromagnetic waves and a subwavelength scale metallic helix. Resonant and non-resonant optical activity associated with axial and transverse THz electromagnetic wave propagation through a metallic helix, respectively, are demonstrated and explained.

Acknowledgements

I graciously thank my supervisor, Dr. Abdul Y. Elezzabi, for all the encouragement, support, and mentorship over the past years. The countless hours that Abdul has spent discussing problems, debating interpretations, and making suggestions have helped shape both the contents of this thesis and my development as a scientist. Never short on creative ideas, Abdul's enthusiasm for science is awe-inspiring and contagious. I have been fortunate to have such a terrific advisor.

I also thank Dr. Tsui for his friendly guidance through my postgraduate career. Whenever I walk into his office, Dr. Tsui has always put aside his work to spend time discussing problems or offering advice. His positive demeanor and kind words have been a great encouragement throughout my years as a graduate student.

I also thank Dr. Fedosejevs, Dr. Jaeger, and Dr. McMullin for their willingness to participate in my candidacy exam, to discuss work interests, to offer career advice, and to provide constructive feedback.

I have benefited greatly from excellent collaborations. In particular, I wish to thank Dr. Mark Johnson from the Naval Research Laboratory for his excellent suggestions and constructive criticisms. He is an excellent role model of a researcher that is committed to both good science and family. I also thank Dr. S. Mujumdar for his enthusiasm for science and his patience in teaching me the principles of scattering and localization.

Much of the work in this thesis would not be possible without the help of the great staff at the University of Alberta. I thank Dr. Ken Westra and Keith Franklin for providing access to the nanofabrication facilities. In addition, thank you to

George Braybrook both for providing excellent scanning electron microscope images and for allowing me to use the gold coater in his lab. Also, I owe thanks to Herbert Dexel, Martin Reidner, and Mike Boissonneault for their great work in the machine shop.

I wish to specially thank my colleagues Scott Irvine, Jonathan Holzman, Anthony Dechant, Graeme Dice, Michael Quong, Vikram Kohli, Corey Baron, and Kirk Rieckmann for their companionship over the many years. Our hilarious coffee breaks and football recesses have made these years enjoyable and fun, even when the thesis seemed overwhelming at times.

I am so appreciative of my parents, Alex and Winnie, and my sister, Maria. Without their words of encouragement, companionship, and tremendous love, this thesis would not have been possible. I am so blessed to have them in my corner.

Finally, I thank my amazing and fun-loving wife, Wendy. I have been incredibly fortunate to share these past years with such a wonderful, down-to-earth, caring, and compassionate person.

List of Figures

Figure 1.1. Light interaction with an arbitrary particle. Light incident upon a particle from the left induces electronic charge motion. The oscillating charges re-radiate in all directions and also convert some of the incident electromagnetic energy into other forms........3

Figure 1.2. Illustration of electromagnetic wave interaction at the surface of (a) a dielectric medium and (b) a metallic medium. An electromagnetic wave incident on the dielectric surface is scattered. On the other hand, an electromagnetic wave incident on a metallic surface (it is assumed that the metal is opaque) is scattered and, in certain situations, may couple to a surface plasmon wave........9

Figure 1.3. Electric field and charge configuration of a surface plasmon polariton wave propagating in the *x*-direction at the interface between medium 1 (dielectric) and medium 2 (metal)........22

Figure 1.4. Dispersion relations for an electromagnetic wave in free-space, an electromagnetic wave in a prism, a SPP at a metal/air interface, and a SPP at a metal/prism interface. At the intersection of the dispersion relations for the electromagnetic wave in a prism and the SPP on a metal/air interface, electromagnetic wave coupling to SPPs is possible........26

Figure 1.5. (a) The Kretschmann configuration and (b) the Otto configuration for prism coupling from an electromagnetic wave to a SPP. Phase matching of electromagnetic waves to SPPs can also be achieved via (c) the grating coupling configuration........28

Figure 1.6. Conceptual illustration of a particle plasmon excited on a subwavelength sized metallic particle........30

Figure 1.7. (a) Illustration of a subwavelength sized metallic sphere in a surrounding dielectric medium excited by an electric field, $E(t)$. By invoking the electrostatic approximation, (b) depicts the same subwavelength sized metallic sphere in a surrounding dielectric medium excited by a static, homogeneous electric field E_s. (c) shows the induced electric field due to the charge density induced by the static, homogeneous electric field E_s........31

Figure 1.8. Polarizability of a subwavelength sized Au particle versus frequency. The resonant particle plasmon response for Au occurs in the visible frequency range........35

Figure 1.9. (a) Excitation of a subwavelength sized metallic particle by an electromagnetic wave induces current density near the surface. (b) The current density results in the accumulation of positive and negative charge at opposing sides of the metallic particle, creating a particle plasmon. The particle plasmon decays via radiative re-emission or non-radiative decay........39

Figure 1.10. A random medium consisting of two types of subwavelength sized constituents composed of medium *1* and medium *2*, with respective permittivity values of ε_1 and ε_2. The random particles are immersed in a background medium having permittivity ε_{eff}...42

Figure 2.1. Transport of photons in a random dielectric medium consisting of a uniform matrix with dielectric inclusions. Photon transport through the medium may be composed of localized photons, scattered photons, back-scattered photons, and ballistic photons..57

Figure 2.2. Probability distribution of the angular coordinate of the scattered radiation at 1 THz from a sapphire sphere where the diameter is (a) 50 μm, (b) 100 μm, and (c) 150 μm. The forward direction is at 180° and the backward direction is at 0°...61

Figure 2.3. Calculated transport mean free path versus frequency for the sapphire particle ensemble used in the experiments. Note that the transport mean free path varies over nearly four orders of magnitude...62

Figure 2.4. Schematic of the THz time-domain spectroscopic setup................................67

Figure 2.5. Typical free-space THz waveform measured with the experimental setup. The ringing after the initial bipolar waveform is due to resonant absorption and re-emission by water vapour in the air. The two subsidiary signals are due to reflections from the front and back faces of the ZnSe electro-optic crystal. The inset shows the noise level prior to the arrival of the THz signal highlighted in the boxed region.....................68

Figure 2.6. Microscopic image of the sapphire microparticles used in the experiments...69

Figure 2.7. (a) Experimental and (b) calculated amplitude spectra of the transmitted THz pulse for various sample widths..70

Figure 2.8. Experimental and calculated (a) spectral bandwidth and (b) total integrated power of the transmitted THz pulses as a function of sample thickness...........................71

Figure 2.9. Experimental and calculated temporal THz waveforms transmitted through sample thickness of (a) 1.68 mm and (b) 7.3 mm. The inset in (a) depicts the reference pulse used in the experiment and simulation, and the inset in (b) plots the tail end of the calculated pulse using ballistic and scattered photons (solid line) and ballistic photons (dotted line)..72

Figure 2.10. Transmitted THz pulse delay relative to the reference pulse versus sample thickness. The delay is measured at the initial rise of the first pulse peak.......................73

Figure 2.11. The experimental (top) and calculated (bottom) temporal THz waveforms transmitted through the sample for a thickness of 1.68 mm. The calculated THz waveform is derived from a modified phase shown in the inset (solid line) along with the unmodified phase (dashed line)..76

Figure 3.1. (a) Illustration of visible electromagnetic wave excitation of a subwavelength scale particle where the particle size is comparable to the skin depth. (b) Illustration of THz electromagnetic wave excitation of a subwavelength scale particle where the particle size is significantly larger than the skin depth....85

Figure 3.2. Electric field lines near a metallic particle that has been immersed in a homogenous electric field. The lightning rod effect results in a higher electric field density near the particle surface....88

Figure 3.3. Images of a FDTD calculation of single-cycle THz pulse excitation of a 70 μm diameter Cu particle at (a) 0 ps, (b) 3.5 ps, (c) 8.5 ps. Shown in (d) is a magnified image of the particle at 8.5 ps....93

Figure 3.4. (a) Vector plot of the electric field in the vicinity of a 70 μm Cu microparticle after excitation by a single-cycle THz pulse. (b) illustrates the corresponding dipolar charge distribution at the surface of the microparticle....93

Figure 3.5. Calculated amplitude of the electric field near the surface of a 70 μm Cu microparticle after excitation by a single-cycle THz pulse versus the distance from the particle surface....94

Figure 3.6. (top) THz electromagnetic wave excitation of a single metallic particle and (bottom) THz electromagnetic wave excitation of an ensemble of metallic particles....95

Figure 3.7. THz pulse transmitted through a 1 mm thick microscope slide and 1 mm thick microscope slides that have been coated with a 70 nm and 300 nm thick Cr film....98

Figure 3.8. Scanning electron microscope image of the Cr particles used in the experiments....99

Figure 3.9. Schematic of the free-space THz generation and electro-optic detection setup used to characterize the THz electric field transmission through the metallic particle ensembles....100

Figure 3.10. (a) The far-field transmission through the Cr medium for $L = 0.6$ mm to $L = 7.0$ mm. The data has been filtered to remove delayed reflection signals in the ZnSe crystal. (b) depicts the transmitted pulses for $L = 0$ mm, 0.6 mm, and 7.0 mm on expanded time and amplitude scales. The inset in (b) shows the normalized transmission spectrum for $L = 0.6$ mm and 7.0 mm....102

Figure 3.11. The measured percentage total power transmission (circles) and relative pulse delay (squares) as a function of L. Best-fit curves for the transmission power and pulse delay show $1/(1+qL)$ and linear dependences, respectively, where $q=0.06\ \mathrm{mm}^{-1}$....103

Figure 3.12. The normalized peak-to-peak THz transmission through a 1 mm thick Cr sample versus θ_{probe} of the <111> ZnSe electro-optic crystal axis. The peak-to-peak electric field amplitudes for a free-space THz pulse and for the transmitted pulse through the Cr medium both illustrate the 3-fold symmetry characteristic of a linearly polarized field........104

Figure 3.13. Parallel and perpendicular electric field components transmitted through free-space and a 1 mm thick sample of Cr microparticles........105

Figure 3.14. THz signal transmitted through (a) a 2.0 mm thick and (b) a 7.7 mm thick sample of Cu microparticles. The black and gray lines correspond to the transmitted signal polarized parallel and perpendicular to the incident polarization, respectively....106

Figure 3.15. The calculated percentage power transmission (filled circles) and relative pulse delay (filled squares) versus *L*. The experimental transmission power (open circles) and relative pulse delay (open squares) are also depicted........108

Figure 3.16. Snapshots of the THz field magnitude within a random 5 mm × 5 mm Cr medium at times (a) 1.25 ps, (b) 8.5 ps, (c) 19.0 ps, and (d) 26.0 ps. In (e), the spatial field distribution map of a 1.6 mm × 1.8 mm region of the Cr medium [corresponding to the boxed region in (d)] shows that a significant amount of the electromagnetic field is trapped within hotspots. The power spectra at six randomly selected hotpots shown in (f) demonstrate the existence of resonant modes........111

Figure 3.17. (left) Calculation structure used in the FDTD calculations consisting of an ensemble of 150 μm circular particles. The panels to the right depict magnified images of the boxed region and show the propagation sequence of the THz field magnitude over a 1 ps duration. The sequence of images illustrates that electromagnetic energy transport through the metallic particle ensemble is governed by nearest neighbour coupling. (b) Calculated transmitted THz electric field through the *L* = 4 mm sample of 150 μm Cr particles along with a reference pulse transmitted through an air path........113

Figure 3.18. Free-space transmitted THz electric field measured through an empty cell and through 1.2 mm thick samples of irregularly shaped Cu, Cr, and Al particles having mean dimensions of 71 μm, 150 μm, and 400 μm, respectively. The transmitted fields are polarized parallel to the incident THz polarization........115

Figure 3.19. Scanning electron microscope images of Cu particle ensembles of sizes (a) 194 μm, (b) 251 μm, (c) 283 μm, (d) 372 μm, (e) 462 μm, (f) 560 μm, and (g) 665 μm........117

Figure 3.20. (a) Time-domain transmission through 3 mm thick ensembles of Cu microspheres where the diameter varies from 194 μm to 665 μm. (b) Power spectra of the transmission through ensembles of Cu spheres having diameters ranging from 194 μm to 372 μm........118

Figure 3.21. (a) Plot of the peak transmission wavelength through the 3 mm thick Cu particle ensembles versus the average particle size. The line is a linear line of best-fit to the data. (b) The transmitted power normalized to the free-space reference at a frequency of 0.09 THz versus the average particle cross-sectional area. The illustration below depicts a THz electromagnetic wave incident on a particle with a smaller cross-sectional area and a particle with a larger cross-sectional area..120

Figure 3.22. FDTD calculation of the induced charge density distribution of a (a) 70 μm diameter particle and (b) 200 μm diameter particle excited by a single-cycle THz pulse...123

Figure 3.23. Scanning electron microscope images of Cr particles having dimensions of (a) 150 ± 50 μm and (b) 40 ± 20 μm. (c) and (d) depict the experimental transmitted THz electric field through the 150 μm and 40 μm size Cr particles, respectively, for various sample thicknesses, in addition to the reference THz pulse transmitted through an empty cell. (e) shows the power spectrum of the experimental transmission through the empty cell, a $L = 0.6$ mm sample of the 150 μm Cr particles and a $L = 0.6$ mm sample of the 40 μm Cr particles. Illustrated in (f) are the experimentally measured effective refractive indices across the transmission bandwidths for the two Cr particle ensembles..............125

Figure 3.24. (a) FDTD calculations of the temporal THz transmitted electric fields through $L = 4$ mm ensembles of Cr particles with mean dimensions of 40 μm and 150 μm. Note that the transmitted pulse through the smaller Cr particles arrives at a later time. (b) The power spectra of the calculated transmission through the two particle ensembles. (c) and (d) illustrate the THz field magnitude in the 150 μm and 40 μm Cr particle ensembles, respectively, at $t = 7.5$ ps. THz field magnitudes at $t = 20.0$ ps in the 150 μm and 40 μm Cr particle ensembles are shown in (e) and (f), respectively...........128

Figure 3.25. (a), (b) and (c) depict the 50 μm, 100 μm, and 150 μm Cr particle chains used in the FDTD calculations, respectively. The chain lengths are 12 mm. (d), (e) and (f) depict the THz field magnitudes in the 50 μm, 100 μm, and 150 μm Cr particle chains, respectively, at an identical time after excitation with a 1 ps wide THz pulse. Note that the THz wave-fronts progress at the same velocity for the three particle chains...130

Figure 3.26. FDTD calculations of (a) the temporal THz transmitted electric field and (b) the spectral power transmission through the 12 mm long Cr particle chains consisting of 50 μm, 100 μm, and 150 μm size particles...131

Figure 3.27. Scanning electron microscope images of (a) irregular and (b) spherical Cu particles of mean dimensions 71 ± 20 μm and 83 ± 15 μm, respectively. (c) depicts the experimental temporal THz transmitted electric field through $L = 2.1$ mm samples of the irregular and spherical Cu particles, and (d) shows their corresponding power spectra...133

Figure 3.28. Scanning electron microscope images of (a) $Cu_{95}Sn_5$ and (b) Cu particles, both having mean dimensions 83 ± 15 μm. (c) depicts the experimental temporal THz transmitted electric field through $L = 2.1$ mm samples of $Cu_{95}Sn_5$ and Cu particles, and (d) illustrates their corresponding power spectra. Shown in (e) are FDTD calculations of the THz transmitted electric fields through identical $L = 2$ mm thick samples of 80 μm diameter W and Cu particles....135

Figure 3.29. Fermi-Dirac Distribution for an ideal gas of free electrons at $T = 0$ and $T > 0$....137

Figure 3.30. Development of a contact potential difference. (a) Band diagram of the metals before they are in contact. (b) Equilibrium band diagram of the metals after they are in contact....139

Figure 3.31. Cartoon illustrating the transport of THz electromagnetic pulse through an ensemble of bimetallic Cu/Au microparticles....140

Figure 3.32. (a) XPS spectra of two Cu/Au microparticle samples with percentage Au coverage of 45 % and 17 %. The characteristic Au 4f and Cu 2p emission lines are labeled in the plot. (b) XPS spectra of the two bimetallic particle samples near the Au 4f emission lines. The dashed line indicates the position of the Au 4f lines for pure Au....142

Figure 3.33. Experimental a) time-domain signal and b) power spectra of the transmitted THz pulses through 2 mm thick Cu-core/Au-layer microparticle samples for varying Au surface coverage, *F*. The inset depicts the reference THz pulse propagated through free-space....144

Figure 3.34. Peak-to-peak transmitted THz electric field amplitude versus Au surface coverage, *F*. The electric field amplitudes are normalized to the transmission through uncoated Cu particles....145

Figure 3.35. The calculated a) time-domain signal and b) frequency spectra of the transmitted THz pulses in response to single-cycle THz pulse excitation for varying τ_{eff}....147

Figure 3.36. Transmitted THz pulses through 2 mm thick samples of uncoated Cu particles (circles) and Cu-core/Cu-layer particles (line)....148

Figure 3.37. Differential phase of the transmission through the Cu-core/Cu-layer sample and through the $F = 44$ %, 32 %, and 17 % Cu-core/Au-layer microparticle samples. The transmission through the Cu-core/Cu-layer sample shows no significant phase accumulation across the transmission bandwidth....149

Figure 3.38. (top) Image of a metallic microparticle (metal 1) coated with alternating layers of metal 2 and metal 1 that is excited with a THz electromagnetic wave. (bottom) Illustration of THz electromagnetic charge induction at the surface of the multi-layered microparticle. The interfaces between the different metal layers each create a contact resistance that impedes charge flow across the interface....151

Figure 3.39. (a) Diagram depicting the sputter deposition method used to fabricate Cu particles coated with multi-layers. (b) Illustration of a single Cu microparticle coated with 4 alternating Au and Cu layers. The alternating layers produce a spatially modulated potential beneath the microparticle surface, which augments the non-radiative losses at the particle surface.....152

Figure 3.40. (a) Time-domain waveforms of the THz pulses transmitted through Cu microparticles with alternating nano-layers. (b) Magnified image of the time-domain THz waveforms transmitted through particle ensembles where the number of layers is 1, 3, and 5. These samples are coated with a 15 nm thick exterior Au layer.....155

Figure 3.41. (a) Experimental and (b) calculated relative spectral transmission amplitude for samples with varying number of layers normalized with respect to the spectral transmission amplitude through uncoated particles.....157

Figure 3.42. Calculated subsurface penetration distance of THz particle plasmon into the Cu multilayered microparticles. Also shown by the solid lines are the experimental skin depth values for Au and Cu.....160

Figure 3.43. Planar split-ring resonator consisting of two concentric rings each with a small gap.....162

Figure 3.44. Illustration of an amorphous metamaterial consisting of random ensembles of dielectric and metallic particles with varying metallic particle volume fraction, *VF*.....163

Figure 3.45. (a) Time-domain waveforms transmitted through an empty sample cell (reference) and 4.5 mm thick Co/sapphire particle mixtures for percentage volume Co varying from 0.0 % to 15.0 %. (b) Time-domain waveforms transmitted through 4.5 mm thick Co/sapphire particle mixtures for percentage volume Co varying from 31.2% to 100%.....165

Figure 3.46. Relative effective refractive index of the metallic/dielectric ensemble measured at a frequency of 0.23 THz versus the Co volume fraction. The plot highlights the three regimes low *VF*, intermediate *VF*, and high *VF*.....166

Figure 3.47. Frequency spectra of the transmission through mixtures of Co and sapphire particles for varying Co particle concentration.....167

Figure 3.48. Time-dependent intensity of the transmitted pulses through 4.5 mm thick ensembles with various *VF* values. The black and gray lines correspond to the transmitted component polarized parallel and perpendicular to the incident polarization, respectively.....169

Figure 3.49. Illustration of the relationship between V_{ave}, δ, and r_{ave}.....171

Figure 3.50. The optical and physical interparticle separation between metallic particles as a function of the Co volume fraction. (b) Effective relative refractive index versus the average optical separation between metallic particles at frequencies of 0.22 THz, 0.17

THz, and 0.12 THz. The diagrams inset in (b) illustrate the relative volume fraction of the metallic and dielectric particles for low, intermediate, and high *VF*.........................172

Figure 3.51. Ray diagram depicting the interaction of an incident THz electromagnetic wave with the metallic/dielectric ensemble for low *VF* and intermediate *VF*. At low *VF*, the transmission consists of ballistic and small-angle scattered electromagnetic waves. As the metallic volume fraction increases, a greater portion of the incident electromagnetic wave is scattered. For high *VF*, the incident wave excites particle plasmons, which cannot be accurately represented in the ray diagrams..........................174

Figure 4.1. Illustration of the ionic motion when a metal is (a) below the melting temperature and (b) above the melting temperature...187

Figure 4.2. (a) Experimental time-domain signals of THz pulses transmitted through 2.3 mm thick random Ga microparticle ensembles measured at various temperatures. The dashed line indicates the arrival time of the peak of the THz pulse. Shown in (b) are the effective real refractive index change and (c) effective imaginary refractive index change versus temperature and frequency. The refractive indices are measured relative to the reference pulse transmitted through the sample at 21.2 C°...191

Figure 4.3. Experimental effective (a) real refractive index change and (b) imaginary refractive index change for 0.1 THz (empty circles) and 0.2 THz (filled circles) at various temperatures. Striking discontinuity in the effective real refractive index occurs at the Ga melting temperature, 29.8 C°..194

Figure 4.4. (a) Size distribution of the Ga microparticles before melting (light bars) and after melting (dark bars). (b) shows the maximum correlation amplitude of transmitted pulses at various temperatures relative to the reference pulse at 21.2 C°. Insets are scanning electron microscope images of (i) the Ga microparticles prior to the heating cycle and (ii) the solidified particles after the heating cycle...196

Figure 4.5. Ga particle ensemble below the melting temperature, at the melting temperature, and above the coalescing temperature...197

Figure 5.1. Illustration of an electron possessing charge and spin angular momentum...203

Figure 5.2. Diagram of the typical density of states of the 3d and 4s electron bands for a ferromagnetic transition metal...204

Figure 5.3. Density of states diagram and the occupation of two spin sub-bands $3d^+$ and $3d^-$ below the Curie temperature...205

Figure 5.4. (left) Ferromagnetic metal with no applied magnetic field composed of many magnetic domains with randomly oriented magnetizations. (right) Ferromagnetic metal immersed in a large magnetic field. The magnetic domains boundaries have been erased and the magnetization of the sample points along the direction of the applied field.......206

Figure 5.5. Conceptual illustration of the origin of anisotropic magnetoresistance in ferromagnetic metals. When a magnetic field is aligned perpendicular to the current direction (a), the spin-orbits of the 3d electrons have minimal electron scattering cross-section. In the parallel case (b), the spin-orbits of the 3d electrons have maximal electron scattering cross-section....208

Figure 5.6. Illustration of a ferromagnetic metal in contact with a nonmagnetic metal. The density of states diagram for the 3d electron bands of the nonmagnetic and ferromagnetic metal are shown below....210

Figure 5.7. Illustration of a ferromagnetic metal in contact with a nonmagnetic metal with a voltage applied across the interface. The density of states diagram for the 3d electron bands of the nonmagnetic and ferromagnetic metal are shown below. A spin-polarized current, I_m, is driven from the ferromagnetic metal into the nonmagnetic metal....211

Figure 5.8. Image seen through a calcite crystal. The inherent birefringence of calcite causes the double image of the text seen through the crystal....217

Figure 5.9. Time-domain THz pulses (gray traces) transmitted through a 2 mm thick ensemble of Co particles when a 0.18 T magnetic field is applied perpendicular (top) and parallel (bottom) to the incident THz polarization. Also shown is the transmitted pulse in the absence of a magnetic field (black traces)....218

Figure 5.10. Normalized transmission amplitude through 3 mm thick Co particle samples versus the B orientation relative to the incident polarization where $|B|$ = 160 mT. The transmission amplitudes have been normalized to the zero-field transmission values. The data have been fitted to $\cos^2\theta$ functions shown by the solid line....219

Figure 5.11. (a) Relative arrival delay (between the parallel and perpendicular magnetic field configurations) of the transmitted pulse through a 2 mm thick Co particle ensemble versus magnetic field strength. (b) depicts magnetization measurements of the Co particles versus magnetic field strength. The arrival delay is plotted in (c) versus sample thickness for an applied magnetic field of 0.18 T and 0 T. The relative arrival delay (between the parallel and perpendicular magnetic field configurations) in (d) is shown versus sample length for an applied magnetic field of 0.18 T....220

Figure 5.12. (a) The integrated spatial profile of the THz transmission (along the direction perpendicular to the applied magnetic field) through a 2 mm thick Co sample for a field of 0 T, +0.18 T, and −0.18 T. The curves have been off-set for clarity. Time-domain transmission measured through a 3 mm thick sample of Cu particles is illustrated in (b) for a magnetic field of 0 T and 0.18 T applied parallel to the THz polarization. (c) shows the time-domain transmission measured through a 2 mm thick Co/wax ensemble for a magnetic field of 0 T and 0.18 T applied parallel to the THz polarization....222

Figure 5.13. Cartoon illustrating the physical origin of THz plasmonic magnetoresistance. The incident THz pulse polarizes the individual particles by inducing finite charge motion at the surface of the particles. The resistivity at the particle surface depends on the orientation of the magnetic field relative to the polarization direction of the incident

THz pulse. The particle plasmon losses are determined by the magnetoresistivity of the particles, which is sensitive to the *B* orientation. For high resistivity, the re-radiated THz pulse is attenuated and delayed..........225

Figure 5.14. (top) Illustration of the relative orientations of the external magnetic field and the polarization of a THz electric field incident on a Co particle. The incident electric field induces current density components parallel and perpendicular to the magnetic field orientation. (bottom) Electric field trajectory of the transmitted THz pulses through 2 mm thick ensemble of magnetized Co particles. The trajectories are shown as the orientation of the magnetic field (0.18 T) is varied over 180°. The relative orientation of the incident THz polarization and the magnetic field are shown in the diagram above..........226

Figure 5.15. (a) Scanning electron microscope image of a collection of porous Ni particles of nominal size δ. (b) A magnified image of a typical Ni particle highlighting an overall spheroid shape and subwavelength columnar microstructure. (c) A conceptual illustration of the excitation of a THz particle plasmon on a metallic microsphere. The incident electric field induces a surface current density, which polarizes the microparticle. The dominant polarization mode for the particle ($\delta \sim \lambda$) is a quadrupolar mode. (d) After excitation, the particle plasmon decays via radiation re-emission or non-radiative decay in the metallic sphere. The non-radiative losses are dictated by the resistivity of the sphere within a skin depth of the surface..........229

Figure 5.16. Time-domain transmitted THz electric field waveforms through porous Ni particles for various *B* field magnitudes, with *B* (a) parallel and (b) perpendicular to the incident THz polarization. The inset in (a) portrays the reference waveform transmitted through an empty polystyrene sample cell. (c) Power and (d) arrival delay of the transmitted THz pulse versus applied external magnetic field strength for the parallel and perpendicular configurations. (e) Power and (f) arrival delay of the transmitted pulse through solid Ni spheroids versus applied external magnetic field strength for the parallel and perpendicular configurations..........232

Figure 5.17. The top panels illustrate the solid (left) and porous (right) structures employed in three-dimensional FDTD, which use spatial and temporal resolutions of 5 μm and 5 fs, respectively. A quadrant of the particles is removed for illustrative purposes to highlight the internal structures. Electric field amplitude images of single-cycle THz pulse excitation of (a) a solid Ni spheroid and (b) a porous Ni spheroid 2 ps after the arrival of the THz pulse. Corresponding charge density images for a solid Ni spheroid [(c),(e),(g)] and a porous Ni spheroid [(d),(f),(h)] at various times. The arrows depict the polarization orientation of the incident electric field..........234

Figure 5.18. (a) Illustration of a ferromagnetic metal in contact with a nonmagnetic metal with a voltage applied across the interface. (b) Illustration of a ferromagnetic metal in contact with a nonmagnetic metal where spin-polarized current is driven by an incident electromagnetic wave..........238

Figure 5.19. Illustration of a subwavelength spinplasmonic structure consisting of a Co particle coated with Au nano-layers excited with a THz electromagnetic field pulse. The spintronic structure is immersed in a magnetic field so as to align the magnetic domains of the Co particle. The incident electromagnetic pulse induces spin-polarized current from the Co particle to the Au layer, creating a spin-dependent interface resistance.....239

Figure 5.20. Illustration of near-field particle plasmon coupled transport across a collection of Co/Au bimetallic particles. Spin accumulation at the F/N bimetallic interfaces gives rise to a magnetically modulated interface resistance. The insets depict scanning electron microscope images of the Co particles used in the experiments........240

Figure 5.21. Time-domain THz transmission signals through 3 mm thick particle ensembles having varying Au coverage, in zero field..242

Figure 5.22. Time-domain THz transmission through (a) Co (0 % Au) (perpendicular), (b) Co (0 % Au) (parallel), (c) Co/Au 35 % (perpendicular), (d) Co/Au 35 % (parallel), (e) Co/Au 42 % (perpendicular) and (f) Co/Au 42 % (parallel) particle ensembles for $|B|$ = 0 T (dark traces) and $|B|$ = 150 mT (light traces). The diagrams depict the orientation of the B field (arrow) relative to the electric field polarization. (g) Normalized transmission amplitude through 3 mm thick Co (filled circle) and Co/Au (empty circle) particle samples versus the field angle relative to the incident polarization, where $|B|$ = 160 mT. The transmission amplitudes for both samples have been normalized to their respective zero-field amplitudes, and the data have been fitted with $\cos^2\theta$ functions shown by the solid lines. Filled squares represent the offset between the curves for the Co and Co/Au samples. Within error, the offset is independent of the B orientation............................244

Figure 5.23. (a) THz electric field amplitude transmitted through Co (0% Au) (diamonds), Co/Au 35 % (circles) and Co/Au 42 % (squares) particle ensembles versus magnetic field strength in the parallel configuration. The Co/Au 42 % samples have about an order of magnitude more intensity attenuation than uncoated Co particles in a magnetic field of B = 150 mT. (b) Delay of the transmitted THz pulse through Co (0% Au) (diamonds), Co/Au 35 % (circles) and Co/Au 42 % (squares) particle ensembles versus magnetic field strength for the parallel configuration. (c) THz electric field amplitude transmitted through Co (0% Au) (diamonds), Co/Au 35 % (circles) and Co/Au 42 % (squares) particle ensembles versus magnetic field strength in the perpendicular configuration. The transmitted electric field amplitude versus the magnetic field strength for the Co/Au 35 % and Co/Au 42 % particle ensembles are shown in (d) and (e), respectively. The inset in (e) shows magnetization measurements of the Co particles up to ±1.0 T. (f) Normalized, time-averaged electric field amplitude (in an applied field of B = 160 mT) transmitted through 3 mm thick samples of Co/Au particles versus the Au film thickness in the perpendicular configuration...247

Figure 5.24. The upper image depicts an illustration of spin accumulation in the Au layer. The lower image shows the measured resistivity of the Au layer versus the film thickness. The resistivities are measured using a four-point probe technique on witness Au films deposited on glass slides..248

Figure 6.1. A human hand is a common example of a chiral medium............................256

Figure 6.2. THz electromagnetic wave interaction with a helical element in the axial configuration and transverse configuration..260

Figure 6.3. Diagram depicting a helical conformation that is characterized by a wire diameter, pitch, and helix diameter...262

Figure 6.4. A diagram of the setup used to characterize the THz on-axis transmission through a subwavelength helix...262

Figure 6.5. The measured right circular $E_r(t)$ (solid line) and left circular $E_l(t)$, (empty circles) electric field pulses through helices of various lengths, along with a reference pulse transmitted through the screening aperture...264

Figure 6.6. Trajectories of the tip of the electric field vector for the transmission through the aperture and helices having m = 4, 6, 8, 10, and 12..265

Figure 6.7. (a) Degree of polarization circularization for the transmitted pulse through the aperture and helices having m = 4, 6, 8, and 12. (b) depicts the normalized time-partitioned Fourier spectra of the right-circularly polarized transmission through the 12 turn helix, using a Fourier window of 3.2 ps. The experimental transmission spectra show a cut off frequency at 0.74 ± 0.05 THz. This cut off behaviour can be understood by considering the guided modes in the helix. Approximating the helix as an infinite cylindrical waveguide, the helix has a cut off frequency of 0.75 THz, in excellent agreement with the experimental data. (c) The frequency-dependent imaginary refractive index difference between the RH and LH fields propagated through the helix calculated over the transient regime and over the steady state regime...268

Figure 6.8. A vector plot of the three-dimensional FDTD-calculated electric field vector along the helical axis at times 0 ps, 4 ps, 7 ps, 14 ps, and 20 ps. The images include a cross-sectional view of the 15 turn helical structure employed in the simulation. The size parameters of the helix used in the simulations physically match those of the helix used in the experiments. The arrow indicates the direction of propagation of the incident THz electric field pulse...270

Figure 6.9. (a) The experimental and FDTD-calculated group delay is plotted versus m. (b) displays the experimental and calculated right-circular and left-circular electric field pulses transmitted through an m = 12 helix. (c) The experimentally measured and three-dimensional FDTD-calculated transmission power spectra for m = 12 are compared. The inset in (c) shows the calculated trajectory of the tip of the electric field vector for m = 12. (d) Calculated and experimental degree of polarization circularization for an m = 12 helix...271

Figure 6.10. A plot of the electric field intensity at t = 14 ps along planes cutting through turn number 8, 9, 10, 11, and 12. The white arrows superimposed on the intensity plots indicate the orientation of the electric field vector on a plane. A representative plot of the

Poynting vector at the plane cutting through turn number 12 shows the cycling behaviour of the electromagnetic energy flow in the helix..273

Figure 6.11. The calculated Poynting vector distributions within four planes perpendicular to the helical axis intersecting turns (a) 8, (b) 9, (c) 10, and (d) 11 of the helix at time t = 8.6 ps.. The helix is centred at (300 μm, 300 μm). The distributions are depicted from a viewpoint of an observer facing the wave propagation direction..........274

Figure 6.12. (a) Several representative Poynting vector streamlines spanning m = 1 to m = 7 captured at an arbitrary time t = 10.6 ps calculated from the three-dimensional FDTD simulations. Nearly all of the streamlines are scattered outside the helix. The width of the streamlines is proportional to the time rate of change of the energy density. The streamlines are depicted with a cross sectional view of the helical structure employed in the simulations. (b) A head-on perspective of the same vector streamlines shown in (a). (c) shows four representative Poynting vector streamlines spanning m = 8 to m = 12 captured at t = 10.6 ps calculated from the three-dimensional FDTD simulations. The yellow and red Poynting vector streamlines are scattered outside the helix after the third turn, while the green and blue streamlines are confined within the helix throughout the 4 turns. (d) shows a head-on perspective of the same vector streamlines shown in (c). (e) Based on the spatial locations where energy flow abruptly changes direction, the fundamental mode consisting of four points A, B, C, and D is constructed, coinciding with the locations where the Poynting vector changes direction.....................................277

Figure 6.13. (left axis) The time-dependent phase difference between the right-circularly polarized and left-circularly polarized pulse components transmitted through the reference (blue), the helix in the parallel configuration (yellow), and the helix in the perpendicular configuration (green). (right axis) The temporal right-circularly polarized waveforms transmitted through the helix are shown for the parallel and perpendicular configurations. The inset shows the reference pulse transmitted through the photopolymer matrix without a helix...281

Figure 6.14. Illustration of the sub-helical structures used in the experiments. The sub-helical structures are characterized by a wire length per revolution...............................282

Figure 6.15. (a) Fourier spectra of the right-circularly polarized pulse transmitted through the helix and sub-helical structures where the wire length/revolution is 408 μm and 189 μm. (b) shows the circular birefringence (the difference in the effective left and right refractive indices) for the helical and sub-helical structures. (c) depicts the frequency-dependent chirality-induced optical path length difference between the right-circularly polarized and left-circularly polarized pulse components for the helical and sub-helical structures. (d) charts the chirality-induced optical path length difference at a central frequency of 0.45 THz versus the wire length/revolution..285

Figure A.1. Configuration of the laser pulse and THz emission with respect to the semiconductor surface..303

Figure A.2. Spatio-temporal evolution of the perpendicular (left) and parallel (right) current densities within n-GaAs at different times for $B = 0$ T. Note that the laser is illuminating the semiconductor surface at $z = 0$ from below at an angle of 45°..............309

Figure A.3. Electrostatic potential as a function of depth in n-GaAs at various times for $B = 0$ T..310

Figure A.4. Spatio-temporal evolution of the perpendicular (left) and parallel (right) current densities within n-GaAs at different times for $B = 6$ T. Note that the laser is illuminating the semiconductor surface at $z = 0$ from below at an angle of 45°..............310

Figure A.5. Electrostatic potential versus depth in InAs at various times for $B = 0$ T....312

Figure A.6. Spatio-temporal evolution of the perpendicular (left) and parallel (right) current densities within InAs at different times for $B = 0$ T. Note that the laser is illuminating the semiconductor surface at $z = 0$ from below at an angle of 45°..............312

Figure A.7. Spatio-temporal evolution of the perpendicular (left) and parallel (right) current densities within InAs at different times for $B = 3$ T. Note that the laser is illuminating the semiconductor surface at $z = 0$ from below at an angle of 45°..............314

Figure A.8. The z-polarized (top) and x-polarized (bottom) temporal waveforms of THz emission from n-GaAs at various magnetic field strengths..318

Figure A.9. (a) Normalized THz emission spectra from n-GaAs at $B = 3$ T and $B = 6$ T. (b) Normalized THz emission spectra from InAs at $B = 3$ T and $B = 12$ T.....................316

Figure A.10. The z-polarized (top) and x-polarized (bottom) temporal waveforms of THz emission from InAs at various magnetic field strengths...317

Figure A.11. THz emission power for a) n-GaAs and b) InAs as a function of the magnetic field strength..319

Figure A.12. Enhancement factor for (a) n-GaAs and (b) InAs as a function of the optical fluence. For n-GaAs, the enhancement is the ratio between the THz emission power at 6 T and 0 T. The enhancement for InAs is the ratio of the THz power at 3 T and 0 T. The inset in (b) is taken from Ref. [7]..321

Figure B.1. (a) The THz electric field and probe electric field are shown in the laboratory coordinate system (x_o, y_o, z_o) and the rotated coordinate system (x_2, y_2, z_2). The laboratory coordinate system is aligned with the [−1,−1, 2], [−1, 1, 0], and [1, 1, 1] directions. (b) The rotated coordinate system (x_2, y_2, z_2) is shown with the quarter wave-plate coordinate system (x_3, y_3, z_3). (c) The coordinate systems for the quarter wave-plate (x_3, y_3, z_3) and Wollaston prism polarizers (x_4, y_4, z_4) are shown..328

Figure F.1. (a) Magnitude and (b) phase spectra of the microwave transmission through the helix (used in Chapter 6) where the helical axis is aligned parallel to the microwave polarization. (c) Magnitude and (d) phase spectra of the microwave transmission through the helix where the helical axis is aligned perpendicular to the microwave polarization........361

List of Tables

Table 1.1. Plasma frequency and collision rate for selected metals. Also shown are the real and imaginary parts of the permittivity for the selected metals at a frequency of 1 THz. The data is taken from Ref. [13]..21

Table A.1. List of parameters used in the numerical simulations....................................307

List of Abbreviations

AMR	anisotropic magnetoresistance
DOS	density of states
F	ferromagnetic
F/N	ferromagnetic/nonmagnetic
FDTD	finite difference time-domain
LH	left-handed
N	nonmagnetic
PC	photoconductive
RH	right-handed
THz	terahertz
TDS	time-domain spectroscopy
TM	transverse magnetic
XPS	x-ray photoelectron spectroscopy

Table of Contents

1. Introduction

1.1 Light Interaction with Small Particles....2

1.2 Scope of the Thesis....10

1.3 Theoretical Background....12

  1.3.1 Electrodynamics in Matter....13

  1.3.2 Microscopic Picture: Dielectrics....16

  1.3.3 Microscopic Picture: Metals....18

  1.3.4 Surface Plasmon Waves....21

    1.3.4.1 Surface Plasmon Polaritons....21

    1.3.4.2 Coupling Electromagnetic Waves into Surface Plasmon Polaritons....25

    1.3.4.3 Particle Plasmons....29

    1.3.4.4 Particle Plasmon Decay....37

  1.3.5 Effective Medium Approximation....40

1.4 Terahertz Time-Domain Spectroscopy....44

2. Terahertz Electromagnetic Wave Propagation in Mesoscopic Dielectric Media

2.1 Scattering of Electromagnetic Waves by Dielectric Particles....54

2.2 Terahertz Time-Domain Spectroscopic Investigation of Scattering Media....56

  2.2.1 Theoretical Background of Electromagnetic Wave Scattering in Strongly Scattering Dielectric Media....59

  2.2.2 Experimental Investigation of Terahertz Electromagnetic Wave Scattering in Strongly Scattering Dielectric Media....64

2.2.3 Results and Discussion....69
2.3 Conclusion....76

3. Terahertz Particle Plasmons

3.1 Background....81
3.2 Terahertz Localized Particle Plasmon on a Single Metallic Particle....87
3.3 Terahertz Electromagnetic Properties of an Ensemble of Metallic Particles...94
3.4 Enhanced Terahertz Transmission through Metallic Particle Ensembles....98
3.5 Calculations of Terahertz Transmission through Metallic Particle Ensembles....107
3.6 Terahertz Transmission through Different Metallic Particle Ensembles....114
3.7 From the Mesoscopic Regime to the Bulk Regime....115
3.8 Further Investigations of Plasmonic-Enhanced Terahertz Transmission....123
3.9 Influence of Contact Resistance on Terahertz Particle Plasmons on Bimetallic Microparticles....136
3.10 Subsurface Probing of Terahertz Particle Plasmons....150
3.11 An Amorphous Metamaterial at Terahertz Frequencies....160
3.12 Conclusion....176

4. Terahertz Time-Domain Spectroscopy of Phase Transition Phenomena in Metallic Particles

4.1 Background....185
4.2 Terahertz Spectroscopic Investigation of Phase Transition Phenomena in Metallic Particles....186
4.3 Conclusion....197

5. Terahertz Spinplasmonics

5.1 Background....202
5.2 Ferromagnetic Metals....203
5.3 Spintronic Devices....208
5.4 Active Plasmonics....212
5.5 Magnetically Anisotropic Terahertz Particle-Plasmon-Mediated Transmission....215
5.6 Isotropic Magnetoresistance Signatures in the Terahertz Transmission through Porous Ferromagnetic Particles....227
5.7 Electron-Spin-Dependent Terahertz Particle-Plasmon-Mediated Transmission....236
5.8 Conclusion....250

6. Terahertz Electromagnetic Wave Propagation in Mesoscopic Chiral Materials

6.1 Background....256
6.2 Axial Terahertz Electromagnetic Wave Propagation in a Helical Structure....260
6.3 Transverse Terahertz Electromagnetic Wave Propagation in a Helical Structure....278
6.4 Conclusion....287

7. Conclusions and Outlook

7.1 Summary....293
7.2 Future Outlook....296

7.3 Conclusion....298

Appendices

A. Model of Magnetic Field Enhanced Terahertz Emission from Semiconductor Surfaces....301
B. Nonlinear Response of <111> ZnSe....325
C. Finite Difference Time-Domain Calculations....329
D. Analysis Techniques....356
E. Metallization Processes and Characterization....359
F. Microwave Transmission Spectra of the Helical Structure....360

Chapter 1:

Introduction

1.1 Light Interaction with Small Particles

The interaction of electromagnetic waves with small particles is ubiquitous and causes common optical effects such as the bluish color of the sky, the cloudiness of milk, and the hues of a rainbow. Despite the striking diversity in these visual phenomena, the fundamental physics underlying their occurrences are the same. All media are comprised of electrons, protons, and neutrons. Upon excitation by an incident electromagnetic wave, the electronic charges are set in motion by the incident electric field. The oscillating charges in turn re-emit radiation in all directions. In addition to re-radiating electromagnetic energy, the electronic charges that constitute the particle may transfer energy into other forms, which appear as a loss in the incident electromagnetic energy, or absorption. Altogether, re-radiation and absorption of electromagnetic waves by the medium give rise to its electromagnetic properties.

Electromagnetic interaction with a medium is strongly dependent on the ratio of its dimensions to the wavelength of radiation, λ. When the medium is much larger than the wavelength, the medium's electromagnetic properties are largely determined by the response of the atoms, which constitute the medium, to the incident radiation. As the relevant dimensions of the medium approach the mesoscopic regime (between the atomic and wavelength scales), the effective electromagnetic properties of the medium can become vastly different than the bulk electromagnetic properties of the constituent material. Many examples of this are found in nature; for instance, fog appears opaque and white, whereas bulk water appears transparent and colorless. In this case, the effective optical properties of fog are vastly different than the optical properties of bulk

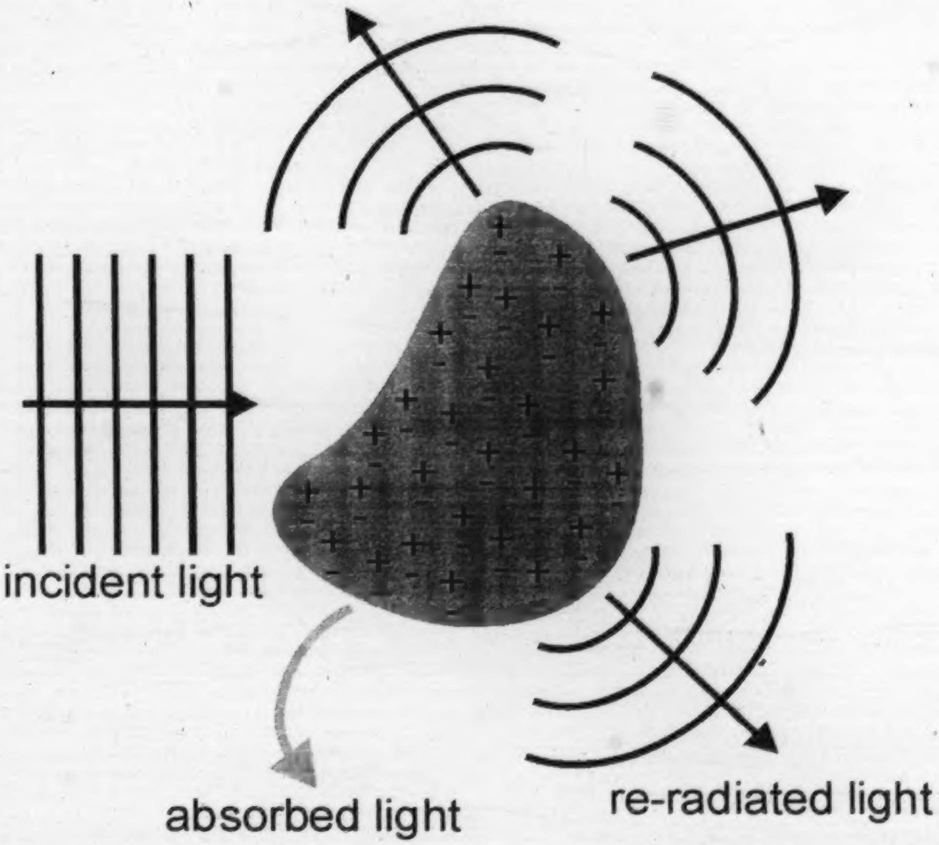
incident light
absorbed light
re-radiated light

Figure 1.1. Light interaction with an arbitrary particle. Light incident upon a particle from the left induces electronic charge motion. The oscillating charges re-radiate in all directions and also convert some of the incident electromagnetic energy into other forms.

water due to light scattering from the individual water droplets. To fully describe the optical properties of fog, one must take into account the intrinsic optical response of the water molecules in addition to extrinsic light scattering at the surface of the droplet.

Currently, the interaction of light with small, subwavelength sized structures has garnered incredible research attention. With the advent of advanced micro- and nano-fabrication capabilities, it has become possible to tailor the electromagnetic response of materials via structural engineering on mesoscopic size scales. Within the last few decades, research groups have demonstrated a wide range of extraordinary electromagnetic effects in media with subwavelength scale dimensions. In the 1990s, researchers discovered photonic band gap media, consisting of a periodic array of scatterers, which collectively inhibit reflection or transmission of light over a frequency range correlated to the spatial periodicity of the scatterers [1]. Another discovery is the demonstration that "artificial" magnetic materials can be constructed from nonmagnetic metals. These artificial materials consist of subwavelength scale split-ring resonators [2]. Electric field incident on the material drives current in the split-rings producing subwavelength sized magnetic dipoles that collectively generate an artificial magnetic response. One of the most exciting developments in the field of photonics is the recent demonstration that a group of subwavelength metallic scattering elements can exhibit negative refractive index at microwave frequencies [3]. In these experiments, microwave radiation propagated through a prism-shaped negative index medium is shown to refract at angles on the "wrong" side of the normal (i.e. negative angles). Recently, the concept of negative refraction has been extended into the visible regime using narrow waveguides consisting of two dissimilar metallic nano-layers sandwiched closely together [4]. The key feature of these waveguides is that their metallic layers support propagating surface plasmon polariton (SPP) waves at visible frequencies. With proper selection of the metallic constituents, the dispersion of the SPP modes supported by the waveguide can possess a negative slope at visible frequencies, leading to anti-parallel group and phase velocities (the energy and phase-fronts propagate in opposing directions). In this situation, the SPP modes propagate through the waveguide as if the waveguide had a negative index of refraction. This negative index behaviour has been confirmed in an experiment similar to the microwave counterpart, where visible light was shown to refract over negative angles when propagated through a prism-shaped SPP waveguide. In contrast to engineered materials, random media possess no spatial periodicity or order; thus, random media constitute the most general class of photonic systems. An electromagnetic wave propagating through a random medium undergoes many scattering events, which can give rise to a rich array of phenomena. In strongly scattering systems composed of subwavelength sized particles, interesting effects such as enhanced backscattering [5], weak localization, and universal conductance fluctuations in light transmission [6] have been observed. A fascinating phenomenon known as photon localization, the photonic analog of electronic localization, has also been predicted to occur in strongly scattering media [7, 8]. Thus far, however, reports of photon localization based on the exponential decay of the transmission through random, strongly scattering media have been debated, as absorption can emulate these signatures [9, 10].

The aforementioned discoveries of extraordinary electromagnetic phenomena arise from the interaction of light with dielectric or metallic structures possessing subwavelength scale heterogeneity. For structures with subwavelength scale dimensions, surface electromagnetic phenomena occurring at the interface between the dielectric or metallic structure and the ambient medium (commonly air) play a significant role in their electromagnetic properties. Radiation incident on a subwavelength sized dielectric structure is strongly affected by wave scattering from the surface of the structure. Generally, scattering occurs when an electromagnetic wave impinges on the interface between different dielectric media [Figure 1.2 (a)]. In the simplest situation where a system consists of two dielectric media with dimensions much larger than the wavelength, scattering occurs only at the single interface between the two media. Reflection and transmission from the single interface are determined by the refractive indices of the media, the angle of incidence, the polarization of the electromagnetic wave, and the geometry of the interface. When the spatial variations of the interface are less than the wavelength of the electromagnetic wave, reflection and refraction are described by the famous Snell's Law. As the number of constituents comprising the system increases, the incident electromagnetic wave undergoes an increasing number of scattering events. The situation becomes more complex as the size of the constituents approaches the wavelength of the electromagnetic wave. In this situation, the electromagnetic wave may undergo many scattering events over several oscillations of the wave, and it becomes increasingly difficult to analytically describe the electromagnetic properties of the system. In this regime, the effect of multiple scattering of light at the dielectric interface is a dominant contributor to the overall electromagnetic properties of the medium.

The physics underlying the interaction of an electromagnetic wave with a metallic medium are more complex than in the dielectric case. An electromagnetic wave incident on a metallic surface may simply scatter from the surface or, in certain situations, couple into a *surface plasmon wave* [Figure 1.2 (b)]. Surface plasmon waves are electromagnetic waves that are confined to the interface of a conductor and an insulator. These waves arise via coupling of the electromagnetic fields to conduction electron oscillations at the surface of the conductor. There are two categories of surface plasmons: surface plasmon polaritons (SPPs) and particle plasmons (or localized surface plasmons). Surface plasmon polaritons are propagating two-dimensional electromagnetic waves coupled to the surface of a conductor. Particle plasmons, on the other hand, are non-propagating electromagnetic fields confined to the surface of a subwavelength sized metallic structure. Since surface plasmons are confined to the surface of a conductor, they are able to concentrate electromagnetic energy over dimensions that are smaller than the wavelength. This characteristic of surface plasmons can lead to often unexpected, fascinating behaviour, especially in subwavelength sized metallic structures.

This thesis continues in the exploration of electromagnetic effects in mesoscopic dielectric and metallic media using THz time-domain spectroscopy. Compared with conventional visible and microwave spectroscopic techniques, time-domain spectroscopic investigations in the THz frequency range possess several advantages. Broadband (~ 1 THz) THz radiation sources enable spectroscopic measurements over a wide range of frequencies with a single measurement. Moreover, direct access to the coherent, time-domain THz electric field allows the extraction of both the amplitude and the phase of the field, without resorting to interferometric techniques commonly used in the visible regime. Combined with the polarization sensitivity of THz radiation detection, THz time-domain spectroscopy enables the direct characterization of the time-dependent amplitude, phase, and polarization of the electric field with femtosecond temporal resolution that is several orders of magnitude better than one oscillation cycle. Another advantage of THz spectroscopy is the relative ease of subwavelength sized sample fabrication relative to analogous investigations at higher frequencies of the visible spectrum. The relatively large wavelength of THz radiation compared to visible radiation implies that subwavelength structures can be easily fabricated without complicated nanofabrication methods. This also means that the sample dimensions can be extremely well-controlled relative to the wavelength of the radiation. In addition to the technical advantages of THz time-domain spectroscopy compared to techniques in neighboring frequency ranges, the THz frequency range is interesting to explore because many materials possess unique properties at THz frequencies. The characteristic vibrational and rotational resonances of many gas and liquid molecules commonly lie at THz frequencies. Moreover, many semiconductors have unique phonon absorption bands in the THz regime. Since many visibly opaque semiconductor and dielectric media are transparent at THz frequencies, THz radiation is ideal for imaging applications. In particular, one promising application of THz radiation is biomedical imaging, since the non-ionizing nature of THz radiation reduces cell damage common to conventional techniques using x-rays. Furthermore, solid state matter shows a stunning range of electromagnetic properties in the THz regime. For example, at THz frequencies, the real permittivity of dielectrics, $\mathrm{Re}[\varepsilon_{dielectric}] \sim 1$, whereas the real permittivity of metals, $\mathrm{Re}[\varepsilon_{metal}] \sim -10^5$. This is strikingly different than the real permittivity of metals at visible frequencies, where $\mathrm{Re}[\varepsilon_{metal}] \sim -10$. Indeed, the wide range of phenomena and the remarkable diversity in the electromagnetic properties of matter at THz frequencies

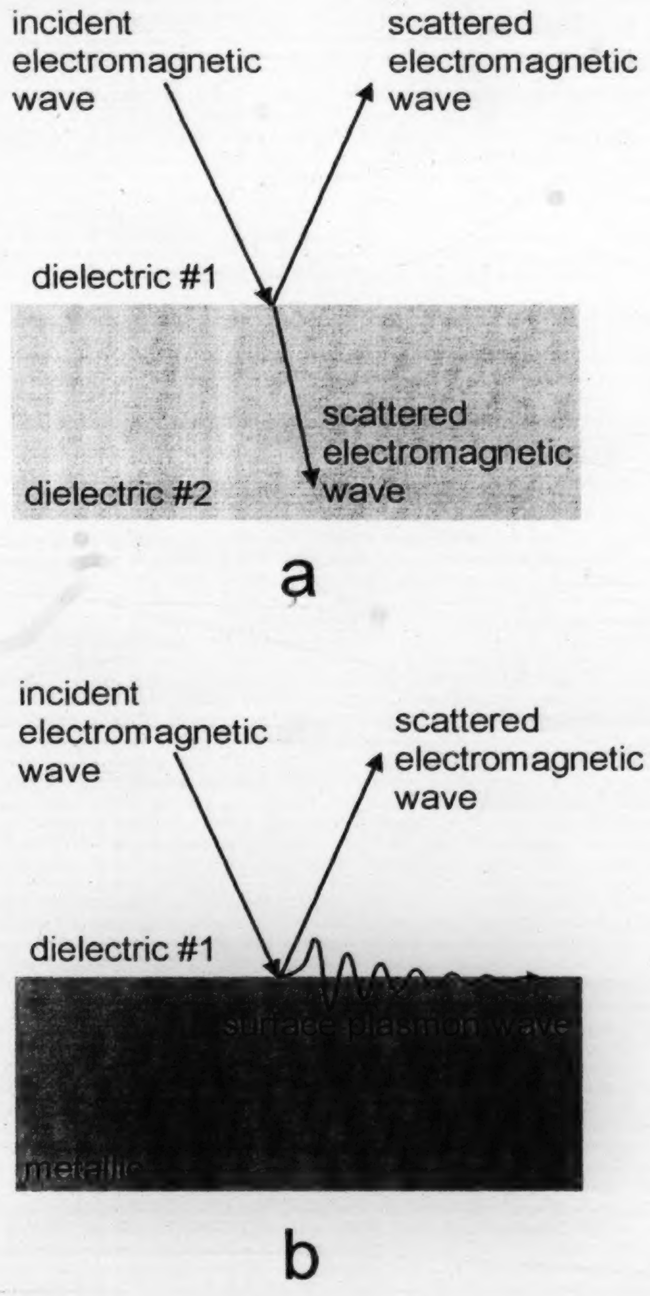
incident electromagnetic wave
scattered electromagnetic wave
dielectric #1
scattered electromagnetic wave
dielectric #2
a
incident electromagnetic wave
scattered electromagnetic wave
dielectric #1
surface plasmon wave
metallic
b

Figure 1.2. Illustration of electromagnetic wave interaction at the surface of (a) a dielectric medium and (b) a metallic medium. An electromagnetic wave incident on the dielectric surface is scattered. On the other hand, an electromagnetic wave incident on a metallic surface (it is assumed that the metal is opaque) is scattered and, in certain situations, may couple to a surface plasmon wave.

makes this regime both scientifically rich and technologically important.

This thesis explores several aspects of THz electromagnetic wave interaction with subwavelength structures. Terahertz electromagnetic scattering within heterogeneous dielectric media, THz surface plasmon interaction with heterogeneous metallic media, and THz optical activity in subwavelength chiral structures are explored with the overall goal of understanding the fundamental electromagnetic interactions on mesoscopic scales that lead to their effective properties.

1.2 Scope of the Thesis

Chapter 2 explores THz electromagnetic wave propagation in strongly scattering random dielectric media composed of subwavelength sized sapphire particles. In particular, it is shown that in the regime where the medium heterogeneity scale is less than the wavelength, the effective medium approximation becomes invalid, marking the onset of diffusive photon transport through the random dielectric ensemble.

Chapter 3 examines THz electromagnetic wave propagation in random media composed of densely packed, subwavelength sized metallic particles. In contrast to dielectric particles, metallic particles are individually opaque at THz frequencies. However, it is shown that dense ensembles of opaque metallic particles can exhibit surprisingly high THz electromagnetic transparency. The transparency of the metallic particle collection arises from the excitation of localized particle plasmons on the individual metallic particles. The close proximity of nearest neighbor particles leads to strong near-field, plasmonic coupling between particles. Such near-field coupling transports THz electromagnetic energy across the extent of the ensemble, which can exceed the skin depth by several orders. The influences of particle size, particle shape, and metal conductivity on the transmission phenomenon are studied. In further investigations of this phenomenon, it is shown that coating the metallic particles with nano-scale layers of a different metal causes strong attenuation of the transmitted radiation. The attenuation arises from interface resistance at the junction between the dissimilar metals. This effect is applied to spatially probe the THz electromagnetic charge induction within the surface of the metallic particles. Experimental results using bimetallic multilayered particles show that particle plasmon formation on the individual particles occurs within a skin depth of the particle surface.

In Chapter 4, THz time-domain spectroscopy is applied as a non-invasive, spectroscopic probe of phase transition phenomena in metallic media composed of subwavelength sized particles. The experimental results reveal marked phase modulation of the THz electromagnetic wave transmission through the metallic medium at the melting point temperature, indicating the onset of solid-liquid phase transformation.

Chapter 5 introduces methods to modulate the THz electromagnetic properties of metallic particle ensembles via electron-spin-dependent phenomena. It is shown that ferromagnetic particle ensembles can exhibit strong, tunable birefringence at THz frequencies with the application of an external magnetic field. The birefringence is caused by anisotropic magnetoresistance inherent to the ferromagnetic medium. Another method to achieve magnetically tunable transmission is via electron-spin-dependent phenomena in ferromagnetic/nonmagnetic composite media. It is demonstrated that an ensemble of ferromagnetic particles coated with nonmagnetic nano-layers shows enhanced magnetic attenuation, delay and pulse re-shaping of the transmission relative to an ensemble of uncoated ferromagnetic particles. The enhanced magnetic effect in the coated particles is attributed to electromagnetically driven electron spin accumulation in the nonmagnetic layer.

Electromagnetic interaction with a subwavelength sized particle that is asymmetric, or chiral, may lead to an effect known as optical activity. To elucidate the relationship between a subwavelength scale chiral structure and its optical activity, Chapter 6 examines THz pulse propagation within subwavelength size helical structures for both axial and transverse electromagnetic wave excitation. In the axial case, it is shown that optical activity manifests as resonant polarization circularization due to resonant propagation modes established along the helical axis. In contrast, for transverse excitation of the helical conformation, non-resonant polarization rotation of the forward scattered radiation is measured. Further investigations of the polarization rotation associated with sub-helical structures in the transverse case reveal that polarization rotation arises from single scattering from the helical structure.

1.3 Theoretical Background

This thesis explores light interaction with mesoscopic media in the context of classical optics, electrodynamics theory, and solid state theory. The fundamental concepts underlying these theories will be introduced in this section to equip the reader with the necessary tools for the remainder of the thesis. Classical electrodynamics in matter will be first discussed, followed by a brief treatment of solid state theory to describe the response of homogeneous dielectrics and homogeneous metals to external electromagnetic excitation. The physics underlying surface plasmon wave phenomena at the surface of metals is discussed, with particular emphasis on localized particle plasmons on subwavelength sized metallic particles. The electromagnetic response of heterogeneous media is often described via effective medium approximations, which will also be introduced. For a comprehensive treatment of these fundamental theories, the reader is referred to classical texts on electrodynamics by Jackson [11] and solid state theory by Ashcroft and Mermim [12].

1.3.1 Electrodynamics in Matter

In the 19th century, James Clerk Maxwell developed a set of equations that describe the spatial and temporal evolution of electric and magnetic fields in matter. Using these equations, Maxwell theoretically showed that light could propagate as a transverse electromagnetic wave. By solving for the speed of the electromagnetic wave and using known electric and magnetic properties of materials, Maxwell arrived at a stunning conclusion: the propagation speed of the electromagnetic wave was equivalent to the speed of light. This remarkable insight inextricably linked the fields of optics and electromagnetism, and has since provided the backbone to classical understanding of light-matter interaction.

At a given location $\boldsymbol{r}$ and time t, an electromagnetic wave exists as oscillating electric, $\boldsymbol{E}(r,t) = \boldsymbol{E}_o\, e^{i(\boldsymbol{k}\cdot\boldsymbol{r}-\omega t)}$, and magnetic, $\boldsymbol{B}(r,t) = \boldsymbol{B}_o\, e^{i(\boldsymbol{k}\cdot\boldsymbol{r}-\omega t)}$, fields, where ω is the frequency of oscillation, $|\boldsymbol{k}| = 2\pi/\lambda$ is the wavevector, and $\boldsymbol{E}_o$ and $\boldsymbol{B}_o$ are the vector electric and magnetic field amplitudes. Upon interacting with a material, the external $\boldsymbol{E}$ and $\boldsymbol{B}$ fields induce polarization, $\boldsymbol{P}$, and magnetization, $\boldsymbol{M}$, responses in the material. The total electromagnetic fields consist of both the externally applied fields associated with the electromagnetic wave and the induced fields arising from the polarization and magnetization of the material. It is useful to define the displacement field, **D**, and the magnetic flux density, **H**, by

$$\boldsymbol{D} = \varepsilon_o \boldsymbol{E} + \boldsymbol{P} \tag{1.3.1.1}$$

$$\boldsymbol{H} = \boldsymbol{B}/\mu_o - \boldsymbol{M} \tag{1.3.1.2}$$

where $\varepsilon_o = 8.854 \times 10^{-12}$ Fm^{-1} and $\mu_o = 4\pi \times 10^{-7}$ NA^{-2} are the permittivity and permeability of free-space, respectively. Maxwell's equations can be subsequently written as

$$\nabla \cdot \boldsymbol{D} = \rho_F \tag{1.3.1.3}$$

$$\nabla \cdot \boldsymbol{B} = 0 \tag{1.3.1.4}$$

$$\nabla \times \boldsymbol{E} = -\partial \boldsymbol{B}/\partial t \tag{1.3.1.5}$$

$$\nabla \times \boldsymbol{H} = \boldsymbol{j}_F + \partial \boldsymbol{D}/\partial t \tag{1.3.1.6}$$

where ρ_F is the free charge and $\boldsymbol{j}_F$ is the free current density. These equations describe the spatial and temporal evolution of electromagnetic fields in matter. The response of the material in the presence of electromagnetic fields is described by the constitutive relations. For the case of a linear (independent of the fields), homogeneous (independent of position), isotropic (independent of direction) medium, the constitutive relations are given by

$$\boldsymbol{P} = \varepsilon_o \chi_e \boldsymbol{E} \tag{1.3.1.7}$$

$$\boldsymbol{M} = \chi_m \boldsymbol{H} \tag{1.3.1.8}$$

such that

$$\boldsymbol{D} = \varepsilon \boldsymbol{E} \tag{1.3.1.9}$$

$$\boldsymbol{H} = \boldsymbol{B}/\mu \tag{1.3.1.10}$$

where χ_e and χ_m are the electric and magnetic susceptibilities, respectively, and $\varepsilon = \varepsilon_o(1+\chi_e)$ and $\mu = \mu_o(1+\chi_m)$. Additionally, the free current density $\boldsymbol{j}_F$ can be related to the external electric field, $\boldsymbol{E}$. The current density in most materials is proportional to the force per unit charge that is described by the Lorentz equation

$$\boldsymbol{j}_F = \sigma(\boldsymbol{E} + \boldsymbol{v} \times \boldsymbol{B}) \qquad (1.3.1.11)$$

where $\boldsymbol{v}$ is the velocity of the charge and σ is the conductivity of the medium. For the common situation where $v \ll$ the speed of light, c, the second term in Equation 1.3.1.11 can be ignored and the free current is given by

$$\boldsymbol{j}_F = \sigma\boldsymbol{E} \qquad (1.3.1.12).$$

Thus, the propagation of electromagnetic waves in materials is governed by three parameters: the permittivity, ε, the permeability, μ, and the conductivity, σ. These parameters in general depend on the frequency of the electromagnetic wave, i.e. $\varepsilon \equiv \varepsilon(\omega)$, $\mu \equiv \mu(\omega)$, and $\sigma \equiv \sigma(\omega)$. It is noteworthy that for a linear, homogeneous, isotropic medium that obeys Ohm's law, the permittivity and conductivity are related via $\varepsilon(\omega) = i\sigma(\omega)/\omega$. To understand the frequency dependence of the three constitutive parameters, consider a medium that is placed in a time-harmonic electric field. The electric field induces an average dipole moment per unit volume in the medium. For a linear, homogeneous, and isotropic medium, the direct relationship between $\boldsymbol{E}$ and $\boldsymbol{P}$ suggests that χ_e describes the response of the material to the driving force $\boldsymbol{E}$. If the response of χ_e is compared to that of a mechanical system driven by a harmonic force, it can be seen by analogy that χ_e depends on the frequency of the driving force. Because the constitutive parameters are different for different frequencies of an electromagnetic wave, it is useful to cast Maxwell's equations in the frequency-domain. If harmonic time dependence is assumed for all the fields, the constitutive relations (1.3.1.9), (1.3.1.10), and (1.3.1.12) are substituted into (1.3.1.3)-(1.3.1.6) to obtain

$$\nabla \cdot \boldsymbol{D} = \rho_F \tag{1.3.1.13}$$

$$\nabla \cdot \boldsymbol{B} = 0 \tag{1.3.1.14}$$

$$\nabla \times \boldsymbol{E} = + i\, \omega\, \mu(\omega)\, \boldsymbol{H} \tag{1.3.1.15}$$

$$\nabla \times \boldsymbol{H} = [\sigma(\omega) - i\, \omega\, \varepsilon(\omega)\,]\, \boldsymbol{E} \tag{1.3.1.16}$$

Maxwell's equations, in addition to the constitutive relations and appropriate boundary conditions for the fields, fully describe the spatial and temporal evolution of electromagnetic fields in matter. The phenomenological parameters ε, μ, and σ describe the macroscopic response of media to external electromagnetic excitation. Physically, the permittivity and conductivity describe the dipole moment per unit volume and free current density, respectively, induced by the incident electric field $\boldsymbol{E}$. The permeability describes the magnetic dipole moment per unit volume induced by the magnetic flux density, $\boldsymbol{H}$. However, these parameters do not inherently explain the microscopic interaction between an electromagnetic wave and matter, and must be extracted from experimental data or solid state theory. Thus, a microscopic picture of matter is required to fully appreciate the physical mechanisms of the interaction between light and matter.

1.3.2 Microscopic Picture: Dielectrics

The macroscopic electromagnetic properties of homogeneous dielectrics arise from microscopic processes that can be separated into three regimes: electronic, dipolar, or ionic. Electronic contributions originate from the displacement of the electron relative to the nucleus, ionic contributions come from the displacement of a charged ion relative to the other ions, and dipolar contributions arise from the displacement of molecules with permanent electric dipoles. Dipolar and ionic portions of the polarizability are relatively small due to the relatively large inertia associated with ions and molecules. Rather, the electromagnetic properties of dielectric media in the optical and infrared regimes are largely due to the electronic polarizability of the constituent atoms. This section briefly overviews the microscopic origins of the electronic contributions to the polarizability of dielectrics.

In dielectric media, electrons are bound to the nucleus. Upon external electromagnetic excitation at a frequency ω, the electrons are driven by the external electric field (magnetic field induced motion is ignored) via Lorentz force. The equation describing the motion of a driven electron in one dimension is given by

$$\frac{\partial^2 x_e}{\partial t^2}+\zeta\frac{\partial x_e}{\partial t}+\omega_o^2 x_e=\frac{e}{m^*}E_o e^{-i\omega t} \qquad (1.3.2.1)$$

where x_e is the electron displacement, ζ describes damping force acting on the bound electron due to collisions, ω_o is the resonance frequency of the electron which is bound to the nucleus, and m^* and e are the effective electron mass and charge, respectively. For low excitation, the electron oscillates at the frequency of excitation

$$x_e(t)=x_o e^{-i\omega t} \qquad (1.3.2.2).$$

Inserting (1.3.2.2) into the equation of motion gives the frequency-dependent response of a bound electron to external electromagnetic excitation

$$x_o(\omega)=\frac{e}{m^*(\omega_o^2-\omega^2-i\zeta\omega)}E_o \qquad (1.3.2.3).$$

The dipole moment, $p(t)$, associated with the electron is

$$p(t)=e\ x_e(t)=\frac{e^2}{m^*(\omega_o^2-\omega^2-i\zeta\omega)}E_o\mathrm{e}^{-i\omega t} \qquad (1.3.2.4).$$

In general, a medium is composed of many electrons with different resonant frequencies and damping coefficients. Assuming that there are N electrons per unit volume, the macroscopic polarizability of the medium is

$$P(\omega)=\frac{Ne^2}{m^*}\left(\sum_j\frac{g_j}{\omega_j^2-\omega^2-i\zeta_j\ \omega}\right)E(\omega) \qquad (1.3.2.5)$$

where g_j is the number of electrons having a resonant frequency of ω_j and a damping force of ζ_j. The relative permittivity of the dielectric, $\varepsilon_{dielectric}(\omega)\equiv\varepsilon_d(\omega)$, can therefore be expressed as

$$\varepsilon_d(\omega)=1+\frac{Ne^2}{\varepsilon_o m^*}\sum_j\frac{g_j}{\omega_j^2-\omega^2-i\zeta_j\ \omega} \qquad (1.3.2.6).$$

Therefore, the collective response of a bulk dielectric system to external electromagnetic excitation arises from the collective damped harmonic motion of the bound electrons. This simple picture also indicates how the permittivity of dielectrics inherently depends on the frequency of the electromagnetic wave, especially at frequencies near the resonance.

1.3.3 Microscopic Picture: Metals

In contrast to dielectrics, valence conduction electrons in a metal are not bound to their parent ions; hence, metals have been classically viewed as a "sea of electrons". In 1900, Drude developed a simple model to account for the electromagnetic properties of metals based on kinetic gas theory [12]. This model is effective in describing the electromagnetic properties of many metals, especially in the lower frequencies of the far-infrared. One should keep in mind, however, that this model does not account for absorption of light by interband electrons, which can become significant at higher frequencies. Additionally, the Drude model assumes that the metal is an ideal electron gas, neglects Coulomb interaction between conduction electrons, and also assumes there is no retardation in the response of the electrons.

In the Drude model, a metal is composed of independent, point-like electrons of mass m which are free to move under the influence of external fields. Upon electromagnetic excitation, electrons undergo drift motion along the direction of the electric field. These electrons randomly collide with other electrons, ions, and defects at a characteristic rate of $\Gamma = \tau^{-1}$, where τ is the average time between collisions. The one-dimensional equation describing the evolution of the position of a free electron, x_e, in an external electric field at a frequency ω is given by

$$\frac{\partial^2 x_e}{\partial t^2} + \Gamma \frac{\partial x_e}{\partial t} = \frac{e}{m} E_o \mathrm{e}^{-i\omega t} \qquad (1.3.3.1).$$

For low excitation, the electrons respond at the frequency of excitation

$$x_e = x_o \, \mathrm{e}^{-i\omega t} \qquad (1.3.3.2).$$

Inserting (1.3.3.2) into (1.3.3.1) gives a velocity associated with one electron, $v_e = \partial x_e / \partial t = v_o \, \mathrm{e}^{-i\omega t}$, of

$$v_o(\omega) = \frac{e \, E_o \, \mathrm{e}^{-i\omega t}}{m(\Gamma - i\omega)} \qquad (1.3.3.3).$$

The current density for a collection of electrons with a density N is given by

$$j_F(\omega) = Nev_e(\omega) = \frac{Ne^2 E_o \, \mathrm{e}^{-i\omega t}}{m(\Gamma - i\omega)} \qquad (1.3.3.4).$$

Invoking Ohm's law, the conductivity of a metal is therefore

$$\sigma(\omega) = \frac{Ne^2\tau}{m(1-i\omega\tau)} \qquad (1.3.3.5).$$

Assuming that the response of the metal arises from only free conduction electrons, (1.3.1.16) can be written as

$$\nabla \times \boldsymbol{H} = \left(\frac{Ne^2\tau}{m(1-i\omega\tau)} - i\omega\varepsilon_o \right) \boldsymbol{E} = -i\omega \left(\varepsilon_o - \frac{Ne^2\tau}{m\omega(\omega\tau+i)} \right) \boldsymbol{E} \qquad (1.3.3.6).$$

where one can define the relative frequency-dependent permittivity of the metal as

$$\varepsilon_{metal}(\omega) = 1 - \frac{Ne^2\tau}{m\omega\varepsilon_o(\omega\tau+i)} = 1 - \frac{\omega_p^2\tau^2}{(\omega^2\tau^2+1)} + \frac{i\omega_p^2\tau}{\omega(\omega^2\tau^2+1)} \qquad (1.3.3.7)$$

Here, the plasma frequency, ω_p, is the characteristic oscillation frequency of the sea of electrons and is expressed as $\omega_p = Ne^2/\varepsilon_o m$. The plasma frequency of metals Au, Ag, Pt, and Cu are shown in Table 1.1. For $\omega\tau >> 1$, then $\varepsilon_{metal}(\omega)$ is approximated as

$$\varepsilon_{metal}(\omega) = 1 - \frac{\omega_p^2}{\omega^2} \qquad (1.3.3.8).$$

It is interesting to note that the plasma frequency determines the nature of electromagnetic wave propagation in a metal. Consider an electromagnetic wave inside a metal described by $\boldsymbol{E}(r,t) = \boldsymbol{E}_o\, e^{i(kr-\omega t)}$, where $k = 2\pi\sqrt{\varepsilon_{metal}(\omega)}/\lambda$ is the wavevector in the metallic medium. For $\omega > \omega_p$, the real part of the metal permittivity is positive, which implies that the wavevector is real. Thus, the electromagnetic wave in the metal is oscillatory in nature and propagation through the metal is allowed. On the other hand, for $\omega < \omega_p$, the real part of the permittivity is negative, which implies that the wavevector is imaginary. As a result, the electromagnetic wave in the metal is spatially attenuated and wave propagation is damped. Since ω_p typically lies in the ultraviolet range for most metals, metals are opaque to electromagnetic radiation at frequencies in and below the visible frequency range.

	Au	Ag	Pt	Cu
ω_p (s^{-1})	1.37×10^{16}	1.37×10^{16}	7.82×10^{15}	1.12×10^{16}
Γ (s^{-1})	4.05×10^{13}	2.73×10^{13}	1.25×10^{14}	1.38×10^{13}
Re[ε(1THz)]	1.12×10^{5}	2.39×10^{5}	5.52×10^{3}	5.45×10^{5}
Im[ε(1THz)]	7.20×10^{5}	1.04×10^{6}	9.24×10^{4}	1.20×10^{6}

Table 1.1. Plasma frequency and collision rate for selected metals. Also shown are the real and imaginary parts of the permittivity for the selected metals at a frequency of 1 THz. The data is taken from Ref. [13].

1.3.4 Surface Plasmon Waves

The interaction of electromagnetic waves with the interface between a metallic medium and a dielectric medium may lead to a rich array of electromagnetic phenomena. In particular, the interface may support electromagnetically coupled charge oscillations known as surface plasmon waves. Surface plasmons are generally categorized into propagating surface plasmon polaritons (SPPs) and non-propagating particle plasmons. The physics underlying both types of surface plasmon waves will be studied in this section. A complete review of surface plasmon waves and its applications is available in Ref. [14].

1.3.4.1 Surface Plasmon Polaritons

Surface plasmon polaritons (SPPs) are two-dimensional surface electromagnetic waves that propagate on the interface between a metallic and dielectric medium and are evanescently confined in the direction perpendicular to the interface. These waves are coupled to charge oscillations at the metallic/dielectric interface. Consider the situation shown in Figure 1.3. A SPP wave propagates along the x-direction and is confined to the interface (defined by the plane $z = 0$) between semi-infinite dielectric (medium 1) and metallic (medium 2) media. The dielectric and metallic media have permittivity values of $\varepsilon_d(\omega)$ and $\varepsilon_{metal}(\omega)$, respectively. The surface charge density associated with the electron

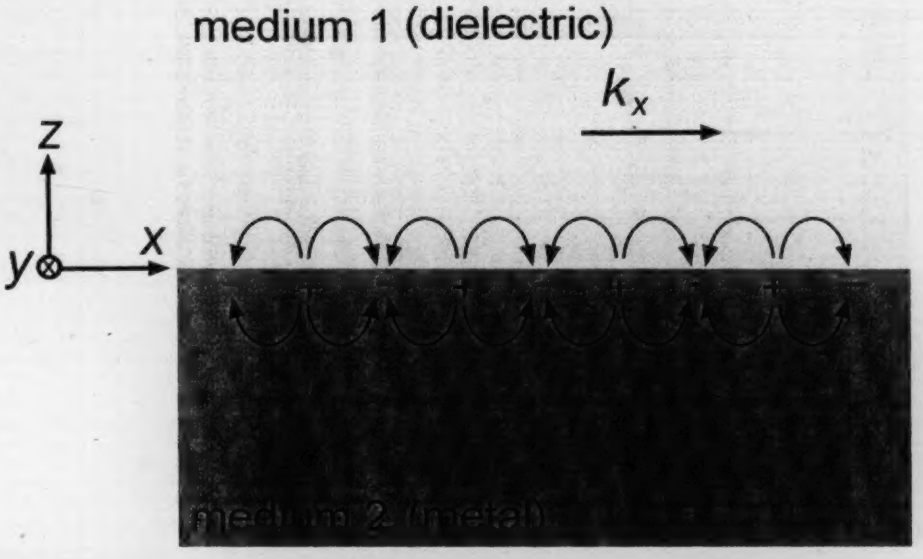

Figure 1.3. Electric field and charge configuration of a surface plasmon polariton wave propagating in the x-direction at the interface between medium 1 (dielectric) and medium 2 (metal).

plasma oscillation sets up macroscopic electric and magnetic fields in the two media with x- and z-components. There is no y-component of the wave since it is assumed that no charge oscillation exists along this direction. The waves have decaying components in the z-direction, confining the wave to the interface.

For an electron plasma wave propagating with frequency, ω, and wavevector, k_x, the expression for the associated electric and magnetic flux density fields are given by

$$\boldsymbol{E} = \boldsymbol{E_1}\, \mathrm{e}^{i(k_{x1}x-\omega t)}\mathrm{e}^{-\alpha_1 z} \qquad \text{for } z > 0 \qquad (1.3.4.1.1)$$

$$\boldsymbol{H} = \boldsymbol{H_1}\, \mathrm{e}^{i(k_{x1}x-\omega t)}\mathrm{e}^{-\alpha_1 z} \qquad \text{for } z > 0 \qquad (1.3.4.1.2)$$

$$\boldsymbol{E} = \boldsymbol{E_2}\, \mathrm{e}^{i(k_{x2}x-\omega t)}\mathrm{e}^{\alpha_2 z} \qquad \text{for } z < 0 \qquad (1.3.4.1.3)$$

$$\boldsymbol{H} = \boldsymbol{H_2}\, \mathrm{e}^{i(k_{x2}x-\omega t)}\mathrm{e}^{\alpha_2 z} \qquad \text{for } z < 0 \qquad (1.3.4.1.4)$$

where $\alpha_{1,2}$ and $k_{x1,x2}$ are the attenuation coefficients and wavevectors of the fields in medium 1 and 2, and $\boldsymbol{E} = (E_x, 0, E_z)$ and $\boldsymbol{H} = (0, H_y, 0)$.

From Maxwellian boundary conditions, the tangential components of $\boldsymbol{E}$ and $\boldsymbol{H}$ must be continuous across the interface. This implies that the propagation vector of the surface plasmon wave is equivalent in the two media, or

$$k_{x1} = k_{x2} = k_x \qquad (1.3.4.1.5).$$

The electric field of the SPP wave gives rise to a finite current density at the surface which is implicitly incorporated via the frequency-dependent permittivity $\varepsilon(\omega)$. Assuming that there is no additional externally induced current density, $j_F = 0$, the magnetic and electric fields of the SPP wave are related via Maxwell's equations

$$\nabla \times \boldsymbol{H} = \varepsilon(\omega)\frac{\partial \boldsymbol{E}}{\partial t} \qquad (1.3.4.1.6)$$

$$(-\partial H_y/\partial z, 0, 0) = -\, i\omega\, \varepsilon(\omega)\ (E_x, 0, E_z) \qquad (1.3.4.1.7)$$

$$\partial H_y / \partial z = i\omega\varepsilon(\omega)\ E_x \qquad (1.3.4.1.8).$$

Evaluating Equation (1.3.4.1.8) for medium 1 (dielectric) and medium 2 (metallic), the relations

$$-\alpha_1 H_y = i\omega\varepsilon_d(\omega)\ E_x \qquad (1.3.4.1.9)$$

$$\alpha_2 H_y = i\omega\ \varepsilon_{metal}(\omega)\ E_x \qquad (1.3.4.1.10)$$

are obtained. Equations (1.3.4.1.9) and (1.3.4.1.10) give the necessary condition for the existence of a SPP wave

$$\frac{\alpha_1}{\alpha_2} = -\frac{\mathrm{Re}[\varepsilon_d(\omega)]}{\mathrm{Re}[\varepsilon_{metal}(\omega)]} \qquad (1.3.4.1.11).$$

Confinement of the SPP wave at the interface (α_1, $\alpha_2 > 0$) requires that the real permittivity of the two media to have opposing signs. This condition is satisfied by an interface consisting of a metal and dielectric (i.e. $\mathrm{Re}[\varepsilon_{metal}(\omega)] < 0$, $\mathrm{Re}[\varepsilon_d(\omega)] > 0$).

Since the fields describe a propagating electromagnetic wave, they must obey the general wave equation

$$\nabla \times \boldsymbol{E} = \frac{\varepsilon(\omega)}{c^2}\frac{\partial^2 \boldsymbol{E}}{\partial t^2} \qquad (1.3.4.1.12)$$

where c is the speed of light.

By inserting (1.3.4.1.1) and (1.3.4.1.3) into (1.3.4.1.12), the relations

$$-k_x^2 + \alpha_1^2 = \varepsilon_d(\omega) / c^2\ \omega^2 \qquad (1.3.4.1.13)$$

$$-k_x^2 + \alpha_2^2 = \varepsilon_{metal}(\omega) / c^2\ \omega^2 \qquad (1.3.4.1.14)$$

are obtained. Using relations (1.3.4.1.13) and (1.3.4.1.14), the dispersion relation of the SPP wave is given by

$$k_x = \frac{\omega}{c}\sqrt{\frac{\varepsilon_d(\omega)\ \varepsilon_{metal}(\omega)}{\varepsilon_d(\omega) + \varepsilon_{metal}(\omega)}} \qquad (1.3.4.1.15).$$

Equation (1.3.4.1.15) dictates the SPP modes that can be occupied for a given energy on a metal/dielectric interface. Plots of the dispersion relations of an SPP mode on a metal/air interface and a free-space electromagnetic wave are shown in Figure 1.4, where it has been assumed that $\varepsilon_d(\omega) = 1$. As seen in the Figure, the dispersion relation for an electromagnetic wave is linear for all frequencies. While the dispersion relation for the SPP closely resembles that of the electromagnetic wave at low frequencies, at higher frequencies the SPP and electromagnetic wave dispersion relations differ considerably. Most importantly, for any given frequency, the dispersion relation for an SPP mode on a metal/air interface is below the dispersion relation for an electromagnetic wave propagating in air. This means that a free-space electromagnetic wave impinging on a metal/air interface cannot excite SPPs because at all frequencies, coupling from an electromagnetic wave to a SPP does not conserve momentum. Rather, free-space radiation incident on the semi-infinite metallic/dielectric interface will simply scatter and/or attenuate.

1.3.4.2 Coupling Electromagnetic Waves into Surface Plasmon Polaritons

A beam of radiation incident on the interface between a metal and a dielectric cannot excite SPP waves due to momentum mismatch between the electromagnetic wave and the SPP. Hence, special momentum matching techniques are required to enable photon to SPP coupling. Common optical techniques include prism coupling and grating coupling, which will be reviewed in this section.

Momentum matching between electromagnetic waves and SPPs can occur in a three layer system consisting of a thin metallic layer sandwiched between two different

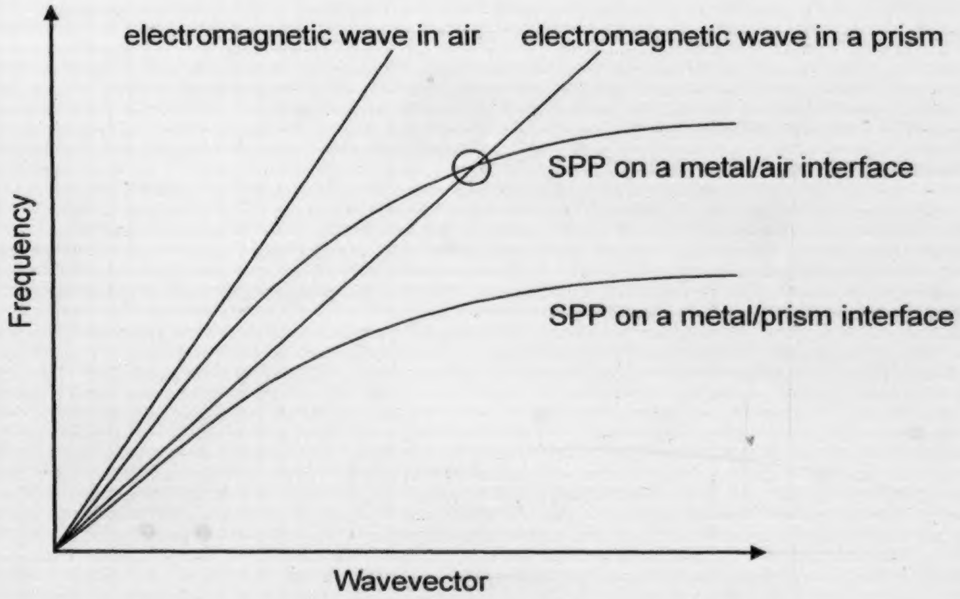
electromagnetic wave in air
electromagnetic wave in a prism
SPP on a metal/air interface
SPP on a metal/prism interface
Frequency
Wavevector

Figure 1.4. Dispersion relations for an electromagnetic wave in free-space, an electromagnetic wave in a prism, a SPP at a metal/air interface, and a SPP at a metal/prism interface. At the intersection of the dispersion relations for the electromagnetic wave in a prism and the SPP on a metal/air interface, electromagnetic wave coupling to SPPs is possible.

dielectrics, one with a lower permittivity and one with a higher permittivity. Commonly, the dielectric with the higher permittivity is in the form of a prism. An electromagnetic wave incident on the prism is refracted toward the metallic film. A prism is ideal for momentum matching because the momentum of the electromagnetic wave can be continuously varied by simply changing the refraction angle. The electromagnetic wave incident from the prism onto the metallic film has a momentum component along the metal surface of

$$k_x = k\sqrt{\mathrm{Re}[\varepsilon_{prism}]}\sin\theta_p \qquad (1.3.4.2.1)$$

where Re[ε_{prism}] is the real part of the permittivity of the prism (its frequency dependence has been omitted here for simplicity) and θ_p is the angle of incidence of the electromagnetic wave onto the metallic film. When momentum matching is achieved, the electromagnetic wave impinging on the metallic layer excites SPPs at the interface between the metal and the dielectric with the lower permittivity. This momentum matching condition it expressed as

$$k_x = \frac{\omega}{c}\sqrt{\mathrm{Re}\left[\frac{\varepsilon_d(\omega)\varepsilon_{metal}(\omega)}{\varepsilon_d(\omega)+\varepsilon_{metal}(\omega)}\right]} = k\sqrt{\mathrm{Re}[\varepsilon_{prism}]}\sin\theta_p \qquad (1.3.4.2.2)$$

where $\varepsilon_d(\omega)$ is the permittivity of the lower real permittivity dielectric. As seen in Figure 1.4, the prism configuration allows for coupling between electromagnetic waves and SPPs by lowering the dispersion relation for electromagnetic waves. When the dispersion relations for the electromagnetic wave and the SPP intersect, the electromagnetic wave can couple directly into charge oscillations while conserving both energy and momentum. There are two common realization of prism coupling shown in Figure 1.5 (a) and 1.5 (b): the Kretschmann [15] and Otto configurations [16].

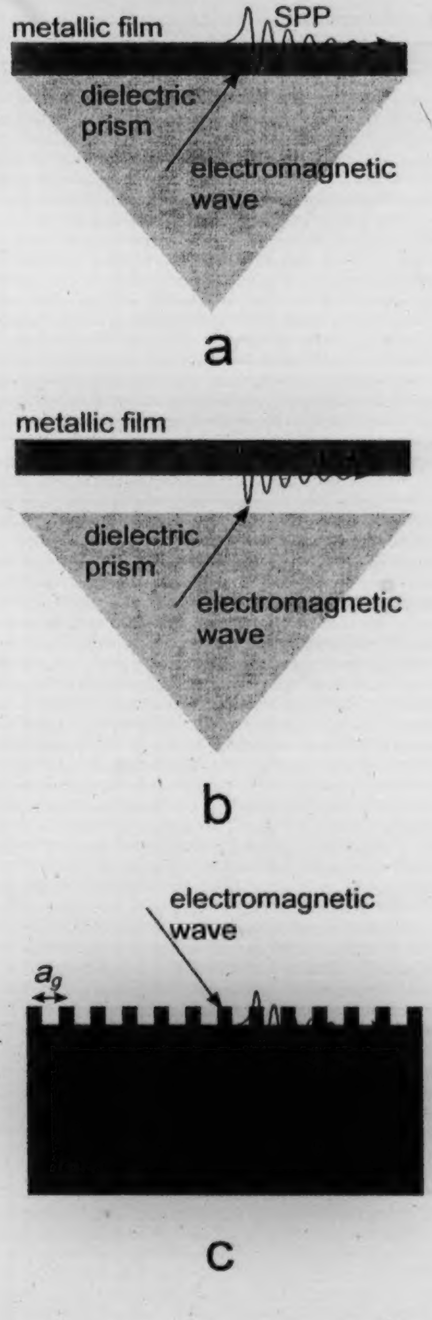
metallic film
SPP
dielectric prism
electromagnetic wave
a
metallic film
dielectric prism
electromagnetic wave
b
electromagnetic wave
a_g
c

Figure 1.5. (a) The Kretschmann configuration and (b) the Otto configuration for prism coupling from an electromagnetic wave to a SPP. Phase matching of electromagnetic waves to SPPs can also be achieved via (c) the grating coupling configuration.

In the former, a metallic film is deposited directly on the prism. Electromagnetic waves impinging on the metallic film at angles greater than the total internal reflection angle tunnel through the film and excite SPP on the other side of the film at the air/metal interface. In the Otto configuration, the metal film is separated from the prism by a small air gap. An electromagnetic wave incident from the prism suffers total internal reflection at the interface between the prism and air. Electromagnetic tunneling across the small air gap excites SPPs at the metal/air interface.

The mismatch in the momentum between an incident electromagnetic wave and a SPP wave can also be surmounted by a grating, as shown in Figure 1.5 (c). In this configuration, the metallic surface is patterned into a one-dimensional periodic grating having a spatial periodicity of a_g. An electromagnetic wave incident on the grating has a momentum component along the grating surface of

$$k\sin\theta_p \pm m_g v_{grating} \tag{1.3.4.2.3}$$

where $v_{grating} = 2\pi/a_g$ is the grating spatial frequency and m_g is the order (=1,2,3,...). Therefore, the grating can provide incident electromagnetic waves with additional momentum due to the spatial periodicity of the grating. Electromagnetic wave coupling into SPPs occurs when the condition

$$k_x = \frac{\omega}{c}\sqrt{\frac{\varepsilon_d(\omega)\varepsilon_{metal}(\omega)}{\varepsilon_d(\omega)+\varepsilon_{metal}(\omega)}} = k\sin\theta_p \pm m_g v_{grating} \tag{1.3.4.2.4}$$

is fulfilled.

1.3.4.3 Particle Plasmons

Surface plasmons can manifest as propagating SPP waves or non-propagating particle plasmons. It has been shown that the former consists of a two-dimensional, propagating surface wave coupled to the charge oscillations at a metal/dielectric interface. Non-propagating particle plasmons, by contrast, are localized excitations of the conduction electrons of a subwavelength metallic structure coupled to a surface electromagnetic field. Due to the subwavelength size of the metallic medium, localized particle plasmons can be generated via direct excitation of a subwavelength metallic particle by an electromagnetic wave. When radiation impinges on the metallic particle, conduction electrons driven by the incident field accumulate at the particle surface. These charges in turn produce an electromagnetic field that is highly confined to the interface between the particle and dielectric ambient, as shown in the illustration in Figure 1.6.

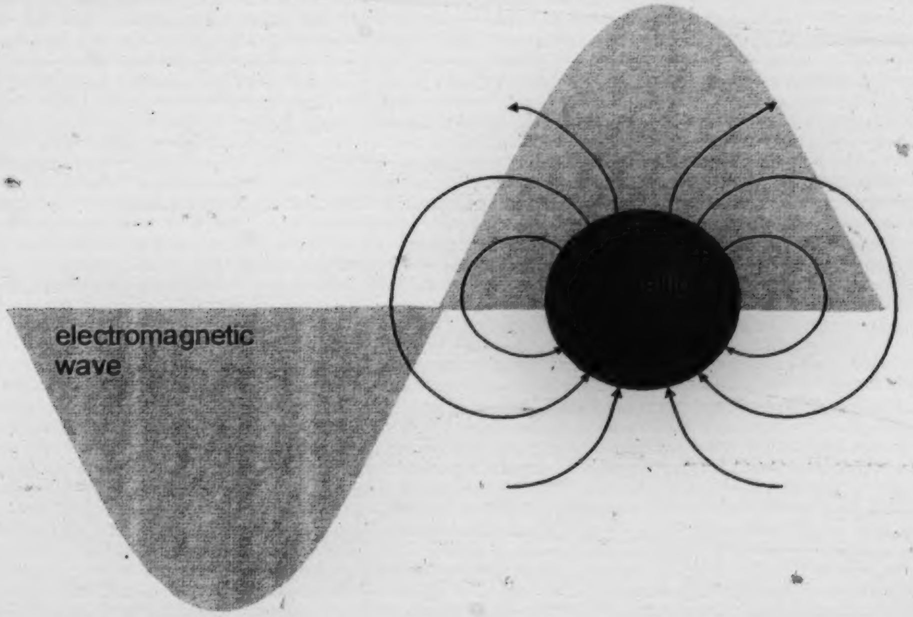

Figure 1.6. Conceptual illustration of a particle plasmon excited on a subwavelength sized metallic particle.

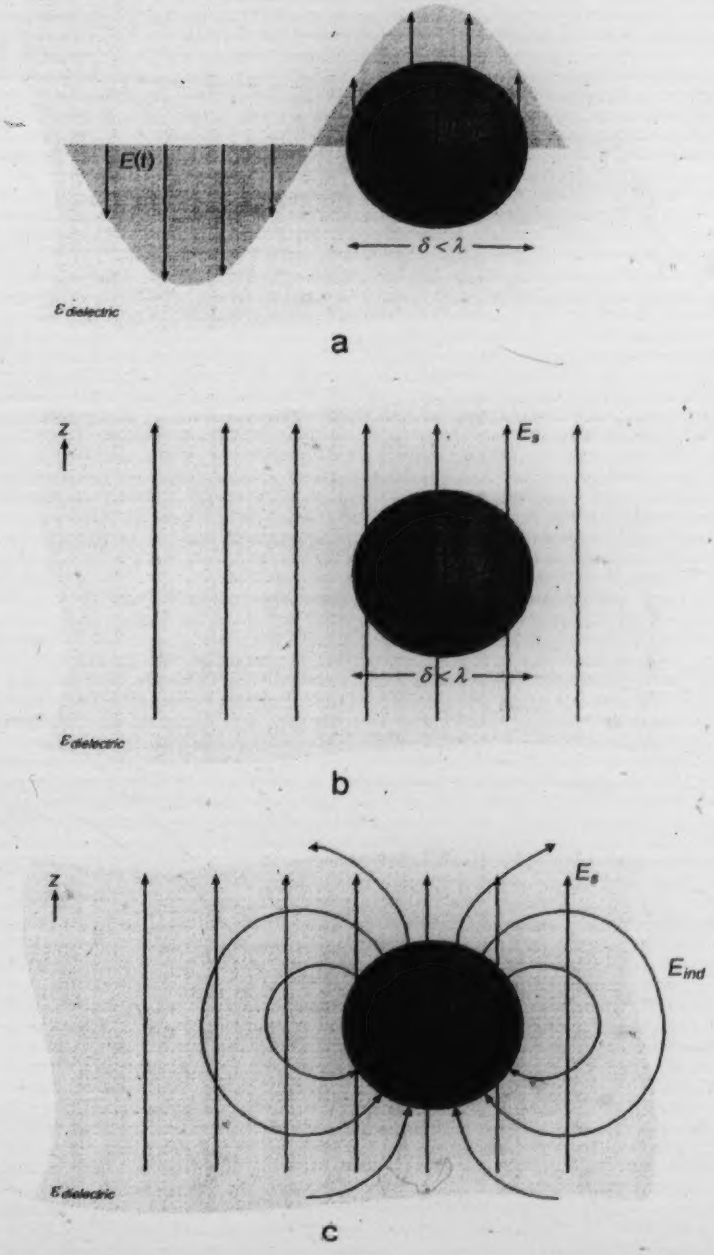
E(t)
δ < λ
ε dielectric
a
z
E s
δ < λ
ε dielectric
b
z
E s
E ind
ε dielectric
c

Figure 1.7. (a) Illustration of a subwavelength sized metallic sphere in a surrounding dielectric medium excited by an electric field, $E(t)$. By invoking the electrostatic approximation, (b) depicts the same subwavelength sized metallic sphere in a surrounding dielectric medium excited by a static, homogeneous electric field E_s. (c) shows the induced electric field due to the charge density induced by the static, homogeneous electric field E_s.

To understand the physics of particle plasmons, the interaction of an electromagnetic wave with a subwavelength spherical metallic particle is examined. Consider a homogeneous, isotropic, metallic sphere with permittivity $\varepsilon_{metal}(\omega)$ placed in a dielectric medium with permittivity $\varepsilon_d(\omega)$ excited by an electromagnetic wave, $E(t)$, as shown in Figure 1.7(a). For a particle having diameter, δ, much smaller than the wavelength, the response of the particle can be described via the electrostatic approximation where the incident electromagnetic wave is approximated as a static, homogeneous electric field oriented along the z-direction, $E_s\hat{z}$ [17]. To qualify this assumption, consider a metallic sphere centred at $z = 0$ with a diameter of δ illuminated by a plane electromagnetic wave. At any instant in time, the electric field amplitude of the wave illuminating the subwavelength sphere is $E(z) = E_o e^{ikz}$. If $\delta/\lambda << 1$, then $e^{-ik\delta/2} \approx e^{ik\delta/2}$, which implies that $E(-\delta/2) \approx E(\delta/2)$. The electric field is approximately uniform over the region occupied by the sphere because the electromagnetic wave has not accrued significant phase over the dimension of the sphere. Hence, the oscillating electromagnetic wave incident on the particle can be replaced by a static, homogeneous electric field.

Using the electrostatic approximation as shown in Figure 1.7(b), the externally applied static, homogeneous electric field, E_s, induces positive and negative charges at opposing sides on the surface of the metallic particle, and thus polarizing the particle. These induced charges produce an electric field which modifies the total electric field in the vicinity of the sphere. The total electric field consists of the electric field inside and outside of the sphere, E_1 and E_2, respectively, which satisfy the scalar potentials

$$E_1 = -\nabla\Theta_1 \qquad (1.3.4.3.1)$$

$$E_2 = -\nabla\Theta_2 \qquad (1.3.4.3.2).$$

At the boundary, the potentials must satisfy the condition

$$\Theta_1 = \Theta_2 \qquad (1.3.4.3.3).$$

Moreover, continuity of the normal component of the displacement vector across the interface between the metallic sphere and the surrounding dielectric, $D_{n1} = D_{n2}$, provides the second boundary condition

$$\varepsilon_{metal}(\omega)\frac{\partial\Theta_1}{\partial r} = \varepsilon_d(\omega)\frac{\partial\Theta_2}{\partial r} \qquad (r = \delta/2) \qquad (1.3.4.3.4)$$

where r is the radial distance from the origin. It has been assumed that the metallic sphere is immersed in a static, homogeneous electric field $E_s\hat{z}$. At far distances from the sphere, the electric field contributions arising from the induced charges attenuate far away, and the total electric field outside of the sphere only consists of the static, homogeneous electric field. Therefore, the potential Θ_2 far away from the sphere is given by

$$\lim_{r\to\infty}\Theta_2 = -E_s z \qquad (1.3.4.3.5).$$

It has been shown in [17] that the scalar potentials satisfying these conditions are

$$\Theta_1 = -\frac{3\varepsilon_d(\omega)}{\varepsilon_{metal}(\omega) + 2\varepsilon_d(\omega)}E_s r\cos\theta \qquad (1.3.4.3.6)$$

and

$$\Theta_2 = -E_s r\cos\theta + \frac{\delta^3}{8}\frac{\varepsilon_{metal}(\omega) - \varepsilon_d(\omega)}{\varepsilon_{metal}(\omega) + 2\varepsilon_d(\omega)}\frac{\cos\theta}{r^2}E_s = \Theta_{2ext} + \Theta_{2ind} \qquad (1.3.4.3.7).$$

where θ is the angle from the $\hat{z}$-axis. The potential outside of the sphere, Θ_2, consists of two terms, Θ_{2ext} and Θ_{2ind}. The first term describes the potential associated with the static, homogeneous electric field. On the other hand, the second term describes the potential associated with the electric field produced by the negative and positive charges induced on opposing sides of the metallic sphere. At far distances from the sphere, the charge distribution of the polarized metallic sphere appears like that of a dipole having a dipole moment p. Indeed, the potential Θ_{2ind} shares a similar functional form as the potential for an ideal dipole having a dipole moment p placed at the origin

$$\Theta_{dip} = \frac{p\cos\theta}{4\pi\varepsilon_d(\omega)r^2} \qquad (1.3.4.3.8).$$

Comparing Θ_{2ind} to Θ_{dip}, the potential of the polarized metallic sphere is that of a dipole where the dipole moment is given by

$$p = 4\pi\varepsilon_d(\omega)\frac{\delta^3}{8}\frac{\varepsilon_{metal}(\omega)-\varepsilon_d(\omega)}{\varepsilon_{metal}(\omega)+2\varepsilon_d(\omega)}E_s \qquad (1.3.4.3.9)$$

The dipole moment describes the response of a metallic sphere to the external excitation. The polarizability of the sphere, κ, is defined as

$$\kappa = 4\pi\frac{\delta^3}{8}\frac{\varepsilon_{metal}(\omega)-\varepsilon_d(\omega)}{\varepsilon_{metal}(\omega)+2\varepsilon_d(\omega)} \qquad (1.3.4.3.10).$$

It is noted that the polarizability shares the same functional form as the Claussius-Mossotti relation [11]. Thus, the far-field response of a subwavelength size metallic sphere immersed in an electrostatic field is dipolar, which arises from the induction of positive and negative charge on opposing sides of the sphere. The frequency dependence of the particle plasmon response is implicitly incorporated through the frequency-dependent permittivity of the metal [Equation (1.3.3.7)]. For example, for a subwavelength sized Au particle, the polarizability as a function of frequency is shown in Figure 1.8, where the permittivity of Au is obtained from the Drude model using experimentally measured parameters [18]. The particle plasmon response is characterized by a sharp resonance in the visible frequency regime where the condition $\varepsilon_{metal}(\omega) = -2$ is satisfied [17]. At the lower frequencies of the far-infrared and THz, the particle plasmon is non-resonant. In this regime, the electromagnetic response of the particle to electromagnetic wave excitation is often referred to as a *non-resonant particle plasmon*.

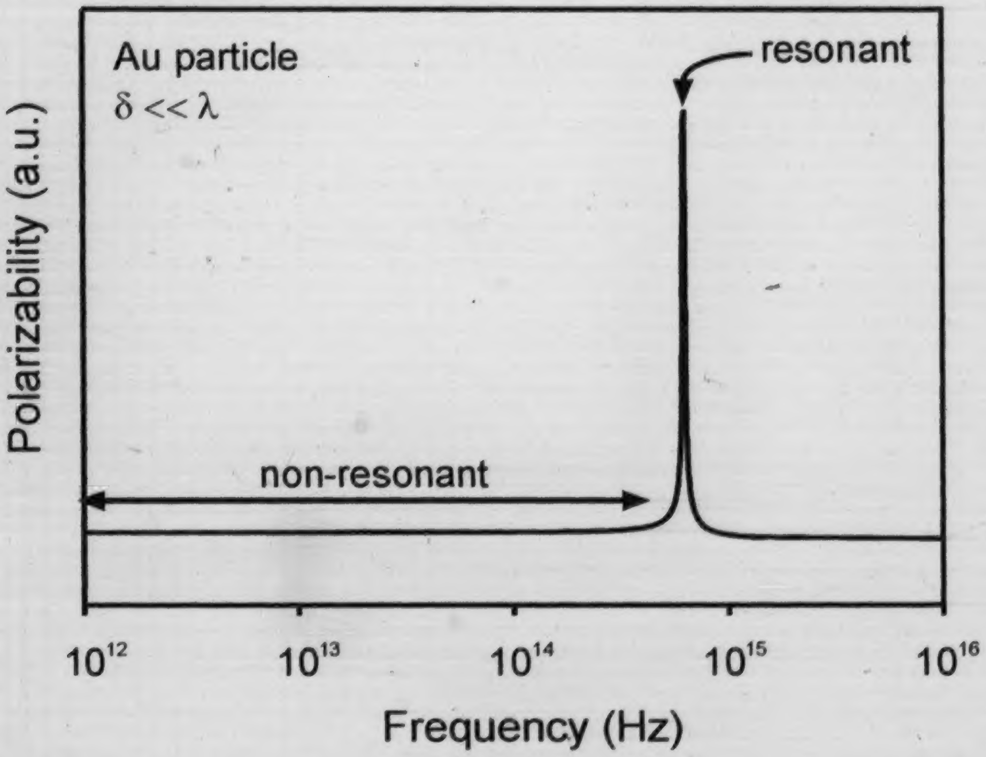

Figure 1.8. Polarizability of a subwavelength sized Au particle versus frequency. The resonant particle plasmon response for Au occurs in the visible frequency range.

From the potentials Θ_{2ext} and Θ_{2ind}, the vector electric field distribution in the vicinity of the metallic sphere can be determined. Using the relation $\boldsymbol{E} = -\nabla\Theta$, the static, homogeneous electric field can be expressed in spherical coordinates as

$$\boldsymbol{E}_s = -\nabla\Theta_{2ext} = E_s(\cos\theta\ \hat{r} - \sin\theta\ \hat{\theta}) \qquad (1.3.4.3.11).$$

where $\hat{r}$ and $\hat{\theta}$ are radial and angular unit vectors in spherical coordinates, respectively. Similarly, the electric field due to the induced charges on the sphere, $\boldsymbol{E}_{ind}$, is given by

$$\boldsymbol{E}_{ind} = -\nabla\Theta_{2ind} = -\frac{\delta^3}{8r^3}\frac{\varepsilon_{metal}(\omega) - \varepsilon_d(\omega)}{\varepsilon_{metal}(\omega) + 2\varepsilon_d(\omega)} E_s(2cos\theta\ \hat{r} + sin\theta\ \hat{\theta}) \qquad (1.3.4.3.12).$$

Assuming that the sphere is immersed in air, where $\varepsilon_d(\omega) = 1$, the induced electric field is given by

$$\boldsymbol{E}_{ind} = -\frac{\delta^3}{8r^3}\frac{\varepsilon_{metal}(\omega) - 1}{\varepsilon_{metal}(\omega) + 2} E_s(2\cos\theta\ \hat{r} + \sin\theta\ \hat{\theta}) \qquad (1.3.4.3.13)$$

It is interesting to derive the vector electric field distribution in the vicinity of the sphere for electromagnetic wave excitation at and below THz frequencies where metals are considered to be perfect conductors. At THz frequencies, $|\varepsilon_{metal}(\omega)| >> 1$, and the electric field $\boldsymbol{E}_{ind}$ given in (1.3.4.3.13) is approximately

$$\boldsymbol{E}_{ind} = -\frac{\delta^3}{8r^3} E_s(2\cos\theta\ \hat{r} + \sin\theta\ \hat{\theta}) \qquad (1.3.4.3.14)$$

At the surface of the metal sphere ($r = \delta/2$), the tangential components of $\boldsymbol{E}_{ind}$ and $\boldsymbol{E}_s$ cancel (as expected for a perfect conductor) and the total electric field $\boldsymbol{E}_{total} = \boldsymbol{E}_s + \boldsymbol{E}_{ind}$ is simply given by

$$\boldsymbol{E}_{total} = -E_s\cos\theta\ \hat{r} \qquad (1.3.4.3.15).$$

Thus, for low frequency (THz and below) excitation of a subwavelength metallic particle immersed in air where $|\varepsilon_{metal}(\omega)| >> 1$, the total electric field at the surface of the metallic sphere is oriented *normal* to the particle surface. Although the metallic particle depolarizes the local electric field at the surface, the net electric field distribution at the metallic sphere surface is oriented along the external electric field orientation. That is, $\boldsymbol{E}_{total}$ is strongest along the direction of the external field ($\theta = 0^{o}$) and approaches zero in the orthogonal direction ($\theta = 90^{o}$).

1.3.4.4 Particle Plasmon Decay

The decay of particle plasmons can be understood by considering a classical picture of electron motion during electromagnetic wave excitation as shown in Figure 1.9. An electromagnetic wave incident on a subwavelength sized metallic particle penetrates into the surface of the particle. The electric field inside the particle shifts the conduction electrons with respect to the fixed positive charge of the lattice ions. Electrons accumulate at one side of the particle resulting in the build-up of negative charge. The attraction between this negative charge and the positive charge of the lattice ions on the opposite side of the particle creates a restoring polarization force on the electrons. Thus, the conduction electrons in the particle oscillate collectively under the influence of an oscillating external excitation field and a background polarization response of the particle. The amplitude of the collective electron oscillations is governed by the *damping*, which can be either radiative or non-radiative [14, 19], as shown in Figure 1.9 (b). Damping causes losses in the particle plasmon, which reduce the amplitude of the electron oscillations. Radiative damping occurs when the conduction electrons emit electromagnetic radiation. Non-radiative damping arises from the dephasing of the oscillation of individual electrons. Electron oscillation dephasing can arise from 1) the electric field associated with the background polarization of the particle or 2) electron scattering with phonons, lattice ions, and other conduction and core electrons. These two distinctive dephasing mechanisms can be understood by considering the general wave equation for an electric field $\boldsymbol{E}$ in a metallic medium [20]

$$\nabla^2 \boldsymbol{E} = \varepsilon(\omega)\frac{\partial^2 \boldsymbol{E}}{\partial t^2} + \sigma(\omega)\frac{\partial \boldsymbol{E}}{\partial t} = \frac{\partial}{\partial t}\left[j_d(\omega) + j_F(\omega)\right] \tag{1.3.4.4.1}$$

where $\varepsilon(\omega)$ is the permittivity, $\sigma(\omega)$ is the conductivity, $j_d(\omega) = \varepsilon(\omega)\, \partial \boldsymbol{E}/\partial t$ is the electron displacement current density arising from the polarization of the metallic medium, and $j_F(\omega) = \sigma(\omega)\, \boldsymbol{E}$ is the free conduction electron current density. The complex conductivity is related to the complex permittivity through $\varepsilon(\omega) = i\sigma(\omega)/\omega$. It is important to note that (1.3.4.4.1) does not employ the Drude model for the permittivity of the metal, since the Drude model implicitly incorporates the free conduction electron current induced by the electric field. Rather, the current density on the right side of Equation (1.3.4.4.1) has been explicitly divided into a displacement current density, $j_d(\omega)$, originating from the polarization of the particle and a conduction current density, $j_F(\omega)$, originating from Lorentz force acting on the free conduction electrons. The imaginary parts of the displacement and free conduction electron current density in (1.3.4.4.1) describe the damping of $\boldsymbol{E}$ in the metallic medium, which in turn, describe the damping of the oscillation of electrons. For a harmonic electric field of the form $E \sim e^{-i\omega t}$, the imaginary part of the currents in (1.3.4.4.1) are given by

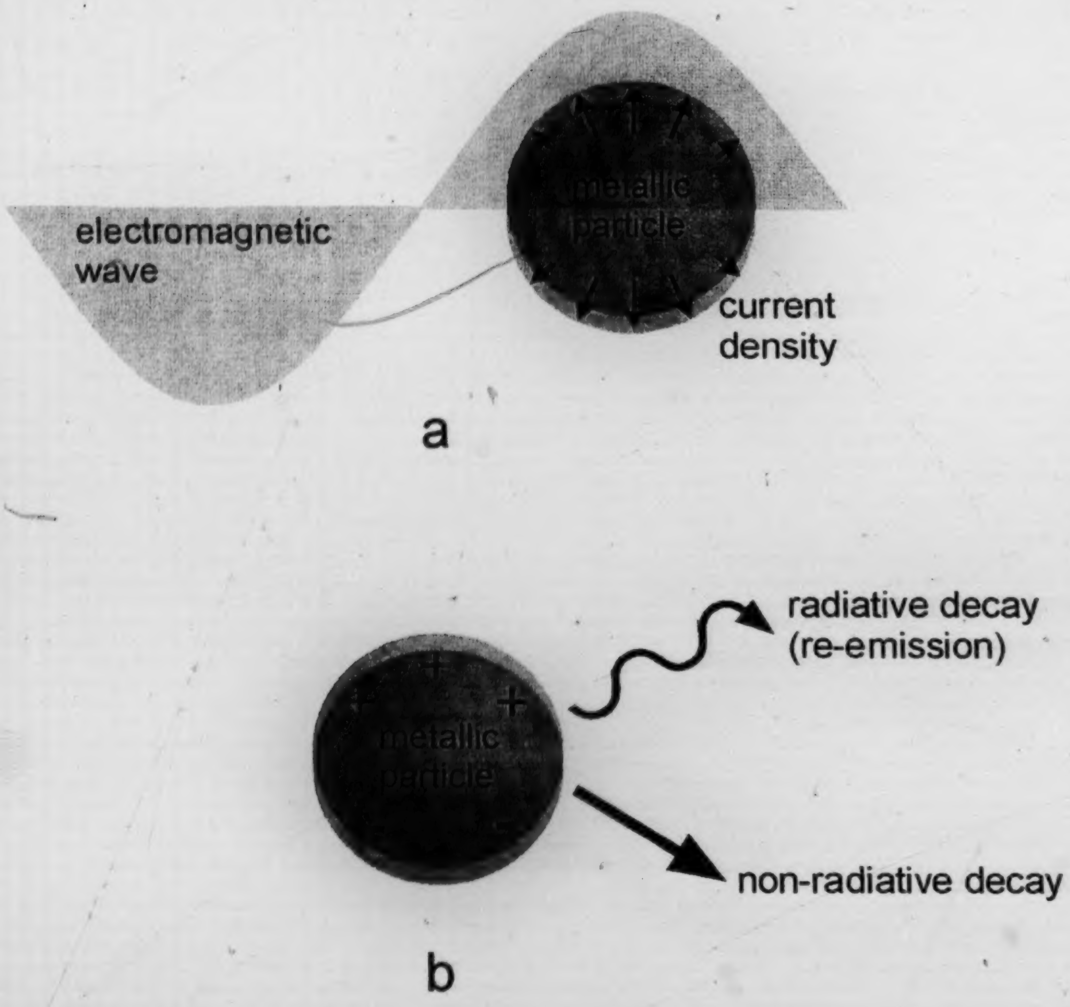
electromagnetic wave
metallic particle
current density
a
radiative decay (re-emission)
metallic particle
non-radiative decay
b

Figure 1.9. (a) Excitation of a subwavelength sized metallic particle by an electromagnetic wave induces current density near the surface. (b) The current density results in the accumulation of positive and negative charge at opposing sides of the metallic particle, creating a particle plasmon. The particle plasmon decays via radiative re-emission or non-radiative decay.

$$j_d(\omega) = -i\omega\, \mathrm{Re}[\varepsilon(\omega)]\, \boldsymbol{E} \qquad (1.3.4.4.2)$$

and

$$j_F(\omega) = \mathrm{Re}[\sigma(\omega)]\, \boldsymbol{E} = \omega^{-1}\, \mathrm{Im}[\varepsilon(\omega)]\, \boldsymbol{E} \qquad (1.3.4.4.3).$$

Since the permittivity of a medium is sensitive to the frequency of excitation, the electron oscillation damping is also frequency-dependent. At frequencies in the visible regime and higher, $|\mathrm{Re}[\varepsilon(\omega)]| > |\mathrm{Im}[\varepsilon(\omega)]|$ which implies that the dominant dephasing mechanism is the background polarization of the medium. However, at THz frequencies and lower where $|\mathrm{Im}[\varepsilon(\omega)]| > |\mathrm{Re}[\varepsilon(\omega)]|$, Ohmic current density is the dominant current density term in Equation (1.3.4.4.1). In this low frequency regime, electron scattering with phonons, lattice ions, and other conduction and core electrons is the dominant electron dephasing mechanism. These dephasing mechanisms can be described via the Drude model for the metal conductivity.

1.3.5 Effective Medium Approximation

In homogeneous media, the constitutive parameters (ε, μ, and σ) do not vary in space and are determined solely by microscopic mechanisms. Heterogeneous media, on the other hand, are characterized by constitutive parameters that show a strong dependence on spatial position. When the spatial fluctuations of the constitutive parameters are significantly less than the wavelength of the electromagnetic wave, the heterogeneous medium (in certain cases) may be replaced by a fictitious macroscopically homogeneous effective medium. Such an effective homogeneous medium possesses effective constitutive parameters ε_{eff}, μ_{eff}, and σ_{eff} that describe the electromagnetic properties of the heterogeneous medium. These effective parameters are derived from an average of the constitutive parameters of the heterogeneous medium's constituents. This section briefly overviews the concept and derivation of effective medium theory. For a complete treatment of this topic, the reader is referred to [21, 22].

Consider the simplest case of a random medium consisting of two types of subwavelength sized constituents composed of medium *1* and medium *2*, with respective permittivity values of ε_1 and ε_2 and respective volume filling fractions of f_1 and f_2. It is assumed that the subwavelength sized constituents are immersed in a background medium with permittivity ε_{eff}. If a single subwavelength sized constituent composed of medium *1* is approximated as having a spherical shape, then its interaction with a static external electric field, E_s, leads to a dipole moment, p, given by [17]

$$p = 3V\varepsilon_{eff}\frac{\varepsilon_1 - \varepsilon_{eff}}{\varepsilon_1 + 2\varepsilon_{eff}}E_s \qquad (1.3.5.1)$$

where V is the volume of the sphere and E_s is the amplitude of the static electric field far from the sphere. It is interesting to note that when $\varepsilon_{eff} = \varepsilon_1$, the dipole moment of the single constituent of medium 1 vanishes because the heterogeneity has been erased, and the medium becomes homogeneous.

In a static electric field, the polarization of the mixture can be described by the net dipole moment, p_n, defined as the average dipole moment of the two constituents, weighted by their respective filling fractions. Assuming that the spheres of the two constituents occupy identical volumes, the net dipole moment is expressed as

$$p_n = 3f_1V\varepsilon_{eff}\frac{\varepsilon_1 - \varepsilon_{eff}}{\varepsilon_1 + 2\varepsilon_{eff}}E_s + 3f_2V\varepsilon_{eff}\frac{\varepsilon_2 - \varepsilon_{eff}}{\varepsilon_2 + 2\varepsilon_{eff}}E_s \qquad (1.3.5.2).$$

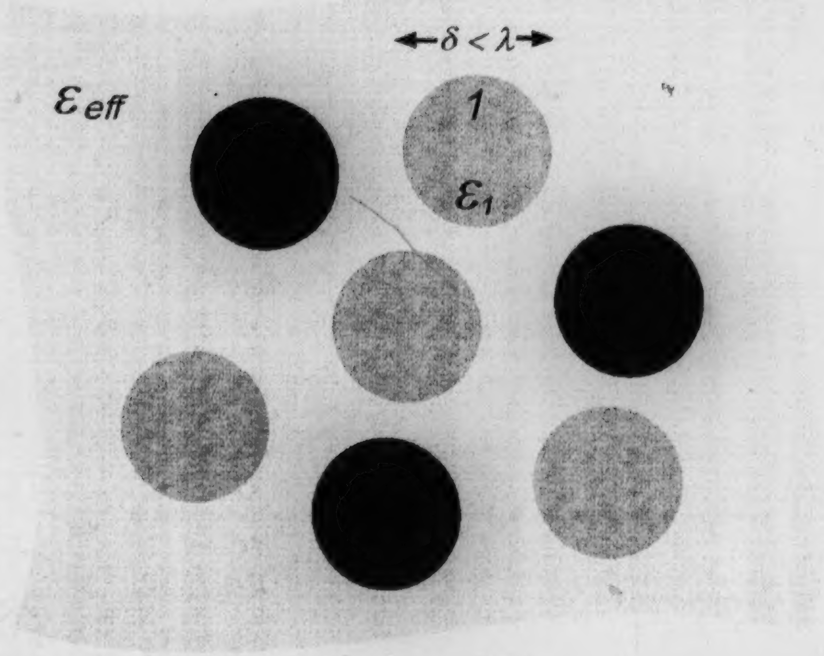
$\leftarrow \delta < \lambda \rightarrow$
ε_{eff}
1
ε_1

Figure 1.10. A random medium consisting of two types of subwavelength sized constituents composed of medium *1* and medium *2*, with respective permittivity values of ε_1 and ε_2. The random particles are immersed in a background medium having permittivity ε_{eff}.

When the condition $p_n = 0$ is fulfilled, Equation (1.3.5.2) can be written as

$$f_1 \frac{\varepsilon_1 - \varepsilon_{eff}}{\varepsilon_1 + 2\varepsilon_{eff}} + f_2 \frac{\varepsilon_2 - \varepsilon_{eff}}{\varepsilon_2 + 2\varepsilon_{eff}} = 0 \qquad (1.3.5.3)$$

For ε_{eff} satisfying Equation (1.3.5.3), the background effective medium exactly cancels out the dipole moment contributions from the two constituents. Physically, this corresponds to the situation where the mixture appears to have no dipole moment and is effectively homogeneous with a permittivity ε_{eff}. Thus, given the filling fraction and the constitutive parameters of the constituents of a mixture, the effective constitutive parameters of the mixture can be calculated from (1.3.5.3). The effective medium approximation is of particular interest in the case where ε_1 is finite and ε_2 is infinite, corresponding to the case of a dielectric and a perfectly conducting metal. In this situation, the effective medium approximation possesses a singularity near $f_2 \equiv f_p = 1/3$, often referred as the percolation threshold [23]. Near percolation, the effective permittivity is

$$\varepsilon_{eff} = \frac{1}{3}\varepsilon_2 (f_p - f_2)^{-1} \quad f_2 < f_p \qquad (1.3.5.4)$$

$$\varepsilon_{eff} = \infty \quad f_2 > f_p \qquad (1.3.5.5).$$

In a three-dimensional sample consisting of spherical components, the percolation threshold physically corresponds to the limit where there is a connected path of a component extending throughout the sample.

Although the effective medium approximation was derived at zero frequency, the description is valid when the dimensions of the constituents are much smaller than the wavelength and the polarization within the constituents is uniform. These conditions are commonly satisfied when the random medium consists of subwavelength, transparent dielectric constituents. In the situation where the dimensions of the constituents are much smaller than the wavelength but the polarization in the constituents is non-uniform, the effective medium approximation breaks down. In this case, the average dipole moment of the mixture is not describable as an average dipole moment of the two constituents weighted by their respective filling fractions. This situation commonly occurs, for instance, when the mixture consists of metallic constituents having dimensions much smaller than the wavelength yet larger than the skin depth of the radiation.

1.4 Terahertz Time-Domain Spectroscopy

This thesis investigates the interaction between mesoscopic dielectric and metallic media with radiation in the THz frequency range. The THz frequency range lies between the microwave and optical regimes. Historically, this frequency regime has been inaccessible by electronic and optical generation methods. While electronic sources such as crystal oscillators have provided electromagnetic signal generation up to 100s GHz, they are unable to generate signals beyond the gigahertz range. Alternatively, optical laser sources have been successful in generating stable, high-frequency, narrow bandwidth radiation. However, these optical methods are not able to generate broadband signals in the THz frequency range. As a result, the development of THz sources has lagged in comparison with microwave and optical technologies. Coherent THz generation was not demonstrated until the 1970s [24]. Since then, with the continued development of femtosecond lasers and quantum electronics, several methods have been developed both to generate and to detect coherent THz radiation [25].

Contemporary THz sources generally rely on either emission from optoelectronic methods, such as from a photoconductive (PC) emitter [25] or a bare semiconductor [26, 27], or from purely optical methods, such as optical rectification [28, 29]. Using the latter technique, a THz pulse is emitted when a nonlinear material is photo-excited with a femtosecond laser pulse. The generation mechanism is rooted in the mixing of optical frequencies in the femtosecond laser pulse to produce a quasi-DC, THz field. Although optical rectification has been demonstrated to produce free-space, wide bandwidth THz pulses (up to 105 THz [30]), the spectral purity of the pulse is poor. Phonon absorption bands of the electro-optic crystal significantly modulate the THz signal near the absorption frequencies. Moreover, the emitted power is relatively low compared to generation from optoelectronic methods.

The most common optoelectronic configuration utilized for THz generation is a PC emitter. Photoconductive emitters rely on the photo-excitation of free carriers in a biased semiconductor gap by a femtosecond laser pulse. The acceleration of excited electrons in the biased gap induces a time-varying dipole that emits free-space, broadband THz radiation. Using this technique, an optical power to THz power conversion efficiency of 0.02% has been achieved [31]. However, this technique is limited in several regards. While high laser pump intensities and high external biasing electric fields are known to increase the amplitude of the emitted radiation from PC THz emitters, the dependence of the THz power on both parameters is inherently limited. Carrier and THz field screening mechanisms have been shown to result in THz power saturation with increasing optical pump power [32]. Moreover, the dependence of the THz power on the external biasing field is constrained by the high-voltage dielectric breakdown of the semiconductor that can lead to electron avalanche across the small photoconductive gap, permanently damaging the THz PC emitter [33].

The optical excitation of bare semiconductor surfaces provides a compact source of broadband THz radiation that circumvents electric field breakdown damage, does not require micro-fabrication and can be easily integrated into large area emitters. In contrast to the planar dipole in PC emitters, photoelectrons in surface emitters are accelerated perpendicular to the surface by a depletion field, creating a time-dependent dipole perpendicular to the semiconductor surface. Although semiconductor surface field values can exceed 10^5 V/cm [34], the THz emission power from surface emitters is typically much weaker than from PC emitters. This is due to polarization-dependent THz refraction at the semiconductor interface, which lowers the radiation efficiency of the perpendicular dipole relative to the planar dipole in the PC arrangement. It has recently been shown that this limitation can be overcome by using a magnetic field to tilt the radiating dipole [35]. However, the mechanism behind the emission is still not fully understood. Several groups [34-36] have performed theoretical investigations of semiconductor THz emitters to elucidate the magnetic enhancement mechanism. Appendix A describes a novel drift-diffusion model of magnetic-field enhanced THz emission from various semiconductor surfaces.

Along with the development of coherent, free-space, broadband THz sources, the advent of femtosecond pulsed lasers has enabled the realization of techniques to measure THz electromagnetic fields directly in the time-domain. The fundamental principle of time-domain THz radiation detection is the use of a short femtosecond pulse as a near-instantaneous sampling probe of the electric field of the THz radiation. By varying the relative delay of the femtosecond probe pulse and the THz radiation, it is possible to map out the electric field of the THz radiation. Coherent, time-domain measurement of THz electric fields is generally achieved through either PC or nonlinear detection. In the former, a femtosecond probe pulse injects free carriers in a semiconductor gap (having a short carrier lifetime) between two metallic electrodes. Induction of the photo-excited carriers by the THz electric field causes a current along the semiconductor gap that is proportional to the instantaneous amplitude of the THz electric field. On the other hand, nonlinear detectors rely on the nonlinear interaction between the sampling probe pulse and the THz radiation in an electro-optic medium. In this scheme, the electric field associated with the THz radiation modifies the index ellipsoid of the electro-optic medium via the Pockels effect. When the probe pulse and THz radiation are collinear in an electro-optic medium, the polarization of the probe pulse is modulated by the refractive index change induced by the instantaneous electric field of the THz pulse. The electric field of the THz radiation is mapped onto a polarization modulation of the probe pulse.

The development of THz radiation detection schemes has enabled access to the free-space, time-domain electric fields. Coupled with existing coherent, free-space, broadband THz sources, dynamic, time-domain THz spectroscopic measurements are achievable over a wide range of frequencies. Terahertz spectroscopic techniques are advantageous over conventional visible spectroscopy since THz detection enables direct access to time-domain electric fields. Moreover, THz time-domain spectroscopy is not confined to waveguide geometries typical in microwave experiments. Thus, time-domain

THz spectroscopy offers a wide latitude with which to study electromagnetic wave phenomena not otherwise achievable with visible and microwave technologies.

Chapter 1 References

[1] D. F. Sievenpiper, M. E. Sickmiller, and E. Yablonovitch, "3D Wire Mesh Photonic Crystal," *Physical Review Letters*, vol. 76, pp. 2480-2483, 1996.

[2] S. Linden, C. Enkrich, M. Wegener, J. F. Zhou, T. Koschny, and C. M. Soukoulis, "Magnetic response of metamaterials at 100 terahertz," *Science*, vol. 306, pp. 1351-1353, 2004.

[3] R. A. Shelby, D. R. Smith, and S. Schultz, "Experimental verification of a negative index of refraction," *Science*, vol. 292, pp. 77-79, 2001.

[4] H. J. Lezec, J. A. Dionne, and H. A. Atwater, "Negative Refraction at Visible Frequencies," *Science*, vol. 316, pp. 430-432, 2007.

[5] M. P. V. Albada and A. Lagendijk, "Observation of Weak Localization of Light in a Random Medium," *Physical Review Letters*, vol. 55, pp. 2692-2695, 1985.

[6] P. Sheng, *Introduction to Wave Scattering, Localization, Mesoscopic Phenomena*. New York: Academic Press, 1995.

[7] P. W. Anderson, "Absence of diffusion in certain random lattices," *Physical Review*, vol. 109, pp. 1492-1505, 1958.

[8] S. John, "Electromagnetic absorption in a disordered medium near a photon mobility edge," *Physical Review Letters*, vol. 53, pp. 2169-2172, 1984.

[9] F. Scheffold, R. Lenke, R. Tweer, and G. Maret, "Localization or classical diffusion of light?," *Nature*, vol. 398, pp. 671-673, 1999.

[10] D. S. Wiersma, J. G. Rivas, P. Bartolini, A. Lagendijk, and R. Righini, "Localization of classical diffusion of light? (reply)," *Nature*, vol. 398, pp. 207, 1999.

[11] J. Jackson, *Classical Electrodynamics*, 2nd ed. New York: John Wiley & Sons, 1975.

[12] N. W. Ashcroft and N. D. Mermim, *Solid State Physics*. Philadelphia: Saunders College, 1976.

[13] M. A. Ordal, L. L. Long, R. J. Bell, S. E. Bell, R. R. Bell, R. W. Alexander, and C. A. Ward, "Optical-properties of the metals Al, Co, Cu, Au, Fe, Pb, Ni, Pd, Pt, Ag, Ti, and W in the infrared and far infrared," *Applied Optics*, vol. 22, pp. 1099-1119, 1983.

[14] S. A. Maier, *Plasmonics: Fundamentals and Applications*. New York: Springer, 2007.

[15] E. Kretschmann and H. Raether, "Radiative decay of non-radiative surface plasmons excited by light," *Z. Naturforschung*, vol. 23A, pp. 2135-2136, 1968.

[16] A. Otto, "Excitation of nonradiative surface plasma waves in silver by method of frustrated total reflection," *Z. Physik*, vol. 216, pp. 398-410, 1968.

[17] C. F. Bohren and D. R. Huffman, *Absorption and Scattering of Light by Small Particles*. New York: John Wiley & Sons, 1983.

[18] M. A. Ordal, R. J. Bell, R. W. Alexander, L. L. Long, and M. R. Querry, "Optical-properties of 14 metals in the infrared and far-infrared - Al, Co, Cu, Au, Fe, Pb, Mo, Ni, Pd, Pt, Ag, Ti, V, and W," *Applied Optics*, vol. 24, pp. 4493-4499, 1985.

[19] C. Sonnichsen, T. Franzl, T. Wilk, G. von Plessen, and J. Feldmann, "Drastic reduction of plasmon damping in gold nanorods," *Physical Review Letters*, vol. 88, pp. 077402, 2002.

[20] D. J. Griffins, *Introduction to Electrodynamics*, 3rd ed. New Jersey: Prentice Hall, 1999.

[21] D. A. G. Bruggeman, "Berechnung verschiedener physickalischer Konstanten von heterogenen Substanzen. I. Dielektrizitatskonstanten und Leitfahigkeiten der Mischkorper aus isotropen Substanzen," *Annalen der Physik*, vol. 24, pp. 636-664, 1935.

[22] P. Chylek, G. Videen, W. Geldart, S. Dobbie, and W. Tso, "Effective Medium Approximation for Hetergeneous Particles," in *Light Scattering by Nonspherical*

Particles: Theory, Measurements, and Geophysical Applications, M. Mishchenko, Ed.: Academic, 2000, pp. 273-308.

[23] D. Stroud, "The effective medium approximations: Some recent developments," *Superlattices and Microstructures*, vol. 23, pp. 567-573, 1998.

[24] K. H. Yang, P. L. Richards, and Y. R. Shen, "Generation of far-infrared radiation by picosecond light pulses in LiNbO3," *Applied Physics Letters*, vol. 19, pp. 320-322, 1971.

[25] D. Mittleman, *Sensing with Terahertz Radiation*. New York: Springer, 2003.

[26] R. McLaughlin, A. Corchia, M. B. Johnston, Q. Chen, C. M. Ciesta, D. D. Arnone, G. A. C. Jones, E. H. Linfield, A. G. Davies, and M. Pepper, "Enhanced coherent terahertz emission from indium arsenide in the presence of a magnetic field," *Applied Physics Letters*, vol. 76, pp. 2038-2040, 2000.

[27] H. Ohtake, S. Ono, M. Sakai, Z. Liu, T. Tsukamoto, and N. Sarukura, "Saturation of THz radiation power from femtosecond-laser-irradiated InAs in a high magnetic field," *Applied Physics Letters*, vol. 76, pp. 1398-1400, 2000.

[28] P. Y. Han and X.-C. Zhang, "Coherent, broadband midinfrared terahertz beam sensors," *Applied Physics Letters*, vol. 73, pp. 3049-3051, 1998.

[29] A. Leitenstorfer, S. Hunsche, J. Shah, M. C. Nuss, and W. H. Knox, "Detectors and sources for ultrabroadband electro-optic sampling: Experiment and theory," *Applied Physics Letters*, vol. 74, pp. 1516-1518, 1999.

[30] C. Kubler, R. Huber, S. Tubel, and A. Leitenstorfer, "Ultrabroadband detection of multi-terahertz field transients with GaSe electro-optic sensors: Approaching the near infrared," *Applied Physics Letters*, vol. 85, pp. 3360-3362, 2004.

[31] G. Zhao, R. N. Schouten, N. v. d. Valk, W. T. Wenckebach, and P. C. M. Planken, "Design and performance of a THz emission and detection setup based on a semi-insulating GaAs emitter," *Review of Scientific Instruments*, vol. 73, pp. 1715-1719, 2002.

[32] G. Rodriguez and A. J. Taylor, "Screening of the bias field in terahertz generation from photoconductors," *Optics Letters*, vol. 21, pp. 1046-1048, 1996.

[33] H. J. Bakker, G. C. Cho, H. Kurz, Q. Wu, and X.-C. Zhang, "Distortion of terahertz pulses in electro-optic sampling," *Journal of the Optical Society of America B*, vol. 15, pp. 1795-1801, 1998.

[34] J. Shan, C. Weiss, R. Wallenstein, R. Beigang, and T. F. Heinz, "Origin of magnetic field enhancement in the generation of terahertz radiation from semiconductor surfaces," *Optics Letters*, vol. 26, pp. 849-851, 2001.

[35] M. B. Johnston, D. M. Whittaker, A. Corchia, A. G. Davies, and E. H. Linfield, "Simulation of terahertz generation at semiconductor surfaces," *Physical Review B*, vol. 65, pp. 165301, 2002.

[36] K. J. Chau and A. Y. Elezzabi, "Two-dimensional drift-diffusion analysis of magnetic field enhanced THz emission from semiconductor surfaces," *Optics Communications*, vol. 242, pp. 295-304, 2004.

Chapter 2:

Terahertz Electromagnetic Wave Propagation in Mesoscopic Dielectric Media

2.1 Scattering of Electromagnetic Waves by Dielectric Particles

When an electromagnetic wave is incident on an interface of two dielectric media with different permittivity values, a phenomenon known as scattering occurs. For the case where the dimensions of the two dielectric media are much larger than the wavelength, scattering occurs only at the single interface between the two media. Reflection and transmission from the single interface are determined by the refractive indices of the media, the angle of incidence, the polarization of the electromagnetic wave, and the geometry of the interface. As the number of constituents comprising the system increases, there are an increasing number of dielectric interfaces, and the incident electromagnetic wave undergoes an increasing number of scattering events. The situation becomes more complex as the size of the constituents approaches the wavelength of the electromagnetic wave. For an ensemble of subwavelength sized dielectric particles, its interaction with an incident electromagnetic wave can be described by its *scattering strength*.

There are two important length scales to quantify the scattering strength of a heterogeneous ensemble of dielectric particles: the mean free path, $\mathrm{\lambda}$, and the wavelength of the electromagnetic wave, λ. The mean free path is the average distance an electromagnetic wave traverses between scattering events and can be calculated by $\mathrm{\lambda} = 1/\sigma_{sc} N_d$, where σ_{sc} is the scattering cross-section of an individual scattering event [1] and N_d is the number density of scatterers. When the wave oscillates many times before scattering, $\lambda >> \mathrm{\lambda}$, the medium is weakly scattering and the medium locally appears homogeneous. As a result, the electromagnetic properties of the heterogeneous medium can be described as a homogeneous effective medium. In the case where $\lambda << \mathrm{\lambda}$, the polarization, phase, and/or the propagation direction of the wave is randomized by many scattering events occurring over a single spatial oscillation of the wave. In this regime, the propagation of an electromagnetic wave through the medium is complex and simple effective medium descriptions become limited. Commonly, descriptions of electromagnetic wave transport through strongly scattering media are based on diffusive photon propagation where the electromagnetic wave is modeled as a collection of photons that exhibit a transport mean free path, $l^* = \lambda\ (1-g)^{-1}$, where g is the average cosine of the scattering angle and $(1-g)^{-1}$ is the number of successive scattering events required for isotropic scattering [2]. When l^* is significantly less than the sample thickness, L, incident coherent light is completely randomized, and the transmission consists of photons that have undergone multiple scattering events.

Recently, electromagnetic wave propagation in strongly scattering dielectric systems has received considerable attention [3]. The complex nature of electromagnetic wave interaction in these structures makes them a platform for the observation of many novel phenomena. For instance, in systems where the probability of scattering is exceedingly high, a phenomenon called photon (or light) localization has been predicted to occur [4], as shown in Figure 2.1. Localization occurs when an electromagnetic wave undergoes many scattering events within the distance of a single wave oscillation such that all propagation paths destructively interfere, and the wave is spatially localized. To date, however, there has been no experimental evidence of this phenomenon due to the difficulty in experimentally observing a localized wave [5, 6]. Nevertheless, studies of electromagnetic wave propagation in strongly scattering media have revealed a host of interesting phenomena. Researchers have shown that a suspension of polystyrene particles in water exhibit an effect known as the coherent backscattering effect [7]. In this effect, electromagnetic radiation incident on the scattering medium preserves its phase coherence in the opposite direction to its incident direction, but not in other directions. The coherent backscattering effect deviates from that expected of classical wave diffusion in a strongly scattering medium, and has been interpreted as a precursor to photon localization. In continued efforts to observe photon localization, researchers have developed a strongly scattering system for visible light consisting of highly perforated GaP [8]. These GaP systems possess both high index contrast and short length scales of refractive index variation, leading to extremely efficient visible light scattering. Measurement of the backscattered radiation from these strongly scattering samples show anomalous rounding of the angular distribution of the backscattered radiation, likely marking the onset of photon localization [9]. To date, research continues on the scattering of electromagnetic radiation in disordered, subwavelength scale media.

2.2 Terahertz Time-Domain Spectroscopic Investigation of Scattering Media

Here, THz time-domain spectroscopy is applied to explore electromagnetic wave propagation through strongly scattering dielectric media. Terahertz time-domain spectroscopy offers several advantages over other methods used to study multiple scattering phenomena. First, the sample size relative to the wavelength can be well-controlled. The broad bandwidth of THz spectroscopic measurements provides access to mean free paths ranging over two orders of magnitude in a single measurement. Furthermore, access to the time-domain electric fields enable access to dynamic, time-dependent scattering effects in the THz waveform.

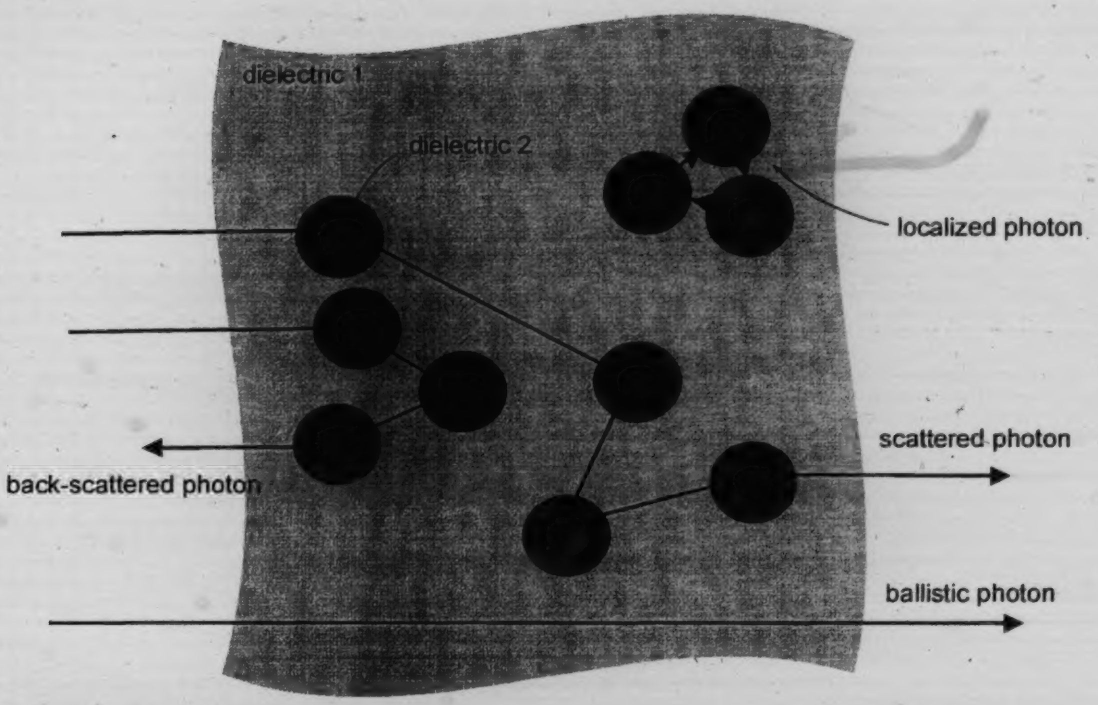
dielectric 1
dielectric 2
localized photon
scattered photon
back-scattered photon
ballistic photon

Figure 2.1. Transport of photons in a random dielectric medium consisting of dielectric inclusions embedded in a uniform matrix. Photon transport through the medium may be composed of localized photons, scattered photons, back-scattered photons, and ballistic photons.

The interaction of broadband THz radiation with heterogeneous dielectric media has been first studied by Pearce and Mittleman [10-13]. In their experiments, the scattering medium studied is composed of thin slabs of mono-disperse Teflon spheres where the sample length, L, and transport mean free path, l^*, satisfy $L/l^* < 40$. By studying the off-axis scattered THz pulses from the sample, the authors characterized the electric field amplitude and phase statistics of waves diffusing through the sample. Earlier, a study of on-axis THz transmission was also reported by the same authors [13]. In order to study the weakly scattering regime, L/l^* was selected to be less than 10. In their experiment, it was found that the on-axis electromagnetic properties of the medium can be approximately described by the effective medium approximation. In more complex heterogeneous systems, however, both weak and strong scattering are present; strong scattering, in particular, may lead to breakdown in effective medium descriptions of heterogeneous dielectric media. In the context of on-axis, THz radiation transmission through a random dielectric medium, this range of scattering remains unexplored.

This section describes experimental and numerical results on the scattering effects on THz electromagnetic wave propagation through dispersive and strongly scattering random media composed of slabs of poly-dispersive sapphire spheres where L/l^* can exceed 300. In contrast to the weakly scattering regime, where scattering-induced effects only cause distortions of the spectral phase [13], significant temporal pulse re-shaping is anticipated in a strongly scattering regime. Through examination of this effect, in addition to transmitted THz pulse features such as group delay, pulse width, spectral width, and the transmitted power, THz transmission through a strongly scattering medium is fully characterized. The experimental measurements are compared with calculated results obtained from a Monte Carlo model based on time-dependent photon transport through the strongly scattering medium. The results of this Chapter have been published in *Applied Physics Letters*, vol. 85, 6284-6286 (2004).

2.2.1 Theoretical Background of Electromagnetic Wave Scattering in Strongly Scattering Dielectric Media

Analytical descriptions of electromagnetic wave propagation in strongly scattering dielectric systems are difficult due to the complex nature of wave interaction with highly heterogeneous media. Here, a photon migration model (developed by Dr. S. Mujumdar) is used to describe THz electromagnetic pulse propagation through a strongly scattering medium composed of an ensemble of subwavelength spherical dielectric particles. In the model, the incident THz electric field pulse is first modeled in the frequency-domain as an ensemble of THz photons that mark the straight-line trajectories of the radiation inside the sample. The amplitude spectrum of the incident pulse, $E_{in}(\omega)$, is decomposed into constituent frequencies with a resolution of 30 GHz, and the profile of $E_{in}(\omega)$ is used to construct a cumulative probability distribution of the frequency of the photons. The transport of each frequency is studied independently since there is no energy transfer between the frequencies. The mean free path $\lambda(\omega)$ of the radiation in the scattering medium is calculated using Mie theory [4].

Scattering is anisotropic over a considerable section of the THz pulse spectrum and is highly sensitive to the particle dimension. For incident radiation at 1 THz, a dielectric particle with diameter of 50 μm leads preferentially to backward scattering [Figure 2.2 (a)], whereas a particle with a diameter of 100 μm preferentially scatters radiation in the forward direction [Figure 2.2 (b)]. In contrast, for a 150 μm diameter particle, incident radiation is preferentially scattered in the lateral directions [Figure 2.2(c)]. The anisotropy in the scattering profile is explicitly incorporated in the model by calculating an anisotropy parameter $g(\omega)$ (which will be further discussed) using Mie theory [4]. The permittivity of sapphire in the THz frequency range is determined from experimental data in Ref. [14].

Essentially, the model emulates the rectilinear propagation of THz photons from successive scattering sites. The sample boundaries are defined by the planes $x = 0$ mm, $x = 50$ mm, $y = 0$ mm, $y = 50$ mm and $z = 0$ mm, $z = L$. A photon at a given frequency ω is launched at the centre of the front face of the sample located at $(x_0, y_0, z_0) = (25$ mm, 25 mm, 0 mm$)$ into the sample where it undergoes a three-dimensional random walk [15]. The longitudinal direction is assumed parallel to the z-axis. Accordingly, the polar and azimuthal angular coordinates of the photon at the time of launch are chosen to be $(\theta_0, \varphi_0) = (0,0)$, so as to simulate an incident collimated beam. At the ith step of the random walk, the photon undergoes a linear displacement p_i and an angular displacement (θ_i, φ_i), giving a new position

$$(x_i + p_i \sin\theta_i \sin\varphi_i,\ y_i + p_i \sin\theta_i \cos\varphi_i,\ z_i + p_i \cos\theta_i) \qquad (2.2.1.1).$$

The probability $P(p_i)$ of traveling a given path length p_i is given by the Lambert Beer law, $P(p_i) = \exp(-p_i / \lambda)$ where λ is the mean free path. Thus, the random paths between scattering events are generated by $p_i = -\lambda \ln \Sigma$ where Σ is a variant uniformly distributed over [0,1].

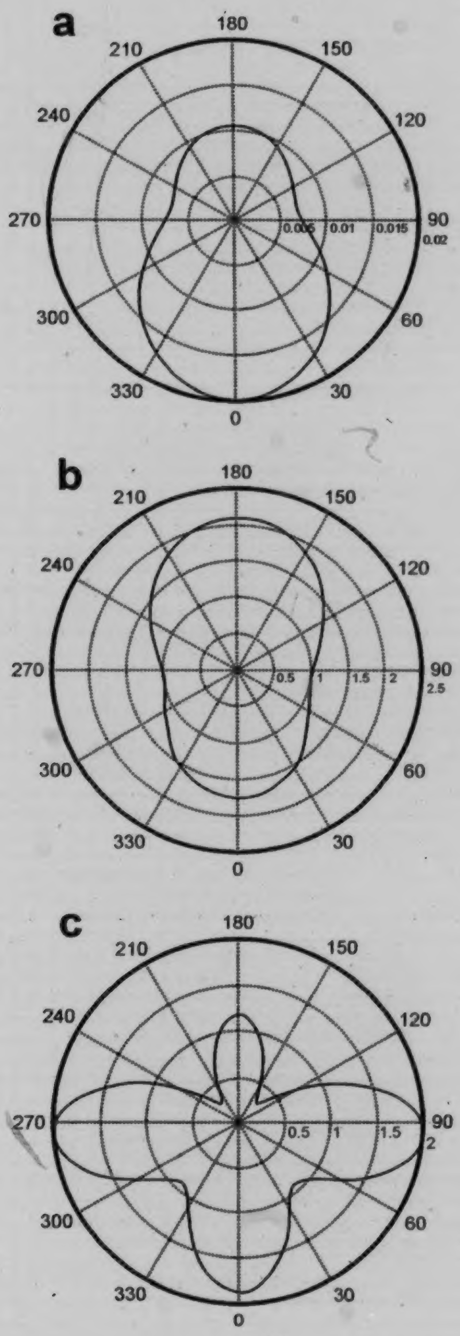

Figure 2.2. Probability distribution of the angular coordinate of the scattered radiation at 1 THz from a sapphire sphere where the diameter is (a) 50 μm, (b) 100 μm, and (c) 150 μm. The forward direction is at 180° and the backward direction is at 0°.

It is important to note that over the bandwidth of the pulse, the transport mean free path, l^*, varies from 3.7 m to 0.5 μm, as shown in Figure 2.3. Hence, a large portion of the incident pulse propagates through the sample without scattering. That is, at the lower frequencies of the pulse where $l^* >> L$, the average linear displacement of a photon is much greater than the sample thickness L. This means that the photon propagates directly through the sample and does not undergo a scattering event. It is only at the higher frequencies of the pulse where $l^* < L$ that the average linear displacement is smaller than the sample thickness. In this regime, the photon must undergo several scattering events in order to traverse across the sample thickness.

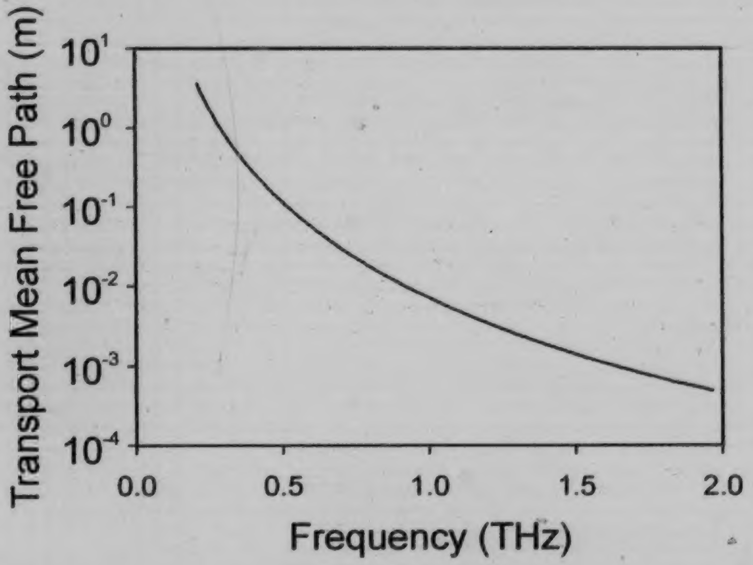

Figure 2.3. Calculated transport mean free path versus frequency for the sapphire particle ensemble used in the experiments. Note that the transport mean free path varies over nearly four orders of magnitude.

Each scattering event causes angular displacements of the incident photon trajectory. Due to symmetry, the azimuthal angle φ_i is uniformly distributed whereas the polar angle θ_i is chosen from a Henyey-Greenstein distribution [16]

$$P(\theta_i) = (1-g^2)/4\pi(1+g^2-2g\cos\theta_i)^{3/2} \tag{2.2.1.2}$$

where the anisotropy parameter $g = <\cos\theta_i>$ is the average cosine of the scattering angle at a particular frequency and refractive index. This distribution gives the probability that the scattered photon will deflect at a given polar angle θ_i. It should be noted that the angles θ_i and φ_i are calculated with respect to a local frame of reference. In this frame, the longitudinal direction is taken as the direction of propagation prior to the scattering event. Accordingly, after the scattering event, the photon position has to be recalculated in the main frame of reference using the appropriate rotational and translational transformations. The random walk of the photon is halted when the photon exits the sample boundaries after undergoing N_s scattering events. Hence, the simulation can be visualized as follows: consider N_s vectors from a set of vectors whose lengths are exponentially distributed as $P(p_i) = \exp(-p_i/\lambda)$, where $P(p_i)$ here is the probability of drawing a vector of magnitude p_i. The vectors are then placed head to tail at angles that are drawn from a set of angles distributed according to the Henyey-Greenstein function. The resultant vector is the total displacement of the photons through the scattering medium. The trajectories of 10^9 photons determine the transport of the pulse. The number of transmitted photons as a function of frequency generates the transmitted electric field spectral amplitude, $E_{tr}(\omega)$. The spectral phase, $\Phi_{tr}(\omega)$, is derived from the average phase of all transmitted photons at frequency ω. That is, for a group of photons at a frequency ω that have traverses an average distance $<L_{tr}(\omega)>$ through the sample, the phase at a frequency ω is given by $\Phi_{tr}(\omega) = \sqrt{\varepsilon_{eff}}\, k_o <L_{tr}(\omega)>$. Again, it is important to note that for the lower frequency components of the pulse where $l^* >> L$, the average distance that the photon traverses is $<L_{tr}(\omega)> = L$. The phase of the individual transmitted photon is calculated from its optical path length using the two-component Bruggeman effective medium approximation [17]. The Bruggeman effective medium approximation gives the effective permittivity ε_{eff} of a two-component system through the following mixing rule

$$f_1\frac{\varepsilon_1-\varepsilon_{eff}}{\varepsilon_1+2\varepsilon_{eff}}+f_2\frac{\varepsilon_2-\varepsilon_{eff}}{\varepsilon_2+2\varepsilon_{eff}}=0 \qquad (2.2.1.3)$$

where f_1 and f_2 are the volume fractions of the two components, and ε_1 and ε_2 are their respective dielectric constants. This effective medium approximation treats both the materials on an equal basis, without labelling them as inclusions and hosts. The Bruggeman effective medium approximation is symmetric with respect to an interchange of materials, and hence is particularly applicable in cases where the volume fractions are comparable, as in the present situation of an ensemble of sapphire spheres.

2.2.2 Experimental Investigation of Terahertz Electromagnetic Wave Scattering in Strongly Scattering Dielectric Media

To experimentally study the strongly scattering medium, a THz time-domain spectroscopy setup is employed. A schematic of the experimental arrangement is depicted in Figure 2.4. In this setup, a PC emitter THz source is employed consisting of a semi-insulated GaAs PC emitter biased across a lithographically defined 100 μm gap between Au electrodes. The biasing field is a 20 V peak-to-peak square wave oscillating at a frequency of 54.321 kHz supplied from a Wavetek 178 Programmable Waveform Synthesizer. Biasing the THz emitter at a high frequency (rather than at a DC voltage) facilitates lock-in detection. By performing lock-in detection at the biasing frequency, lower frequency acoustic noise and laser fluctuations are avoided, and the signal-to-noise ratio of the measured signal is enhanced. Terahertz pulses are generated and detected using < 20 fs, 800 nm, linearly polarized pulses supplied from a Ti:sapphire Kerr-lens mode-locked laser (Femtosource Pro, Femtolasers Produktions GmbH) at a repetition rate of 80 MHz. The beam from the Ti:sapphire laser is split into a weak 30 mW probe beam (used for detection of the THz radiation) and a 250 mW pump beam (used for generation of the THz radiation). The pump pulse photo-excites the THz PC emitter, generating electron-hole pairs in the semiconductor gap between the electrodes. Acceleration of the electron-hole pairs results in the free-space radiation of a single-cycle THz pulse. The emitted THz pulse is collected and collimated by a 2 inch diameter, off-axis, gold-coated parabolic mirror having a focal length of 25.4 mm. To sample the THz waveform, both the probe and THz beams must be spatially overlapped. This overlap is achieved by using two different methods. In one method, the probe and THz beams are overlapped using a 50:50, 2 inch diameter pellicle beam-splitter, which consists of a 2 μm thick polymer membrane stretched over a flat metal frame. The pellicle beam-splitter is employed since the thinness of the membrane eliminates multiple reflections associated with thicker glass beam-splitters. Moreover, the pellicle is highly transparent to THz radiation and does not introduce spurious distortions in the THz waveform. Another method to achieve spatial overlap between the probe and THz beams is by directing the probe beam through a 2 mm hole (aligned at the center of the parabolic mirror) drilled through the back of a parabolic mirror. This method is advantageous because it precludes lower frequency acoustic noise associated with the pellicle. The THz detection process is based on the second-order nonlinearity in non-centrosymmetric materials. In particular, as the THz and probe beams co-propagate in an electro-optically active crystal, the magnitude of the THz pulse can be mapped onto the polarization state of the probe pulse. Thus, after the two beams are overlapped in space, the THz beam and visible probe beam are co-focused in a ZnSe <111> electro-optic detector by another 2 inch diameter, off-axis, gold-coated parabolic mirror with a focal length of 25.4mm. In the <111> ZnSe crystal, the phase of the linearly polarized probe beam is modulated by the index change caused by the THz pulse. The THz pulse-induced phase change of the probe is converted into an intensity modulation by a quarter wave-plate and Wollaston prism, which split the probe into two orthogonally polarized components. Here, the slow and fast axes of the quarter wave-plate are aligned at 45° with respect to the incident probe polarization. Hence, a linearly polarized wave incident on the wave-plate is converted into an elliptically polarized wave. Subsequently, a Wollaston prism is employ to separate the beam into two orthogonally polarized components. The ordinary and extraordinary transmission axes of the Wollaston prism are aligned parallel and perpendicular to the incident polarization. In this way, the degree of polarization ellipticity of the probe beam, which is measured in the difference of the intensities of the orthogonally polarized beams from the Wollaston prism, is linearly proportional to the magnitude of the THz electric field. The intensities of the two polarization components from the Wollaston prism are then measured using two photo-detectors. The photo-currents from the two photo-detectors are electronically differenced and then amplified. The THz signal is frequency filtered using a Stanford Research Systems SR560 now-noise preamplifier and a Stanford Research Systems SR830 DSP lock-in amplifier, and the signal is recorded by a data acquisition program written in LabView.

In these experiments, temporal overlap between the THz pulse and the probe pulse is required to sample the THz waveform. To achieve this overlap, mechanical delay lines are used to vary the time delay between the probe pulse and THz pulse. The mechanical delay line consists of two delay-motors: a pico-motor delay line and a femto-motor delay line. The larger pico-motor translates in 12 μm steps, corresponding to a temporal step size of 80 fs. The finer femto-motor translates in 70 nm steps, corresponding to a temporal step size of 0.463 fs. Thus, the pico-motor delay line and the femto-motor delay line provide both coarse and fine temporal resolution to sample the THz waveform. Shown in Figure 2.5 is a typical time-domain waveform of a THz pulse propagated through free space. The THz pulse encompasses frequencies ranging from 0.1 THz up to 1 THz, corresponding to a range of wavelengths from 3 mm to 300 μm.

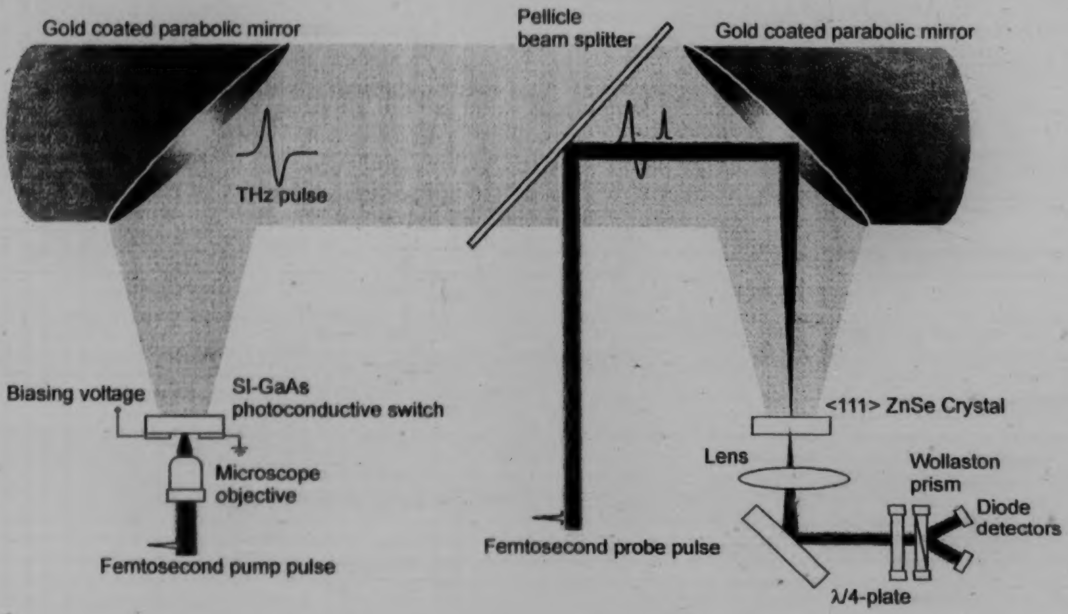
Gold coated parabolic mirror
Pellicle beam splitter
Gold coated parabolic mirror
THz pulse
Biasing voltage
SI-GaAs photoconductive switch
Microscope objective
Femtosecond pump pulse
<111> ZnSe Crystal
Lens
Wollaston prism
Diode detectors
Femtosecond probe pulse
λ/4-plate

Figure 2.4. Schematic of the THz time-domain spectroscopic setup.

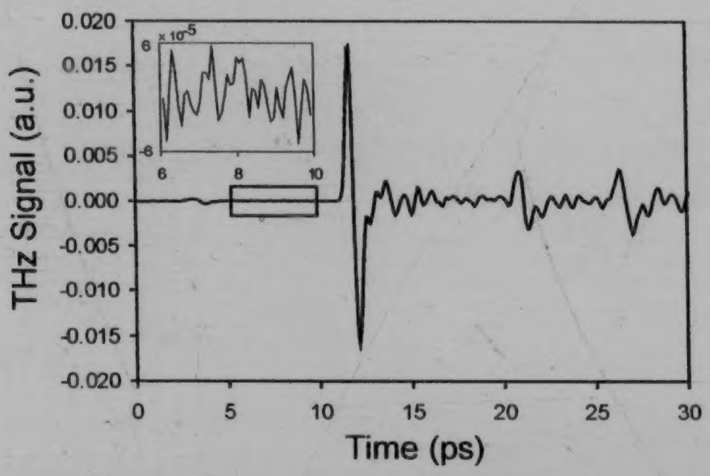

Figure 2.5. Typical free-space THz waveform measured with the experimental setup. The ringing after the initial bipolar waveform is due to resonant absorption and re-emission by water vapour in the air. The two subsidiary signals are due to reflections from the front and back faces of the ZnSe electro-optic crystal. The inset shows the noise level prior to the arrival of the THz signal highlighted in the boxed region.

In the experiments, the collimated THz electric field pulse is directed towards a 5 cm diameter sample cell containing poly-disperse, subwavelength sized sapphire spheres that have a mean diameter, $\delta = 100\ \mu m$ and a fill fraction of 0.50. Shown in Figure 2.6 is a microscope image of the sapphire particles. The transport mean free path for the particle ensemble is estimated from the scattering cross-section and anisotropy parameter of an individual sapphire particle obtained from Mie theory in conjunction with the number density of scatterers. Using the estimated l^* as shown in Figure 2.3, it is calculated that variation of the sample cell width from 0 to 14 mm permits the investigation of a wide range of scattering regimes where L/l^* ranges from 0.001 to 300.

Figure 2.6. Microscopic image of the sapphire microparticles used in the experiments.

2.2.3 Results and Discussion

The data shown in Figure 2.7 (a) demonstrates the effect of increasing sample thickness on the transmission spectrum. In contrast to the low frequency constituents, which exhibit longer λ, the high frequency components of the incident pulse decay rapidly as the sample thickness increases. As a result, the bandwidth of the pulse spectrum decreases markedly from 0.97 THz to 0.5 THz as the sample thickness increases from 0 mm to 4 mm. As shown in Figure 2.7 (b), this spectral narrowing is predicted by the photon migration model. For samples thicker than 4 mm, the higher frequencies (1 THz) have already been scattered outside of the detection acceptance angle, and only a gradual decrease in the spectral width is observed.

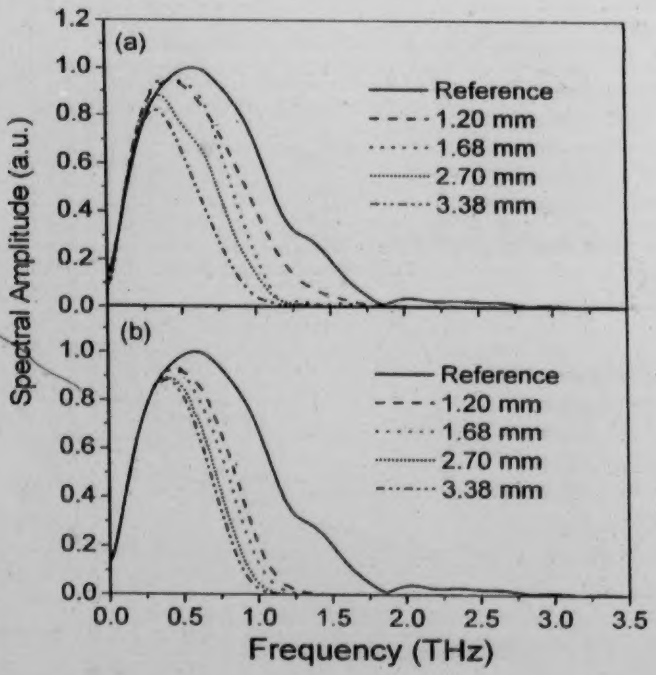

Figure 2.7. (a) Experimental and (b) calculated amplitude spectra of the transmitted THz pulse for various sample widths.

Over the entire scattering range, the measured and calculated spectral bandwidths reasonably agree as shown in Figure 2.8(a). The agreement underlines the applicability of the photon transport model to predict spectral quantities of on-axis field propagation through strongly scattering media. Figure 2.8 (b) depicts the measured and calculated normalized power transmitted through the scattering samples. Similar to the bandwidth profile, a rapid fall (~ 60 %) in the THz transmission power is witnessed for $0 < L < 6$ mm. The marked power decay in this thickness interval is due to selective scattering of the high frequency components. In this critical region, where the transmitted power is most sensitive to the sample thickness, an excellent agreement in the calculated and measured transmission power is observed. For sample thickness greater than 6 mm both the experimental and calculated transmission powers are weakly dependent upon the sample width. A slight offset between the experiment and calculations in this region is caused by the high polarization sensitivity of the experimental detection, which is non-existent in the model. That is, the experimental setup does not permit the detection of near-forward scattered de-polarized THz radiation. Overall, the model succeeds in emulating the observed bandwidth and power of the THz transmission as a function of sample thickness.

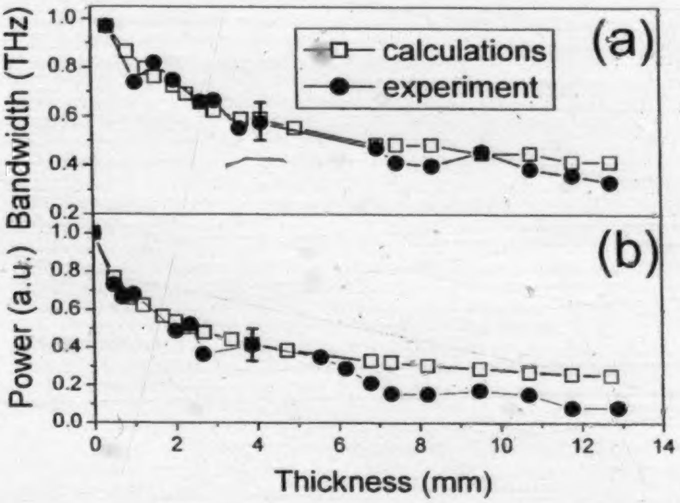

Figure 2.8. Experimental and calculated (a) spectral bandwidth and (b) total integrated power of the transmitted THz pulses as a function of sample thickness. Representative error bars are shown which describe the variation in the measurement for various realizations of the random medium.

Figure 2.9. Experimental and calculated temporal THz waveforms transmitted through sample thickness of (a) 1.68 mm and (b) 7.3 mm. The inset in (a) depicts the reference pulse used in the experiment and simulation, and the inset in (b) plots the tail end of the calculated pulse using ballistic and scattered photons (solid line) and ballistic photons (dotted line).

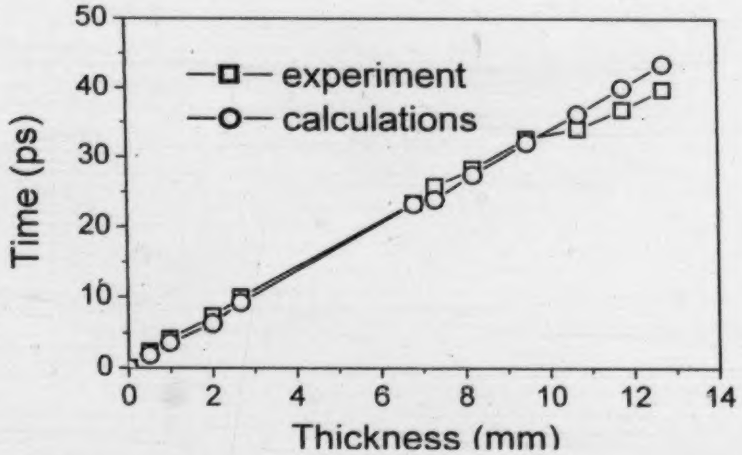

Figure 2.10. Transmitted THz pulse delay relative to the reference pulse versus sample thickness. The delay is measured at the initial rise of the first pulse peak.

Figure 2.9 (a) and 2.9 (b) depict the calculated and experimentally measured THz pulses through the random medium for sample thickness values of 1.68 and 7.3 mm, respectively. Although the spectral bandwidth of the transmitted pulses is similar, the pulse widths of the calculated and experimentally measured waveforms are substantially different. In the calculated waveforms, a significant portion of the lower frequency components are present prior to the arrival of the main pulse, as evidenced by the slowly rising pulse feature prior to the first peak of the pulse. Since the main pulse in the calculations primarily consists of higher frequency components, the pulse features appear "sharper" and the pulse width appears to be substantially smaller than that measured in the experiments. It will be shown that the disparity in the pulse widths obtained from the experiments and calculations is due to the spectral phase, which governs the coherent superposition of the frequency components of the pulse. While the pulse widths from the experiment and theory differ, the group delays exhibit good quantitative agreement for thickness values up to 14 mm, as shown in Figure 2.10. Due to strong scattering, the experimental pulse shape develops increasingly large subsidiary peaks following an initial bipolar pulse as the sample thickness increases. It is interesting to note that these distinct pulse shape features are well described by the model. To investigate the origin of this effect, Figure 2.9 (b) compares two calculated pulse profiles, where one is generated from the ballistic photons and the other from the ballistic and the earliest arriving scattered photons. Evidently, the trailing oscillations in the pulse are caused by the scattered photons reaching the detector.

While the model and experiment agree in regards to group delay and scattering-induced pulse distortion, spectral decay, and power attenuation, it should be noted that this agreement is based on the phase insensitivity of the aforementioned pulse characteristics. Clearly, the pulse width is highly sensitive to the effective dispersion of the random medium and the relative phase accumulated during propagation. Thus, comparison of the calculated pulse widths with the experiment offers a good test into the applicability of the effective medium approximation commonly used to describe electromagnetic wave propagation through heterogeneous random media. By mapping the random sample on an effective homogeneous medium described by the Bruggeman effective medium approximation, it is found that the calculated pulse widths underestimate the experimental pulse duration by a factor of ~2. This discrepancy confirms the inadequacy of the classical effective medium approximation for spherical scatterers with a size parameter above $x = \delta\pi/\lambda \sim 1$ [17]. Accordingly, for higher frequencies of the THz pulse, phase modifications are required. As there exists no effective medium approximation that yields accurate results for $x > 1$, the effective medium approximation is empirically modified by introducing a small second order corrective phase factor. This was done as follows: the unmodified phase is expanded into a series expansion in terms of ω yielding $\Phi_{tr}(\omega) = A\ (\omega + 0.01\ \omega^2)$ radians, where A is the constant of proportionality. The coefficient of the second order term is iteratively modified, while testing the agreement between the experimental and numerical pulses. This is done until a good fit is obtained, from which a phase of $\Phi_{tr}(\omega) = A(\omega + 0.09\omega^2)$ radians is achieved. A plot of the modified and unmodified phases in the inset of Figure 2.11 illustrates the phase correction introduced by this method. The calculated pulse shape using the modified phase maintains the pulse delay, and the pulse stretch now agrees excellently with the experimental pulse. For strongly scattering media, the Bruggeman effective medium approximation underestimates the phase accrued by the higher frequency photons where $x > 1$. The physical origin of this additional phase acquired by the higher frequency photons is unknown. One possible cause of this effect could be surface wave phenomena on the surface of the dielectric particles. In previous work [18], it was shown that terahertz radiation incident on a dielectric sphere (larger than the wavelength) could partly travel around the surface of the sphere as a surface wave. A similar effect in the subwavelength sapphire particles in the experiments would account for the additional propagation distance (and hence, phase accumulation) of the higher frequency components. Additional experiments are required to determine the precise cause of the additional phase accumulation.

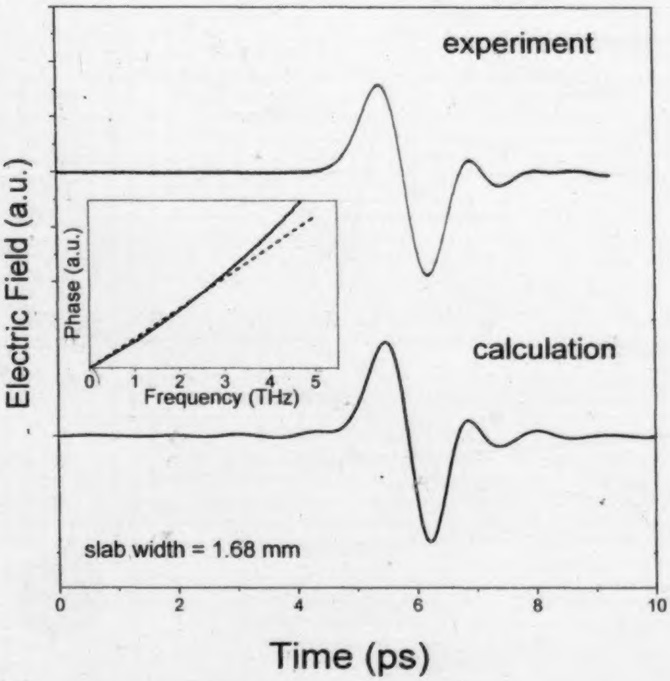

Figure 2.11. The experimental (top) and calculated (bottom) temporal THz waveforms transmitted through the sample for a thickness of 1.68 mm. The calculated THz waveform is derived from a modified phase shown in the inset (solid line) along with the unmodified phase (dashed line).

2.3 Conclusion

This Chapter reports on experimental and theoretical studies of THz electromagnetic pulse propagation in highly scattering random dielectric media. Through examination of the transmitted THz pulse features such as pulse shape, group delay, pulse width, spectral width, and the transmitted power, THz electric field transmission through a strongly scattering medium is fully characterized. The experimental results have been compared to calculations based on a photon migration model. The calculated variations of the THz pulse group propagation delay and scattering-induced effects, such as temporal pulse distortion, spectral decay, and power attenuation as a function of sample thickness are in good agreement with the experimental data. For the strongly scattering sample used, the high sensitivity of the experimental pulse width to the effective dispersion of the medium provides ideal conditions for verifying the applicability of the widely accepted effective medium approximation. It is found that for scattering size parameter $x \geq 1$, the effective medium approximation underestimates the accumulated pulse phase acquired during pulse propagation. The breakdown of effective medium approximations in this regime suggests the onset of diffusive photon transport through the scattering medium. The insights provided by this work are vital to the application of THz spectroscopy to image subwavelength sized, highly scattering structures [19-21].

Chapter 2 References

[1] C. F. Bohren and D. R. Huffman, *Absorption and Scattering of Light by Small Particles*. New York: John Wiley & Sons, 1983.

[2] A. Ishimaru, *Wave Propagation and Scattering in Random Media*. New York: Academic, 1978.

[3] P. Sheng, *Introduction to Wave Scattering, Localization, Mesoscopic Phenomena*. New York: Academic Press, 1995.

[4] P. W. Anderson, "Absence of diffusion in certain random lattices," *Physical Review*, vol. 109, pp. 1492-1505, 1958.

[5] F. Scheffold, R. Lenke, R. Tweer, and G. Maret, "Localization or classical diffusion of light?," *Nature*, vol. 398, pp. 671-673, 1999.

[6] D. S. Wiersma, J. G. Rivas, P. Bartolini, A. Lagendijk, and R. Righini, "Localization of classical diffusion of light? (reply)," *Nature*, vol. 398, pp. 207, 1999.

[7] M. P. V. Albada and A. Lagendijk, "Observation of Weak Localization of Light in a Random Medium," *Physical Review Letters*, vol. 55, pp. 2692-2695, 1985.

[8] F. J. P. Schuurmans, D. Vanmaekelbergh, J. v. d. Lagemaat, and A. Lagendijk, "Strongly Photonic Macroporous Gallium Phosphide Networks," *Science*, vol. 284, pp. 141-143, 1999.

[9] F. J. P. Schuurmans, M. Megens, D. Vanmaekelbergh, and A. Lagendijk, "Light Scattering near the Localization Transition in Macroporous GaP Networks," *Physical Review Letters*, vol. 83, pp. 2183-2186, 1999.

[10] J. Pearce, K. Doyle, Z. Jian, J. Diebel, and D. M. Mittleman, "Nonstationary time-domain statistics of multiply scattered broadband terahertz pulses," *Journal of the Optical Society of America B*, vol. 23, pp. 1506-1510, 2006.

[11] J. Pearce, Z. Jian, and D. M. Mittleman, "Statistics of Multiply Scattered Broadband Terahertz Pulses," *Physical Review Letters*, vol. 91, pp. 043903, 2003.

[12] J. Pearce, Z. Jian, and D. M. Mittleman, "Spectral shifts as a signature of the onset of diffusion of broadband terahertz pulses," *Optics Letters*, vol. 29, pp. 2926-2928, 2004.

[13] J. Pearce and D. M. Mittleman, "Propagation of single-cycle terahertz pulses in random media," *Optics Letters*, vol. 26, pp. 2002-2004, 2001.

[14] D. Grischkowsky, S. Keiding, M. v. Exter, and C. Fattinger, "Far-infrared time-domain spectroscopy with terahertz beams of dielectrics and semiconductors," *Journal of the Optical Society of America B*, vol. 7, pp. 2006-2015, 1990.

[15] S. Mujumdar, S. Cavalieri, and D. S. Wiersma, "Temperature-tunable random lasing: numerical calculations and experiments," *Journal of the Optical Society of America B*, vol. 21, pp. 201-207, 2004.

[16] A. Yodh, B. Tromberg, E. Sevick-Muraca, and D. Pine, "Diffusing photons in turbid media," *Journal of the Optical Society of America A*, vol. 14, pp. 136-136, 1997.

[17] P. Chylek, G. Videen, W. Geldart, S. Dobbie, and W. Tso, "Effective Medium Approximation for Heterogeneous Particles," in *Light Scattering by Nonspherical Particles: Theory, Measurements, and Geophysical Applications*, M. Mishchenko, Ed.: Academic, 2000, pp. 273-308.

[18] R. A. Cheville, R. W. McGowan, and D. Grischkowsky, "Time resolved measurements which isolate the mechanisms responsible for terahertz glory scattering from dielectric spheres," *Physical Review Letters*, vol. 80, pp. 269-272, 1998.

[19] P. Y. Han, G. C. Cho, and X.-C. Zhang, "Time-domain transillumination of biological tissues with terahertz pulses," *Optics Letters*, vol. 25, pp. 242-244, 2000.

[20] B. B. Hu and M. C. Nuss, "Imaging with terahertz waves," *Optics Letters*, vol. 20, pp. 1716-1718, 1995.

[21] D. M. Mittleman, S. Hunsche, L. Boivin, and M. Nuss, "T-ray tomography," *Optics Letters*, vol. 22, pp. 904-906, 1997.

Chapter 3:

Terahertz Particle Plasmons

3.1. Background

The optical properties of small, subwavelength metallic structures have interested both artists and scientists for hundreds of years. The unique electromagnetic properties of these structures arise from coupling between an incident electromagnetic wave and the collective conduction electron oscillations of the metallic particle, referred to as a localized particle plasmon excitation [1, 2]. Localized particle plasmons on subwavelength metallic particles can give rise to electromagnetic properties that are foreign to the bulk metal. Small nano-particles of gold or silver, for instance, can show a diverse range of colors due to resonant absorption and scattering at frequencies near their particle plasmon resonance. Historically, the stunning optical properties of these particles have been used for the creation of stained glass windows and works of art such as the Lycurgus cup [3]. It is remarkable that subwavelength metallic particles continue to be an important element in a wide range of contemporary technological applications.

Subwavelength metallic particles possess several unique electromagnetic properties which make them suitable for modern photonics applications. Electromagnetic excitation of a subwavelength metallic particle results in highly confined surface fields, which enhances the electromagnetic energy density near the particle surface relative to that of the incident electromagnetic wave. The enhancement arises from two physical effects: resonant excitation of the particle plasmon resonance discussed in Chapter 1 and the lightning rod effect due to the crowding of electric field lines near the particle surface, especially at sharp features [4-6]. The former is highly sensitive to the frequency of the incident electromagnetic wave, while the latter is purely geometrical in origin. The highly enhanced fields associated with particle plasmons are ideal for many applications requiring large, local electromagnetic fields such as luminescence [7] and nonlinear processes [8, 9]. In particular, one of the most exciting applications of particle plasmons is surface enhanced Raman scattering. Raman scattering describes inelastic scattering between an electromagnetic wave and a molecule, mediated by a vibrational or rotational mode of the molecule [7]. In this process, an incoming electromagnetic wave is shifted in energy by the characteristic energy of the vibrational or rotational mode of the molecule. The efficiency of the Raman scattering process is commonly described in terms of a scattering cross section. Typically, Raman scattering cross sections range between 10^{-31} cm^2/molecule and 10^{-29} cm^2/molecule. Surface enhanced Raman scattering describes the use of metallic nanostructures in the vicinity of a Raman active molecule to enhance the efficiency of Raman scattering. Using roughened Au or Ag nanostructures with gaps on the order of a few nanometers, surface enhanced Raman scattering has resulted in stunning increases in the Raman scattering cross section by factors up to 10^{14} [10, 11].

Localized particle plasmons associated with subwavelength metallic particles have also been widely employed for sensing applications. For a spherical particle with a subwavelength diameter, the resonance frequency of the particle plasmon corresponds to the condition where $\mathrm{Re}[\varepsilon_{metal}(\omega)] = -2\, \varepsilon_d(\omega)$, where $\varepsilon_d(\omega)$ is the permittivity of the dielectric medium surrounding the particle. The localization of the particle plasmon fields in the immediate vicinity of the particle surface means that the resonance frequency is highly dependent on $\varepsilon_d(\omega)$ within the evanescent near-field surrounding the particle. Hence, small changes in $\varepsilon_d(\omega)$ (for instance, via adsorption of molecules on the particle surface) can be monitored by a change in the resonant particle plasmon frequency [12].

One unique feature of particle plasmons is their ability to concentrate electromagnetic energy over subwavelength extents. The volume over which a particle plasmon confines electromagnetic energy is primarily governed by the size of the particle with respect to the wavelength of the incident radiation. Hence, electromagnetic energy incident on a subwavelength metallic particle is effectively squeezed into a subwavelength volume. This property is highly useful in the continuing efforts to miniaturize existing photonic information technology into the nano-scale to achieve higher density devices [13]. Whereas the size and density of a photonic waveguide is typically limited by the diffraction limit (on the order of the wavelength), metallic nanostructures can strongly localize electromagnetic energy below the diffraction limit via localized particle plasmons. Quinten et al. [14] initially proposed the idea of plasmonic waveguides constructed from linear arrays of closely spaced, subwavelength sized Ag particles. Near-field coupling between adjacent particles transports electromagnetic energy over the extent of the waveguide, with sub-diffractive confinement. This principle was experimentally demonstrated by Maier et al. [15] using a waveguide consisting of a chain of closely spaced Ag nanorods. In their experiment, the entrance of the waveguide is locally illuminated with a near-field optical microscope at a frequency corresponding to the particle plasmon resonance. Electromagnetic energy is channelled from the entrance of the waveguide to the exit via near-field interaction between particles. A fluorescent polymer bead placed at the end of the waveguide radiates into the far-field when excited by electromagnetic energy. Using this method, energy transport along the particle chain is detected in the far-field by the fluorescence at the exit of the waveguide. Since the waveguide is excited at the particle plasmon resonance, there are high losses associated with resonant absorption. Hence, propagation lengths using these waveguides are on the order of 1 μm or less. Research continues on the development of methods to overcome the inherent losses of particle plasmon waveguides. One promising technique involves imbedding the particles in a medium with optical gain [16].

The study of particle plasmons has been primarily conducted in the visible regime using metallic nano-particles. This is because the particle plasmon resonance for metals such as Au and Ag typically occurs at visible frequencies or higher. On the other hand, the non-resonant particle plasmon response of subwavelength sized metallic particles at the lower frequencies of the THz range has received relatively little research attention. The physics underlying non-resonant particle plasmons at THz frequencies is fundamentally different than resonant particle plasmons at visible frequencies. At THz frequencies, the resonant particle plasmon response of subwavelength microparticles is inaccessible since $\mathrm{Re}[\varepsilon_{metal}(\omega)] \sim -10^5$. This large permittivity also dictates that incident THz electromagnetic radiation cannot infiltrate deeply into the metallic medium, since the skin depth is on the order of 100s nm. Hence, non-resonant particle plasmons can be excited on *subwavelength* sized particles having dimensions *many orders of magnitude larger than the skin depth* (Figure 3.1). This contrasts with resonant particle plasmon at visible frequencies, where the diameter of the nano-particle is less than both the wavelength and the skin depth of the incident radiation. The dephasing mechanisms are another fundamental difference between resonant and non-resonant particle plasmons. As discussed in Chapter 1, the dominant dephasing mechanism for resonant particle plasmon at visible frequencies is the background polarization of the particle. This dephasing mechanism arises when the electric field inside the particle shifts the conduction electrons with respect to the fixed positive charge of the lattice ions. Electrons accumulate at one side of the particle, leaving a positive charge of the lattice ions at the other side of the particle. The attraction between the negative charge and the positive charge on opposing sides of the particle creates a restoring polarization force on the electrons. This differs from non-resonant particle plasmons at THz frequencies, whose dephasing mechanism is dependent on the resistivity of the particle near the surface. Indeed, non-resonant particle plasmons excited at THz frequencies constitute a novel, hitherto unexplored, regime of plasmonic interaction, distinctly different from resonant particle plasmons at visible frequencies.

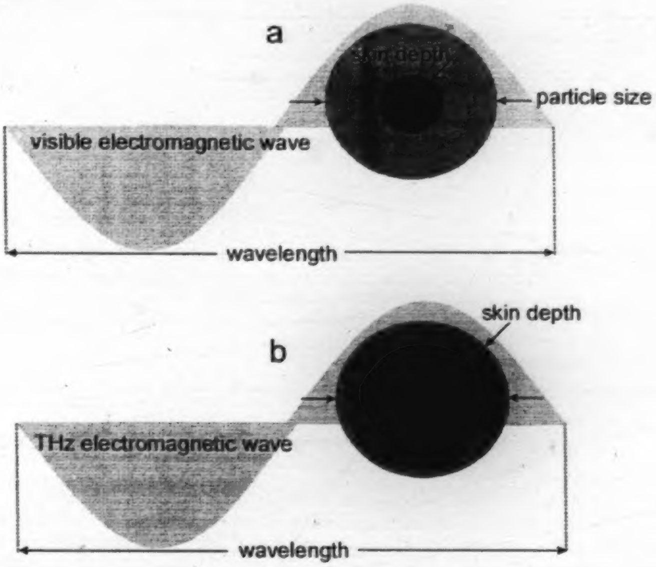

Figure 3.1. (a) Illustration of visible electromagnetic wave excitation of a subwavelength scale particle where the particle size is comparable to the skin depth. (b) Illustration of THz electromagnetic wave excitation of a subwavelength scale particle where the particle size is significantly larger than the skin depth.

In this Chapter, the interaction of THz electromagnetic waves with subwavelength metallic media is studied. Non-resonant particle plasmon excitation of a single, independent subwavelength metallic particle by a THz electromagnetic wave is explored using finite difference time-domain (FDTD) calculations of Maxwell's Equations. In ensembles of subwavelength metallic particles excited by THz electromagnetic waves, mutual interaction between particle plasmons plays a dominant role in the collective electromagnetic properties of the ensemble. It is shown that a dense ensemble of subwavelength sized metallic particles can show surprising transparency to THz radiation. Interestingly, the enhanced THz electromagnetic wave transmission cannot be described using effective medium approximations. The origin of the enhanced transmission is resolved via FDTD calculations of THz electromagnetic wave interaction with a collection of metallic particles. It is shown that THz electromagnetic wave propagation through the ensemble of metallic particles is mediated by near-field particle plasmon interaction between nearest neighbor particles. The influences of particle size, particle shape, and metal conductivity on the effective THz electromagnetic properties of particle ensemble are experimentally and numerically studied. In continuing investigation of THz particle plasmons, it is shown that collections of metallic particles that have been coated with nano-layers of a different metal show diminished THz transparency due to non-radiative particle plasmon losses at the interface between the two dissimilar metals. This interface resistive effect is applied to probe the THz electromagnetic sub-surface charge induction in bimetallic layered particles. The experimental results show that plasmonic interaction between the incident THz electromagnetic wave and the metallic particle occurs within a sub-surface distance comparable to the skin depth. This Chapter further explores the THz electromagnetic properties of an amorphous metamaterial consisting of ensembles of dielectric and metallic inclusions. It is shown that the effective electromagnetic properties of the amorphous metamaterial show a nonlinear dependence on the relative volume fraction of the metallic and dielectric inclusions. This behaviour is resolved by considering the particle plasmon interactions between the metallic inclusions. The contents of this Chapter have been published in *Physical Review Letters*, vol. 94, 173904 (2005); *Physical Review B*, vol. 72, 075110 (2005); *Physical Review B*, vol. 73, 085419 (2006); and *Applied Physics Letters*, vol. 90, 131114 (2007).

3.2. Terahertz Localized Particle Plasmon on a Single Metallic Particle

As discussed in Chapter 1, a THz electromagnetic wave incident on a subwavelength metallic particle excites a localized non-resonant particle plasmon. The formation of the THz particle plasmon is governed by two mechanisms; 1) the THz electromagnetic wave incident on the particle surface penetrates hundreds of nanometers into the metal where it induces charge motion (or current density), and 2) the dipolar electric field is formed by the accumulation of negative and positive charge at opposite sides of the particle's surface. At the surface, the dipolar electric field associated with the localized particle plasmon is oriented normal to the particle surface and has a net orientation along the direction of the excitation electric field.

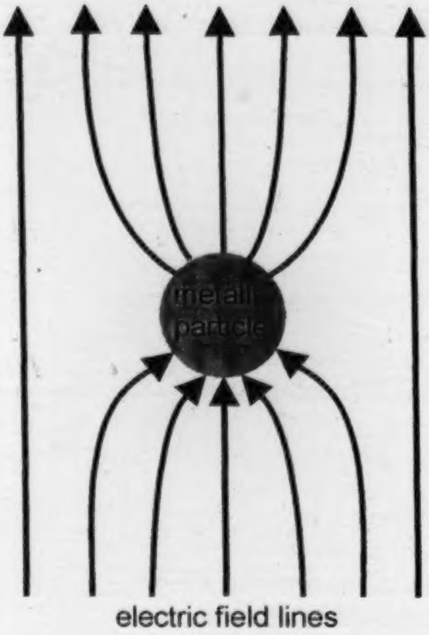

Figure 3.2. Electric field lines near a metallic particle that has been immersed in a homogenous electric field. The lightning rod effect results in a higher electric field density near the particle surface.

Similar to particle plasmons at other frequencies, non-resonant particle plasmons at THz frequencies possess two important features: high electromagnetic energy density near the surface and subwavelength containment of electromagnetic energy. The latter arises because the excitation of a particle plasmon converts some of the incident electromagnetic energy into the conduction electron oscillations of the particle. The spatial extent of these electron oscillations is determined by the size of the particle with respect to the wavelength of the electromagnetic wave. Hence, electromagnetic energy can be confined into a subwavelength volume. Due to the lightning rod effect (or antenna effect), the electric field near the surface has a higher electromagnetic energy density than that of the incident electromagnetic wave. The lightning rod effect is a purely geometrical effect that occurs at the surface of good conductors. As seen in Figure 3.2, this causes crowding of the field lines at the surface of the particle, enhancing the local energy density. When a THz electromagnetic wave is incident on a subwavelength metallic particle, the electric field lines terminate normal to the metallic surface. The field lines terminate perpendicular to the surface because the conduction electrons of the metal respond nearly instantaneously to a THz electric field [17]. That is, when a THz electric field is applied to the metal, the conduction electrons shift so as set up a depolarization field that precisely cancels the tangential component of the externally applied electric field at the surface. This occurs if the metal is a good conductor, and the conduction electrons of the metal respond to external excitation faster than the oscillation period of the THz electromagnetic wave. The "goodness" of a conductor can be qualified by considering a conductor that obeys Ohm's law

$$\boldsymbol{j}_F = \sigma \boldsymbol{E} \qquad (3.2.1).$$

where $\boldsymbol{j}_F$ is the free current density, σ is the conductivity, and $\boldsymbol{E}$ is the electric field. The current density flow must cause a change in the local charge density obeying charge conservation, described by

$$\nabla \cdot \boldsymbol{j}_F = -\partial\rho/\partial t \qquad (3.2.2)$$

Inserting Equation (3.2.1) into Equation (3.2.2), the time evolution of free charge is described by

$$\partial\rho/\partial t = -\sigma\,(\nabla \cdot \boldsymbol{E}) = -(\sigma/\varepsilon_o)\,\rho \qquad (3.2.3)$$

for a linear, homogeneous, isotropic medium. The solution to Equation (3.2.3) has the form

$$\rho(t) = \rho(0)\ \mathrm{e}^{-(\sigma/\varepsilon_o)\,t} \qquad (3.2.4)$$

Thus, an initial free charge density $\rho(0)$ dissipates over some characteristic time $t_d = \varepsilon_o/\sigma$. The time constant t_d relative to the oscillation period of an electromagnetic wave provides a measure for the conductivity of a medium at a given frequency. For a perfect conductor, $\sigma = \infty$ and $t_d = 0$; the metal responds instantaneously to the introduction of free charge and is a good conductor at all frequencies. At THz frequencies, t_d for nearly all conductors is much shorter than the oscillation period. For example, Cu has a measured conductivity of $5 \times 10^7\ (\Omega\ \mathrm{m})^{-1}$ in the GHz range [18], corresponding to $t_d = 0.2\times10^{-18}$ s, which is significantly less than the THz oscillation period.

To visualize the electric fields associated with a THz non-resonant localized particle plasmon, the THz electromagnetic properties of a single, isolated subwavelength metallic microparticle are studied using Maxwell's equations. Maxwell's equations are employed to describe the spatial and temporal distribution of the electric and magnetic fields in the presence of the metallic microparticle

$$-\frac{\partial \boldsymbol{H}}{\partial t}=\frac{1}{\mu_o}\nabla\times\boldsymbol{E} \tag{3.2.5}$$

$$\frac{\partial \boldsymbol{D}}{\partial t}=\nabla\times\boldsymbol{H} \tag{3.2.6}.$$

Here, $\boldsymbol{H}$ is the magnetic flux density, $\boldsymbol{D}$ is the displacement field, $\boldsymbol{E}$ is the electric field, and μ_o is the free space permeability. To solve Equations (3.2.5) and (3.26), many numerical methods can be employed. One of the most widely used techniques is the Finite Difference Time-Domain (FDTD) method (refer to Appendix C which describes the algorithm employed). The FDTD method is advantageous due to its relative simplicity and ease of use. In this method, the material properties of each grid point of the simulation space can be independently specified, enabling electromagnetic modeling using a wide range of materials and material geometries. Since FDTD is a time-domain technique, the response of the material to broadband electromagnetic pulse excitation over a wide range of frequencies can be obtained with a single simulation. Moreover, the FDTD solves the complete spatial and temporal electric and magnetic fields, which permits animated displays of the electromagnetic field interaction and evolution within the simulation space.

In the calculations, Equations (3.2.5) and (3.26) are discretized to yield finite difference expressions for the electromagnetic field components. The electromagnetic response of the metallic medium to the incident electromagnetic field is described by the Drude model of $\varepsilon_{metal}(\omega)$. By re-casting the relation $\boldsymbol{D} = \varepsilon_{metal}(\omega)\,\boldsymbol{E}$, where $\boldsymbol{D}$ and $\boldsymbol{E}$ are the displacement and electric fields, respectively, into the time-domain through Fourier transformation, the supplementary equation is generated

$$\Gamma\frac{\partial \boldsymbol{D}}{\partial t}+\frac{\partial^2 \boldsymbol{D}}{\partial t^2}=\omega_p^2\varepsilon_o\boldsymbol{E}+\Gamma\varepsilon_o\frac{\partial \boldsymbol{E}}{\partial t}+\varepsilon_o\frac{\partial^2 \boldsymbol{E}}{\partial t^2} \qquad (3.2.7).$$

In combination with the Equations (3.2.5) and (3.26), the fields $\boldsymbol{E}$, $\boldsymbol{D}$, and $\boldsymbol{H}$ are solved for all time and space in the simulation domain. The spatial resolution and the temporal step size of the calculations are 5 μm and 5 fs, respectively.

Shown in Figure 3.3 is a FDTD calculation of THz electromagnetic pulse excitation of a single metallic (Cu) microparticle having a diameter of 75 μm immersed in free space. In the calculations, the THz pulse propagates upward from the bottom of the images and is polarized in the plane of the images (transverse magnetic or TM). The spectral contents of the THz pulse are centred at 0.6 THz with a 1 THz bandwidth. The images in Figure 3.3 (a) to 3.3 (d) correspond to snapshots of the THz electric field magnitude at various times. Figure 3.3 (a) shows the single-cycle polarized THz pulse propagating at $t = 0.0$ ps towards the subwavelength sized metallic particle. As the THz pulse is incident on the particle at 3.5 ps, corresponding to the image in Figure 3.3 (b), it is evident that negligible THz electric field amplitude is present inside the particle. This is because the skin depth of the THz electromagnetic wave is significantly less than the particle diameter. At 3.5 ps, the total electric field illustrated in Figure 3.3 (b) consists of both the external THz field and the electric field arising from the induced charges at the particle's surface. In this frame of the calculation, it is not possible to separate the external and induced-charge contributions to the total electric field. The electric field arising from the induced charges, however, can be visualized after the passage of the THz electric field pulse, at 8.5 ps. As shown in Figure 3.3 (c) and Figure 3.4 (a), after passage of the THz electric field pulse, the electromagnetic fields around the particle are confined to the surface and exhibit strong dipole-like signatures. Such a surface field is attributed to the excitation of charge oscillations on the particle oriented along the polarization of the THz electric field pulse. From $\nabla \cdot \boldsymbol{D} = \rho_F$, the charge density distribution associated with the dipolar electric fields can be obtained. As shown in Figure 3.4 (b), the induced charge density illustrates dipolar charge induction by the incident THz pulse, where positive and negative charge density accumulate at opposing sides of the particle. The induced charge densities are coupled to an electromagnetic field confined to the surface of the particle. As shown in Figure 3.5, the dipolar electric field associated with the induced charge density is strongest directly above the surface of the particle and decays exponentially within a distance of 250 μm. This distance is less than the central wavelength of the THz pulse, $\lambda = 500$ μm, implying that the surface fields are confined to the near-field region in the immediate vicinity of the particle.

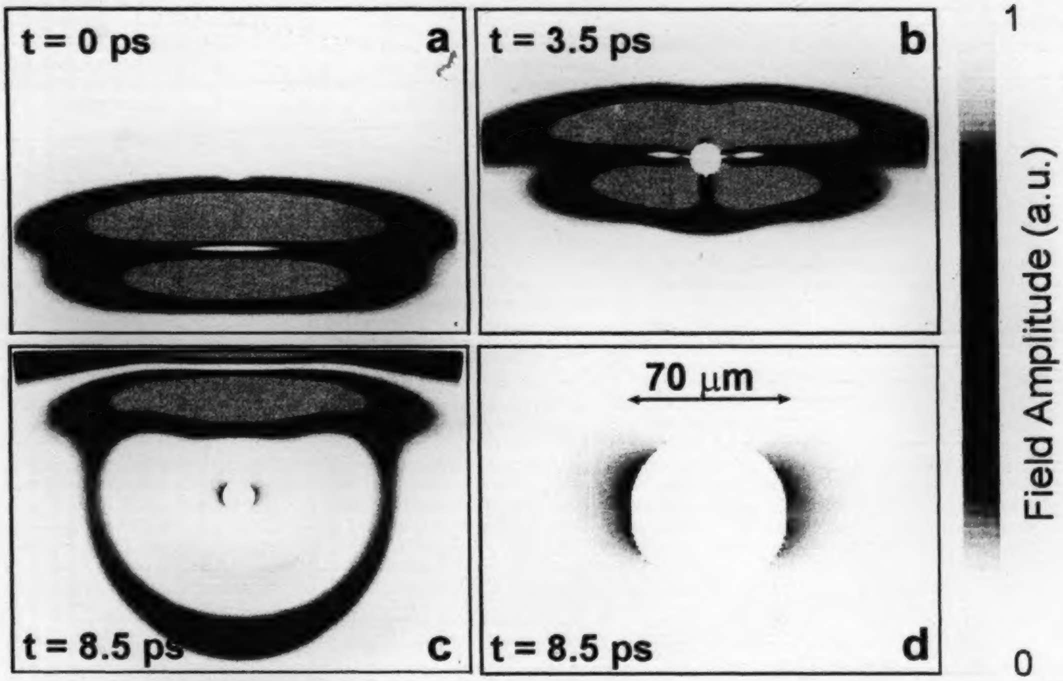

Figure 3.3. Images of a FDTD calculation of single-cycle THz pulse excitation of a 70 μm diameter Cu particle at (a) 0 ps, (b) 3.5 ps, (c) 8.5 ps. Shown in (d) is a magnified image of the particle at 8.5 ps.

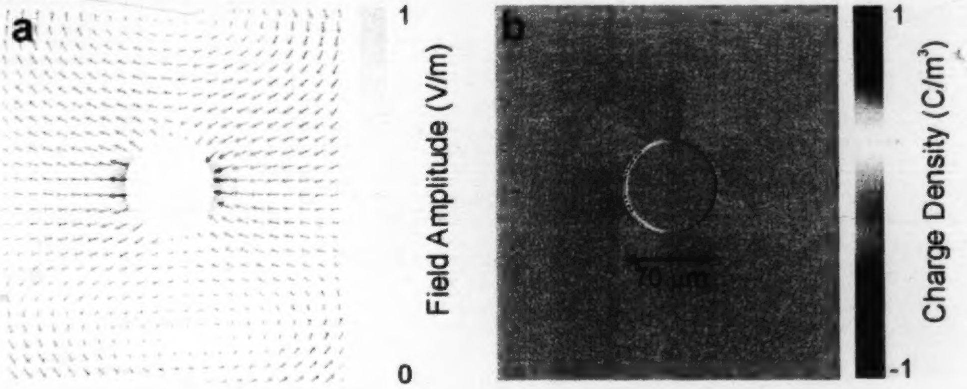

Figure 3.4. (a) Vector plot of the electric field in the vicinity of a 70 μm Cu microparticle after excitation by a single-cycle THz pulse at 8.5 ps of the simulation shown in Figure 3.3. (b) illustrates the corresponding dipolar charge distribution at the surface of the microparticle.

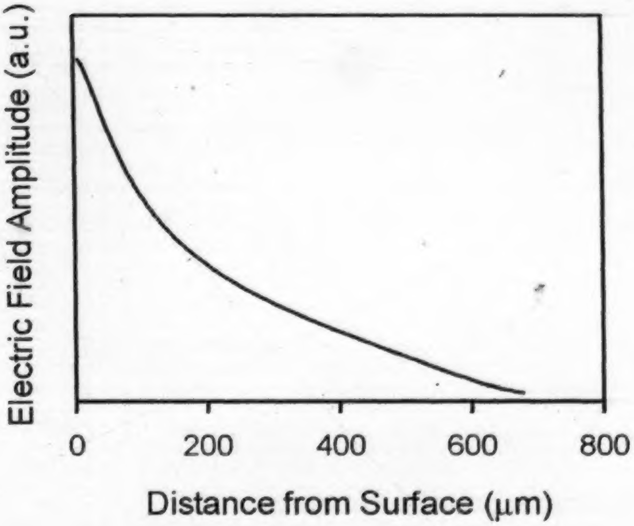

Figure 3.5. Calculated amplitude of the electric field outside the surface of a 70 μm Cu microparticle after excitation by a single-cycle THz pulse versus the distance from the particle surface.

3.3. Terahertz Electromagnetic Properties of an Ensemble of Metallic Particles

In ensembles of subwavelength metallic particles, shown in Figure 3.6, electromagnetic interaction between the particles plays an important role in the overall electromagnetic properties of the ensemble. Since the particles are electromagnetically coupled, each particle is excited by the external electric field in addition to the field scattered from all the other particles. Depending on the separation between the particles, two regimes of interaction exist: far-field interaction and near-field interaction. To illustrate, consider an ensemble of particles having diameters much smaller than the wavelength of the electromagnetic wave. The incident electromagnetic wave excites oscillations of the conduction electrons at the surface of individual metallic particles, which, to a first order, can be described as a collection of oscillating dipoles, $p(t)$. The electric field, $E_p(r,t)$, associated with a single dipole, consists of quasi-static ($\propto 1/r^3$), near-field ($\propto 1/r^2$) and far-field ($\propto 1/r$) terms and is expressed as [19]

$$E_p(r,t) = \frac{1}{4\pi\varepsilon_o}\left(\frac{1}{r^3}p(t) + \frac{1}{r^2 c}\frac{\partial p(t)}{\partial t} + \frac{1}{c^2 r}\frac{\partial^2 p(t)}{\partial t^2}\right) \qquad (3.3.1).$$

In a random ensemble of subwavelength size metallic particles, the mutual interaction between particles is strongly influenced by the inter-particle separation, *s*, and the evanescent decay distance of the particle plasmon, *d*. For $s/d > 1$, the interaction between particles is governed by far-field dipolar absorption and re-radiation exhibiting an r^{-1} dependence. However, for closely-spaced subwavelength metallic particles such that $s/d \ll 1$, the inter-particle interaction via the near-field of the dipolar field (exhibiting an r^{-3} dependence) strongly couples the particles.

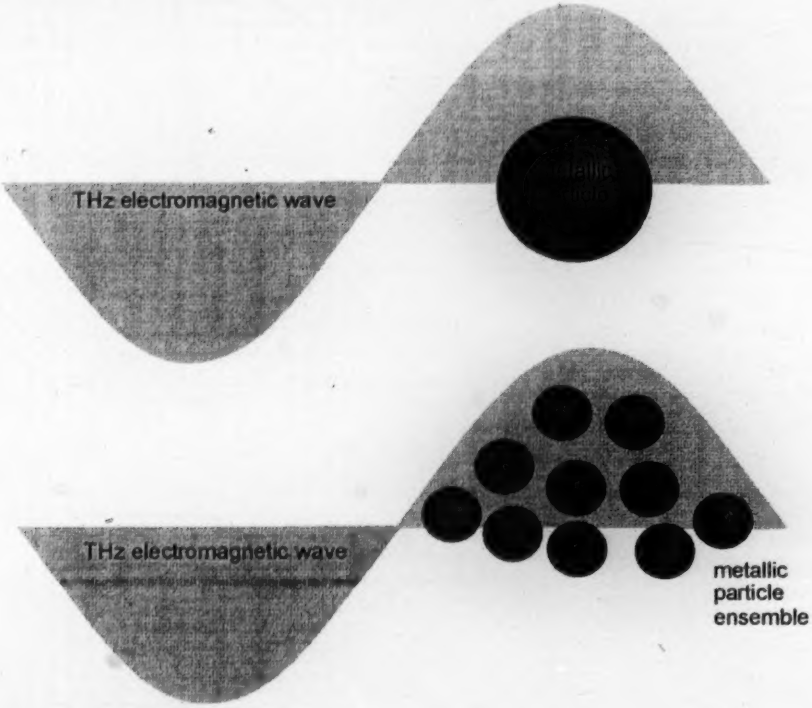

Figure 3.6. (top) THz electromagnetic wave excitation of a single metallic particle and (bottom) THz electromagnetic wave excitation of an ensemble of metallic particles.

The complex interactions between metallic particles make it difficult to analytically describe the electromagnetic properties of the ensemble. One common technique to determine the electromagnetic properties of subwavelength metallic particle collections is via effective medium approximations [1, 20]. The effective medium approximation replaces an inhomogeneous medium with a fictitious homogeneous effective medium which expresses the linear response of the whole inhomogeneous sample to an external electric field. Thus, rather than laboriously describing the microscopic interactions between the constituents, the entire heterogeneous medium is described by a single effective parameter. For a review of various effective medium approximations used to describe heterogeneous metallic media, the reader is referred to Kreibig and Vollmer [1].

Effective medium approximations have been commonly employed to describe the optical properties of nano-scale metallic clusters at visible frequencies [1, 2, 21]. However, effective medium approximations often fail for heterogeneous metallic media at THz frequencies. The validity of effective medium approximations is governed by the quasi-static limitation. In the quasi-static limitation, the electric and displacement fields throughout the heterogeneous medium must be approximately uniform. To illustrate, consider a subwavelength metallic sphere having a diameter of δ. The sphere is centred at $z = 0$ and illuminated by a plane wave. For the field amplitude within the particle to be uniform, there must be minimal absorption over the particle dimension, or

$$\boldsymbol{x}\,\mathrm{Im}[\sqrt{\varepsilon_{metal}(\omega)}\,] \ll 1 \tag{3.3.2}$$

where $\mathrm{Im}[\sqrt{\varepsilon_{metal}(\omega)}\,]$ is the imaginary part of the metal refractive index and $\boldsymbol{x} = \pi\delta/\lambda$ is the size parameter. Similarly, there must be minimal spatial variation of the electromagnetic wave in the sphere, which implies that the wavelength inside the sphere is much greater than the particle size, or

$$x \,\mathrm{Re}[\sqrt{\varepsilon_{metal}(\omega)}\,] << 1 \qquad (3.3.3)$$

where Re[$\sqrt{\varepsilon_{metal}(\omega)}$] is the real part of the metal refractive index. Combining these two inequalities gives the condition for the quasi-static limitation

$$x\,|\sqrt{\varepsilon_{metal}(\omega)}\,| << 1 \qquad (3.3.4).$$

Micron-scale heterogeneous metallic media typically do not obey the quasi-static limitation at THz frequencies. To qualify this, the inequality (3.3.4) is determined for a 1 μm diameter Au particle having a permittivity at 1 THz of $\varepsilon_{Au}(1\text{ THz}) \approx -0.7 \times 10^4 + i\, 1.8 \times 10^5$ excited by an electromagnetic wave with a wavelength of 300 μm (corresponding to a frequency of 1 THz):

$$x\,|\sqrt{\varepsilon_{metal}(\omega)}\,| = 432\,\pi/300 = 4.5 > 1 \qquad (3.3.5)$$

Thus, for metallic particles with micron scale diameters, *the effective medium approximation is not valid at THz frequencies*. Therefore, THz electromagnetic wave excitation of ensembles of subwavelength sized metallic particles with micron-scale dimensions constitutes an intriguing regime of light-matter interaction. A THz electromagnetic wave incident on the particles is expected to excite non-resonant localized particle plasmons on the individual particles. Due to the highly heterogeneous THz electric field distribution in the particle ensemble, however, the mutual interactions between particles that give rise to its global electromagnetic properties are not describable by averaging methods such as the effective medium approximation. Therefore, the exploration of the interaction of THz electromagnetic waves with ensembles of subwavelength sized metallic particles constitutes a regime of plasmonic interaction that has yet to be fully explored.

3.4. Enhanced Terahertz Transmission through Metallic Particle Ensembles

Metals are nearly perfect reflectors at THz frequencies. The high reflectivity of metals at THz frequencies is due to their large permittivity values. Cr, for instance, possesses a real permittivity of $\mathrm{Re}[\varepsilon_{Cr}\,(1\ \mathrm{THz})] \sim -10^4$ [22] and a corresponding skin depth of $\alpha_{Cr}\,(1\ \mathrm{THz}) \sim 100$ nm. Therefore, THz radiation incident upon a bulk Cr sample that is thicker than the skin depth is nearly totally reflected, and no THz radiation transmits. This effect is illustrated in Figure 3.7 showing THz pulses with a 1 THz bandwidth transmitted through nano-scale Cr films evaporated on Pyrex microscope slides. As seen in the Figure, there is minimal THz transmission through the 70 nm thick Cr film deposited on a microscope slide of 1 mm thickness, and as the Cr film thickness increases to 300 nm, there is nearly no measurable THz transmission.

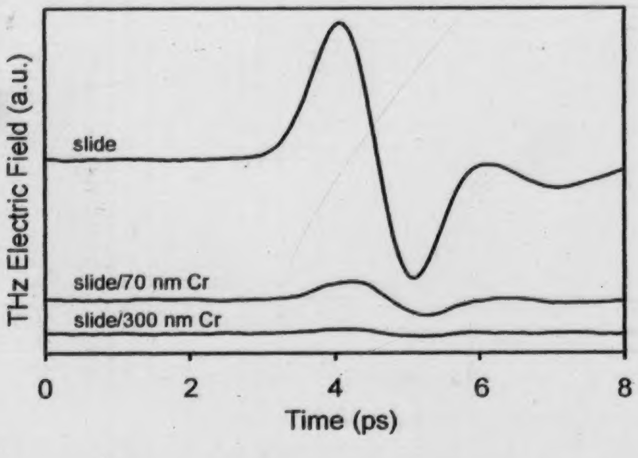

Figure 3.7. THz pulse transmitted through a 1 mm thick microscope slide and 1 mm thick microscope slides that have been coated with a 70 nm and 300 nm thick Cr film.

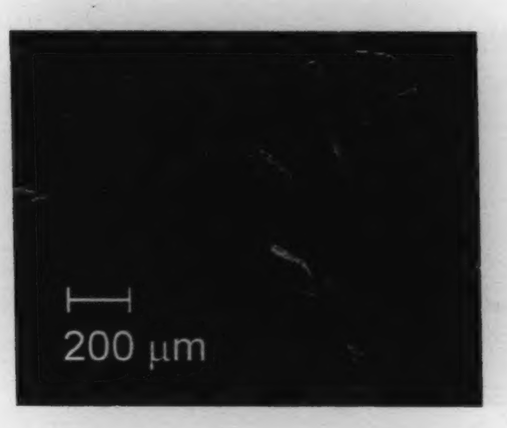

Figure 3.8. Scanning electron microscope image of the Cr particles used in the experiments.

In this section, the THz electromagnetic properties of an ensemble of subwavelength sized Cr particles are studied using THz time-domain spectroscopy. The metallic particle ensemble consists of 99.3 % pure Cr particles that are randomly shaped and poly-dispersed, with a mean dimension δ = 150 μm and a volume packing fraction, f_{Cr} = 0.52. The particle are immersed in air. A scanning electron microscope image of the particles is shown in Figure 3.8. The THz spectroscopic experiments are performed with a similar setup as described in Chapter 2. As shown in Figure 3.9, single-cycle, linearly polarized THz pulses centred at 0.6 THz with a 1 THz bandwidth are generated from a GaAs PC switch excited with focused < 20 fs, 800 nm laser pulses. The collimated beam is directed towards a 6 cm diameter polystyrene sample cell housing the Cr particles. The time-domain electric field transmission in addition to its polarization coherence is measured to characterize electromagnetic wave transport through the medium. The on-axis THz electric field pulse transmitted through the ensemble, $E_{tr}(t)$, is coherently detected via an optically gated 500 μm thick <111> ZnSe electro-optic crystal

[23], and time-resolved information is obtained by varying the delay between the THz pulse and a sampling probe pulse.

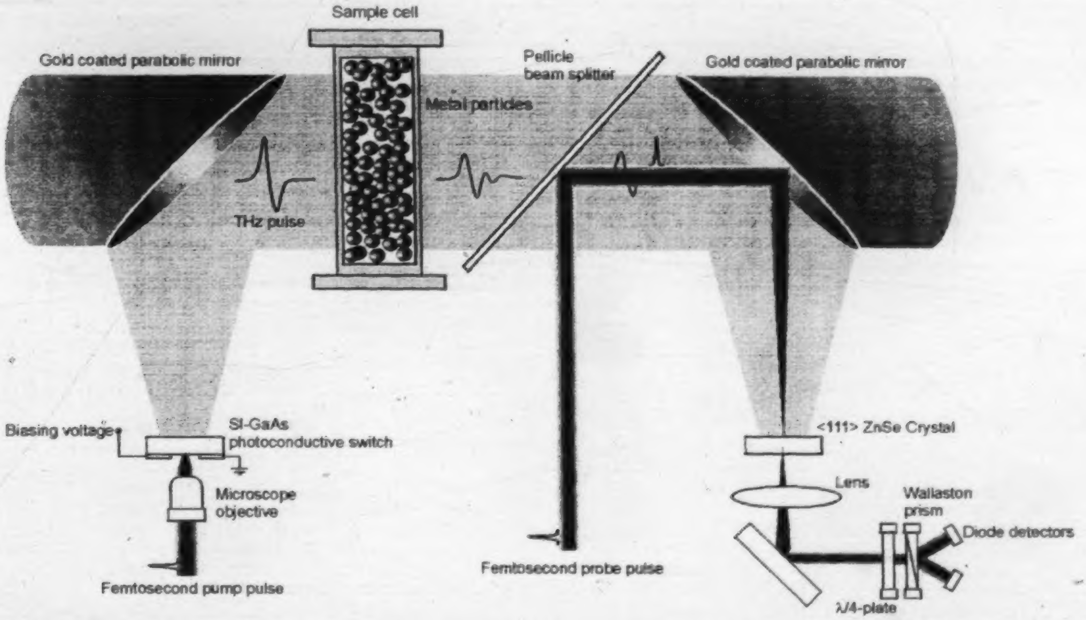
Sample cell
Gold coated parabolic mirror
Pellicle beam splitter
Gold coated parabolic mirror
Metal particles
THz pulse
Biasing voltage
SI-GaAs photoconductive switch
Microscope objective
Femtosecond pump pulse
Femtosecond probe pulse
<111> ZnSe Crystal
Lens
Wallaston prism
Diode detectors
λ/4-plate

Figure 3.9. Schematic of the free-space THz generation and electro-optic detection setup used to characterize the THz electric field transmission through the metallic particle ensembles.

Intuitively, given that the particle size and average inter-particle spacing are both smaller than the wavelengths encompassed by the THz pulse, the ensemble of Cr particles is expected to show nearly no THz transmission. However, significant electric field transmission for sample thickness, *L*, up to 7.0 mm (five orders of magnitude larger than α_{Cr}) is observed. Figure 3.10 (a) depicts the THz transmission for 0.6 mm $\leq L \leq$7.0 mm referenced to the transmission through an empty sample cell corresponding to $L = 0$ mm. In general, the time-resolved signals are characterized by several broad oscillations, which are relatively delayed as *L* increases. The reference pulse is localized in time (within ~ 1 ps); upon impulsive excitation of the sample, it requires a finite time for energy to propagate through the sample. To estimate the energy propagation velocity through the sample, the delay of the transmitted field is measured. Here, the delay corresponds to the time difference between the peak intensity of the reference pulse and the peak intensity of the transmitted pulse (refer to Appendix D for a discussion of the analysis techniques). This delay estimates the time is takes for electromagnetic energy to propagate from one end to the sample to the other end. Shown in Figure 3.11 is the relative pulse delay as a function of sample thickness, referenced to an equivalent air path. The measured delay translates to an electromagnetic energy velocity of 0.60 ± 0.03 c or an effective macroscopic real permittivity of $\mathrm{Re}[\varepsilon] \sim 2.8 \pm 0.2$. It should be noted that the effective macroscopic permittivity reported here describes the overall response of the metallic particle ensemble to THz electromagnetic wave excitation, but is not derived from the effective medium approximation. As shown previously, the effective medium approximation is not valid for metallic particles with micron scale dimensions in the THz frequency range. As L increases from 0.6 to 7.0 mm, the durations of the transmitted electric field pulses are broadened to 6 and 10 ps, respectively. The pulse broadening is attributed to strong dispersive effects magnified for increasing L. Due to the absence of significant intrinsic material resonances for bulk Cr at THz frequencies (i.e. 1 THz $\ll$ ω_p), this dispersion must originate from the extrinsic structural characteristics of the random metallic medium.

Figure 3.11 illustrates the percentage far-field transmitted power as a function of L. From $L = 0.6$ mm to $L = 7.0$ mm, the total integrated transmission power, $\int |E_{tr}(t)|^2 \, dt$, decreases from 3.0 to 0.4 %. The power decay versus sample thickness is fitted to a fit-line with a functional form $1/(1+qL)$, where q is a fitting parameter. As shown in the

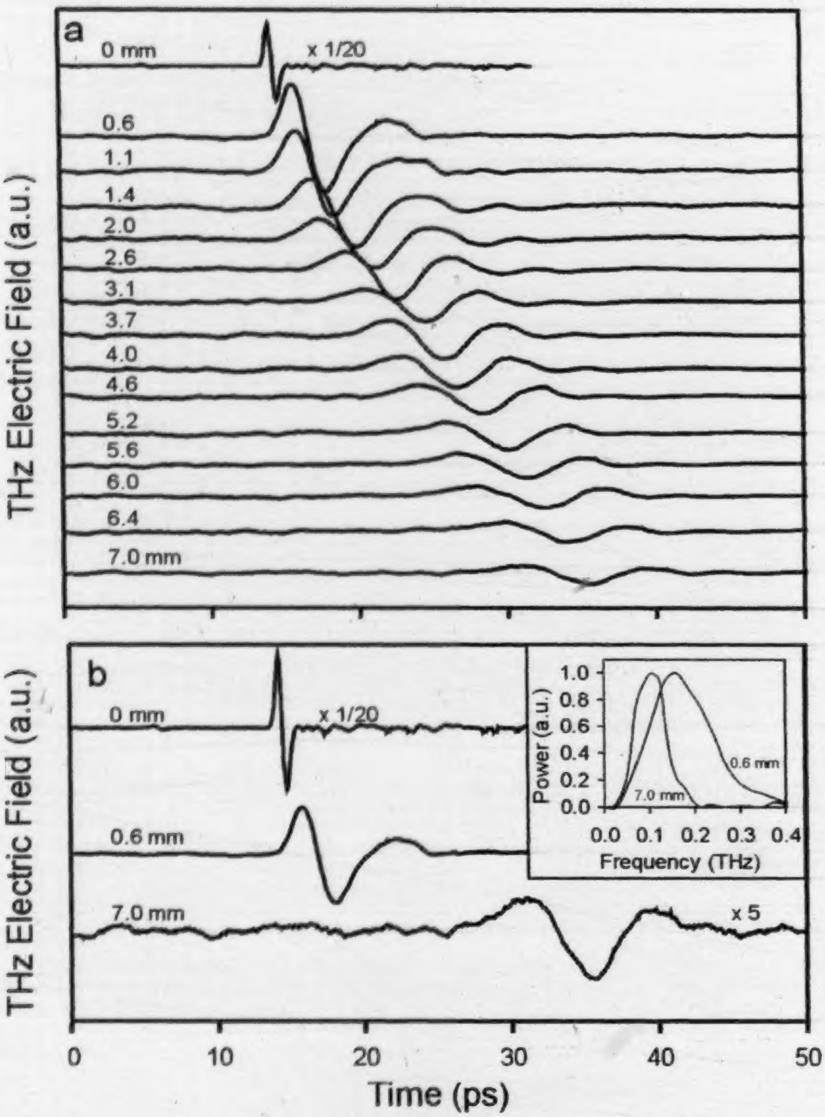

Figure 3.10. (a) The far-field transmission through the Cr medium for *L* = 0.6 mm to *L* = 7.0 mm. The data has been filtered to remove delayed reflection signals in the ZnSe crystal. (b) depicts the transmitted pulses for *L* = 0 mm, 0.6 mm, and 7.0 mm on expanded time and amplitude scales. The inset in (b) shows the normalized transmission spectrum for *L* = 0.6 mm and 7.0 mm.

Figure, the line of fit corresponds to a fitting parameter, $q = 0.06\ \mathrm{mm}^{-1}$. The power decay profile contrasts to the exponential decay dependence due to absorption in a homogeneous effective medium [20]. This further suggests that the THz electromagnetic properties of the mesoscopic metallic particle ensemble cannot be described by effective medium approximations.

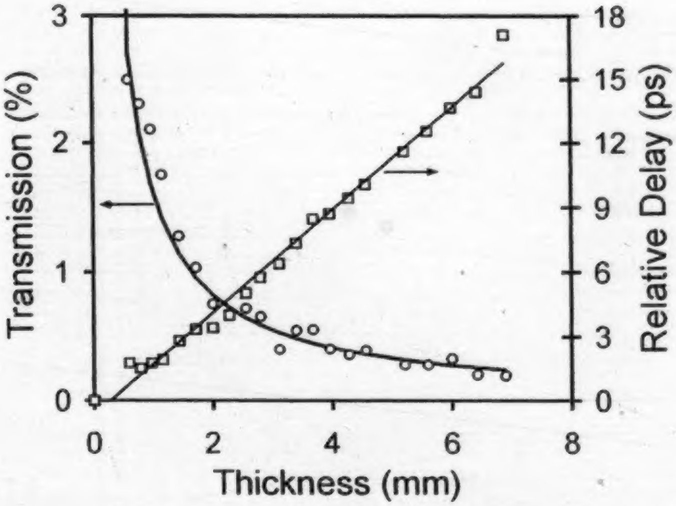

Figure 3.11. The measured percentage total power transmission (circles) and relative pulse delay (squares) as a function of *L*. Best-fit curves for the transmission power and pulse delay show $1/(1+qL)$ and linear dependences, respectively, where $q = 0.06\ \mathrm{mm}^{-1}$.

The polarization purity of the transmitted field provides further insights into the nature of the enhanced THz transmission phenomenon. Comparison of the transmitted polarization with the linear polarization of the incident pulse directly maps the degree of coherence of the energy transport mechanism onto a polarization change. Electric field dephasing due to incoherent random scattering destroys the incident pulse polarization state, whereas coherent electromagnetic propagation preserves the incident polarization. The transmitted electric field polarization is measured by varying the angular orientation of the optical axis of the <111> ZnSe crystal relative to the probe polarization, θ_{probe}. For the incident linearly polarized THz pulse, the crystallographic axes of <111> ZnSe dictate that the electro-optic response exhibits 3-fold symmetry (120°) about θ_{probe} (refer to Appendix B). This symmetry vanishes for an unpolarized THz pulse. As shown in Figure 3.12, the dependence of the electric field amplitude on θ_{probe} for the transmission through a 1 mm thick Cr particle ensemble is in excellent agreement with measurements for the free-space linearly polarized THz electric field pulse. The close agreement indicates that, despite the inherent opacity of the metallic particles and the random nature of the particle collection, the transmission through the Cr particle ensemble preserves the incident polarization state.

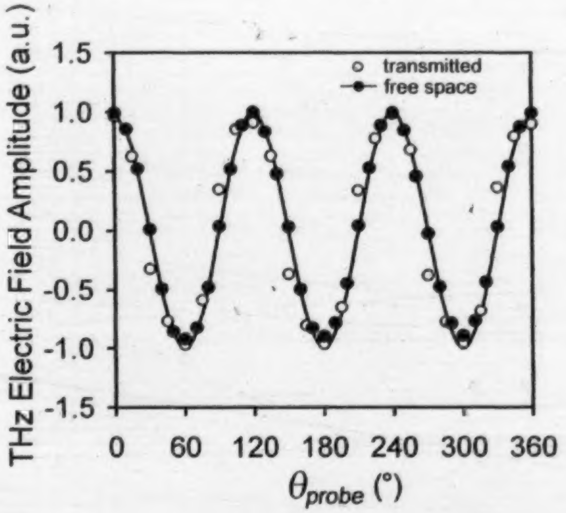

Figure 3.12. The normalized peak-to-peak THz transmission through a 1 mm thick Cr sample versus θ_{probe} of the <111> ZnSe electro-optic crystal axis. The peak-to-peak electric field amplitudes for a free-space THz pulse and for the transmitted pulse through the Cr medium both illustrate the 3-fold symmetry characteristic of a linearly polarized field.

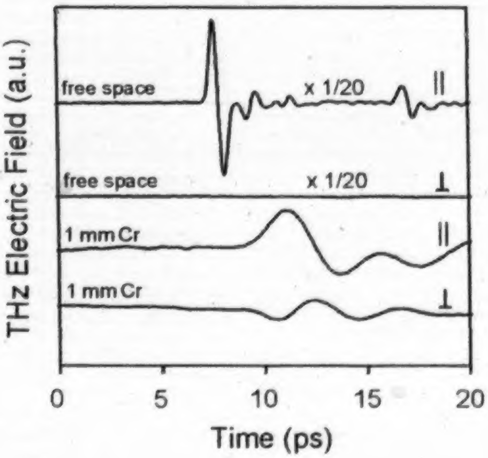

Figure 3.13. Parallel and perpendicular electric field components transmitted through free-space and a 1 mm thick sample of Cr microparticles.

The polarization purity of the transmission can be quantified by measuring the parallel and perpendicular electric field components of the transmitted electric field, $E_{tr,\|}(t)$ and $E_{tr,\perp}(t)$ respectively. Orthogonal polarization components of the transmission are obtained by measuring the transmitted THz electric field at two angles of the <111> ZnSe orientation, θ_{probe}, rotated by 30° with respect to each other. As representatively shown for a 1 mm thick sample of Cr particles in Figure 3.13, high polarization purity is evident from the relatively small amplitude of the THz electric field component measured in the perpendicular direction relative to the parallel direction. Based on the electric field amplitudes of the parallel and perpendicular components, a polarization purity of $[|E_{tr,\|}(t)|-|E_{tr,\perp}(t)|]/|E_{tr,\|}(t)| = 0.70 \pm 0.01$ is measured. This is less than the polarization purity of 0.993 ± 0.005 measured for the reference THz pulse propagating through air (Figure 3.13). Nevertheless, the polarization purity of the transmitted electric fields though the metallic particle ensemble suggests that the electric field transmission is polarized and that electromagnetic energy propagates coherently through the metallic medium.

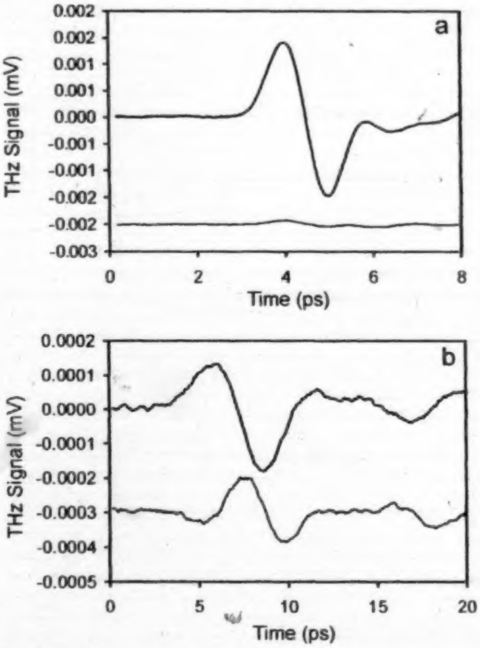

Figure 3.14. THz signal transmitted through (a) a 2.0 mm thick and (b) a 7.7 mm thick sample of Cu microparticles. The black and gray lines correspond to the transmitted signal polarized parallel and perpendicular to the incident polarization, respectively.

To further understand the polarization preservation of the transmitted THz pulse through the metallic ensembles, the influence of sample length on the transmitted THz electric field polarization is investigated. Figure 3.14 plots the $E_{tr,\parallel}(t)$ and $E_{tr,\perp}(t)$ transmitted pulses through 2.0 mm thick and 7.7 mm thick ensembles of Cu microparticles. The Cu microparticles have a mean diameter of 71 ± 20 μm and a packing fraction of 0.51 ± 0.05. For the L = 2.0 mm thick sample, Figure 3.14 (a) illustrates that the electric field transmitted through the 2.0 mm thick Cu microparticle collection preserves the incident linear polarization with a polarization purity of 0.95 ±

0.01. This indicates that the 2.0 mm sample thickness is less than the dephasing scale length of the electromagnetic energy transport mechanism. However, when the sample thickness is greater than the dephasing scale length, the polarization is expected to be randomized. Indeed, as the sample thickness increases to 7.7 mm, the electric field amplitudes of $E_{tr,\|}(t)$ and $E_{tr,\perp}(t)$ are comparable, indicating that the transmission is nearly unpolarized. For the 7.7 mm thick sample, the polarization purity is 0.40 ± 0.01. For increasing L, the electromagnetic pulse propagated through the sample undergoes an increasing number of scattering events, which randomizes the transmitted polarization and impairs the overall coherence of electromagnetic energy transport. From the data, it is inferred that the depolarization length of the electromagnetic transport through the Cu microparticles is on the order of several millimetres.

3.5 Calculations of Terahertz Transmission through Metallic Particle Ensembles

To further explore the enhanced, polarized THz transmission phenomenon, FDTD calculations of THz pulse propagation through an ensemble of subwavelength size metal particles are performed. Due to the subwavelength size of the particles, to a good approximation, the metallic particles can be viewed as a collection of circular particles that extend infinitely in the third dimension. It should be noted that a three-dimensional model would enable a more complete picture of the experiments as the particle plasmon associated with the particles depends on the dimensionality. In three dimensions, the particle plasmon fields are effectively confined to a smaller surface area, which would appear as an enhancement in the local fields. However, full three-dimensional FDTD calculations over the length scales of the sample require enormous computational effort in comparison to the current model and are not currently feasible. The two-dimensional calculations are adequate in illustrating the underlying physics of the phenomenon, and the conclusions of the calculations can be employed to interpret the experimental results. The structure used in the calculations is a randomly generated ensemble of metallic (Cr) particles with a circular cross section having $\delta = 150$ µm and a sample packing fraction of 0.56. The single-cycle THz pulse incident on the ensemble is centred at 0.6 THz with a 1 THz bandwidth, matching the THz pulses used in the experiments. The average transmission is measured by integrating the total electric field incident upon a line detector emulating the experimental detection. At each *L*, the transmission is evaluated for numerous random sample configurations.

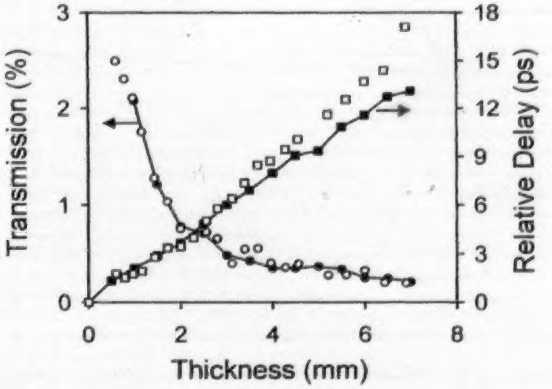

Figure 3.15. The calculated percentage power transmission (filled circles) and relative pulse delay (filled squares) versus *L*. The experimental transmission power (open circles) and relative pulse delay (open squares) are also depicted.

As shown in Figure 3.15, the FDTD-calculated transmission characteristics demonstrate agreement with experimental observations. It should be noted that the packing fraction of the sample in the calculations (0.56) is larger than the experimentally measured packing fraction of the sample used in the experiments (0.51), which is required to obtain quantitative agreement between the experiment and calculations.

Nevertheless, it is remarkable that the percentage power of the enhanced THz electric field transmission and the $1/(1+qL)$ power versus the sample length are accurately predicted. The slightly higher packing fraction used in the calculations is required to describe the electromagnetic properties of the three-dimensional ensembles. Augmenting the packing fraction in the two-dimensional system effectively increases the surface area of the particles, which more accurately accounts for non-radiative losses occurring at the surface of the three-dimensional particles used in the experiments. As seen in Figure 3.15, the numerical and experimental relative pulse delays are in good agreement from $0 < L < 4$ mm. For $L > 4$ mm, the calculations underestimate the experimentally measured pulse delays. This is attributed to the poly-disperse distribution of particle sizes and the irregular shapes of the Cr particles, both of which cause increased particle surface area and are not incorporated in the numerical model. In particular, it will be later shown in this Chapter that particle irregularity can cause significant pulse delay.

Further examination of the internal electric field dynamics from the calculations suggests that the physical origin of the enhanced THz transmission is due to near-field interaction between particles. In particular, the calculations show that electromagnetic energy is confined into the subwavelength spaces between metallic particles. Figure 3.16 (a) to 3.16 (d) depicts snapshots of the spatio-temporal evolution of the THz pulse fields for $L = 5$ mm at representative times, t. At $t = 1.25$ ps, the incident polarized THz pulse couples into particle plasmons on the individual particles, evidenced by the high electric fields near the particles' surfaces. The snapshot at time $t = 8.5$ ps shows that electromagnetic energy is squeezed in the free space gaps between the particles. An initial electromagnetic wave-front appears as a large amplitude band progressing through the random metallic medium, as shown at $t = 19.0$ ps [Figure 3.16 (c)]. By tracking the wave-front as it advances through the system, an electromagnetic energy velocity of 0.65 c is measured, in excellent agreement with experimentally measured values of 0.63 c. At $t = 26$ ps, this leading wave-front approaches the boundary ($L = 5$ mm) and radiates into free-space. Hence, this initial wave-front coherently propagated through the metallic particle sample corresponds to the measured far-field transmission. The wave-front in Figure 3.16 (d) appears straight relative to the wave-front in Figures 3.16 (b) and (c). At the back of the sample, the wave-front appears straight since the pulse spreads out as it propagates through the random medium. Even after the passage of the initial wave-front, significant electromagnetic energy is still trapped at various random locations. A spatial distribution map of the time-integrated electromagnetic field within the random medium [Figure 3.16 (e)] clearly illustrates the existence of highly localized electric field hotspots. At these locations, electromagnetic energy is stored via near-field electromagnetic re-circulation between metal particles [24]. The frequency spectrum at isolated hotspots shown in Figure 3.16 (f) demonstrates distinct resonant modes between 0.1 THz and 1.6 THz. Due the random phases of the electric field localized within these hotspots, the collective radiation leakage from these locations into the far-field interferes destructively and can only be detected locally. Hence, a prevailing challenge is to realize the near-field, time-domain visualization of these hotspots in random metallic media.

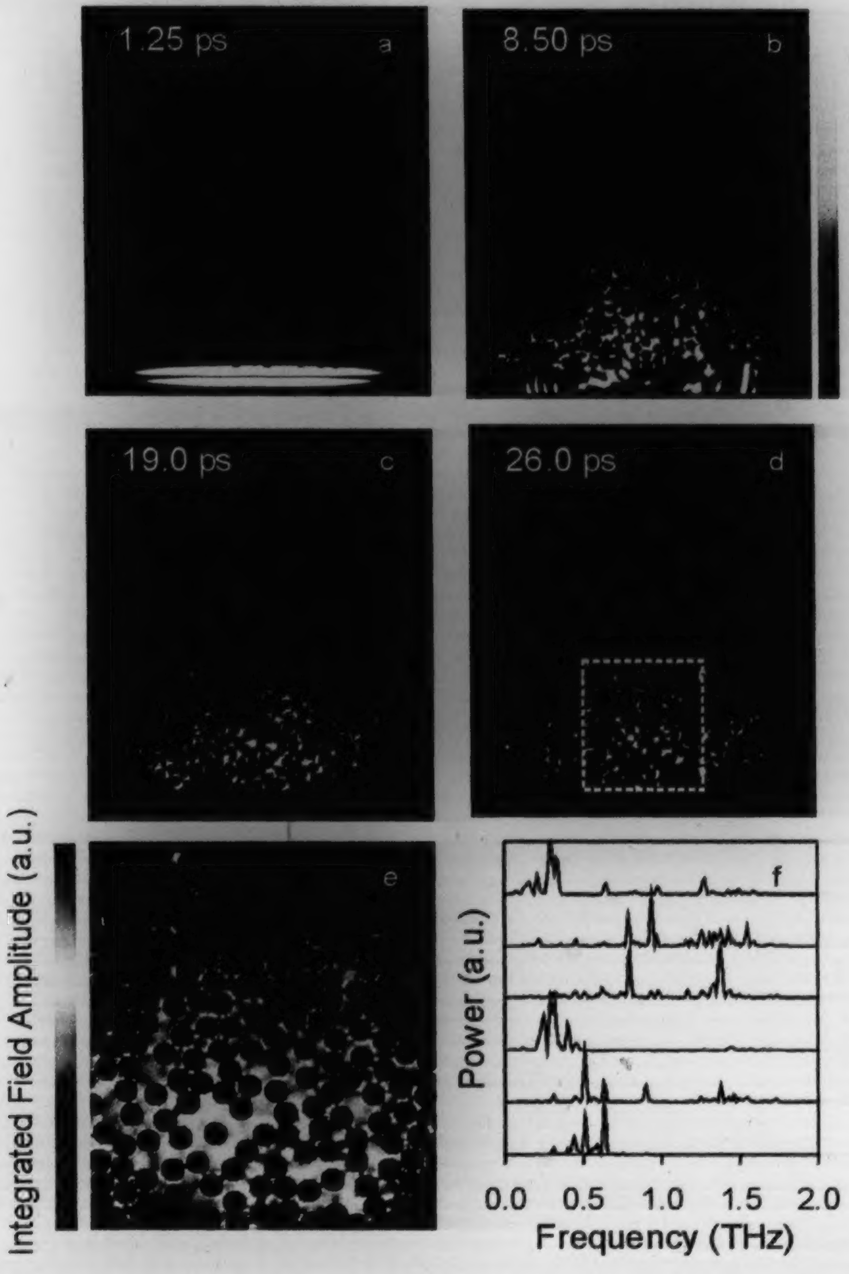

Figure 3.16. Snapshots of the THz field magnitude within a random 5 mm × 5 mm Cr medium at times (a) 1.25 ps, (b) 8.5 ps, (c) 19.0 ps, and (d) 26.0 ps. In (e), the spatial field distribution map of a 1.6 mm × 1.8 mm region of the Cr medium [corresponding to the boxed region in (d)] shows that a significant amount of the electromagnetic field is trapped within hotspots. The power spectra at six randomly selected hotspots shown in (f) demonstrate the existence of resonant modes.

Additional FDTD calculations of THz pulse excitation of an ensemble of metallic particles shows that inter-particle interaction within the ensemble is mediated by near-field coupling between particles. Figure 3.17 demonstrates images from an FDTD calculation of single-cycle, 1 ps wide THz pulse illumination of an $L = 4.0$ mm sample of randomly placed 150 μm Cr particles. The circular particles have an exact diameter of 150 μm and a 0.50 packing fraction. The time evolution of the electric field magnitude from $t = 0$ ps to $t = 1.0$ ps in a small region of the medium is shown in the right panels of Figure 3.17. At $t = 0$ ps, particle plasmon excitation is evident from the high electric fields near the particles' surfaces. At later times, $t > 0$ ps, the images clearly illustrate electromagnetic energy propagation via near-field particle plasmon coupling. Over the 1 ps interval, the surface fields on the particles propagate via nearest neighbor coupling from particle to particle across the metallic medium over a distance of ~ 600 μm. Thus, through such near-field particle-to-particle coupling, the THz electromagnetic field is transported across subwavelength size metallic particle ensembles over distances several orders of magnitude larger than the metal's skin depth.

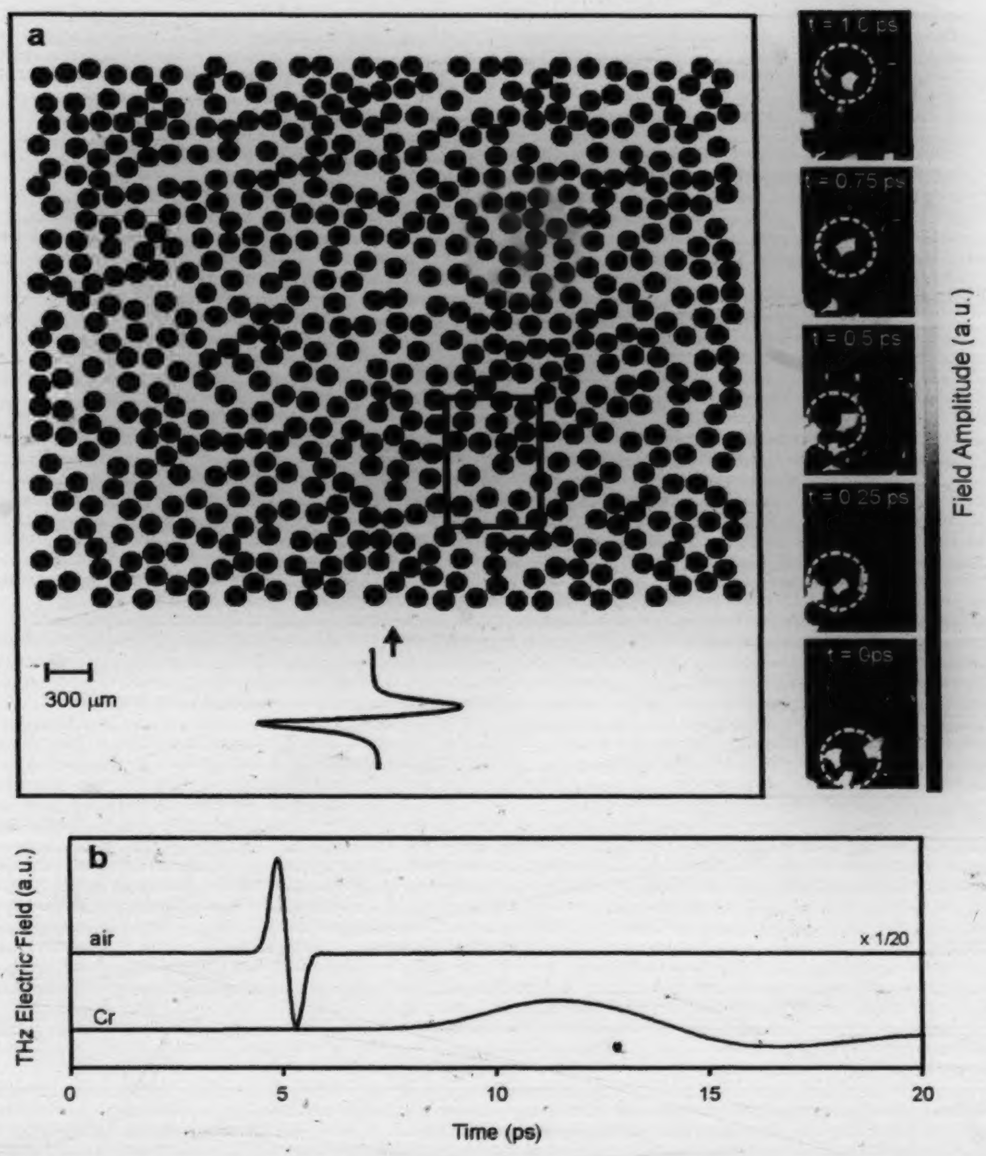

Figure 3.17. (left) Calculation structure used in the FDTD calculations consisting of an ensemble of 150 μm circular particles. The panels to the right depict magnified images of the boxed region and show the propagation sequence of the THz field magnitude over a 1 ps duration. The sequence of images illustrates that electromagnetic energy transport through the metallic particle ensemble is governed by nearest neighbor coupling. (b) Calculated transmitted THz electric field through the L = 4 mm sample of 150 μm Cr particles along with a reference pulse transmitted through an air path.

The calculated pulse shape transmitted through the particles also shows similarities to the experimentally measured transmission. As shown in Figure 3.17 (b), the FDTD calculation accurately predicts the general characteristics of the pulse shape propagated through the metallic particle ensemble. The calculated transmitted electric field through the L = 4 mm sample of 150 μm Cr particles is delayed and broadened with respect to the THz pulse transmitted through an air path, and the ~ 1.4 % transmitted electric field amplitude is on the same order of magnitude as the ~0.4 % transmitted electric field amplitude measured in the experiments. Discrepancies in the experimental and calculated transmitted electric field amplitude are attributed to the lower packing fraction (0.50) used in this FDTD calculation relative to previous calculations of Figure 3.15.

3.6. Terahertz Transmission through Different Metallic Particle Ensembles

The enhanced THz transmission through dense metallic particle collections is not specific to any particular metal type or particle size and has been observed through a wide variety of metallic media with varying subwavelength particle sizes. To highlight this universality, Figure 3.18 depicts experimental transmitted THz pulses through L = 1.2 mm thick samples of densely packed Cu, Cr, and Al particles having mean dimensions of 71 ± 20 μm, 150 ± 50 μm, and 400 ± 100 μm, respectively. The transmitted pulses depicted in Figure 3.18 are polarized along the incident polarization direction. The time-resolved signals are characterized by temporally delayed and broadened field oscillations relative to the reference pulse transmitted through an empty cell. When compared to an air path, the relative delays introduced by the L = 1.2 mm Cu, Cr, and Al particle ensembles are 2.6 ± 0.1 ps, 4.8 ± 0.1 ps, and 3.0 ± 0.1 ps, respectively.

The transmitted electric fields have drastically disparate amplitudes. Compared to the reference THz pulse, the field amplitude through the Cu ensemble is 20.7 %, while the relative electric fields transmitted through the Cr and Al ensembles are only 3.4 % and 1.0 %, respectively. The large variation in the amplitude and the arrival time of the transmitted THz pulses through the different metallic media reveals a rich dependence of the transmission phenomenon on particle shape, size and metal type. These variables will be explored further in this Chapter.

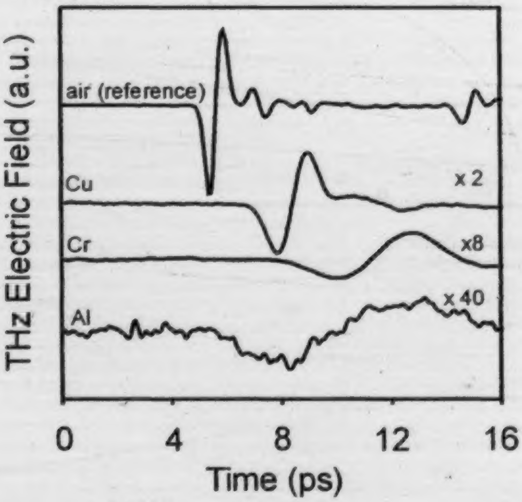

Figure 3.18. Free-space transmitted THz electric field measured through an empty cell and through 1.2 mm thick samples of irregularly shaped Cu, Cr, and Al particles having mean dimensions of 71 μm, 150 μm, and 400 μm, respectively. The transmitted fields are polarized parallel to the incident THz polarization.

3.7 From the Mesoscopic Regime to the Bulk Regime

The metallic particle size relative to the radiation wavelength is an important parameter governing the THz electric field transmission through an ensemble of metallic particles. When the metallic particle size is in a mesoscopic regime (particle size between the wavelength and atomic scales), incident electromagnetic radiation polarizes the individual particles, and near-field coupling between particles transports electromagnetic energy across an ensemble. The heterogeneity scale of the particles relative to the wavelength dictates the degree of the polarizability of the particles. Breaking the metallic particle size down to the nano- and atomic scales such that $\delta < a$ will recover the bulk optical properties of the metal. This is because for a collection of metallic particles having $\delta < a$ and $\delta < \lambda$, the electromagnetic properties of the ensemble can be described by the effective medium approximation. As the metallic particle volume fraction of the ensemble increases to 100 %, the effective electromagnetic properties of the ensemble are equivalent to that of a bulk metal. On the other hand, if the particle size increases well beyond the size of the wavelength, geometrical optics takes over. That is, the incident electromagnetic wave cannot polarize the particle, and is totally reflected from the metallic surface.

Here, the influence of the particle size on the enhanced THz electric field transmission through metallic particle ensembles is studied as the particle size increases from the subwavelength regime into the bulk regime. Terahertz time-domain spectroscopy is employed to characterize the THz electric field transmission through Cu particle ensembles where the average particle diameters are 194 ± 9 μm, 250 ± 10 μm, 283 ± 8 μm, 372 ± 17 μm, 462 ± 17 μm, 560 ± 15 μm, and 670 μm ± 30. In reporting the particle sizes, the nominal size corresponds to the average particle diameter and the error represents one standard deviation. Scanning electron microscope images of the particles are shown in Figure 3.19.

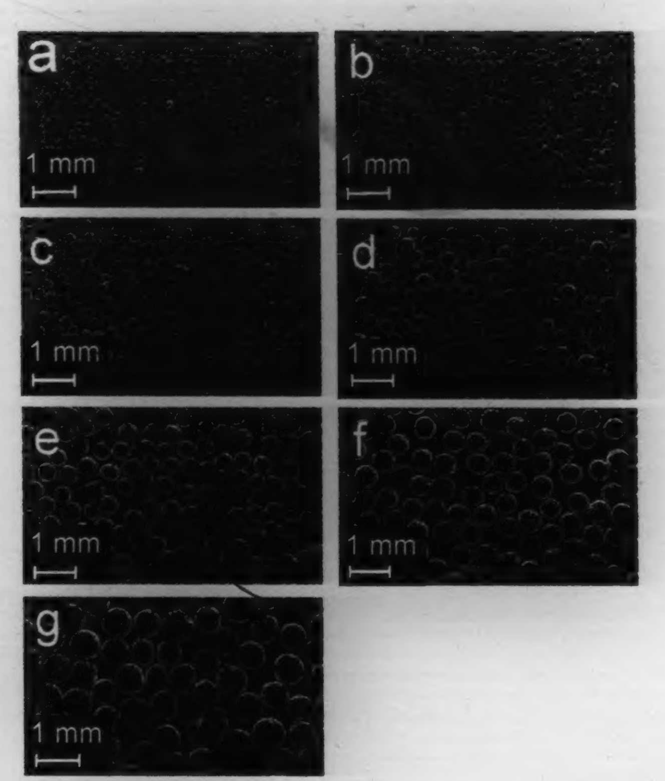

Figure 3.19. Scanning electron microscope images of Cu particle ensembles of sizes (a) 194 μm, (b) 251 μm, (c) 283 μm, (d) 372 μm, (e) 462 μm, (f) 560 μm, and (g) 665 μm.

Shown in Figure 3.20 are the time-domain waveforms and the associated Fourier spectra of THz pulses transmitted through Cu particle ensembles where the particle sizes range from 194 ± 9 μm to 670 ± 30 μm. The thickness of the ensemble is kept constant at 3.0 mm. As the average particle size increases from 194 μm to 372 μm, the THz electric field transmission amplitude is dramatically reduced by a factor of greater than 3. Associated with this attenuation is a shift in the central frequency of the transmission from 1.0 THz to 0.8 THz, indicating a preferential attenuation of the higher frequency components of the THz pulse. As the size of the particles increases, the shorter wavelength components of the incident THz pulse cannot efficiently polarize the particles. As a result, these higher frequency components do not couple across the medium and are not radiated into the far-field. There is nearly no transmission when the particle size exceeds 462 μm, since over the bandwidth of the incident THz pulse, $0.2 < \delta/\lambda < 2.3$ and the wavelengths encompassed by the THz pulse cannot polarize the individual particles.

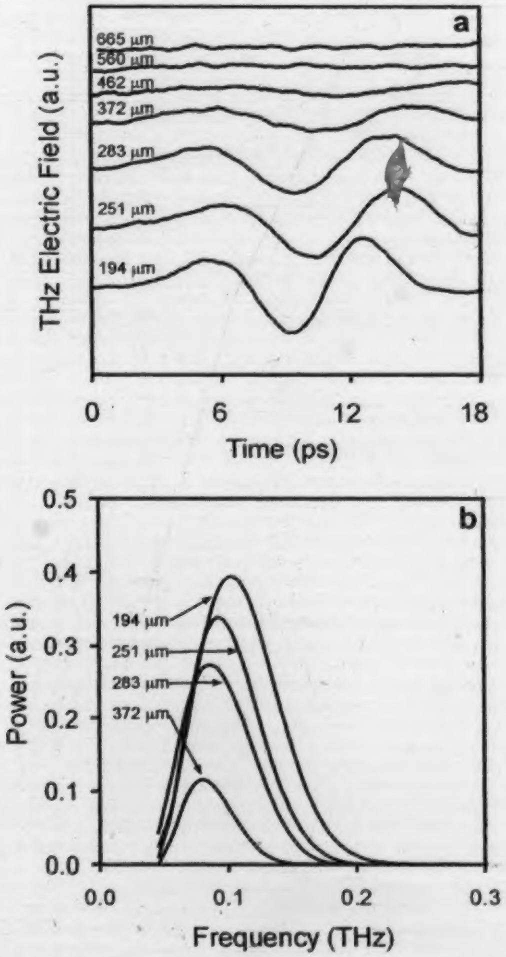

Figure 3.20. (a) Time-domain transmission through 3 mm thick ensembles of Cu microspheres where the diameter varies from 194 μm to 665 μm. (b) Power spectra of the transmission through ensembles of Cu spheres having diameters ranging from 194 μm to 372 μm.

As discussed in Chapter 1, an electromagnetic wave incident on a subwavelength sized metallic sphere embedded in free-space induces a dipole moment, $p(\omega)$, that is given by

$$p(\omega) = \pi \frac{\delta^3}{2} \frac{\varepsilon_{metal}(\omega) - 1}{\varepsilon_{metal}(\omega) + 2} E_s \tag{3.7.1}$$

where δ is the particle diameter. At THz frequencies, where $|\varepsilon_{metal}(\omega)| >> 1$, the dipole moment of the particle is approximately

$$p = \pi \frac{\delta^3}{2} E_s \tag{3.7.2}$$

which corresponds to a polarizability given by

$$\kappa = \pi \frac{\delta^3}{2} \tag{3.7.3}$$

Thus, the polarizability of a subwavelength sphere excited by an incident THz electromagnetic wave is independent of the metal permittivity and is purely geometrical. The frequency dependence of the non-resonant particle plasmon response is implicit in the assumption that the particle size is smaller than the electromagnetic wavelength. Coupling of an incident electromagnetic wave into a non-resonant particle plasmon only occurs when the particle size is less than the wavelength. As the particle size increases beyond the wavelength scale, the incident electromagnetic wave cannot polarize the particle. Figure 3.21 (a) plots the peak transmitted wavelength versus the average particle size. With increasing particle size, it is shown that the peak transmitted wavelength increases linearly. This direct proportionality indicates that the THz particle plasmon response scales directly with wavelength, which is consistent with the picture that coupling of an incident THz electromagnetic wave into a particle plasmon is a geometrical effect determined by *the particle size with respect to the wavelength.*

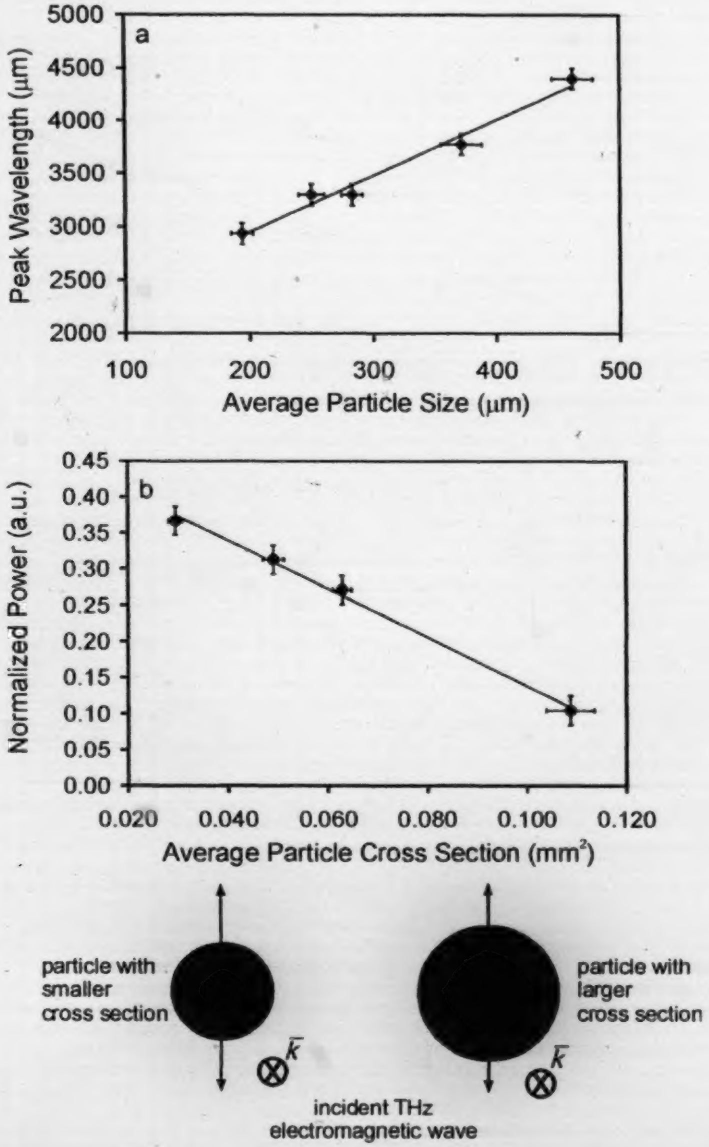

Figure 3.21. (a) Plot of the peak transmission wavelength through the 3 mm thick Cu particle ensembles versus the average particle size. The line is a linear line of best-fit to the data. (b) The transmitted power normalized to the free-space reference at a frequency of 0.09 THz versus the average particle cross-sectional area. The illustration below depicts a THz electromagnetic wave incident on a particle with a smaller cross-sectional area and a particle with a larger cross-sectional area.

When a THz electromagnetic wave is incident on a subwavelength sized particle, not all the incident energy is coupled into the localized particle plasmon, but a large portion is scattered by the particle. Intuitively, the amount of electromagnetic energy "lost" to scattering from the metallic particle should be inversely proportional to the cross sectional area of the particle. As the particle cross sectional area increases, a larger portion of the incident electromagnetic energy is reflected and less electromagnetic energy is coupled into the localized particle plasmon at the surface of the particle. In the limit where the cross-sectional area of the particle is infinite, the incident electromagnetic wave is completely reflected. Figure 3.21 (b) shows the experimentally measured transmitted power (through the 3 mm thick Cu particle collections) normalized to the free space transmitted power at a frequency of 0.09 THz plotted versus the average particle cross sectional area. It should be noted that a frequency of 0.09 THz corresponds to a wavelength of 3.3 mm, which is much greater than the average particle sizes in the experiments. As shown in Figure 3.21 (b), the normalized transmitted power at 0.09 THz decreases as the average particle cross sectional area of the particle increases via an inverse proportionality. This effect can be physically understood by considering that the incident THz electromagnetic wave interacts with only the conduction electrons at the surface of the metallic particles. Due to the larger surface area to volume ratio of the smaller metallic particles relative to the larger particles, a greater percentage of conduction electrons can participate in localized particle plasmon excitation.

The effect of the particle size on the polarizability of a single particle is illustrated via FDTD calculations of pulsed THz electromagnetic excitation of two isolated metallic particles having dimensions of 70 μm and 200 μm. The excitation pulse is a single-cycle

THz transient with a 1 THz bandwidth and centred at 0.6 THz. In the calculations, a single-cycle THz pulse propagates upward toward the metallic particle. To map out the charge density induced by the external THz electric field pulse, the induced charge density distribution is calculated by taking the divergence of the vector displacement field distribution. Figure 3.22 illustrates the instantaneous induced charge density distribution at the surface of the two particles after THz pulse excitation taken at the same time. For the 70 μm diameter particle, the THz electric field pulse induces a dipolar charge density distribution where conduction electrons at the surface of the two halves of the particle oscillate anti-parallel. As the particle size increases to 200 μm, the predominant polarization mode induced by the THz electric field pulse is quadrupolar. The magnitude of the charge density distribution for the larger particle is significantly weaker than the dipolar charge density distribution of the smaller particle. The peak charge density of the quadrupolar distribution is reduced to ~ 60 % relative to the peak charge density of the dipolar distribution. The larger metallic particle is not efficiently polarized by the incident THz pulse, since a significant portion of the incident pulse is reflected by the larger particle and only the lower frequency components of the pulse can polarize the particle.

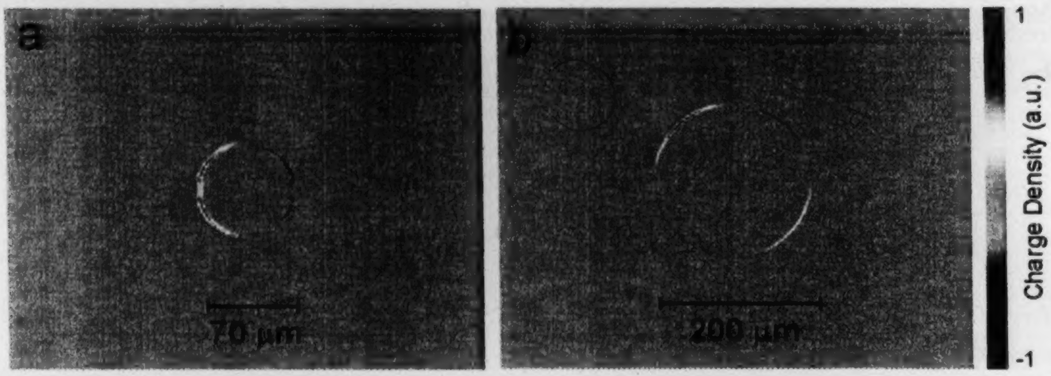

Figure 3.22. FDTD calculation of the induced charge density distribution of a (a) 70 μm diameter particle and (b) 200 μm diameter particle excited by a single-cycle THz pulse.

3.8 Further Investigations of Plasmonic-Enhanced Terahertz Transmission

To further study the plasmonic-enhanced THz transmission through subwavelength metallic particles, the dependences of the THz electric field transmission on the particle dimension, particle shape, and metallic conductivity are investigated.

The THz electric field transmission through the mesoscopic metallic particle ensemble is inherently dependent on the size of the particles. It was shown in Section 3.7 that the electromagnetic properties of the particle ensemble approach those of bulk metal as the particle size exceeds the wavelength. Here, the effect of *mesoscopic* particle size on the enhanced THz electric field transmission is explored. Comparative transmission measurements are performed using two Cr particle ensembles with mean subwavelength dimensions of 150 ± 50 μm and 40 ± 20 μm and similar volume packing fractions of 0.5. By comparing the THz electric field transmission through the two samples shown in Figure 3.23, it is evident that the transmitted electric field through the 150 μm Cr particles exhibits temporally broader oscillations and a lower bandwidth than the transmitted electric field through the 40 μm particles. For a representative sample length of 0.6 mm, the 40 μm and 150 μm particle ensembles show transmission bandwidths of 0.35 THz and 0.23 THz, respectively. As illustrated in Figure 3.23 (e), the higher frequencies (> 0.4 THz) of the transmitted electric field are preferentially extinguished as the particles' size is increased from 40 μm to 150 μm. Such a bandwidth reduction with increasing particle size occurs in conjunction with a central frequency shift from 0.24 THz to 0.20 THz as the particle size increases from 40 μm to 150 μm. The change in the central transmission frequency is attributed to a change in polarizability of the individual particles as the size increases.

As evident from Figure 3.23 (c) and 3.23 (d), the THz electric field pulse shape and arrival time of the pulse is also dependent on the particle size. The relative delay of the transmission through the 40 μm Cr particles indicates slowed particle plasmon propagation through the smaller particles. By measuring the arrival times of the first peak of the transmitted THz pulses as a function of *L*, propagation velocities of 0.47 ± 0.01 *c* and 0.50 ± 0.01 *c* are measured through the 40 μm and 150 μm particle ensembles, respectively. Intuitively, this can be understood as arising from the increased metal surface area in the smaller Cr particles, which augments the electromagnetic energy propagation distance. This interpretation will be further supported by FDTD calculations in later discussions within this section.

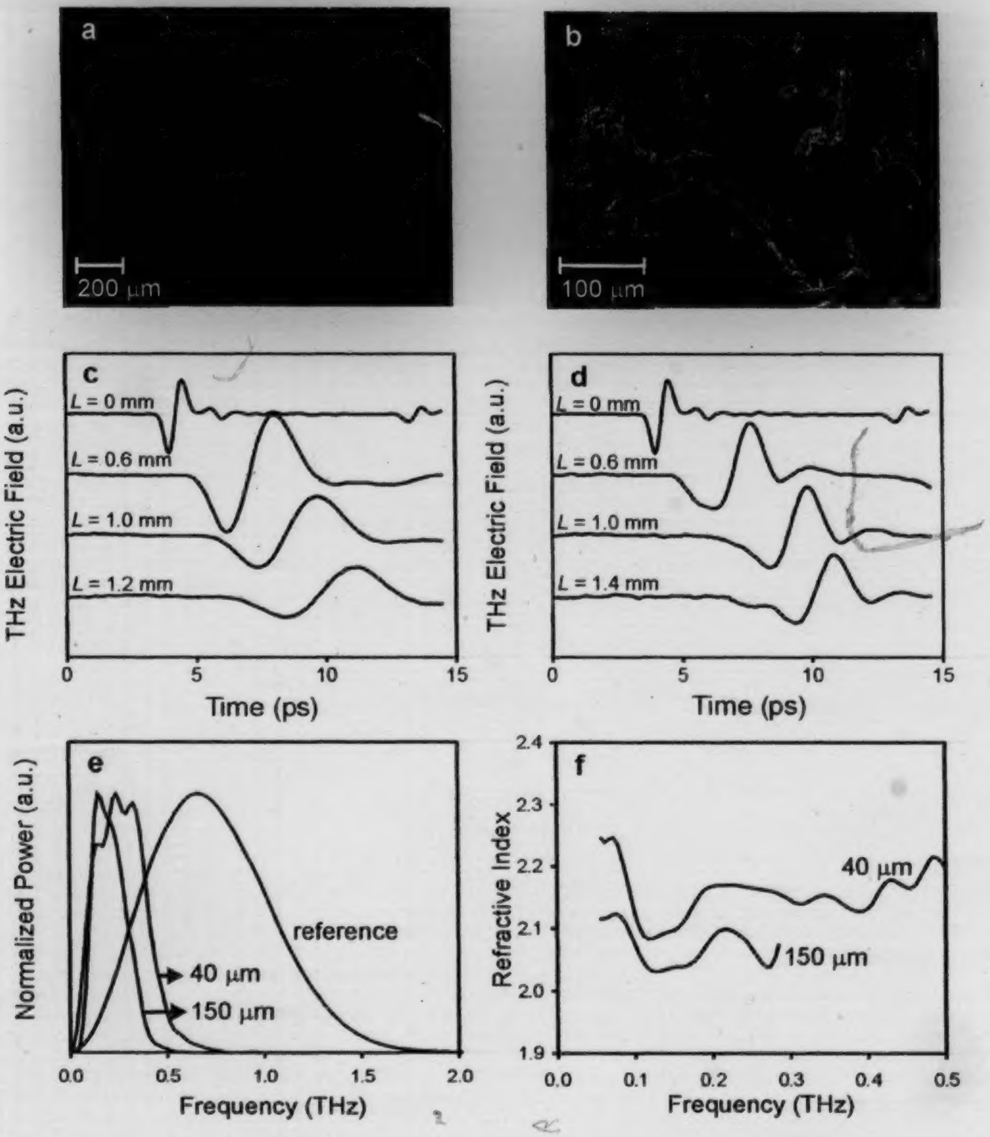

Figure 3.23. Scanning electron microscope images of Cr particles having dimensions of (a) 150 ± 50 μm and (b) 40 ± 20 μm. (c) and (d) depict the experimental transmitted THz electric field through the 150 μm and 40 μm size Cr particles, respectively, for various sample thicknesses, in addition to the reference THz pulse transmitted through an empty cell. (e) shows the power spectrum of the experimental transmission through the empty cell, a $L = 0.6$ mm sample of the 150 μm Cr particles and a $L = 0.6$ mm sample of the 40 μm Cr particles. Illustrated in (f) are the experimentally measured effective refractive indices across the transmission bandwidths for the two Cr particle ensembles.

To analyze the dispersion characteristics of the two Cr ensembles, their effective frequency-dependent refractive indices, $n_{eff}(\omega)$ are determined (refer to Appendix D). Here, the effective refractive index describes the global response of particles to the incident electromagnetic wave and is not derived from the effective medium approximation. Shown in Figure 3.23(f) are the effective refractive indices of the 40 μm and 150 μm particle ensembles obtained by averaging six independent measurements for each particle collection. Reducing the granular dimensions increases the effective refractive index of the metallic particle ensembles. The refractive indices for the 40 μm and 150 μm Cr samples are approximately 2.15 ± 0.05 and 2.05 ± 0.05, respectively, over their electric field transmission bandwidths. Interestingly, the refractive indices of these Cr samples are characterized by large dispersion across the bandwidth of the transmitted electric field, which, in addition to the frequency-dependent attenuation, causes pulse width broadening for increasing sample length [25].

To further investigate the effect of particle size, the experimental results are compared with FDTD calculations. The calculated THz electric field transmission through 4 mm thick ensembles of Cr particles with mean dimensions of 40 μm and 150 μm are shown in Figure 3.24. The calculated transmitted electric field through the smaller particles is spectrally wider [Figure 3.24 (a)] and temporally delayed [Figure 3.24 (b)] with respect to the transmitted electric field through the larger particles. Such behavior is in accordance with previous experimental observations. To visualize the origin of this delay, snapshots of the electromagnetic wave progression through the two Cr particle ensembles are shown in Figure 3.24 (c) to 3.24 (f). At t = 7.5 ps, the free-space THz pulse incident on the ensemble couples into particle plasmon oscillations of the metallic particles. From t = 7.5 ps to 20 ps, electromagnetic energy propagates as a high intensity wave-front explicitly highlighted in Figure 3.24 (c) to 3.24 (f). Examination of the images at t = 20 ps [Figure 3.24 (e) and 3.24 (f)] clearly show that the wave-front progresses slower through the 40 μm Cr particles relative to the 150 μm Cr particles. By tracking the wave-front progression through the metallic media, propagation velocities of 0.62 ± 0.01 c and 0.66 ± 0.01 c are measured through the 40 μm and 150 μm particle ensembles, respectively. The trend in the propagation velocity versus the particle size is similar to the experiments.

The FDTD calculations enable interpretation of slower wave propagation in ensembles of smaller particles. Due to the random nature of the medium, there is inherent directionality scramble of the electromagnetic wave with each nearest neighbor interaction. By increasing the number of particles across a given sample length (i.e. by decreasing the particle size), increased directionality scramble augments the effective energy propagation distance, causing a delay of the transmitted THz radiation. To demonstrate that the origin of this delay is due to directionality scramble, FDTD calculations are performed where directionality scramble is absent. Here, the THz pulse is confined to propagate along 12 mm long chains of randomly positioned particles with sizes of 50 μm, 100 μm, and 150 μm, as shown in Figure 3.25 (a), 3.25 (b), and 3.25 (c). In such configurations, lateral confinement results in unidirectional near-field particle plasmon coupling.

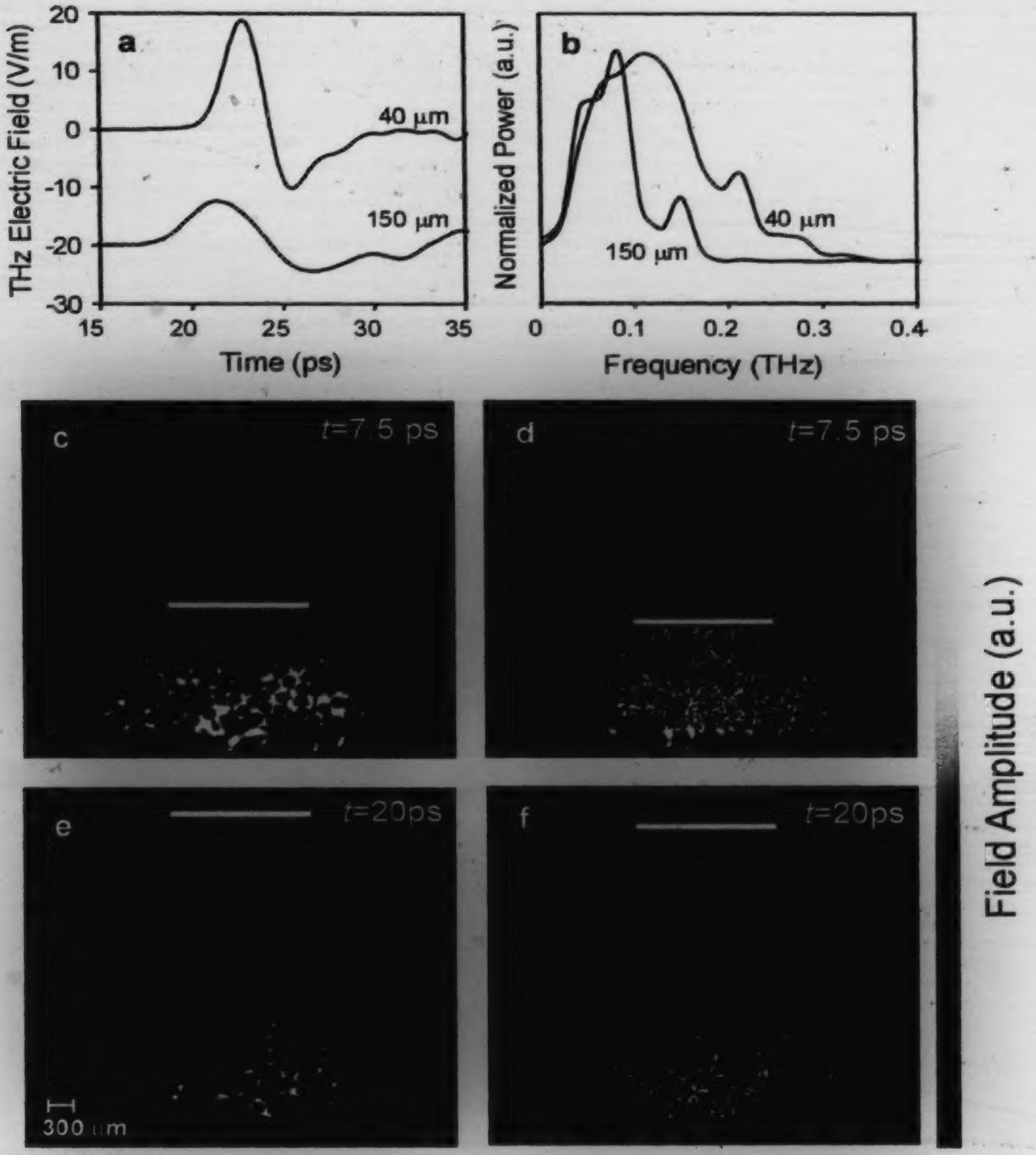

Figure 3.24. (a) FDTD calculations of the temporal THz transmitted electric fields through $L = 4$ mm ensembles of Cr particles with mean dimensions of 40 µm and 150 µm. Note that the transmitted pulse through the smaller Cr particles arrives at a later time. (b) The power spectra of the calculated transmission through the two particle ensembles. (c) and (d) illustrate the THz field magnitude in the 150 µm and 40 µm Cr particle ensembles, respectively, at $t = 7.5$ ps. THz field magnitudes at $t = 20.0$ ps in the 150 µm and 40 µm Cr particle ensembles are shown in (e) and (f), respectively. The packing fraction in the simulations is 0.50.

As shown in Figure 3.25 (d), 3.25 (e), and 3.25 (f), snapshots of the electric field magnitudes at a particular time show that the THz pulses propagate at similar velocities through the different particle chains. Accordingly, the transmitted electric field pulse through the three particle chains all arrive at the same time, as evident in Figure 3.26 (a). Particle plasmon coupling in the three particle chains can only occur along the forward direction. The absence of directionality scramble implies that the electromagnetic pulses along the three chains propagate over equivalent distances. While the size of the particles does not affect the electromagnetic propagation speed, it does influence the spectral contents of the electric field transmission. As shown in Figure 3.26 (a), the transmitted field associated with the chain of 50 μm size particles consists of higher frequency oscillations than that associated with the 100 μm and 150 μm particle chains. The spectral contents of the transmitted electric field pulses are explicitly shown in Figure 3.26 (b). The Figure illustrates that the electric field transmission through the 50 μm, 100 μm, and 150 μm particle chains exhibit bandwidths of 0.36 THz, 0.25 THz, and 0.15 THz, respectively. Thus, the increasing bandwidth with decreasing particle size is accompanied by a shift of the central frequency toward higher frequencies, consistent with the previous experimental trend shown in Figure 3.23 (e). Differences in the transmission spectra for the 50 μm, 100 μm, and 150 μm particle chains arise from the frequency-dependent polarizability of the individual particles. As the particle size increases, the higher frequency components of the incident THz pulse cannot couple into the particle plasmon oscillations of the particles and are removed from the transmission spectra.

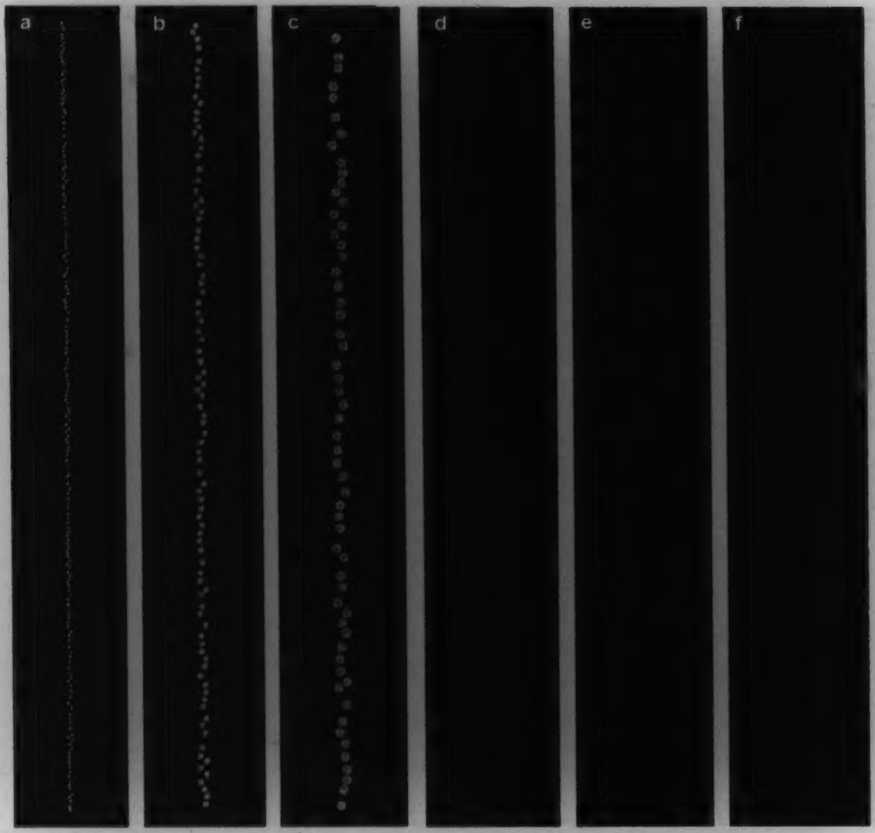

Figure 3.25. (a), (b) and (c) depict the 50 μm, 100 μm, and 150 μm Cr particle chains used in the FDTD calculations, respectively. The chain lengths are 12 mm. (d), (e) and (f) depict the THz field magnitudes in the 50 μm, 100 μm, and 150 μm Cr particle chains, respectively, at an identical time after excitation with a 1 ps wide THz pulse. Note that all the THz wave-fronts progress at the same velocity for the three particle chains.

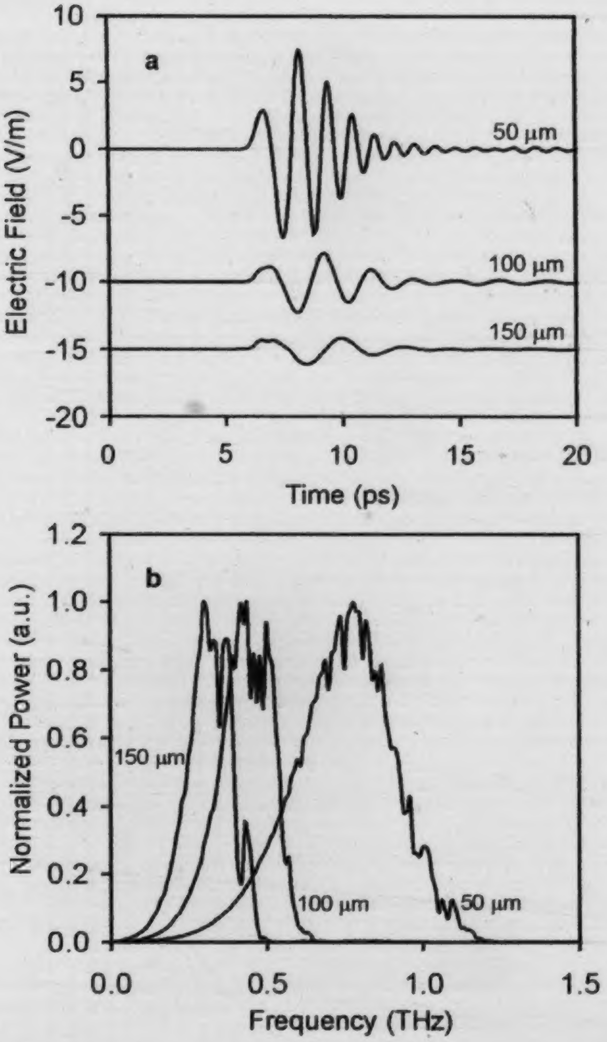

Figure 3.26. FDTD calculations of (a) the temporal THz transmitted electric field and (b) the spectral power transmission through the 12 mm long Cr particle chains consisting of 50 μm, 100 μm, and 150 μm size particles.

Due to inherent surface sensitivity of particle plasmon phenomena, particle shape is a key parameter in the interaction of electromagnetic waves with subwavelength metallic particles [26-28]. To qualitatively investigate the effect of particle shape on the plasmonic-enhanced THz electric field transmission, two separate Cu samples are employed consisting of spherical and irregularly shaped particles. Figures 3.27 (a) and 3.27 (b) depict scanning electron microscope images of the irregularly shaped and spherical samples having mean particle dimensions of 83 ± 15 μm and 71 ± 20 μm, respectively. Since the size difference between the particles is 2.4% of the central THz pulse wavelength of 500 μm, to a good approximation, the effect of particle size in the comparative measurements is insignificant. As illustrated in time-domain THz signals in Figure 3.27 (c), particle shape does not strongly influence the transmitted temporal pulse shape. Similarly, the transmission bandwidth does not vary between the irregular and spherical Cu particles [Figure 3.27 (d)], indicating that the polarizability associated with the individual Cu particles do not strongly depend on the exact particle shape so long as the size of the particles is in a subwavelength regime. However, the THz pulse transmitted through the spherical Cu particles arrives earlier than the transmitted electric field through the irregular particles. For the representative sample length of 2.1 mm, the transmitted electric field through the spherical Cu particles arrives 1.2 ± 0.1 ps earlier than that through the irregularly shaped Cu particles. Such a delay suggests that particle irregularity causes slowed plasmonic propagation through the metallic particles. The origin of the delay is understood as follows: since the transmission is mediated by plasmonic fields propagating along the particles' surfaces, increasing the particle surface area effectively increases the plasmonic propagation distance, which manifests as a delay in the transmitted electric fields. As evident in Figure 3.27, particle irregularity also slightly diminishes the transmission amplitude through the metallic media. For a sample length of 2.1 mm, the transmitted electric field through the irregularly-shaped Cu particles is 8 ± 2% less than the electric field transmission through the spherical Cu particles. The diminished electric field amplitude transmitted through the irregularly shaped particles is attributed to the enhanced non-radiative losses at the particle surface. Since the irregular particles have a much greater surface area than the spherical particles, the particle plasmon non-radiative losses are greater for the irregularly shaped particles.

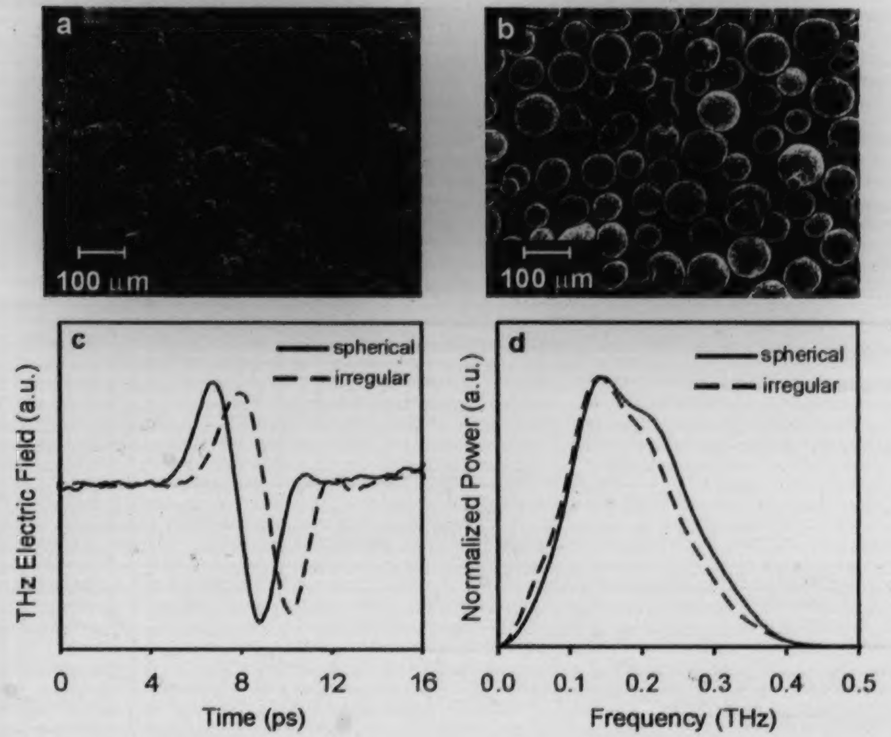

Figure 3.27. Scanning electron microscope images of (a) irregular and (b) spherical Cu particles of mean dimensions 71 ± 20 μm and 83 ± 15 μm, respectively. (c) depicts the experimental temporal THz transmitted electric field through $L = 2.1$ mm samples of the irregular and spherical Cu particles, and (d) shows their corresponding power spectra.

In addition to particle size and shape, the electromagnetic properties of the metallic ensembles are dependent on the conductivity of the metal. In high conductivity metals, electrons exhibit a long mean free path, which minimizes resistive loss associated with electron scattering. To study the effect of metal conductivity on the enhanced THz electric field transmission, comparative measurements of the transmission through Cu and $Cu_{95}Sn_5$ alloy particles are performed. These samples have been selected due to their identical physical sizes and shapes, since both samples consist of 83 ± 15 μm diameter spheres, as illustrated in Figure 3.28. However, due to the lower conductivity of the $Cu_{95}Sn_5$ alloy particles as compared to pure Cu, it is anticipated that the electric field transmission through the Cu will exhibit less attenuation. Indeed, as shown in Figure 3.28, the THz electric field transmission through the L = 2.1 mm Cu sample is dissimilar from the transmission through the L = 2.1 mm $Cu_{95}Sn_5$ sample. The peak-to-peak amplitude of the Cu THz electric field transmission is 1.3 times larger than the transmission through $Cu_{95}Sn_5$, directly indicating decreased attenuation. Moreover, the transmitted electric field through the Cu particles arrives slightly earlier (0.2 ± 0.1 ps) than that through the $Cu_{95}Sn_5$ particles. Despite discrepancies in the amplitudes and arrival times of the transmitted pulses, the pulse shape and frequency spectra of the transmission through the granular Cu and $Cu_{95}Sn_5$ do not differ within experimental error, as evident in Figure 3.28. The congruent transmission spectra are attributed to the similar microscopic structural features and particle sizes of the two metallic samples.

To further illustrate this effect, FDTD calculations of THz transmission through two identical particle ensembles composed of dissimilar metals having significantly different conductivities in the far-infrared regime are performed. Here, W and Cu metals have been chosen since the Drude parameters for the permittivity of both metals are known [29]. Figure 3.28 (e) shows the calculated time domain transmission through 2 mm thick samples of W and Cu particles having diameters of 80 μm. In accordance with experimental observations, the transmission pulse shape does not change by altering the conductivity. However, the THz electric field transmission amplitude through Cu is slightly larger relative to the transmission through W due to decreased resistive loss. Finite difference time-domain calculations qualitatively confirm that the metal conductivity directly affects the losses.

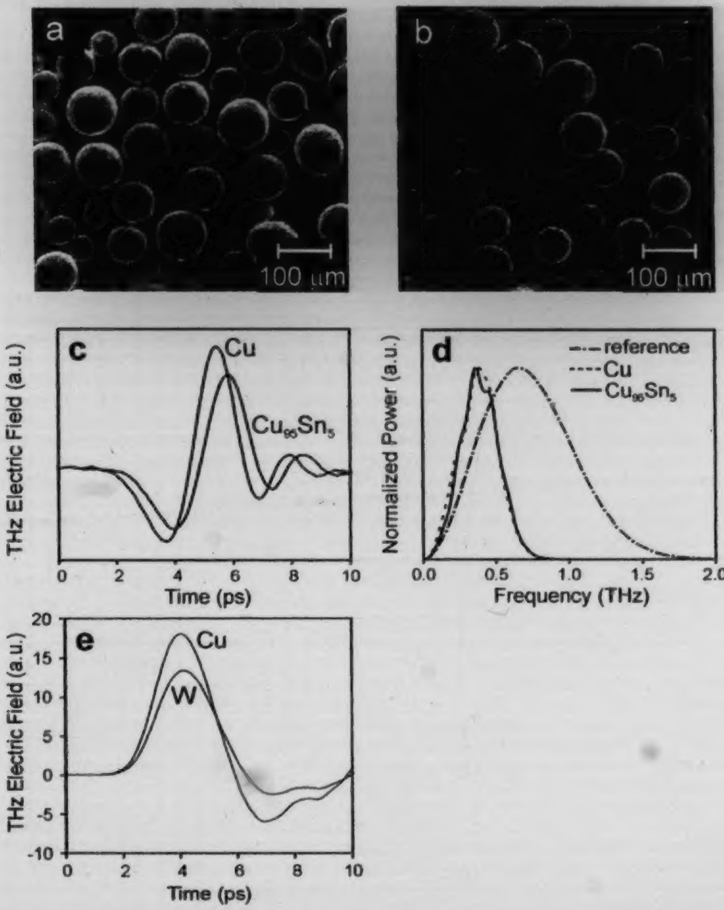

Figure 3.28. Scanning electron microscope images of (a) $Cu_{95}Sn_5$ and (b) Cu particles, both having mean dimensions 83 ± 15 μm. (c) depicts the experimental temporal THz transmitted electric field through $L = 2.1$ mm samples of $Cu_{95}Sn_5$ and Cu particles, and (d) illustrates their corresponding power spectra. Shown in (e) are FDTD calculations of the THz transmitted electric fields through identical $L = 2$ mm thick samples of 80 μm diameter W and Cu particles.

3.9 Influence of Contact Resistance on Terahertz Particle Plasmons on Bimetallic Microparticles

To date, investigations of surface plasmon waves at THz frequencies have been restricted to studies of surface plasmon polaritons on monometallic surfaces such as films, wires, and hole arrays [30-33] and studies of particle plasmons on monometallic particles [25, 34]. In this section, a novel class of THz plasmonic material is introduced that is composed of two types of metallic species. It is shown that the THz plasmonic response of the bimetallic material can be controllably tuned by varying the relative composition of the metallic species.

Bimetallic media show unique and diverse electromagnetic properties dependent on the relative composition and distribution of the metallic species. When a medium is composed of two metals, the metals may be completely intermixed, forming an alloy, or remain segregated, forming a heterogeneous mixture. Alloyed bimetallic media can be modelled by an average dielectric function between those of the parent metal species [35-37]. Heterogeneous bimetallic mixtures, on the other hand, typically have electromagnetic properties that differ substantially from those of the constituents and cannot be described as a superposition of the dielectric functions of the parent metals [1, 38-42].

Bimetallic heterogeneous mixtures are unique due to the contact or interface resistance that develops between the two dissimilar metals in intimate contact. The origin of the contact resistance between two metals can be understood by considering the classical free electron ideal gas model. Metals can be viewed as an ideal gas of free electrons subject to the Pauli Exclusion Principle. According to the Pauli Exclusion

Principle, no two electrons can have identical quantum numbers describing their wavefunctions. If a metal is composed of N_e electrons, then each of the N_e electrons must have its own unique wavefunction. At ground state (temperature of the system is at absolute zero), electrons in a metal will occupy electron states with the lowest energy levels and continue occupying states with higher energy levels until all the N_e electrons are accommodated. The energy of the topmost filled energy level is defined as the Fermi energy, E_F. As the temperature of the system, T, is increased from absolute zero, electrons may vacate previously occupied energy levels and fill previously unoccupied energy levels. The probability that a wavefunction at energy E' will be occupied in an ideal electron gas at a given temperature T at equilibrium is given by the Fermi-Dirac Distribution

$$f(E') = \frac{1}{1 + e^{(E' - \mu_c)/k_B T}} \tag{3.9.1}$$

which is depicted in Figure 3.28 for $T = 0$ and $T > 0$. The quantity k_B is the Boltzmann constant and μ_c is the chemical potential. The chemical potential is the energy at which $f(E') = 1/2$.

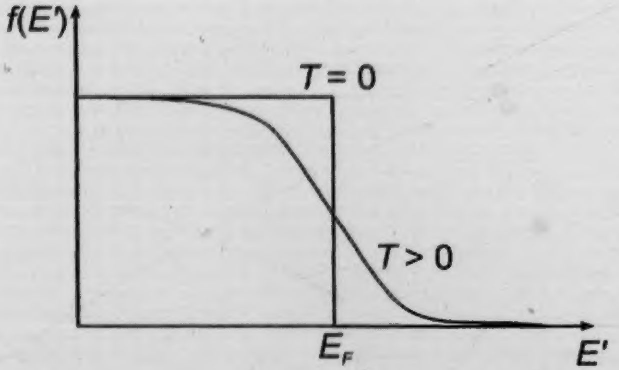

Figure 3.29. Fermi-Dirac Distribution for an ideal gas of free electrons at $T = 0$ and $T > 0$.

At the surface of the metal, the electrons of the metal are bound by the energy difference between an electron at rest in vacuum just outside the metal and an electron at the Fermi level. This energy difference is defined by the work function of the metal, $e\phi$, given by

$$e\phi = E_c - E_F \tag{3.9.2}$$

where E_c is the energy of the electrons at the bottom of the conduction band relative to the vacuum energy, E_{vac}. Suppose there are two metals, metal 1 and metal 2, that are connected in a manner that allows electrons to flow from one to another. If the two metals have different work functions, as shown in Figure 3.30 (a), metal 1 has many unoccupied levels of energies that are lower than many of the occupied ones of metal 2. When the metals are in contact, electrons that are occupying levels near the Fermi energy of metal 2 will leave metal 2 into metal 1. Metal 2 thus becomes positively charged and all the electrons in metal 2 will now have a lower potential energy. Simultaneously, the electrons in metal 1 will have a higher potential energy. Electrons will flow from metal 2 to metal 1 until the chemical potential of the two metals are equivalent. The electrostatic charge buildup at the interface creates a potential difference, $e\phi_1 - e\phi_2$, which opposes further charge flow. This potential difference effectively gives rise to an interface resistance [43-45]. The spatial extent of the region of charge buildup at the interface is on the order of the Thomas Fermi screening length, which is typically several Angstroms.

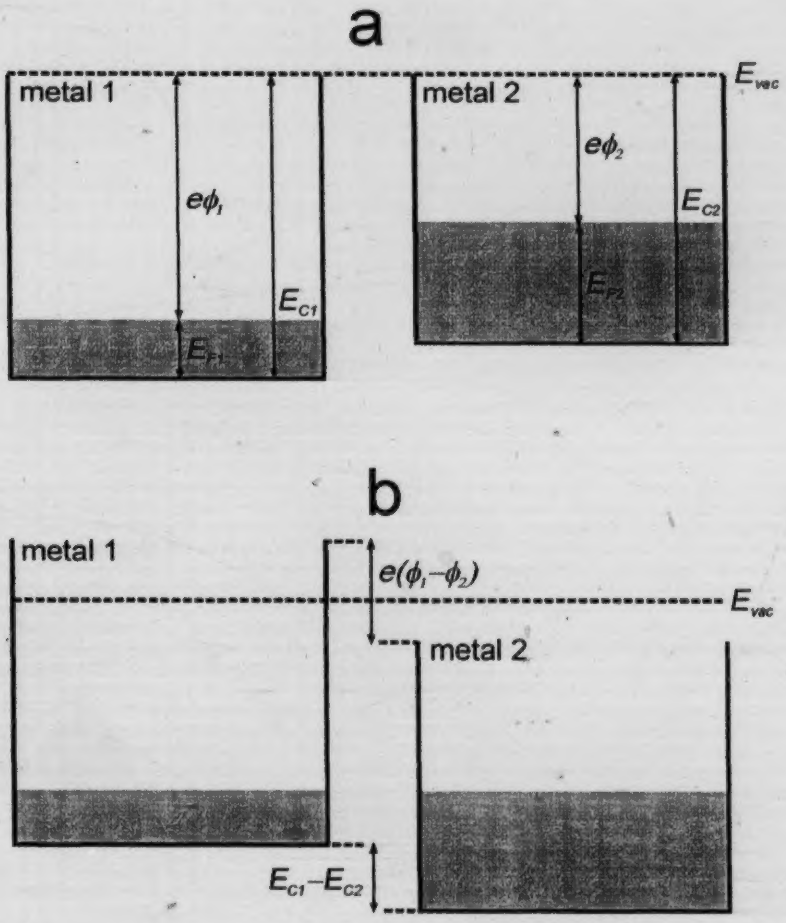
a
metal 1
metal 2
$e\phi_1$
$e\phi_2$
E_{vac}
E_{C1}
E_{C2}
E_{F1}
E_{F2}
b
metal 1
metal 2
$e(\phi_1-\phi_2)$
E_{vac}
$E_{C1}-E_{C2}$

Figure 3.30. Development of a contact potential difference. (a) Band diagram of the metals before they are in contact. (b) Equilibrium band diagram of the metals after they are in contact.

Here, a bimetallic THz plasmonic medium consisting of a dense collection of Cu microparticles layered with Au nano-layers is studied. The work functions of Cu and Au are 4.4 eV and 4.3 eV, respectively [43]; when the two metals are in contact, a contact resistance develops between them. The Cu particles used in the experiments have a spherical shape and a diameter, δ, that ranges from 68 to 98 μm. The Cu-core/Au-layer microparticles are fabricated by sputter depositing a 40 nm thick Au layer on dispersed spherical Cu particles (refer to Appendix D for a description of the sputtering processes). The Au coverage, or equivalently, Au/Cu contact area, is varied by systematically re-orienting the Cu particles during the Au deposition process, which exposes uncoated Cu surface area for Au coverage. The THz electromagnetic properties of the sample are examined using THz time-domain spectroscopy as previously described.

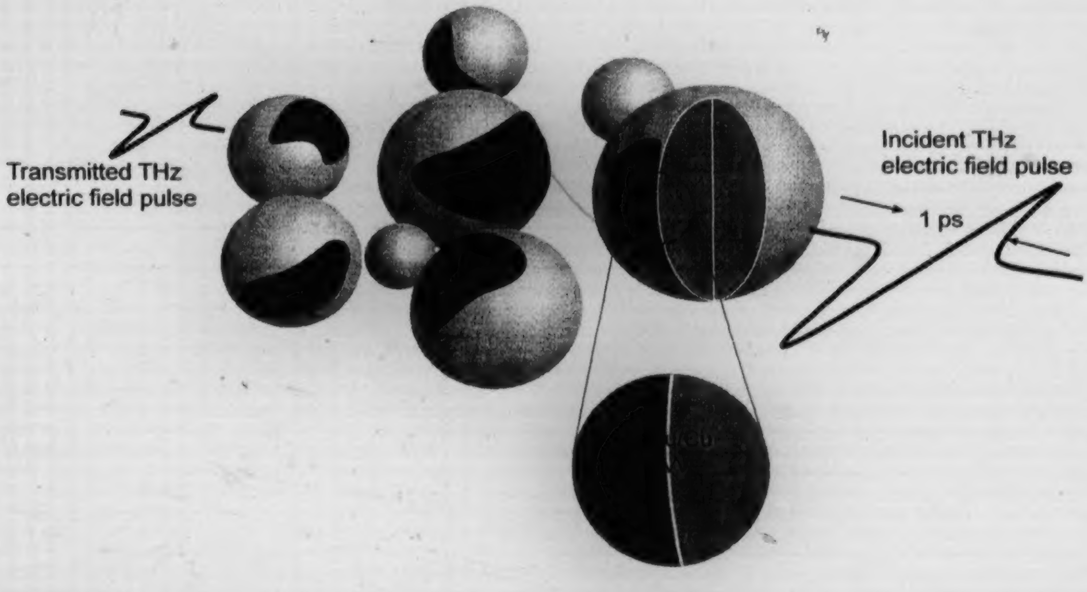

Figure 3.31. Cartoon illustrating the transport of a THz electromagnetic pulse through an ensemble of bimetallic Cu/Au microparticles. A contact resistance develops at the interface between the Cu and Au metals.

Since electromagnetic charge induction occurs on the outer surface of the bimetallic composite, it is essential to characterize the atomic composition directly at the particles' surface. The surface of the microparticles may consist of pure Au or a Cu/Au alloy due to miscibility and inter-diffusion of Cu into Au. Thus, x-ray photoelectron spectroscopy (XPS) is performed to determine the exact composition of the microparticle surface. The XPS spectra are collected by AXIS 162 (Kratos) spectrometer using monochromated Al Kα (1486.6 eV) radiation in fixed analyzer transmission mode. The XPS spectra of two samples of Cu particles that have relative high and relatively low percentage Au surface coverage are shown in Figure 3.32 (a), with the characteristic Cu 2p and Au 4f lines labelled. The Au 4f emission lines from the sample with the higher Au percentage coverage have a significantly higher intensity than the lines from the sample with lower Au percentage coverage. Shifts in the characteristic Au 4f emission lines relative to that of a pure Au sample reveal whether alloying between Au and Cu has occurred on the particle. As seen in Figure 3.32 (b), the characteristic Au 4f spectral lines of the two bimetallic samples show no shift of the Au 4f energy levels relative to the 4f energy levels in a pure Au sample (highlighted by the dashed line), indicating the absence of Cu/Au alloying directly at the surface of the bimetallic particles. Within the sampling depth of the XPS spectra, it can be concluded that the surface of the particles is heterogeneous, consisting of a Cu particle covered with a pure Au layer. The percent Au coverage is quantified by the relative magnitudes of the Au and Cu peaks in the XPS spectra; samples with higher Au coverage exhibit larger Au peaks and, correspondingly smaller Cu peaks. On five bi-metallic samples, XPS analysis reveals that the percentage Au surface coverage of the particles is F = 17 %, 24 %, 32 %, 44 %, and 47 %.

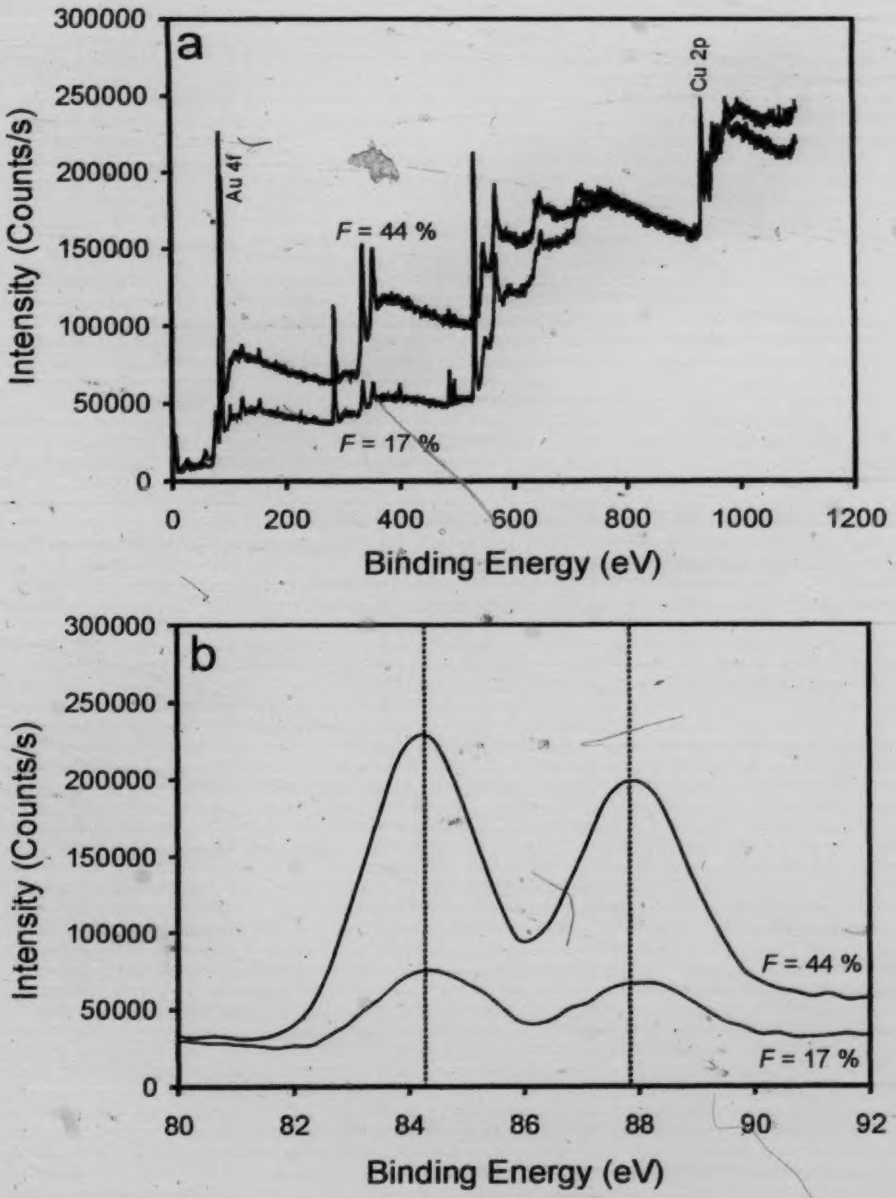

Figure 3.32. (a) XPS spectra of two Cu/Au microparticle samples with percentage Au coverage of 45 % and 17 %. The characteristic Au 4f and Cu 2p emission lines are labeled in the plot. (b) XPS spectra of the two bimetallic particle samples near the Au 4f emission lines. The dashed lines indicate the positions of the Au 4f lines for pure Au.

The interface resistance at the boundary between the Cu-core and Au-shell nanolayer augments the effective resistivity of the particle. For independent electron scattering processes, ρ_{eff} can be described by Matthiessen's rule [46]

$$\rho_{eff} = \rho_{Au} + \rho_{Cu} + \rho_{Au/Cu} = \frac{m^*}{Ne^2\tau_{eff}} \tag{3.9.3}$$

where $\rho_{Au,Cu}$ is the resistivity contribution from Au (Cu), $\rho_{Au/Cu}$ is the intrinsic interface resistivity between the metals, τ_{eff} is the effective electron scattering time, and m^* is the effective electron mass. Since the thickness of the Au layer is less than the THz skin depth, the influence of the thin interfacial layer on the non-radiative decay of particle plasmons can be examined from the THz electromagnetic properties of the bimetallic particle ensemble.

Figure 3.33 (a) illustrates $E_{tr}(t)$ transmitted through the five, 2 mm thick bimetallic Cu-core/Au-layer samples having the same packing fractions ~ 0.50, along with the reference free-space pulse. The transmitted pulse shape evolves from a multi-lobe, oscillatory pulse for the pure Cu particles to a single lobe followed by a slowly rising tail for $F = 47$ %. This is reflected in the frequency-domain, where the transmission spectrum peaks at 0.32 ± 0.05 THz for the uncoated Cu particles and as F increases to 47 %, shifts toward 0.10 ± 0.05 THz [Figure 3.33 (b)]. The most striking feature is the THz electric field transmission amplitude reduction with increasing F. Remarkably, increasing F from 17 to 47 % dramatically attenuates $E_{tr}(t)$ by 88 ± 3 %, as shown in Figure 3.33. The linear decrease in the electric field amplitude with increasing surface coverage reflects the direct proportionality between the interface area and the interface resistance. The large attenuation in the Cu-core/Au-layer particles is surprising since Cu and Au have similar dielectric functions (ε_{Au}(1 THz)= $-1.12 \times 10^5 + 7.20 \times 10^5\, i$, $\varepsilon_{Cu} = -5.45 \times 10^5 + 1.20 \times 10^6\, i$ [29]) and thus, their optical responses at THz frequencies are expected to be alike. Since $h << \delta$, the attenuation cannot be ascribed to infinitesimal ($8h^3/\delta^3 \approx 10^{-9}$) volume difference between the Cu and Cu-core/Au-layer particles. Rather, the amplitude attenuation with increasing F arises from resistance at the bimetallic interface between the Cu and Au.

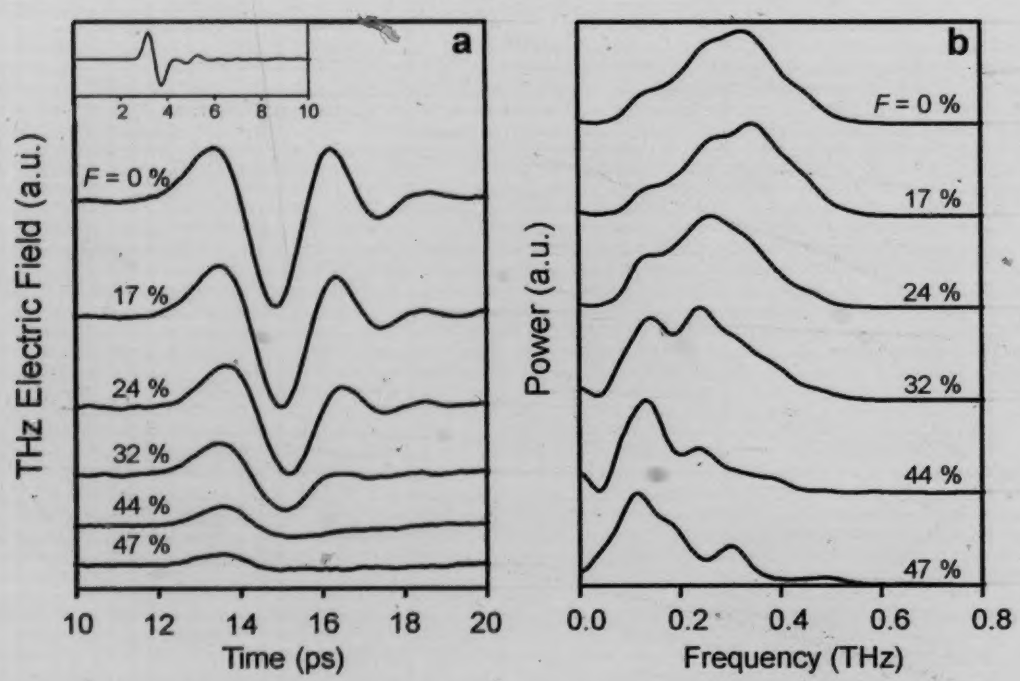

Figure 3.33. Experimental a) time-domain signal and b) power spectra of the transmitted THz pulses through 2 mm thick Cu-core/Au-layer microparticle samples for varying Au surface coverage, F. The inset depicts the reference THz pulse propagated through free-space.

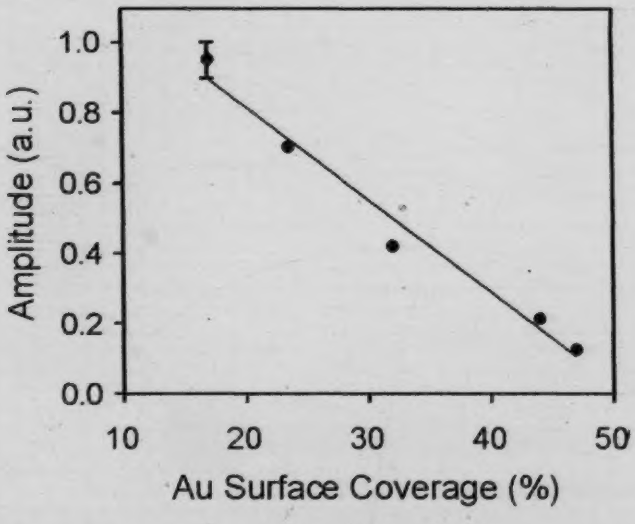

Figure 3.34. Peak-to-peak transmitted THz electric field amplitude versus Au surface coverage, *F*. The electric field amplitudes are normalized to the transmission through uncoated Cu particles.

One can obtain a simple physical understanding of the phenomenon by considering a semi-quantitative one-dimensional damped harmonic oscillator model of the plasmon oscillations driven by the THz electric field, $E_{in}(t)$. For low amplitude THz electric field amplitude such that electron motion follows the THz electric field linearly, the use of the harmonic approach is adequate for the discussion to follow. This model enables the deduction of the amplitude reduction and temporal behaviour of the plasmon-mediated THz transmission. The collective polarization, $P(t)$, of the particle ensemble is modeled by

$$\frac{\partial^2 P(t)}{\partial t^2}+\frac{2}{\tau_{eff}}\frac{\partial P(t)}{\partial t}+\omega_{eff}^2 P(t)\propto E_{in}(t) \tag{3.9.4}$$

where $\omega_{eff}^2 = \dfrac{N_{eff}e^2}{\varepsilon_o m^*}$ is the effective plasma frequency of the particle composite and N_{eff} is the density of active electrons participating in the plasmon oscillations. It should be noted that since the metal particles fill a volume fraction $f = 0.50$ and the THz pulse interacts only with the electrons within α of the surface, the effective electron density can be calculated through $N_{eff} = \dfrac{6fN\alpha}{\delta}$ [47, 48]. Given $N = 10^{28}$ m^{-3}, $f = 0.5$, $m^* \sim 1.49m$, $\alpha = 100$ nm, and $\delta = 84$ μm, the effective plasma frequency of the particle composite is $\omega_{eff} = 10^{14}$ rad/s. Shown in Figure 3.35 (a) are plots of the calculated far-field transmitted electric field $E_{tr}(t) \propto \partial^2 P(t)/\partial t^2$ in response to single cycle THz pulse excitation for τ_{eff} varying from 25 fs (derived from a Cu room temperature resistivity $\rho_{dc,Cu} = 1.7$ μΩ cm) to 0.1 fs.

The model results show reasonable agreement with the experimental data. Interestingly, as τ_{eff} decreases, the calculated $E_{tr}(t)$ is attenuated by 90 %, and the frequency spectra red-shifts from 0.32 ± 0.02 THz to 0.21 ± 0.02 THz. Furthermore, the $E_{tr}(t)$ pulse shape evolves from a multi-lobe pulse to a single-lobe pulse with decreasing τ_{eff}, in agreement with the experimentally observed trend. From the model in conjunction with the experimental data, the 88 ± 3 % electric field attenuation as F increases from 0% to 47 % represents a reduction in τ_{eff} by two orders of magnitude (corresponding to a two order of magnitude increase in ρ_{eff}). Thus, the damped harmonic oscillator model succeeds in providing a simple, physical interpretation of the observed phenomenon. However, further theoretical work, which incorporates near-field electromagnetic interaction between bimetallic particles, is required.

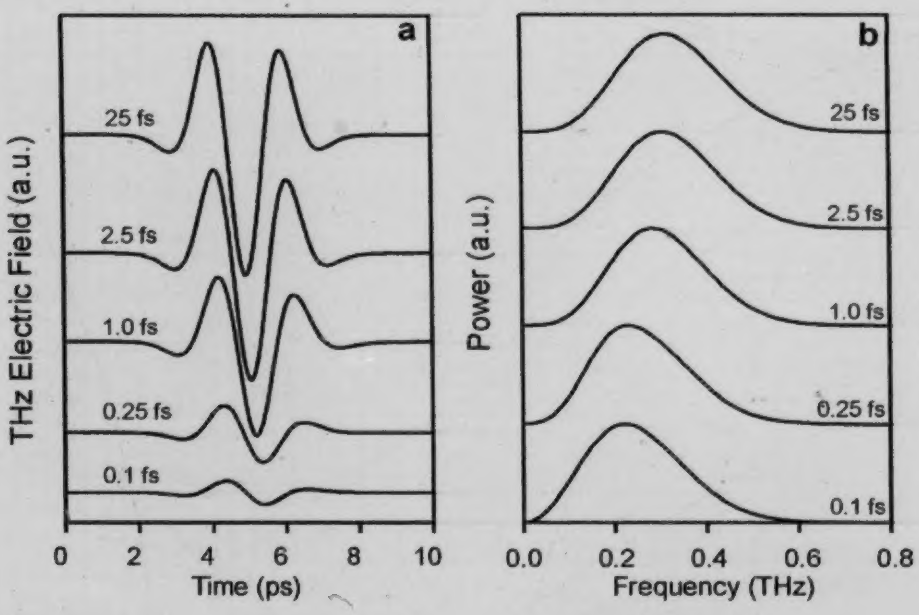

Figure 3.35. The calculated a) time-domain signal and b) frequency spectra of the transmitted THz pulses in response to single-cycle THz pulse excitation for varying τ_{eff}.

To further explore the origin of the interface resistance effect on the plasmon-mediated THz electric field transmission, control experiments are performed with monometallic Cu-core/Cu-layer particles. Due to the absence of both a potential barrier and alloying at the interface between the Cu core and the Cu layer, the only source of interface resistance for the monometallic samples is electron scattering from the rough interface topography. The samples are composed of 40 nm Cu layers which are sputter deposited onto pure Cu particles (identical to those used to fabricate the Cu/Au samples). These Cu/Cu monometallic particles have a Cu surface coverage of 24 %. In contrast to the bimetallic Cu-core/Au-layer particles, however, the monometallic Cu-core/Cu-layer particles exhibit no measurable attenuation and show no electric field pulse reshaping, as shown in Figure 3.36. This supports the fact that electric field pulse reshaping in the Cu-core/Au-layer bimetallic samples arises from electronic dissimilarities between core-layer metallic species.

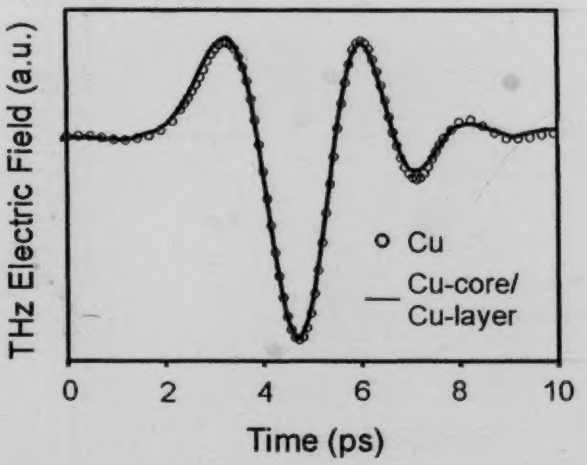

Figure 3.36. Transmitted THz pulses through 2 mm thick samples of uncoated Cu particles (circles) and Cu-core/Cu-layer particles (line).

The phase characteristics and temporal evolution of the experimental $E_{tr}(t)$ provide further insight into the attenuation phenomenon. In particular, the $E_{tr}(t)$ phase reveals that the effect of the interface resistance is not purely resistive. Shown in Figure 3.37 is the differential phase, $\Delta\Phi(\omega) = \Phi(\omega) - \Phi_{ref}(\omega)$, where $\Phi(\omega)$ is the phase of $E_{tr}(t)$, and $\Phi_{ref}(\omega)$ is the phase of the reference transmitted pulse through the uncoated Cu. The transmission is characterized by significant dispersion; at frequencies below 0.2 THz, $E_{tr}(t)$ acquires ~ 1 radian as F increases from 17 % to 47 %. The additional phase arises from the phase lag between the electric field and the induced currents in the skin layer, which is determined by the microparticles' reactance. That is, increased Au coverage results in a slower polarization response to the driving THz electric field, manifesting as a phase accumulation in $E_{tr}(t)$. In the temporal domain [Figure 3.33 (a)], the drastic attenuation of the subsidiary lobes of the pulse as *F* increases further shows that increasing *F* not only augments the Joule loss, but also increases the reactance. It is believed that the physical origin of the reactive response can be ascribed to dynamical screening at the bimetallic interface [49, 50]. Charge screening de-phases collective electron motion such that electrons in the particle are no longer synchronous with the driving THz field. Since screening becomes prominent only after the initial rise of the pulse [Figure 3.33 (a)], it is infered that screening dynamics occurs on the order of a picosecond. This time-scale, however, is significantly longer than typical electron screening processes in metals, which occur on the order of femtoseconds. Hence, further investigations are required to resolve the physical mechanisms of this screening process.

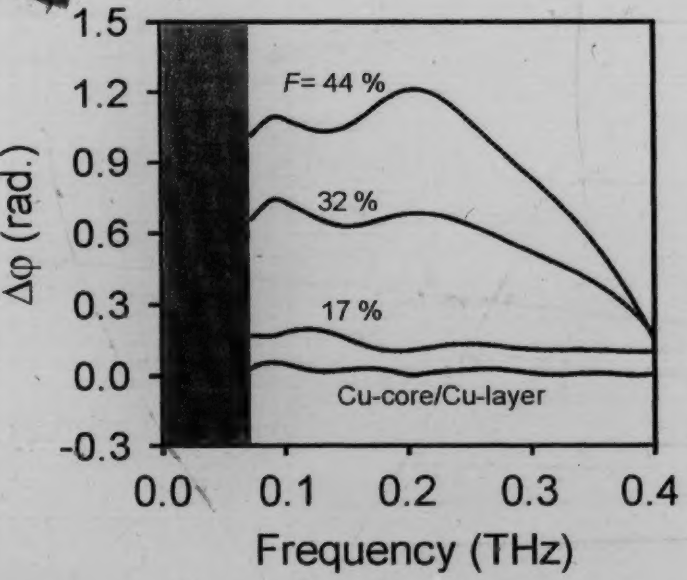

Figure 3.37. Differential phase of the transmission through the Cu-core/Cu-layer sample and through the $F = 44$ %, 32 %, and 17 % Cu-core/Au-layer microparticle samples. The transmission through the Cu-core/Cu-layer sample shows no significant phase accumulation across the transmission bandwidth.

3.10 Subsurface Probing of Terahertz Particle Plasmons

The excitation of localized non-resonant particle plasmons at THz frequencies is governed by the interaction of THz electromagnetic waves with the electrons near the surface of the particle. Within a finite distance into the particle, $\xi(\omega)$, the formation of the THz particle plasmon is governed by two mechanisms: 1) the THz electromagnetic wave incident on the particle surface penetrates hundreds of nanometers into the metal where it induces charge motion, and 2) the dipolar electric field is formed by charge accumulation at the particle's surface [34]. Notably, it remains a challenge to experimentally probe these mechanisms within the nano-scale region below the metallic surface, especially for non-planar geometries. The development of sensitive experiments to access the electromagnetic interactions beneath the surface of metals would not only provide insights into the nature of THz electromagnetic wave penetration in subwavelength structures, but also offer additional clues into the mechanism of THz particle plasmon formation and their associated non-radiative losses. The pursuit of these objectives is important for the continued development of research into low-frequency plasmonic behaviour.

Here, the THz electromagnetically induced charge motion within a depth $\xi(\omega)$ is investigated by exploiting the localized potential barrier that develops at the interface between dissimilar metals in intimate contact. By overlaying subwavelength particles with spatially-varying series of alternating metallic nano-layers, the interfacial potential barriers between the layers locally augment the non-radiative losses of electromagnetically induced current, as shown in Figure 3.38. The interfaces, therefore, provide extremely spatially localized probes of charge induction. The scale length of THz induced charge motion within the microparticles is extracted by varying the number of nano-layers, M, and their thicknesses, *h*, over nano-scale distances from the surface.

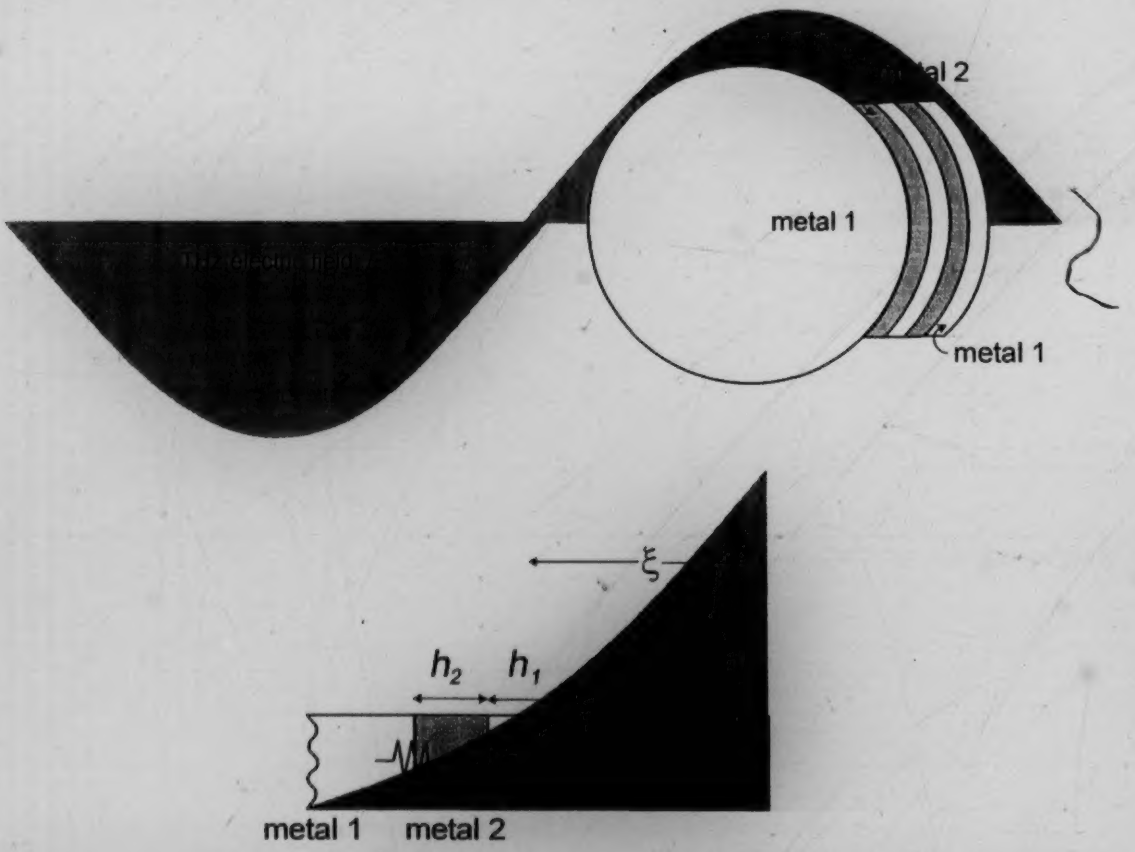

Figure 3.38. (top) Image of a metallic microparticle (metal 1) coated with alternating layers of metal 2 and metal 1 that is excited with a THz electromagnetic wave. (bottom) Illustration of THz electromagnetic charge induction at the surface of the multi-layered microparticle. The interfaces between the different metal layers each create contact resistances that impede charge flow across the interface.

The sample used in the experiments consists of ensembles of subwavelength Cu microspheres having a radius ranging from 34 to 49 μm, which are coated with alternating layers of Au and Cu films. The microparticle ensembles are 2.3 ± 0.1 mm thick and are packed in a polystyrene cell to a filling fraction of ~ 0.5. The THz electromagnetic properties of the ensembles are investigated using THz time-domain spectroscopy.

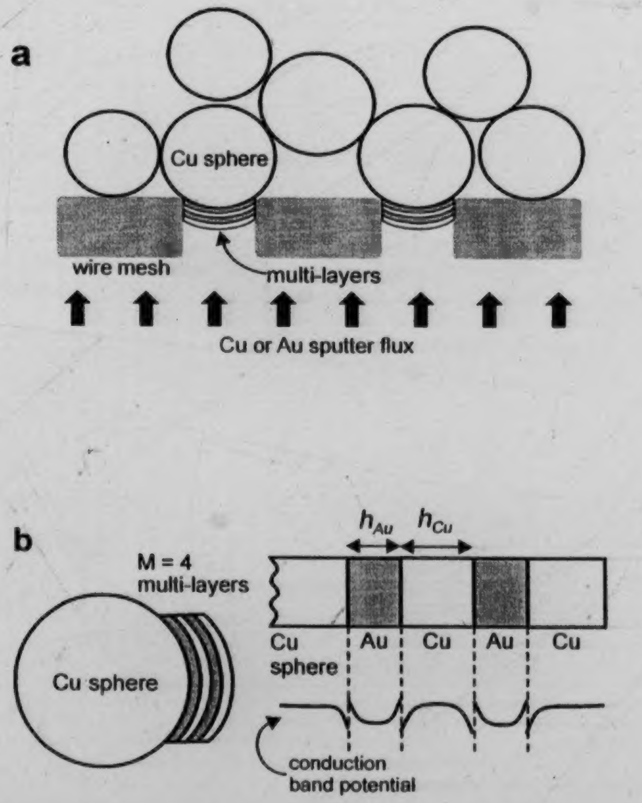
a
Cu sphere
wire mesh
multi-layers
Cu or Au sputter flux
b
M = 4
multi-layers
h_{Au}
h_{Cu}
Cu sphere
Cu
sphere
Au
Cu
Au
Cu
conduction
band potential

Figure 3.39. (a) Diagram depicting the sputter deposition method used to fabricate Cu particles coated with multi-layers. (b) Illustration of a single Cu microparticle coated with 4 alternating Au and Cu layers. The alternating layers produce a spatially modulated potential beneath the microparticle surface, which augments the non-radiative losses at the particle surface.

As illustrated schematically in a diagram in Figure 3.39 (a), multi-layered microparticle samples are fabricated by sputter-coating Cu microspheres with alternating nano-layers (up to 5 layers) of Au and Cu. The nominal Au and Cu layer thicknesses are h_{Au} = 15 nm and h_{Cu} = 43 nm respectively. The Au and Cu nano-layers produce a spatially modulated conduction band potential beneath the particle surface [Figure 3.39 (b)], augmenting the non-radiative losses near the surface at the coated regions. It is carefully ensured that the various particle samples have identical metallic coverage deposited on their surfaces within ± 1%. To achieve precise control of the coverage of the particles during the sputter deposition, the particle samples are masked by a wire mesh having 40 μm × 40 μm rectangular openings. The Cu particles exposed through the wire mesh openings are coated with ~ 40 μm × 40 μm square patches of alternating metallic layers covering 7% of the total particle surface area.

Figure 3.40 (a) shows typical time-domain THz pulses transmitted through particle collections with varying M. The transmitted waveforms originate from coherent far-field re-radiation of the excited particle ensemble. As seen in the Figure, coating the Cu particles with a 15 nm thick Au nano-layer results in a significant 41 ± 1 % amplitude reduction of the transmitted THz electric field pulses. Surprisingly, the addition of a 43 nm thick Cu layer on top of a 15 nm thick Au layer gives rise to 20 ± 1 % less attenuation relative to particles coated with only a 15 nm thick Au layer. Evidently, there is reduced loss in the bi-layered particles despite the presence of an additional interfacial Au/Cu contact potential. Overall, the time-domain waveforms show that the transmitted THz pulse amplitude is strongly dependent on the exterior layer of the multi-layers. While multi-layer films with an exterior Au layer (e.g. Au, Au/Cu/Au, and Au/Cu/Au/Cu/Au) show attenuation up to 64 ± 1 %, multi-layers with an exterior Cu layer (e.g. Cu/Au/Cu/Au and Cu/Au) exhibit much lower attenuation of only 21 ± 1 %. Interestingly, the addition of more interfaces near the particle surface does not directly correlate with increased attenuation. Rather, the attenuation exhibits an alternating trend with the addition of successive layers. This behaviour can be understood by considering the relative effect of the metallic layer thicknesses on the magnitude of the attenuation arising from the interfaces. Since the penetrating THz electric field and its associated current density decay abruptly into the medium, interfaces that are closer to the surface will make significantly larger contributions to the transmission attenuation. Thus, particles coated with multi-layers that have a 15 nm exterior Au layer show greater attenuation than those that have a 43 nm Cu exterior layer since the interface potential barrier in the former case is closer to the surface where the majority of the induced current density resides. Further examination of the waveforms for the $M = 1$, 3, and 5 samples (all having an exterior Au layer but varying numbers of layers beneath this exterior Au layer) illustrates a weak dependence of the transmission attenuation for $M > 3$ [Figure 3.40 (b)]. This indicates that contact potential barriers lying > 73 nm from the surface (corresponding to the total thickness of the $M = 3$ multi-layers) do not contribute to the THz electric field attenuation.

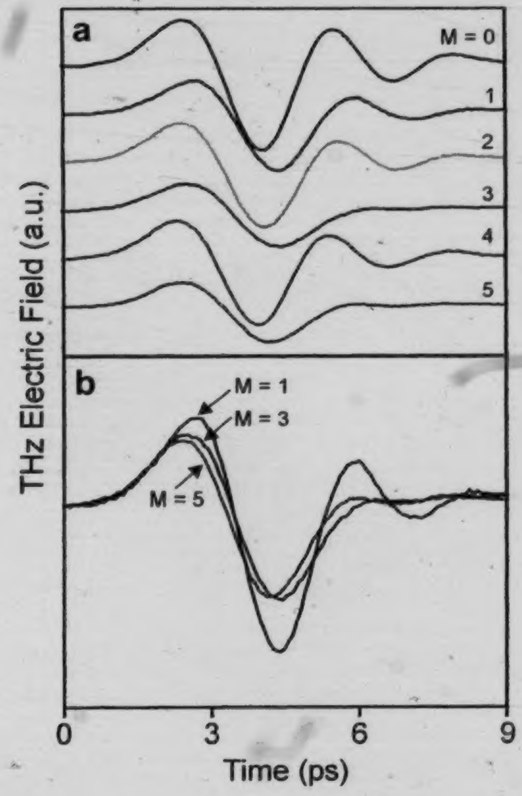

Figure 3.40. (a) Time-domain waveforms of the THz pulses transmitted through Cu microparticles with alternating nano-layers. (b) Magnified image of the time-domain THz waveforms transmitted through particle ensembles where the number of layers is 1, 3, and 5. These samples are coated with a 15 nm thick exterior Au layer.

The time-domain waveforms reveal pulse re-shaping with increasing M, where the pulse shape evolves from quadrupolar (M = 0), to tri-polar (M = 1), to quadrupolar (M = 2), to bi-polar (M = 3), to quadrupolar (M = 4), and finally to bi-polar (M = 5). This pulse re-shaping suggests frequency-dependent attenuation arising from the multi-layers. To study this frequency dependence, the configurationally-averaged, relative spectral transmission amplitude $\Phi_M(\omega) = \langle E_M(\omega)\rangle / \langle E_o(\omega)\rangle$ is determined, where $\langle E_M(\omega)\rangle$ is the average spectral amplitude of the transmission through samples with M

(=1,2,3,4,5) layers and $\langle E_o(\omega)\rangle$ is the average spectral amplitude of the nominal transmission through uncoated Cu particles. $\Phi_M(\omega)$ is obtained by averaging the transmission for multiple (> 10) random realizations of the ensemble, where the packing fraction and sample thickness are kept constant. The spectral amplitudes are calculated over the transmission bandwidth from 0.2 THz to 0.4 THz. As shown in Figure 3.41 (a), the relative transmission amplitude for M = 1 varies from 0.89 at 0.2 THz down to 0.68 at 0.4 THz. Adding a 43 nm Cu layer over top of the Au-layered particles enhances the transmissivity of the mono-layered particles. Over the same frequency range, $\Phi_2(\omega)$ is larger than $\Phi_1(\omega)$ and shows less attenuation at higher frequencies. For M = 3, $\Phi_3(\omega)$ decreases significantly from 0.2 THz to 0.4 THz and is as low as 0.25 at the higher frequency end of the spectrum. Interestingly, these results suggest that non-radiative losses arising from the interface are frequency-dependent, where the higher frequency components of the pulse are more attenuated than the lower frequency components. Moreover, it is shown that the spectral amplitude $\Phi_M(\omega)$ alternates from high to low with the successive addition of layers, similar to the observed trends in the time-domain waveforms. The similarities between $\Phi_4(\omega)$ and $\Phi_5(\omega)$ with $\Phi_2(\omega)$ and $\Phi_3(\omega)$, respectively, point out that interfaces lying below the first several layers from the surface contribute minimally to the attenuation.

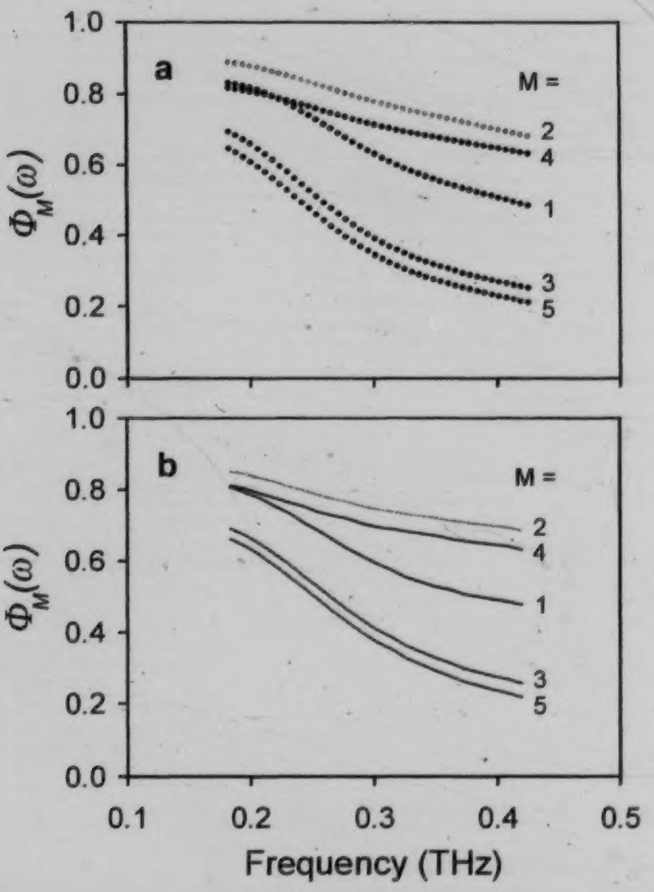

Figure 3.41. (a) Experimental and (b) calculated relative spectral transmission amplitude for samples with varying number of layers normalized with respect to the spectral transmission amplitude through uncoated particles.

To describe the sub-surface THz particle plasmon dynamics, a model is developed accounting for non-radiative losses at each interface. Initially the case for an uncoated particle is examined. When $\boldsymbol{E}_{in}(r,\omega)$ is incident on a metallic particle, 1) charge induction creates a transient current density, $\boldsymbol{j}(r,\omega) = \boldsymbol{j}_o(\omega)\, e^{-r/\xi(\omega)}$, where $\boldsymbol{j}_o(\omega)$ is the current density at the surface and r is the distance from the surface, and 2) surface charge accumulation results in a depolarization field $\boldsymbol{E}_{depol}(r,\omega)$. The non-radiative decay within the particle is described through $\Psi(\omega) \propto \int j(r,\omega) \cdot E(r,\omega)\, dv$, where $E(r,\omega) = E_{in}(r,\omega) + E_{depol}(r,\omega)$ is the total electric field and dv is the volume element of the particle. Since the current density is related to the total field via $E(r,\omega) = \rho(\omega)\, j(r,\omega)$, the total non-radiative decay is $\Psi(\omega) \propto \int \rho(\omega)\, j^2(r,\omega)\, dv$. However, the situation is different for coated microparticles, where the interfaces introduce additional sources of dissipation. For a series of n identical interfaces located at distances h_1, h_2, ... , h_n, below the surface, non-radiative decay includes the bulk dissipation $\Psi(\omega)$ in addition to localized losses at each interface. The total non-radiative loss for the coated particles can be described via

$$\Psi'(\omega) \propto \Psi(\omega) + \sum_i^n \int \rho_{Au/Cu}(\omega)\ \delta(r-h_i)\ j^2(r,\omega)\ dv$$

$$= \Psi(\omega) + F \sum_i^n \rho_{Au/Cu}(\omega)\ j^2(h_i,\omega) \tag{3.10.1}$$

where $\rho_{Au/Cu}(\omega)$ is the interface resistivity between the Cu and Au layers and F describes the average fractional surface coverage of the particles and accounts for the partial coverage of the particles. Thus, the normalized spectral transmission amplitude relative to uncoated particles, can be expressed as

$$\Psi_N(\omega) = 1 - \frac{F\ \rho_{Au/Cu}(\omega)\ j_o^2(\omega)\ \sum_i^n e^{-2h_i/\xi(\omega)}}{\Psi(\omega)} \tag{3.10.2}$$

where $A\ (= F\ \rho_{Au/Cu}(\omega)\ j_o^2(\omega)\ \Psi^{-1}(\omega)) > 0$ is a dimensionless ratio describing the fractional non-radiative losses due to the interface relative to the bulk dissipation. It should be noted that the parameter A incorporates the degree of surface coverage of the particles, F, and can be estimated from the experimental data. In order to implement the above model to determine A and $\xi(\omega)$, the distances h_1, h_2, ... , h_n, are obtained from measured values of h_{Au} and h_{Cu}. As seen in Figure 3.41 (b), there is excellent agreement between the calculated $\Phi_M(\omega)$ obtained from Equation (3.10.2) and the experimental data. Most notably, the model concurrently describes, with great accuracy, the preferential attenuation of the higher frequency components, the oscillating behaviour of $\Phi_M(\omega)$ with the addition of successive Au/Cu nano-layers, in addition to the similarities in $\Phi_4(\omega)$ and $\Phi_5(\omega)$ with $\Phi_2(\omega)$ and $\Phi_3(\omega)$, respectively.

An important outcome of the model is the direct characterization of the effective penetration distance of the sub-surface charge induction, $\xi(\omega)$. As shown in Figure 3.42, $\xi(\omega)$ shows a notable frequency dependency, where it varies from 100 nm at 0.2 THz to 60 nm at 0.4 THz. For a planar geometry, the region of induced charge oscillation precisely corresponds to the skin depth, $\alpha(\omega) \approx \sqrt{2/\sigma\omega\mu}$) [17]. Plotted in Figure 3.42 is the classical planar skin depth values for Cu, $\alpha_{Cu}(\omega)$, and for Au, $\alpha_{Au}(\omega)$, from 0.1 THz to 0.5 THz, based on experimental data from Ref. [51]. Interestingly, at higher frequencies, $\xi(\omega)$ approaches 72 nm at 0.42 THz, similar to that of $\alpha_{Cu}(\omega)$. At lower frequencies (< 0.25 THz), $\xi(\omega)$ slightly deviates from the $1/\sqrt{\omega}$ dependency of the classical skin depth, suggesting that the validity of the plane wave approximation used to derive the electromagnetic skin depth on a planar surface [17] becomes questionable. It should also be noted that contributions from the anomalous skin effect [52] may further account for the discrepancies between $\xi(\omega)$ and $\alpha(\omega)$. When the electromagnetic field driving the electrons suffers appreciable damping over the distance the electron traverses between collisions, the electron velocity becomes dependent on the field at prior positions along the electron mean free path. This anomalous skin effect results in a decreased skin depth relative to that predicted by the classical Drude model.

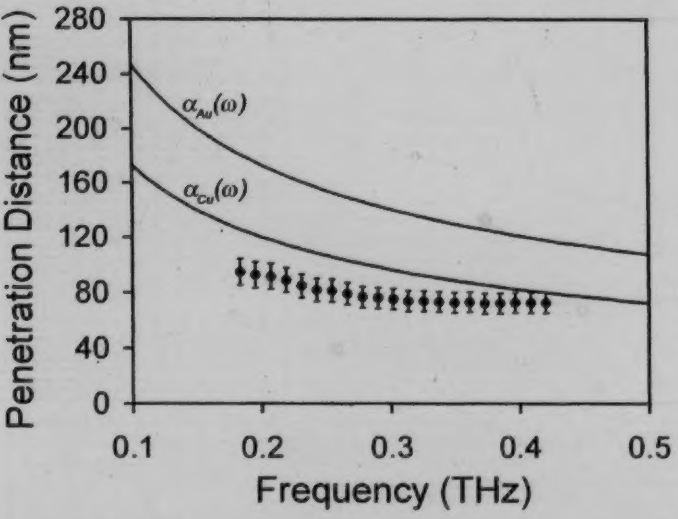

Figure 3.42. Calculated subsurface penetration distance of THz particle plasmon into the Cu multilayered microparticles. Also shown by the solid lines are the experimental skin depth values for Au and Cu.

3.11 An Amorphous Metamaterial at Terahertz Frequencies

The concept that the electromagnetic response of a material can be tailored via periodic variations in its structure has been the motivation for some of the greatest discoveries in modern photonics. One example is photonic crystals [53], which consist of dielectric media possessing a periodic modulation of their refractive indices. This variation is achieved by inserting periodic scattering elements of a different dielectric constant into a host medium. The scattering elements collectively inhibit reflection or transmission of electromagnetic waves over a frequency range (called the "photonic band gap") that is correlated to the spatial periodicity of the scatterers. Typically, the size and periodicity of the scattering elements are on the order of the wavelength.

Metamaterials represent another profound discovery based on the premise that the response of a material can be controlled via periodic structural variation. In contrast to photonic crystals, metamaterials consist of ordered scattering elements where the size and order of the scatterers are much smaller than the wavelength of the electromagnetic wave. In this situation, the scattering elements are the microscopic "building blocks" of the artificial material, analogous to atoms in conventional matter. The metamaterial can be characterized by an effective permittivity. Akin to the permittivity of naturally occurring media, the effective permittivity of the artificial material can be altered by changing the size, shape, and properties of the microscopic constituents comprising the metamaterial.

Metamaterials operating in the THz and microwave frequency regime have provided entirely new possibilities in the manipulation and control of low frequency electromagnetic waves. Pendry et al. [47] demonstrated that a three-dimensional lattice of micron-scale metallic wires can be viewed as an effective medium with an electron density determined by the volume fraction of the wires. In another report, Wu et al. [48] have shown that the collective electromagnetic response of a sub-wavelength, two-dimensional lattice of metallic wires can exhibit a reduced plasma frequency, thus behaving like a high-pass filter in the THz frequency regime. Interestingly, an artificial magnetic response at THz frequencies has been shown to arise from metamaterials constructed from subwavelength scale split-ring resonators composed of nonmagnetic metals [54]. These split ring resonators consist of two planar concentric rings that both have a small gap, as shown in Figure 3.43. Electric field incident on the material drives current in the split-rings producing subwavelength sized magnetic dipoles that collectively generate an artificial magnetic response. Further, using a prism-shaped material consisting of an array of split ring resonators in conjunction with a wire array, Shelby et al. [55] demonstrated that microwaves propagated through the material refract at angles on the "wrong" side of the normal, i.e. at negative angles. Thus, unlike almost all naturally occurring materials, this artificial material exhibits a negative refractive index.

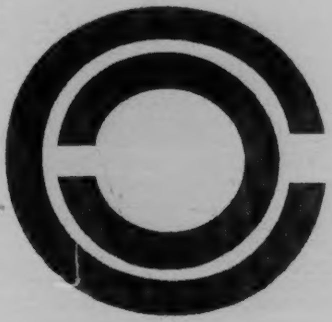

Figure 3.43. Planar split-ring resonator consisting of two concentric rings each with a small gap.

To date, all studies of metamaterials at THz frequencies have employed a *periodic or ordered* array of subwavelength sized scattering elements. On the other hand, random media lacking spatial order or periodicity are the antipode of periodic structures and constitute the most general class of photonic systems. While subwavelength periodic structures can be considered the metamaterial analog of naturally occurring crystalline materials, random media, by the same justification, can be viewed as the metamaterial analog of naturally occurring amorphous materials. Similar to its periodic counterpart, the effective electromagnetic properties of amorphous metamaterials can be altered by changing the size, shape, and properties of the microscopic constituents. With this motivation, this sections explores an entirely new class of amorphous THz metamaterial consisting of a random ensemble of subwavelength sized scatterers composed of dielectric and metallic media, as shown in Figure 3.44. The effective permittivity of the amorphous artificial material is altered by changing the relative volume fractions of the metallic and dielectric constituents. Surprisingly, the effective permittivity shows a nonlinear dependence on the relative volume fraction of the constituents. This behaviour is resolved by considering non-resonant particle plasmon interactions between metallic constituents.

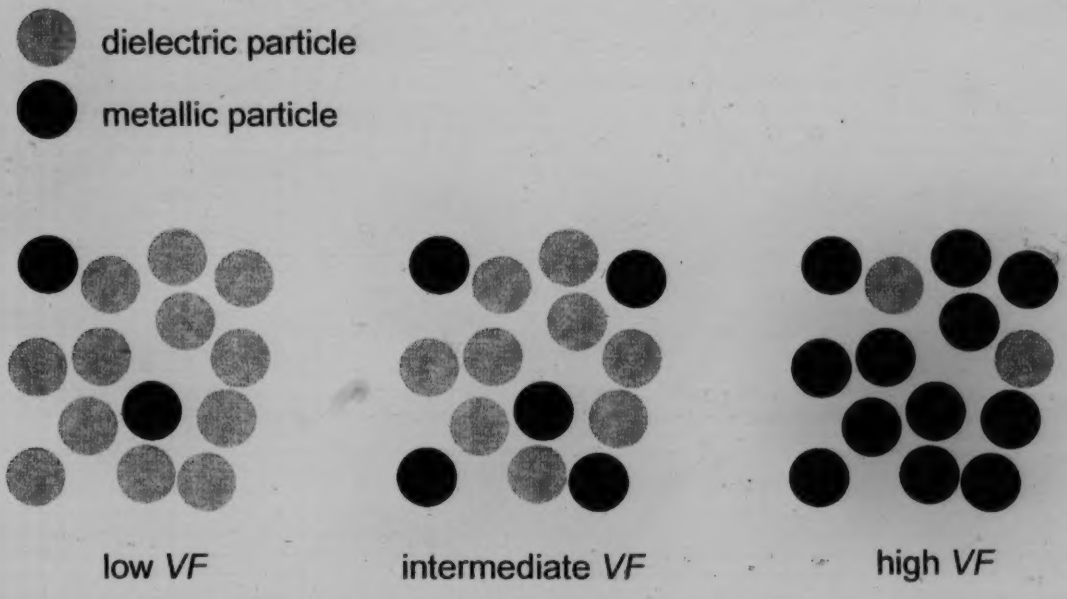

Figure 3.44. Illustration of an amorphous metamaterial consisting of random ensembles of dielectric and metallic particles with varying metallic particle volume fraction, *VF*.

The amorphous metamaterial employed in the studies consists of a 4.5 mm thick mixture of semi-spherical Co metallic microparticles having a mean dimension of 74 ± 23 μm and spherical sapphire dielectric microparticles having a mean dimension of 100 ± 12 μm. In reporting the size of the particles, the error describes the distribution of the particle sizes within one standard deviation from the mean value. Co metallic particles are employed since they can be easily separated from the dielectric particles by a magnet. Moreover, the dielectric properties of sapphire and Co are well-known in the THz frequency range. Using THz time-domain spectroscopy, the THz electric field transmission through the amorphous metamaterial is studied as a function of the metallic particle volume fraction, *VF*, ranging from 0% to 100%.

Shown in Figure 3.45 are representative time-domain THz waveforms transmitted through metallic/dielectric particle ensembles where the volume fraction Co, *VF*, ranges from 0.0 % up to 100 %. The plot illustrates the transmitted waveforms polarized parallel to the incident polarization. As the metallic particle volume fraction increases, there are three distinctive regimes in the time-domain waveforms: 1) for low *VF* (0.0 % < *VF* < 7.2 %), the addition of metallic particles minimally affects the arrival delay of the THz pulse, 2) for intermediate *VF* (15.0 % < *VF* < 63.2 %), the THz pulse is significantly delayed relative to *VF* = 0 %, and 3) for high *VF* (81.9 % < *VF* < 100.0 %), the addition of the metallic particles causes marked advancement of the transmitted pulse. The relative effective refractive index of the ensemble is extracted from the time-domain waveforms referenced to *VF* = 0 %. The plot in Figure 3.46 of the relative effective refractive index (at a central frequency of 0.23 THz) versus *VF* illustrates the aforementioned trends observed in the time-domain plots. For low *VF*, there is minimal change in the relative effective refractive index, which is constant at ~ 0.03. There is a marked increase of in the effective refractive index to ~ 0.10 for intermediate *VF* (15.0 % < *VF* < 63.2 %). As *VF* increases from 81.9 % to 100 %, the relative effective refractive index decreases to −0.12.

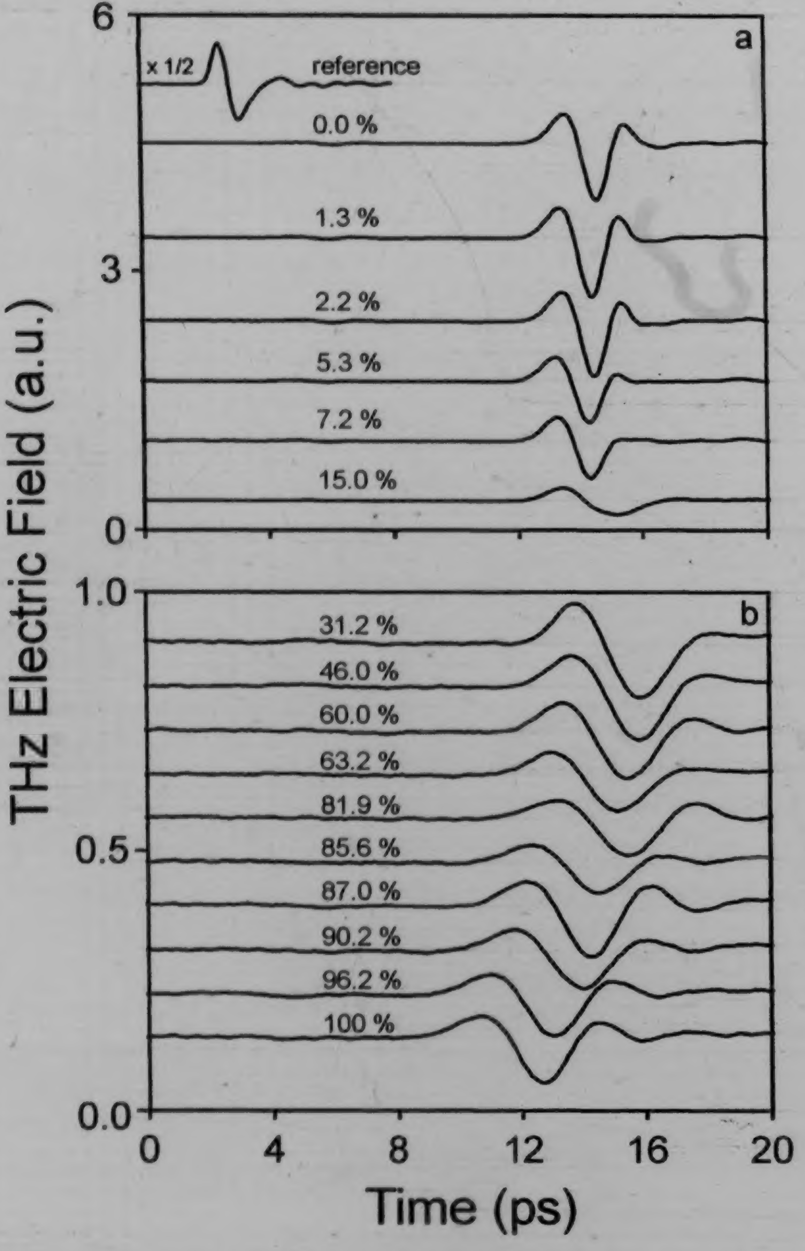

Figure 3.45. (a) Time-domain waveforms transmitted through an empty sample cell (reference) and 4.5 mm thick Co/sapphire particle mixtures for percentage volume Co varying from 0.0 % to 15.0 %. (b) Time-domain waveforms transmitted through 4.5 mm thick Co/sapphire particle mixtures for percentage volume Co varying from 31.2% to 100%.

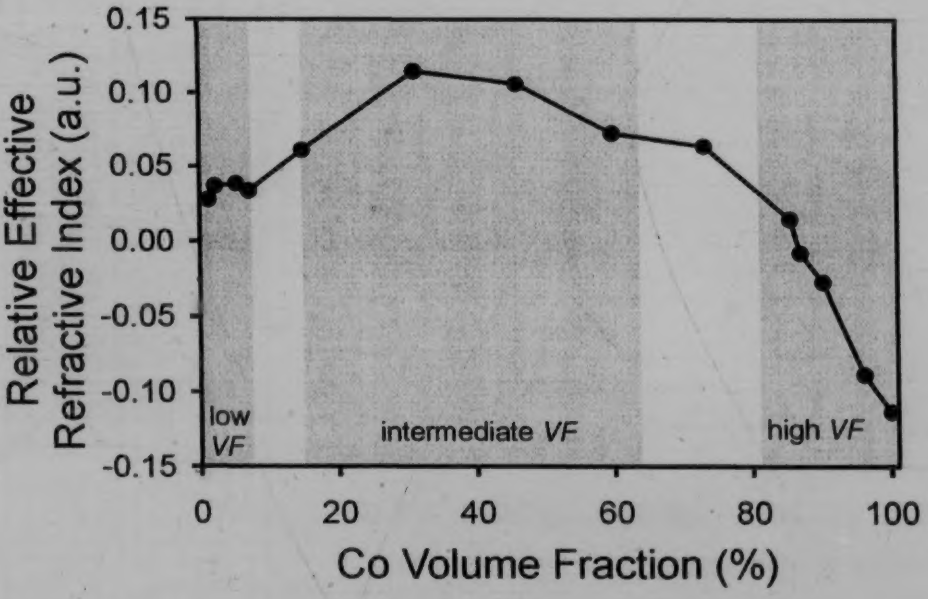

Figure 3.46. Relative effective refractive index of the metallic/dielectric ensemble measured at a frequency of 0.23 THz versus the Co volume fraction. The plot highlights the three regimes low *VF*, intermediate *VF*, and high *VF*.

Representative transmission power spectra for Co/sapphire ensembles having *VF* ranging from 0.0 % to 81.9 % are shown in Figure 3.47. The main features of this graph are the frequency-dependent attenuation for low *VF* and the frequency-independent attenuation for high *VF*. The transmission through the dielectric ensemble (*VF* = 0 %) contains measurable frequency components from 0.1 THz to 0.8 THz. As *VF* increases to 15.0 %, nearly all the frequency components above 0.4 THz are extinguished. Preferential attenuation of the higher frequency components is ascribed to the frequency-dependent scattering cross section of the subwavelength metallic particles. The scattering cross section, C_{sc}, of a particle is defined by the energy of the incident wave incident on an area C_{sc} that is equivalent to the total energy scattered in all directions by the particle. According to Rayleigh scattering, a single subwavelength scattering element embedded in a homogeneous medium has a scattering cross section proportional to λ^{-4}. Hence, a metallic particle preferentially scatters the higher frequency components of the incident electromagnetic pulse relative to the lower frequency components, which causes the observed frequency-dependent attenuation. It should be noted, however, that Rayleigh scattering assumes a single, independent spherical particle embedded in a homogeneous medium. Since the surrounding medium in the vicinity of the particles contains other scatterers, exact λ^{-4} dependence is not observed in the spectral dependence of the attenuation. As *VF* increases from 46.0 % to 81.9 %, the transmitted power is reduced by approximately 50%. In contrast to the trends observed for low *VF*, however, an increase in *VF* from 46.0 % to 81.9 % causes nearly frequency-independent attenuation across the transmission bandwidth. In this regime, Rayleigh scattering from the individual metallic particles does not fully account for the attenuation.

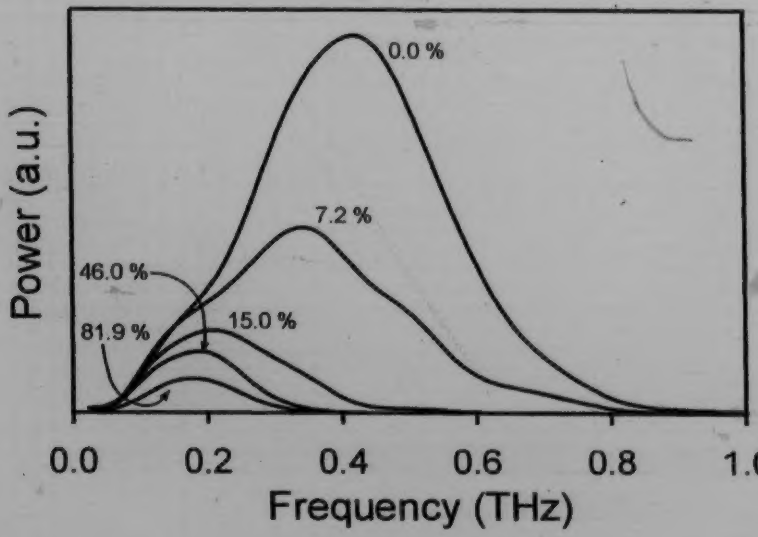

Figure 3.47. Frequency spectra of the transmission through mixtures of Co and sapphire particles for varying Co particle concentration.

To gain greater insight into the nature of electromagnetic wave propagation through the sample, Figure 3.48 plots the time-dependent intensity profiles of the transmission components polarized parallel (black lines) and perpendicular (gray lines) to the incident polarization. For $VF = 1.3$ %, the transmitted THz pulse is polarized along the incident polarization. The relatively weak pulse component measured in the perpendicular direction is attributed to small angle scattering from the dielectric constituents. For $VF = 60$ %, the commensurate intensity of the parallel and perpendicular pulse components indicates that the transmitted electromagnetic wave is unpolarized. Moreover, the significant delay relative to $VF = 0$ % suggests that the THz pulse effectively propagates a longer distance in the $VF = 60$ % sample than in the $VF = 0$ % sample. For $VF = 60$ %, both the unpolarized transmission and the delay can be attributed to increased polarization-randomizing scattering. As seen in Figure 3.48, the transmitted pulse through the $VF = 100$% sample arrives earlier and is polarized along the incident polarization, indicative of particle plasmon coupling.

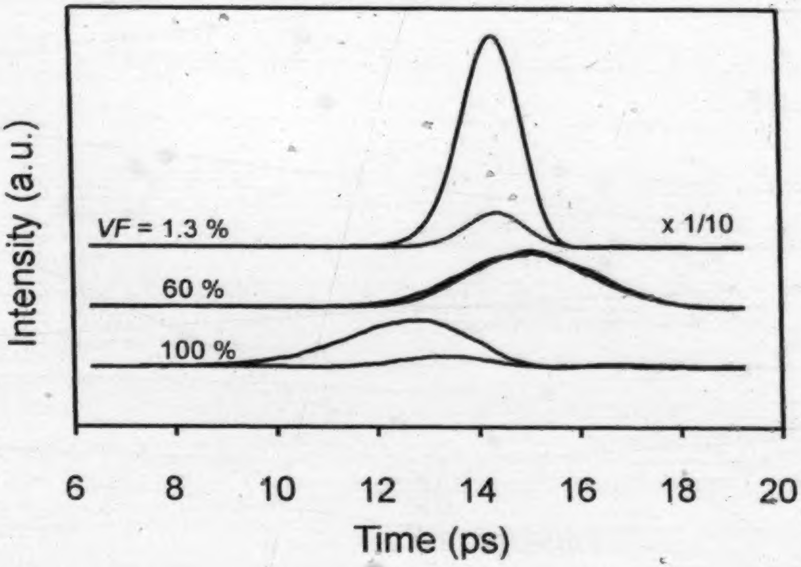

Figure 3.48. Time-dependent intensity of the transmitted pulses through 4.5 mm thick ensembles with various *VF* values. The black and gray lines correspond to the transmitted component polarized parallel and perpendicular to the incident polarization, respectively.

Electromagnetic wave interaction with the amorphous metamaterial is strongly dependent on the separation distance between metallic particles. Based on the metallic particle volume fraction, the average inter-particle separation between metallic particles, *s*, can be estimated. Approximating the Co particles as spheres, the average volume occupied by a single Co particle is

$$V_1 = \frac{4\pi}{3}\left(\frac{\delta}{2}\right)^3 \qquad (3.11.1).$$

Based on the total volume of Co in the metamaterial,

$$V_{Co} = m_{Co} / u_{Co} \qquad (3.11.2)$$

where u_{Co} is the density of Co, the number of Co particles is

$$N_{Co} = V_{Co}/V_1 \qquad (3.11.3).$$

The total volume occupied by the metamaterial, V_{total}, is approximated by

$$V_{total} = (V_{Co} + V_{sapphire})/f \qquad (3.11.4)$$

where $V_{sapphire}$ is the total volume of sapphire in the metamaterial and f (~0.50) is the packing fraction of the metallic and dielectric particles. The average volume of space occupied by a single Co particle is

$$V_{ave} = V_{total} / N_{Co} \qquad (3.11.5).$$

As shown in Figure 3.49, for a collection of Co particles that have been isotropically distributed throughout the mixture, the radius of the volume of space occupied by a single Co particle is

$$r_{ave} = (3V_{ave}/4\pi)^{1/3} \qquad (3.11.6).$$

Therefore, the average separation between nearest neighbor metallic particles measured from the surface of the particles is

$$s_{ave} = 2\, r_{ave} - \delta \qquad (3.11.7)$$

The *optical* inter-particle separation accounts for the effective refractive index of the medium surrounding the metallic particles, n_s. The effective index of the surrounding medium is sensitive to *VF* because the addition of metallic particles displaces a volume otherwise occupied by dielectric particles. For $VF \approx 0$ %, for instance, n_s is averaged between the refractive indices of air ($n_{air} = 1$) and sapphire, $n_{sapphire}$. As metallic particles are added to the ensemble, there is decreasing volume fraction of sapphire particles and the medium surrounding the metallic particles is, to a greater extent, composed of air. In the limit where $VF = 100$ %, the metallic particles have completely displaced the sapphire particles and are only surrounded by air, such that $n_s = 1$. The effective refractive index surrounding the metallic particles can be estimated using a Beer effective medium description [1],

$$n_s = \frac{f\, n_{sapphire} V_{sapphire}}{V_{total}} + \left(1 - \frac{f\, V_{sapphire}}{V_{total}}\right) \quad (3.11.7).$$

Therefore, the average optical inter-particle separation is

$$s_{ave,opt} = s_{ave}\, n_s \quad (3.11.8).$$

Thus, the presence of dielectric particles between the metallic particles effectively increases the separation distance between particles.

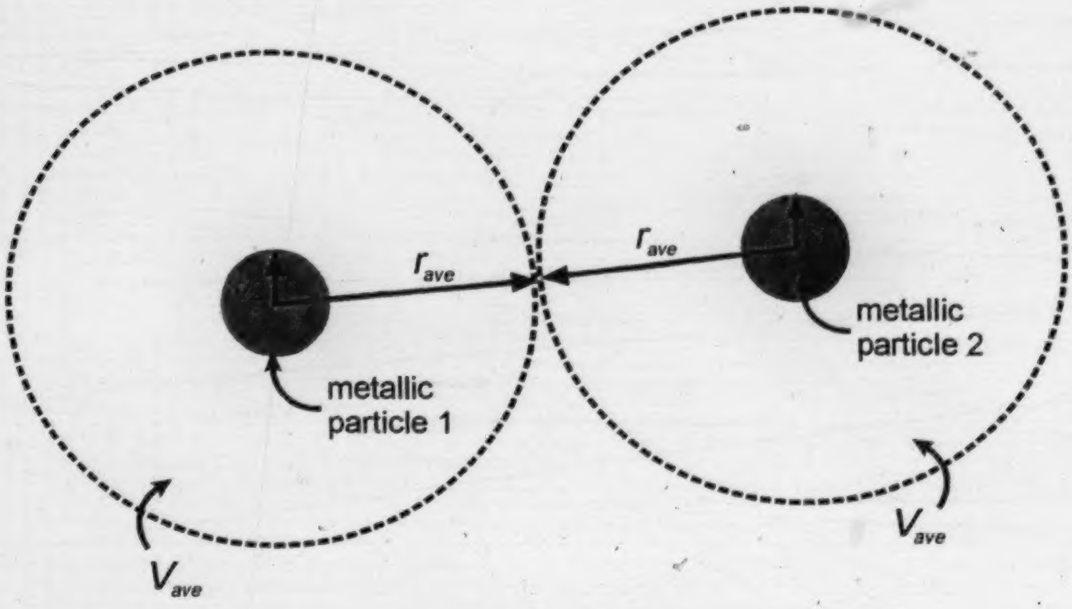
r_{ave}
r_{ave}
metallic particle 1
metallic particle 2
V_{ave}
V_{ave}

Figure 3.49. Illustration of the relationship between V_{ave}, δ, and r_{ave}.

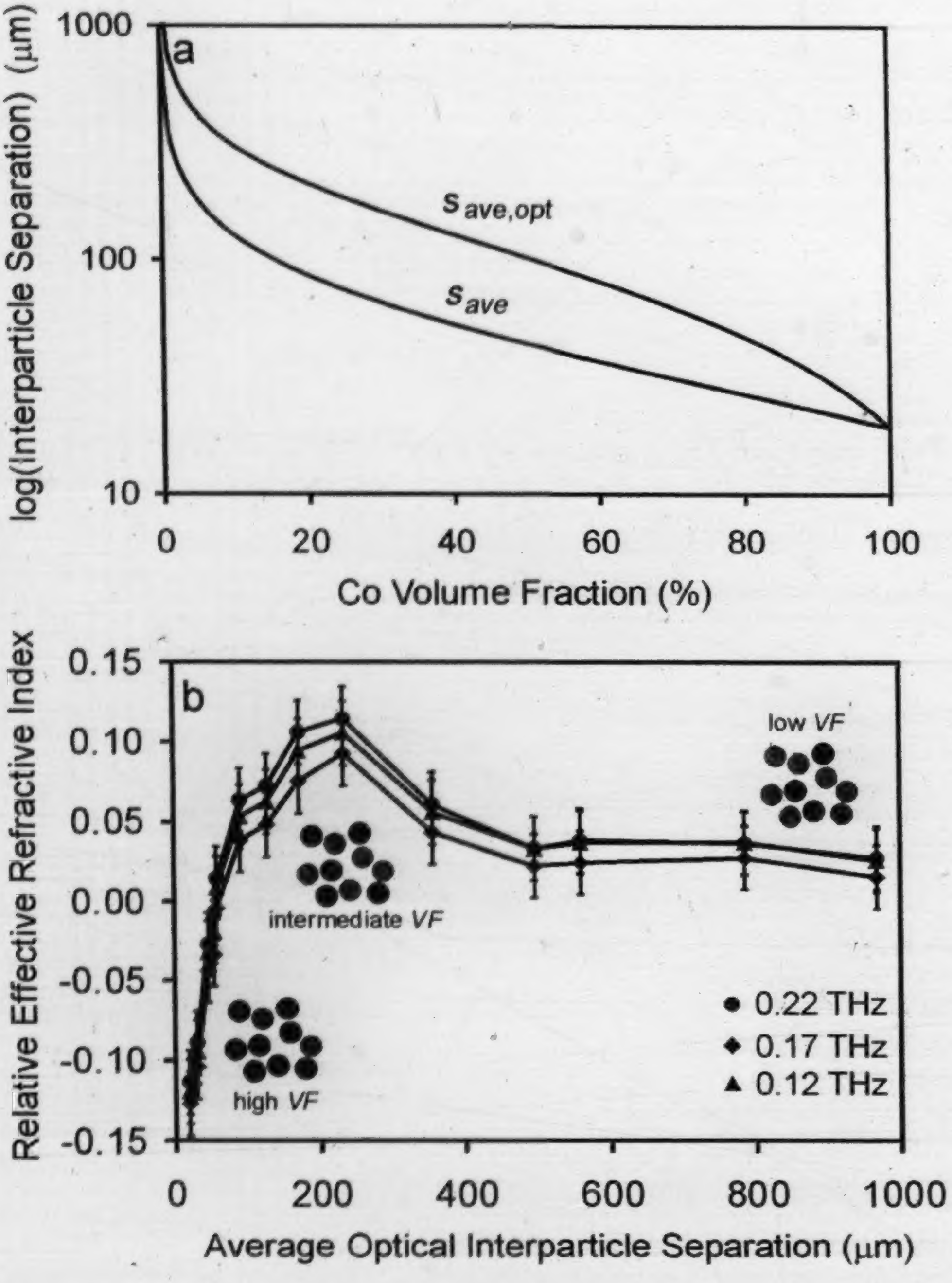

Figure 3.50. The optical and physical interparticle separation between metallic particles as a function of the Co volume fraction. (b) Effective relative refractive index versus the average optical separation between metallic particles at frequencies of 0.22 THz, 0.17 THz, and 0.12 THz. The diagrams inset in (b) illustrate the relative volume fraction of the metallic and dielectric particles for low, intermediate, and high *VF*.

Electromagnetic wave interaction with the amorphous metamaterial can be interpreted by considering the influence of s_{ave} and $s_{ave,opt}$ on the interaction between metallic particles. Figure 3.50 (a) depicts s_{ave} and $s_{ave,opt}$ versus the Co volume fraction. For all values of *VF*, $s_{ave} < s_{ave,opt}$. Over the range 10 % < *VF* < 80 %, the optical interparticle separation is approximately twice the physical interparticle separation. As *VF* approaches 100 %, both s_{ave} and $s_{ave,opt}$ approach 19 μm.

Figure 3.50 (b) shows the relative effective refractive index of the ensemble versus $s_{ave,opt}$ at frequencies 0.22 THz, 0.17 THz, and 0.12 THz. For *VF* ranging from 0.0 % to 7.2 %, the addition of metallic particles does not appreciably affect the transmission, since the effective refractive index of the ensemble remains constant at ~ 0.02. In this regime, the metallic particles are separated by 496 μm < $s_{ave,opt}$ < 968 μm. This corresponds to an average physical separation between particles of 216 μm < s_{ave} < 448 μm. Hence, the metallic particles are, on average, physically separated by distances several times greater than the diameter of the dielectric particles. This implies that the spacing between metallic particles is occupied by several dielectric particles. Mutual interaction between metallic particles is negligible, and the metallic particles act like independent scatterers, removing electromagnetic energy from the incident beam via Rayleigh scattering. Since the transmission in this regime is polarized, the electromagnetic transmission through the amorphous metamaterial arises from electromagnetic waves propagating directly through the sapphire particles, which constitute the ballistic transmission, and electromagnetic waves that have been scattered by small angles, which constitute the scattered transmission [Figure 3.51 (a)].

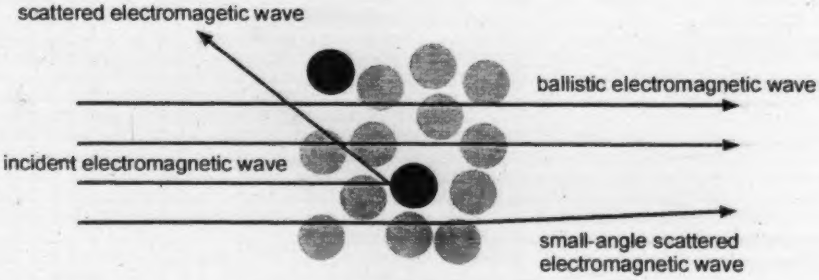
scattered electromagetic wave
ballistic electromagnetic wave
incident electromagnetic wave
small-angle scattered electromagnetic wave

low *VF*

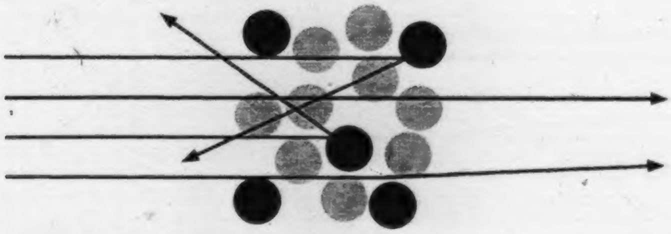

intermediate *VF*

Figure 3.51. Ray diagram depicting the interaction of an incident THz electromagnetic wave with the metallic/dielectric ensemble for low *VF* and intermediate *VF*. At low *VF*, the transmission consists of ballistic and small-angle scattered electromagnetic waves. As the metallic volume fraction increases, a greater portion of the incident electromagnetic wave is scattered. For high *VF*, the incident wave excites particle plasmons, which cannot be accurately represented in the ray diagrams.

For intermediate *VF* (15.0 % < *VF* < 63.2 %), the metallic particles are separated, on average, by 128 μm < $s_{ave,opt}$ < 356 μm, corresponding to an average physical separation between 53 μm < s_{ave} < 149 μm. In this regime, there are a comparable number of metallic and dielectric particles, since the spacing between metallic particles contains, on average, approximately one dielectric particle. Hence, electromagnetic wave interactions with both the metallic and dielectric constituents must be considered. As shown in Figure 3.50 (b), the effective refractive index shows two trends for intermediate *VF*: the effective refractive index peaks at 0.10 for $s_{ave,opt}$ ~ 200 μm and subsequently decreases to 0.01 as $s_{ave,opt}$ approaches 128 μm. The former is attributed to augmented scattering by the metallic and dielectric inclusions, while the latter is caused by the onset of particle plasmon coupling. As the volume fraction of opaque metallic particles increases beyond $VF = 15.0$ %, the amount of ballistic electromagnetic waves propagated directly through the dielectric particles decreases. A greater portion of the transmitted pulse is mediated by scattered electromagnetic waves that must propagate in the gaps between the opaque metallic particles. This results in an increased propagation path-length for the transmitted electromagnetic pulse, which manifest as an increase in the effective refractive index. At $s_{ave,opt} \sim 200 \pm 10$ μm, the effective refractive index begins to decrease, marking the onset of near-field particle plasmon interaction between metallic particles. It is interesting to note that $s_{ave,opt} \sim 200 \pm 10$ μm corresponds to a physical separation distance between particles of $s_{ave} \sim 80$ μm, which is slightly *less than the diameter of one dielectric particle*. At this value of $s_{ave,opt}$, near-field interaction between metallic particles, occurring over subwavelength extents, begins to governs the propagation of electromagnetic energy across the ensemble. As $s_{ave,opt}$ decreases from 200 μm to 53 μm, there is a further decrease in the index of the ensemble from ~ 0.10 ± 0.02 to ~ 0.01 ± 0.02, indicating particle plasmon-mediated transmission.

For high VF (81.9 % < VF < 100 %), the effective refractive index decreases from 0.01 to −0.10 due to particle plasmon coupling. In this range, the metallic particles are separated by 19 μm < $s_{ave,opt}$ < 68 μm, corresponding to an average physical separation ranging 19 μm < s_{ave} < 33 μm. The average spacing between metallic particles is significantly less than the diameter of the dielectric particles. The absence of straight-line trajectories through dielectric particles precludes ballistic electromagnetic wave propagation, and nearly all the transmission is mediated by near-field particle plasmon interaction between metallic particles.

3.12 Conclusion

In conclusion, the findings of this Chapter shed insight into the nature of THz electromagnetic wave interaction with single subwavelength metallic microparticles, ensembles of subwavelength metallic microparticles, and mixtures of subwavelength dielectric and metallic microparticles. A THz electromagnetic wave incident on a single subwavelength metallic particle is shown to excite non-resonant localized particle plasmons, consisting of oscillations of the conduction electrons near the surface of a subwavelength metallic structure coupled to an electromagnetic field confined to the near-field region of the particle surface. In an ensemble of subwavelength metallic particles, electromagnetic coupling between the particles plays an important role in the ensemble's effective electromagnetic properties. Surprisingly, it is shown that a dense ensemble of subwavelength sized metallic particles can show enhanced, polarized THz electric field transmission. Finite difference time-domain calculations reveal that the origin of the enhanced transmission is due to near-field particle plasmon coupling between nearest neighbor particles. The influences of particle size, particle shape, and metal conductivity on the plasmonic-enhanced THz electric field transmission are explored. In further investigations, it is shown that collections of metallic particles that have been coated with nano-layers of a different metal show strong attenuation of the THz electric field transmission due to non-radiative particle plasmon decay at the interface between the two dissimilar metals. This phenomenon is applied to a unique non-invasive method to probe the sub-surface charge motion of THz particle plasmons excited on metallic subwavelength particles. Furthermore, this Chapter explores an entirely novel class of amorphous THz metamaterial consisting of random ensembles of subwavelength sized dielectric and metallic constituents. It is shown that the effective permittivity of the amorphous metamaterial exhibits a nonlinear dependence on the relative volume fraction of the constituents. This behaviour is resolved by considering non-resonant particle plasmon interactions between metallic constituents.

Chapter 3 References

[1] U. Kreibig and M. Vollmer, *Optical Properties of Metal Clusters*, vol. 25. Berlin: Springer-Verlag, 1995.

[2] S. A. Maier, *Plasmonics: Fundamentals and Applications*. New York: Springer, 2007.

[3] C. Sonnichsen, "Plasmons in metal nanostructures," in *Physics*, vol. Doctorate of Philoshophy. Munich: University of Munich, 2001, pp. 134.

[4] J. Gersten and A. Nitzan, "Electromagnetic theory of enhanced Raman scattering by molecules adsorbed on rough surfaces," *Journal of Chemical Physics*, vol. 73, pp. 3023-3037, 1980.

[5] J. Grand, M. Lamy de la Chapelle, J.-L. Bijeon, P.-M. Adam, A. Vial, and P. Royer, "Role of localized surface plasmons in surface-enhanced Raman scattering of shape-controlled metallic particle sin regular arrays," *Physical Review B*, vol. 72, pp. 033407, 2005.

[6] P. F. Liao and A. Wokaun, "Lightning rod effect in surface enhanced Raman scattering," *Journal of Chemical Physics*, vol. 76, pp. 751-752, 1981.

[7] R. W. Boyd, *Nonlinear Optics*, 2nd ed. San Diego, CA: Academic Press, 2003.

[8] J. L. Coutaz, M. Neviere, E. Pic, and R. Reinisch, "Experimental study of surface-enhanced second-harmonic generation on silver gratings," *Physical Review B*, vol. 32, pp. 2227-2232, 1985.

[9] H. J. Simon, D. E. Mitchell, and J. G. Watson, "Optical second-harmonic generation with surface plasmons in silver films," *Physical Review Letters*, vol. 33, pp. 1531-1534, 1974.

[10] K. Kneipp, H. Kneipp, I. Itzkan, R. R. Dasari, and M. S. Feld, "Surface enhanced Raman scattering and biophysics," *Journal of Physics: Condensed Matter*, vol. 14, pp. R597-R624, 2002.

[11] S. M. Nie and S. R. Emery, "Probing single molecules and single nanoparticles by surface-enhanced Raman scattering," *Science*, vol. 275, pp. 1102, 1997.

[12] T. Klar, M. Perner, S. Grosse, G. von Plessen, W. Spirkl, and J. Feldmann, "Surface-plasmon resonances in single metallic nanoparticles," *Physical Review Letters*, vol. 80, pp. 4249-4252, 1998.

[13] W. L. Barnes, A. Dereux, and T. W. Ebbesen, "Surface plasmon subwavelength optics," *Nature*, vol. 424, pp. 824-830, 2003.

[14] M. Quinten, A. Leitner, J. R. Krenn, and F. R. Aussenegg, "Electromagnetic energy transport via linear chains of silver nanoparticles," *Optics Letters*, vol. 23, pp. 1331-1333, 1998.

[15] S. A. Maier, P. G. Kik, H. A. Atwater, S. Meltzer, E. Harel, B. E. Koel, and A. A. G. Requicha, "Local detection of electromagnetic energy transport below the diffraction limit in metal nanoparticle plasmon waveguides," *Nature Materials*, vol. 2, pp. 229-232, 2003.

[16] G. D. Dice, S. Mujumdar, and A. Y. Elezzabi, "Plasmonically enhanced diffusive and subdiffusive metal nanoparticle-dye random laser," *Applied Physics Letters*, vol. 86, pp. 131105, 2005.

[17] J. A. Stratton, *Electromagnetic Theory*. New York: McGraw-Hill, 1941.

[18] C. A. Balanis, *Advanced Engineering Electromagnetics*. New York: John Wiley, 1989.

[19] D. H. Auston, K. P. Cheung, and P. R. Smith, "Picosecond Photoconducting Hertzian Dipoles," *Applied Physics Letters*, vol. 45, pp. 284-286, 1984.

[20] C. F. Bohren and D. R. Huffman, *Absorption and Scattering of Light by Small Particles*. New York: John Wiley & Sons, 1983.

[21] V. M. Shalaev, "Electromagnetic Properties of Small-Particle Composites," *Physics Reports*, vol. 272, pp. 61-137, 1996.

[22] M. Weber, "Handbook of Optical Materials." New York: tle></tit, 2003.

[23] J. F. Holzman, F. E. Vermeulen, S. E. Irvine, and A. Y. Elezzabi, "Free-space detection of terahertz radiation using crystalline and polycrystalline ZnSe electro-optic sensors," *Applied Physics Letters*, vol. 81, pp. 2294-2296, 2002.

[24] A. A. Maradudin, R. F. Wallis, and G. I. Stegeman, "Surface Polariton Reflection and Transmission at a Barrier," *Solid State Communications*, vol. 46, pp. 481-485, 1983.

[25] K. J. Chau, G. D. Dice, and A. Y. Elezzabi, "Coherent Plasmonic Enhanced Terahertz Transmission through Random Metallic Media," *Physical Review Letters*, vol. 94, pp. 173904, 2005.

[26] M. Futamata, Y. Maruyama, and M. Ishikawa, "Local electric field and scattering cross section of Ag nanoparticles under surface plasmon resonance by finite difference time domain method," *Journal of Physical Chemistry B*, vol. 107, pp. 7607-7617, 2003.

[27] K. L. Kelly, E. Coronado, L. L. Zhao, and G. C. Schatz, "The Optical Properties of Metal Nanoparticles: The Influence of Size, Shape, and Dielectric Environment," *Journal of Physical Chemistry B*, vol. 107, pp. 668-677, 2003.

[28] J. P. Kottman, O. J. F. Martin, D. R. Smith, and S. Schultz, "Spectral response of plasmon resonant nanoparticles with a non-regular shape," *Optics Express*, vol. 6, pp. 213-219, 2000.

[29] M. A. Ordal, L. L. Long, R. J. Bell, S. E. Bell, R. R. Bell, R. W. Alexander, and C. A. Ward, "Optical-properties of the metals Al, Co, Cu, Au, Fe, Pb, Ni, Pd, Pt, Ag, Ti, and W in the infrared and far infrared," *Applied Optics*, vol. 22, pp. 1099-1119, 1983.

[30] F. Miyamaru and M. Hangyo, "Anomalous terahertz transmission through double-layer metal hole arrays by coupling of surface plasmon polaritons," *Physical Review B*, vol. 71, pp. 165408, 2005.

[31] D. X. Qu and D. Grischkowsky, "Observation of a new type of THz resonance of surface plasmons propagating on metal-film hole arrays," *Physical Review Letters*, vol. 93, pp. 196804, 2004.

[32] D. X. Qu, D. Grischkowsky, and W. L. Zhang, "Terahertz transmission properties of thin, subwavelength metallic hole arrays," *Optics Letters*, vol. 29, pp. 896-898, 2004.

[33] J. Saxler, J. G. Rivas, C. Janke, H. P. M. Pellemans, P. H. Bolivar, and H. Kurz, "Time-domain measurements of surface plasmon polaritons in the terahertz frequency range," *Physical Review B*, vol. 69, pp. 155427, 2004.

[34] K. J. Chau and A. Y. Elezzabi, "Terahertz transmission through ensembles of subwavelength-size metallic particles," *Physical Review B*, vol. 72, pp. 075110, 2005.

[35] M. Gaudry, J. Lerme, E. Cottancin, M. Pellarin, J. L. Vialle, M. Broyer, B. Prevel, M. Treilleux, and P. Melinon, "Optical properties of (AuxAg1-x)(n) clusters embedded in alumina: Evolution with size and stoichiometry," *Physical Review B*, vol. 64, pp. 085407, 2001.

[36] S. Link, Z. L. Wang, and M. A. El-Sayed, "Alloy formation of gold-silver nanoparticles and the dependence of the plasmon absorption on their composition," *Journal of Physical Chemistry B*, vol. 103, pp. 3529-3533, 1999.

[37] H. Z. Shi, L. D. Zhang, and W. P. Cai, "Composition modulation of optical absorption in AgxAu1-x alloy nanocrystals in situ formed within pores of mesoporous silica," *Journal of Applied Physics*, vol. 87, pp. 1572-1574, 2000.

[38] F. Hubenthal, T. Ziegler, C. Hendrich, M. Alschinger, and F. Trager, "Tuning the surface plasmon resonance by preparation of gold-core/silver-shell and alloy nanoparticles," *European Physical Journal D*, vol. 34, pp. 165-168, 2005.

[39] M. Moskovits, I. Srnova-Sloufova, and B. Vickova, "Bimetallic Ag-Au nanoparticles: Extracting meaningful optical constants from the surface-plasmon extinction spectrum," *Journal of Chemical Physics* vol. 116, pp. 10435-10446, 2002.

[40] P. Mulvaney, "Surface plasmon spectroscopy of nanosized metal particles," *Langmuir*, vol. 12, pp. 788-800, 1996.

[41] B. Rodriguez-Gonzalez, A. Burrows, M. Watanabe, C. J. Kiely, and L. M. L. Marzan, "Multishell bimetallic AuAg nanoparticles: synthesis, structure and optical properties," *Journal of Materials Chemistry*, vol. 15, pp. 1755-1759, 2005.

[42] R. K. Roy, S. K. Mandal, and A. K. Pal, "Effect of interfacial alloying on the surface plasmon resonance of nanocrystalline Au-Ag multilayer thin films," *European Physical Journal B*, vol. 33, pp. 109-114, 2003.

[43] N. W. Ashcroft and N. D. Mermim, *Solid State Physics*. Philadelphia: Saunders College, 1976.

[44] A. J. Bennett and C. B. Duke, "Self-consistent-field model of bimetallic interfaces. 1. Dipole effects," *Physical Review B*, vol. 160, pp. 541, 1967.

[45] A. J. Bennett and C. B. Duke, "Metallic interfaces. 2. Influence of exchange-correlation and lattice potentials," *Physical Review B*, vol. 162, pp. 578, 1967.

[46] C. Kittel, *Introduction to Solid State Physics*, 7th ed. New York: John Wiley & Sons, 1996.

[47] J. B. Pendry, A. J. Holden, W. J. Stewart, and I. Youngs, "Extremely low frequency plasmons in metallic nanostructures," *Physical Review Letters*, vol. 76, pp. 4773-4776, 1996.

[48] D. Wu, N. Fang, C. Sun, X. Zhang, W. J. Padilla, D. N. Basov, D. R. Smith, and S. Schultz, "Terahertz plasmonic high pass filter," *Applied Physics Letters*, vol. 83, pp. 201-203, 2003.

[49] G. Landry, Y. Dong, J. Du, X. Xiang, and J. Q. Xiao, "Interfacial capacitance effects in magnetic tunneling junctions," *Applied Physics Letters*, vol. 78, pp. 501-503, 2001.

[50] D. M. Newns, "Dielectric response of a semi-infinite degenerate electron gas," *Physical Review B*, vol. 1, pp. 3304, 1970.

[51] M. A. Ordal, R. J. Bell, R. W. Alexander, L. L. Long, and M. R. Querry, "Optical-properties of 14 metals in the infrared and far-infrared - Al, Co, Cu, Au, Fe, Pb, Mo, Ni, Pd, Pt, Ag, Ti, V, and W," *Applied Optics*, vol. 24, pp. 4493-4499, 1985.

[52] R. G. Chambers, "Anomalous skin effect in metals," *Nature*, vol. 165, pp. 239-240, 1950.

[53] D. F. Sievenpiper, M. E. Sickmiller, and E. Yablonovitch, "3D Wire Mesh Photonic Crystal," *Physical Review Letters*, vol. 76, pp. 2480-2483, 1996.

[54] T. J. Yen, W. J. Padilla, N. Fang, D. C. Vier, D. R. Smith, J. B. Pendry, D. N. Basov, and X. Zhang, "Terahertz Magnetic Response from Artificial Materials," *Science*, vol. 303, pp. 1494-1496, 2004.

[55] R. A. Shelby, D. R. Smith, and S. Schultz, "Experimental verification of a negative index of refraction," *Science*, vol. 292, pp. 77-79, 2001.

Chapter 4:

Terahertz Time-Domain Spectroscopy of Phase Transition Phenomena in Metallic Particles

4.1 Background

With the recent emergence of THz time-domain spectroscopy (TDS) as a powerful tool for investigating far-infrared optical properties of materials, THz TDS continues to find novel applicability in a wide range of areas. THz TDS is advantageous in comparison to intensity-based far-infrared spectroscopic techniques since THz TDS accesses both the electric field amplitude and its phase; thus it reveals richer information on the optical properties of materials than intensity-based measurements. Several investigations [1-4] have utilized THz electric field transmission measurements to obtain the optical properties of transparent media such as dielectrics and superconductors Alternatively, reflection-based THz time-domain spectroscopy has been applied to characterize a variety of semiconductors such as InSb [5] and highly doped Si [6, 7]. Extending these techniques to perform spectroscopic investigations of highly opaque media such as metal remains a challenge. The relative permittivity of bulk metals at a frequency ω is given approximately by $\varepsilon_{metal}(\omega) = 1 - \omega_p^2/(i\Gamma\omega - \omega^2)$. Since $\mathrm{Re}[\varepsilon_{metal}(\omega)] \sim -10^5$ for all metals at THz frequencies, bulk metals are highly reflective and cannot be probed using transmission- and reflection- based THz time-domain spectroscopy arrangements.

A phenomenon that can be exploited to overcome the inherent metallic opacity is to alter the subwavelength scale metallic microstructure to modify its effective THz electromagnetic transparency. In such mesoscopic metallic media, the effective permittivity becomes a function of both the intrinsic metallic properties and the extrinsic microstructure. In particular, when the heterogeneity scale is much less than or comparable to the THz radiation wavelength, the material can *appear* as an effective dielectric and exhibit significant on-axis THz transmission. Since THz electromagnetic interaction with a heterogeneous metallic medium is a surface-mediated phenomena resulting from the induction of induced surface charges, the amplitude, the arrival delay, the phase, and the polarization of the transmitted electric field are highly sensitive to the particle's size, conductivity, and shape. This transmission sensitivity facilitates transmission-based THz time-domain spectroscopy as a broadband spectroscopic probe of metallic media.

4.2 Terahertz Spectroscopic Investigation of Metallic Phase Transition

Terahertz time-domain spectroscopy is applied to study intrinsic, temperature-dependent phase transitions in a metallic particle ensemble. A phase transitions is defined as a transformation of a thermodynamic system from one phase to another. A distinguishing feature of phase transitions is an abrupt change in one or more physical properties of the material with a small change in a thermodynamic quantity such as temperature. For instance, when the specific energy of a metal is raised to the latent heat of fusion, the metal changes from the solid phase to the liquid phase. The microscopic mechanism for melting can be understood by considering the motions of ions in the solid and liquid states. Prior to melting, the ions that constitute the metal remain relatively fixed in the vicinity of their equilibrium positions. As the metal is heated above the melting temperature, the ions acquire enough energy leave their equilibrium positions and wander relatively large distances, resulting in a liquid state. This microscopic picture is depicted in Figure 4.1. Melting of solid metal is a typical example of a first order phase transition. First order phase transitions are those in which the substance releases or absorbs heat energy during the phase change. Since the energy cannot be absorbed or released instantaneously by the substance at the phase transition temperature, first order phase transitions are characterized by a mixed phase regime in which different phases of the medium coexist.

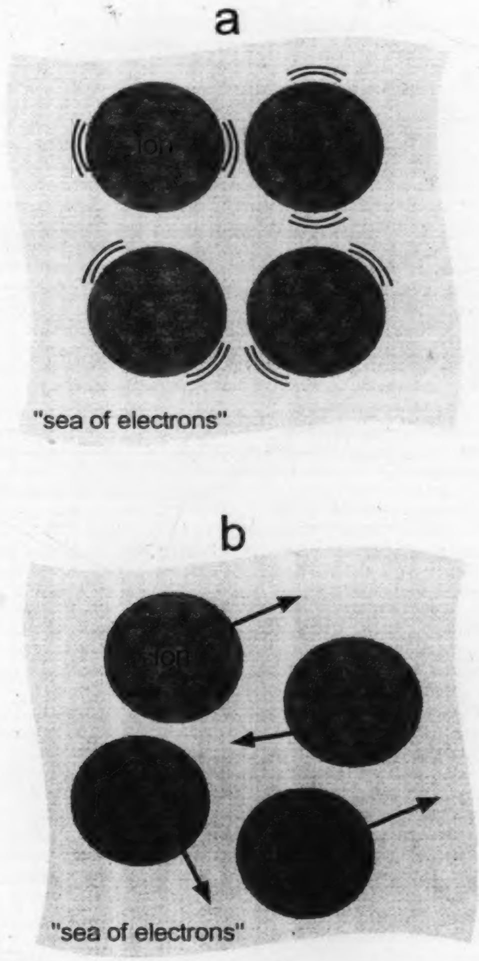

Figure 4.1. Illustration of the ionic motion when a metal is (a) below the melting temperature and (b) above the melting temperature.

To date, metallic phase transitions are widely investigated using calorimetry techniques, such as AC-calorimetry [8]. A disadvantage of this method is that an invasive physical contact is required to accurately measure heat flow through the metallic sample. To overcome this constraint, several groups [9-11] have employed the photo-acoustic effect to non-invasively probe metallic phase transformations. In such experiments, phase transition modulates the acoustic signal generated at the surface of a sample when a surrounding ambient gas has been heated by a periodically modulated light beam. However, such mechanism requires a gas that is highly absorbing to the illuminating light, and interpretation of the acoustic signal is restricted by the complex nature of heat transfer between the solid metallic sample and surrounding gas [11]. Here, THz time-domain spectroscopy is applied as a non-invasive, direct probe of phase and structural transitions in metallic media. The results of this Chapter have been published in *Applied Physics Letters*, vol. 90, 041920 (2007).

Gallium is a unique metallic element existing at room temperature as solid α-Ga consisting of a mixture of stable molecular and metallic phases. Solid α-Ga is a complex phase described as a metallic molecular crystal with strong Ga_2 bonds and weaker intermolecular forces, whereas liquid Ga is more free-electron like [12]. At a frequency of 1.55 μm, the permittivity of liquid Ga has been estimated to be approximately 7 times larger than the permittivity of α-Ga [13]. Gallium possesses one of the lowest melting points of all metals (T_m = 29.8 C°), which provides an ideal platform to study metallic solid-liquid phase transformation behaviour via THz time-domain spectroscopy. Gallium microparticles are prepared by cooling bulk 99.99% Ga pellets to 77 K and mechanically grinding the Ga pellets to achieve a powder having an average particle size of 109 ± 10 μm and a packing fraction of ~ 0.4 ± 0.1. In order to probe the phase transition of the Ga microparticles, a THz TDS setup is employed similar to that described in Chapter 2. The

THz radiation is focused onto a polystyrene sample cell housing an $L = 2.3$ mm thick collection of the random Ga microparticles to a spot size of ~ 1 mm^2. To examine the temperature-dependent THz transmissivity of the particles, the Ga particles are homogeneously heated, at a rate of 0.08 C°/min, from room temperature up to a temperature, T, of 38.2 C° (> T_m). Because the time over which the temperature increases is much longer than the heat diffusion time across the thin sample (< 1 s), it is ensured that the sample temperature is at equilibrium during the transmission measurements. The microparticles ensemble temperature is monitored (within ± 0.1 C°) via a thermocouple inserted into the particle collection adjacent to the THz beam probing spot. During the measurements, both the beam spot size and location are kept fixed, thus ensuring that the THz radiation interacts with the same random realization of the particle ensemble throughout the temperature variation.

Melting is a thermal effect, and the temporal duration over which melting occurs is determined by the time over which heat can diffuse and equilibrate throughout the sample. The experiments are carefully designed and performed at an extremely slow heating rate (0.08 C°/min) in order to ensure that equilibrium conditions are established through the measurements. To quantify this condition, the heat diffusion times are estimated for both Ga metal (a lower bound) and air (an upper bound) through a distance of 2.3 mm corresponding to the sample thickness. Gallium has a thermal conductivity, $H_{th} = 40$ Wm^{-1}K^{-1}, a density, $u = 5.91$ g/cm^3, and a heat capacity, $C = 25.86$ J mol^{-1}K^{-1}. For air, $H_{th} = 0.02$ Wm^{-1}K^{-1}, $u = 1251$ g/m^3 and $C = 29.12$ J mol^{-1}K^{-1}. From these quantities, the thermal diffusivity, D_{th}, is given by

$$D_{th} = H_{th} u^{-1} C^{-1} \qquad (4.2.1).$$

Based on Equation 4.2.1, the thermal diffusivity of Ga is 19 × 10^{-6} m^2/s . Likewise, the thermal diffusivity of air is 9 × 10^{-6} m^2/s. The characteristic diffusion time over a distance L is estimated by $t_{diff} = L^2/D_{th}$, giving $t_{diff} = 0.6$ s and $t_{diff} = 0.28$ s assuming that the sample is completely filled with air and gallium, respectively. The sample used in the experiments is a mixture of air and gallium, and the characteristic heat diffusion time for the sample will lie between those bounds. To obtain an upper bound of time lagged thermal effects, assume that it requires 0.6 s for heat to diffuse from one end of the sample to another. Over this time interval, a time-lagged temperature increase of 0.08 C°/min × 0.6 s = 0.0008 C° (<< error in the temperature measurement) may develop across the sample. Since the time over which the temperature of the sample increases is much slower than the heat diffusion time across the sample thickness, it can be confidently concluded that the samples have reached thermal equilibrium as the THz TDS measurements are taken.

Figure 4.2 (a) illustrates the time-domain THz electric field waveforms, $E_{tr}(t)$, transmitted through Ga particle collections measured at various temperatures. Notably, for temperatures below the melting point ($T < T_m$), the bipolar pulses transmitted through the particle collection all have an initial peak at a time $t = 3.1$ ps. The fact that the arrival delay, the amplitude, and the pulse shape of the transmitted pulses do not change throughout the temperature range 22.4 C° < T < 29.7 C° suggests an absence of phase transformation or any changes to the Ga metallic properties. However, once the temperature reaches the melting temperature of 29.9 C°, a temporal advancement (or early arrival) of the pulse peak by 0.3 ps provides evidence of the onset of a significant transformation in the electronic properties of the Ga particles. Although the pulse corresponding to T = T_m = 29.9 C° is temporally advanced, interestingly, the pulse shape remains unaltered at T_m. Further heating of the Ga microparticles from 29.9 C° to 38.2 C° induces striking pulse shape transformation where the pulse is attenuated and broadened in time.

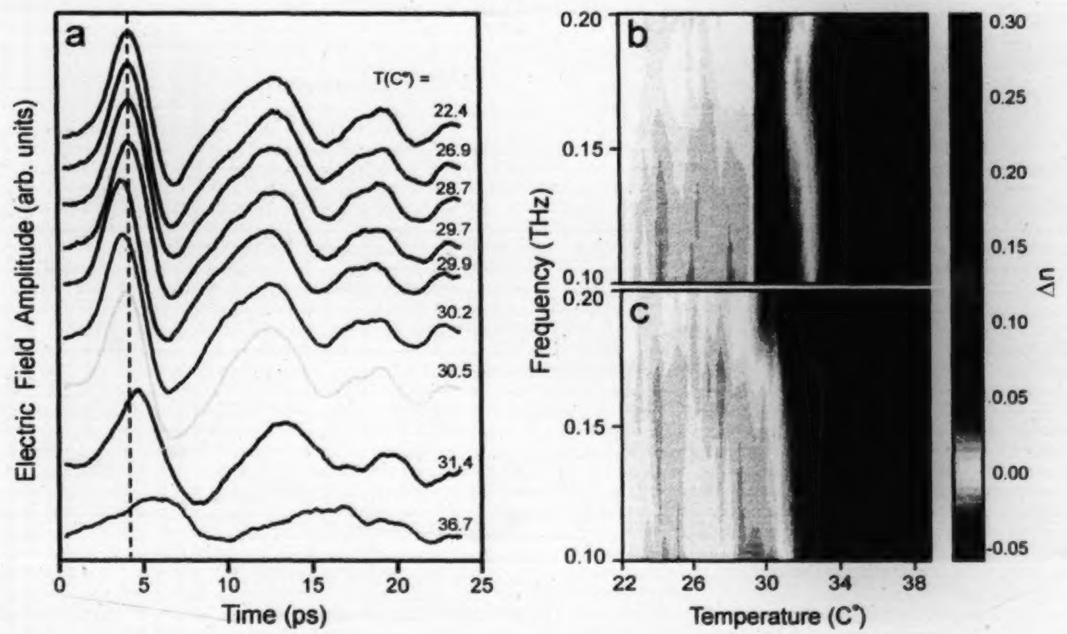

Figure 4.2. (a) Experimental time-domain signals of THz pulses transmitted through 2.3 mm thick random Ga microparticle ensembles measured at various temperatures. The dashed line indicates the arrival time of the peak of the THz pulse. Shown in (b) are the effective real refractive index change and (c) effective imaginary refractive index change versus temperature and frequency. The refractive indices are measured relative to the reference pulse transmitted through the sample at 21.2 C°.

Accompanying the temporal pulse shape trend with increasing temperature is a marked progressive delay and attenuation of E_{tr} (t). The pulse temporal shape, delay and amplitude trends for T > T_m suggest conglomeration between adjacent, near-touching Ga particles. Because the THz transmission through the particle collections is mediated by nearest neighbor coupling between particles, conglomeration of the nearest neighbor particles quenches radiation propagation mechanism. As the particles coalesce, the particles become larger and begin to exhibit metallic bulk-like electromagnetic properties, resulting in reduced transmission amplitude. Similarly, particle conglomeration results in a higher metal filling fraction, which increases the effective index of the particle ensemble and manifests as a temporal delay of the transmitted pulse.

To further explore the temperature-dependent evolution of the waveforms, the frequency-dependent relative effective refractive index of the transmitted THz electric fields is analyzed. The effective real refractive index change, $\Delta n_r = [\Phi(\omega) - \Phi_{ref}(\omega)] / kL$, and the effective imaginary refractive index change, $\Delta n_i = \log[E(\omega)/E_{ref}(\omega)] / kL$, are obtained as a function of temperature, T. In these relations, $\Phi(\omega)$, $\Phi_{ref}(\omega)$, $E(\omega)$, and $E_{ref}(\omega)$ are the phase of the transmitted pulse, the phase of the reference pulse transmitted through the sample at T_{ref} = 21.2 C°, the amplitude of the transmitted pulse, and the amplitude of the reference pulse, respectively. Shown in Figure 4.2 (b) and 4.2 (c) are Δn_r and Δn_i versus T over a frequency range between 0.1 THz and 0.2 THz (corresponding to the bandwidth of the transmitted pulse). As shown in the plot, there is negligible refractive index change between the temperature range 21.2 C° < T < T_m. At T_m = 29.9 C°, Δn_r decreases abruptly. As shown in Figure 4.2 (b), this sharp discontinuity in Δn_r precisely at T_m is consistent over the entire transmission bandwidth. The abrupt, frequency-independent change in Δn_r suggests that the *intrinsic* electronic properties of Ga have been altered at T_m and is strongly indicative of metallic phase transformation. Interestingly, the onset of phase transition eludes detection in Δn_i, as Δn_i remains approximately zero up to T ~ 30.5 C° [Figure 4.2 (c)]. With further increase in the sample temperature above 30.5 C°, both Δn_r and Δn_i show large increases over the transmission bandwidth as a function of T. These significant increases in the complex effective refractive indices of the ensemble show that the particle ensemble becomes less transparent to the THz pulse for $T > T_m$ due to coalescing of nearest neighbor particles. The strikingly different effective refractive index features for the range $T < T_m$, $T \approx T_m$, and $T > 30.5$ C° highlight three distinctive regimes where 1) the particles have not melted (constant Δn_r and Δn_i), 2) the particles have melted but remain granular (discontinuity in Δn_r, but constant Δn_i), and 3) the particles have melted and are coalesced (large increases in both Δn_r and Δn_i).

The temperature-dependent Δn_r and Δn_i trends at two frequencies, $\omega_1 = 0.1$ THz and $\omega_2 = 0.2$ THz are charted in Figure 4.3 (a) and 4.3 (b). As shown in Figure 4.3 (a), for 21.2 C° < T < 29.9 C°, Δn_r is nearly zero. Upon reaching T_m, the real part of the relative effective index exhibits a notably large, discontinuous jump of −0.06, indicative of an abrupt change in the intrinsic properties of Ga associated with metallic solid-liquid phase transformation. Above the melting temperature, Δn_r is strongly affected by conglomeration of the particles, which changes the underlying *extrinsic* microstructure of the ensemble. This extrinsic effect influences the effective index of the ensemble in a fundamentally different way than the intrinsic metallic phase transition at T_m. For $T > T_m$, Δn_r increases from −0.06 to ~0.3 between 29.9 C° and 33.0 C° and beyond T > 33.0 C°, is constant at ~0.3. Particle conglomeration occurring at $T > T_m$ increases the effective real refractive index of the ensemble, causing the arrival delay of the transmitted pulses. Δn_i exhibits similar overall trends as Δn_r. Below the melting temperature, Δn_i shows negligible temperature dependence and is approximately zero. As shown in Figure 4.3 (b), $\Delta n_i(\omega_2)$ increases linearly for $T > T_m$ and saturates at 0.2 for T > 33.0 C°.

Such an increase in the imaginary effective refractive index reveals increased absorption or scattering losses within the ensemble due to particle melting and subsequent coalescing. In contrast to $\Delta n_i(\omega_2)$, $\Delta n_i(\omega_1)$ does not significantly increase from zero until the temperature exceeds 30.5 C° > T_m. The slightly different trends observed for $\Delta n_i(\omega_1)$ and $\Delta n_i(\omega_2)$ suggest that the higher frequency components of the pulse are more sensitive to particle conglomeration than the lower frequency components. Overall, the real and imaginary parts of the complex effective index of the sample exhibit high sensitivity to the solid-liquid phase transition of the Ga microparticles and subsequent melting and coalescing dynamics beyond T_m.

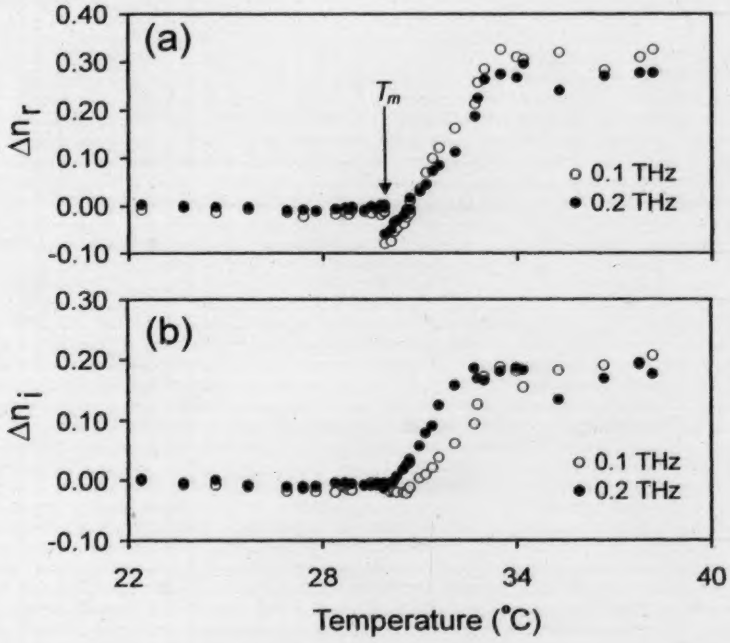

Figure 4.3. Experimental effective (a) real refractive index change and (b) imaginary refractive index change for 0.1 THz (empty circles) and 0.2 THz (filled circles) at various temperatures. Striking discontinuity in the effective real refractive index occurs at the Ga melting temperature, 29.8 C°.

The refractive index behaviour for T > T_m shows interesting particle conglomeration behaviour of the Ga particles, where the microparticles begin to form interconnected networks. The experimental results show that coalescing does not occur concurrently with particle melting. To quantify the temperature where the particles begin to coalesce, the correlation function, $C(\tau) = < E_{tr}(t+\tau_1)\ E_{ref}(t) >$ is calculated, where $E_{tr}(t+\tau_1)$ is the sample pulse (at a given temperature T) shifted by a time τ_1 and $E_{ref}(t)$ is the reference pulse transmitted at reference temperature T_{ref}. It is noted that referencing the correlation function to the transmitted signal at T_{ref} cancels out the effect of setup's inherent spectral response since the spectral response of the system is fixed throughout the temperature variation. Because the only experimental variable is the sample temperature, changes in $C(\tau)$ as a function of T arise directly from temperature-dependent changes in the transmissivity of the Ga sample. As highlighted in the plot of the maximum correlation amplitude versus T [Figure 4.4 (b)], the transmitted pulse remains highly correlated even for T = 30.5 C° > T_m. Thus, at temperatures exceeding the melting transition, the extrinsic microstructure of the particle ensemble has not changed. However, at a coalescing temperature, T_c = 30.5 C°, there is a significant decrease in $C(\tau)$, marking the onset of particle conglomeration and transmission quenching. Because the particles must overcome their surface energy prior to liquefying, T_c is slightly higher than the bulk melting temperature. As shown in Figure 4.4 (b), $C(\tau)$ decreases to 0.35 at 33.0 C°, and for T > 33.0 C°, the maximum correlation amplitude saturates and remains fixed. The experimental results reveal a narrow temperature range, $T_m < T < T_c$, where the individual particles have melted, yet the nearest neighbor particles do not conglomerate.

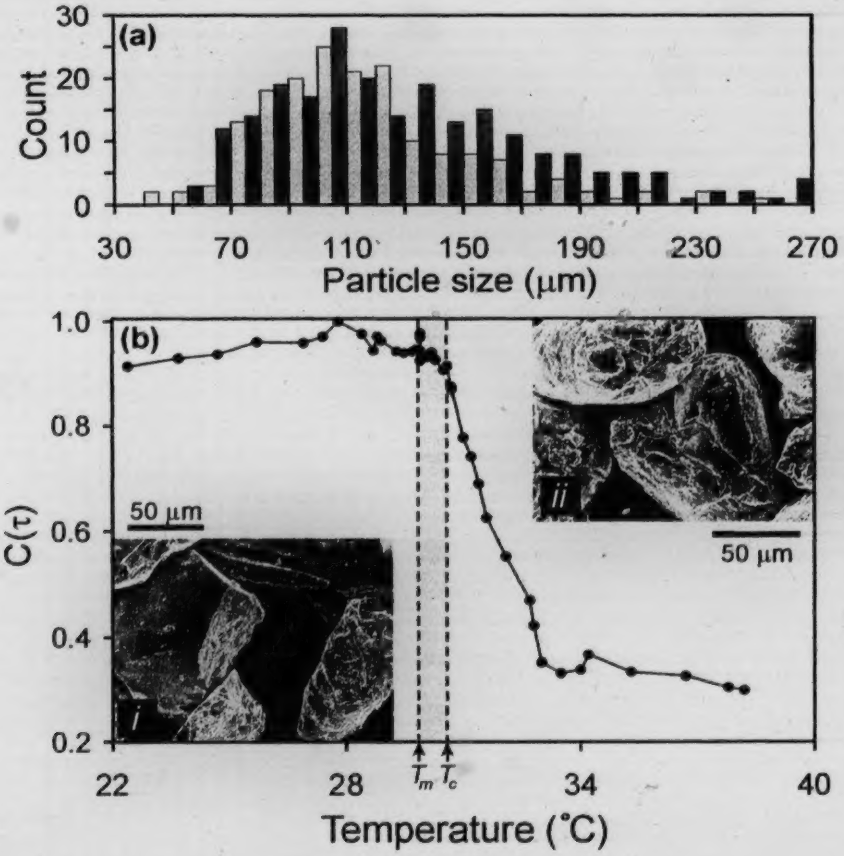

Figure 4.4. (a) Size distribution of the Ga microparticles before melting (light bars) and after melting (dark bars). (b) shows the maximum correlation amplitude of transmitted pulses at various temperatures relative to the reference pulse at 21.2 C°. Insets are scanning electron microscope images of (i) the Ga microparticles prior to the heating cycle and (ii) the solidified particles after the heating cycle.

The Ga particle collection undergoes significant structural transformation over the heating cycle. After heating the particles above T_m and cooling back to room temperature, the nearest neighbor particles have coalesced at small regions conjoining the particles, but overall, the ensemble retains a granular appearance and structure with no significant decrease in the total volume. The individual particles shapes are slightly distorted by the heating. As shown in the scanning electron microscope images in the insets of Figure 4.4 (b), the particles prior to heating are characterized by sharp edges and flat faces. After cycling the temperature, the particles are rounded and have a rougher surface. Although heating induces shape change in the particles and coalescing between nearest neighbour particles, the overall size distribution of the ensemble after heating is not significantly affected. As shown in Figure 4.4 (a), the size distribution of the particles is nearly identical before and after heating. This further confirms that over the heating cycle, the particles do not fully conglomerate to form particles with augmented sizes. Rather, nearest neighbour particles join at small sections of the particles that are in direct contact with each other, as shown in Figure 4.5.

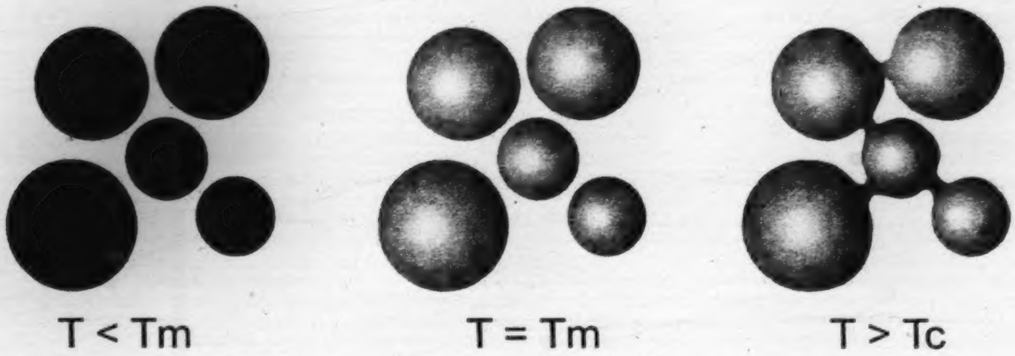

Figure 4.5. Ga particle ensemble below the melting temperature, at the melting temperature, and above the coalescing temperature.

4.3 Conclusion

In conclusion, THz TDS has been employed to study the solid-liquid phase transition of Ga. While THz spectroscopic measurements of metals are not typically achievable with bulk metallic samples, the enhanced THz transmission through metallic microparticles is exploited to probe the intrinsic electronic properties of Ga as a function of temperature. It is shown that the Ga microparticles individually melt at T_m, but do not coalesce until $T_c > T_m$. This work represents the first non-invasive spectroscopic investigation of melting dynamics of microparticles and provides a novel technique for the study of phase transitions in metallic powders.

Chapter 4 References

[1] D. Grischkowsky, S. Keiding, M. v. Exter, and C. Fattinger, "Far-infrared time-domain spectroscopy with terahertz beams of dielectrics and semiconductors," *Journal of the Optical Society of America B*, vol. 7, pp. 2006-2015, 1990.

[2] M. Khazan, I. Wilke, and C. Stevens, "Surface impedance of T1-2212 thin films at THz-frequencies," *IEEE Transactions on Applied Superconductivity*, vol. 11, pp. 3537-3540, 2001.

[3] D. M. Mittleman, R. H. Jacobsen, R. Neelamani, R. G. Baraniuk, and M. C. Nuss, "Gas sensing using terahertz time-domain spectroscopy," *Applied Physics B*, vol. 67, pp. 379-390, 1998.

[4] S. Mujumdar, K. J. Chau, and A. Y. Elezzabi, "Experimental and numerical investigation of terahertz transmission through strongly scattering sub-wavelength size spheres," *Applied Physics Letters*, vol. 85, pp. 6284-6286, 2004.

[5] S. C. Howells and L. A. Schlie, "Transient terahertz reflection spectroscopy of undoped InSb from 0.1 to 1.1 THz," *Applied Physics Letters*, vol. 69, pp. 550-552, 1996.

[6] S. Nashima, O. Morikawa, K. Takata, and M. Hangyo, "Measurement of optical properties of highly doped silicon by terahertz time domain reflection spectroscopy," *Applied Physics Letters*, vol. 79, pp. 3923-3925, 2001.

[7] A. Pashkin, M. Kempa, H. Nemec, F. Kadlec, and P. Kuzel, "Phase-sensitive time-domain terahertz reflection spectroscopy," *Review of Scientific Instruments*, vol. 74, pp. 4711-4717, 2003.

[8] M. Kano, "Adiabatic calorimeter for the purpose of calorimetry in the solid, liquid and supercooled phases of metals," *Journal of Physics E*, vol. 22, pp. 907-912, 1989.

[9] P. Korpiun and R. Tilgner, "The photoacoustic effect at first-order phase transition," *Journal of Applied Physics*, vol. 51, pp. 6115-6119, 1980.

[10] F. A. McDonald and G. C. Wetsel Jr., "Generalized theory of the photoacoustic effect," *Journal of Applied Physics*, vol. 49, pp. 2313-2322, 1978.

[11] E. V. Mejia-Uriarte, M. Nararrete, and M. Villagran-Muniz, "Signal processing in photoacoustic detection of phase transitions by means of the autospectra correlation-based method: Evaluation with ceramic BaTiO3," *Review of Scientific Instruments*, vol. 75, pp. 2887-2891, 2004.

[12] X. G. Gong, G. L. Chiarotti, M. Parrinello, and E. Tosatti, "α-gallium: A metallic molecular crystal," *Physical Review B*, vol. 43, pp. 14277-14280, 1991.

[13] A. V. Krasavin, A. V. Zayats, and N. I. Zheludev, "Active control of surface plasmon-polaritons," *Journal of Optics A - Pure and Applied Optics*, vol. 7, pp. S85-S89, 2005.

Chapter 5:

Terahertz Spinplasmonics

5.1 Background

Electrons are one of the elementary building blocks of matter. The electromagnetic properties of an electron are derived from its two fundamental features: charge and spin angular momentum (Figure 5.1). These two basic properties enable the manipulation of electrons for technological applications. The goal of *electronics* is the manipulation of the transport of electrons via the charge of an electron. This is achieved by applying external electric or magnetic fields, which move a single electron or ensembles of electrons via Lorentz force. The electron transport can also be manipulated by the inherent spin associated with electrons [1]. Spin can refer to the angular momentum of a single electron, which is detected by its magnetic moment, or the average angular momentum of an ensemble of electrons manifested by a macroscopic magnetization. The control of spin involves the manipulation of a single spin or few spin system, or the control of the population and/or the phase of the average spin of an ensemble of electrons. The latter requires a material that is spin-polarized; that is, the material contains an unequal number of spin-up and spin-down electrons. Ferromagnetic (F) media are a key ingredient in spintronics devices since these materials inherently possess non-equilibrium spin population, and hence their electron population is spin-polarized. To understand the underpinnings of spintronic devices, therefore, one must appreciate the fundamental physics of ferromagnetic solid state materials.

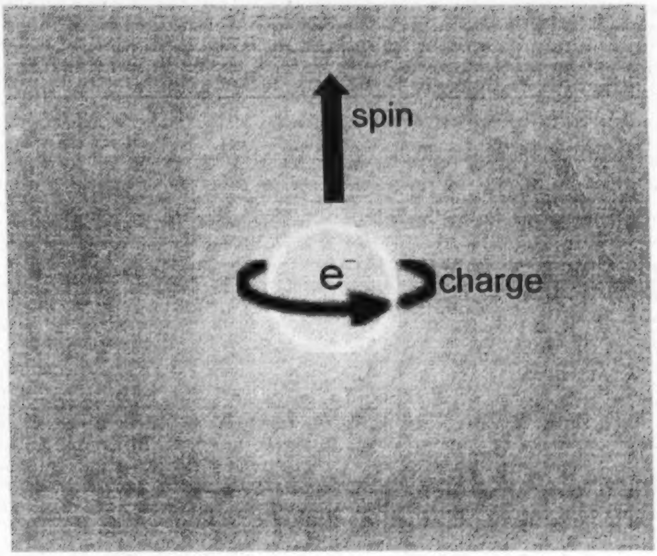

Figure 5.1. Illustration of an electron possessing charge and spin angular momentum.

5.2 Ferromagnetic Metals

Ferromagnetic media are unique since they exhibit spontaneous magnetism arising from the alignment of their magnetic dipole moments. The magnetic dipole moments are oriented parallel to each other by a mutual interaction called ferromagnetic coupling [2]. The origin of ferromagnetic coupling in ferromagnetic transition metals Fe, Co, and Ni can be understood by considering the band diagram of the 3d electrons. Figure 5.2 shows the typical form of the density of states, $DOS(E')$, of the 3d and 4s electron bands as a function of energy, E'. It is noteworthy that the electron shells that are closer to the nucleus than the 3d shell are filled and thus do not contribute to the magnetic dipole moment.

There are two distinctive features in Figure 5.2: 1) the 3d and 4s bands overlap over an energy interval where they are both filled with electrons and 2) the width of the

3d band is very narrow with respect to the width of the 4s band. The narrowness of the 3d band means that the kinetic energy of the 3d electrons is less than that of the 4s electrons. The narrow density of states diagram for the 3d electrons more closely resembles the sharp distinctive states of a free atom than the density of states diagram for the 4s electrons. Hence, it can be physically interpreted that the 3d electrons are closer to their parent nucleus than the 4s electrons, enabling interaction between the 3d electrons of neighboring atoms. This interaction is known as ferromagnetic coupling.

The 3d electron band can be considered as the superposition of two sub-bands, $3d^+$ and $3d^-$, corresponding to the parallel and anti-parallel alignment of the spin angular momentum of the electrons. In nonmagnetic (N) metals such as Cu, Au, and Ag, the 3d band is completely filled. The disparity between the $3d^+$ and $3d^-$ sub-bands disappears, which means that it is not possible to induce a spin polarization. However, since the 3d band in ferromagnetic transition metals is not completely filled, the $3d^+$ and $3d^-$ sub-bands are not equally populated. It is therefore possible for ferromagnetic transition metals to exhibit magnetism.

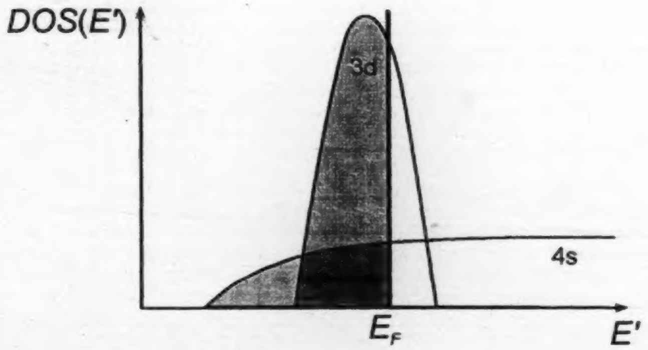

Figure 5.2. Diagram of typical density of states of the 3d and 4s electron bands for a ferromagnetic transition metal.

As seen in Figure 5.2, the narrow width of the 3d band also suggests that the electron density of states is very high. If the Fermi level lies within this band, a very small shift in the energy levels of the 3d$^+$ and 3d$^-$ sub-bands can create a considerable difference between the populations of the two spin sub-bands. In particular, ferromagnetic coupling between neighboring 3d electrons can produce a relative shift in the energies of the 3d$^+$ and 3d$^-$ sub-bands. The imbalance of the populations of the two spin sub-bands induces a spontaneous spin polarization, which results in a magnetization. The spontaneous magnetization arising from ferromagnetic coupling vanishes when the temperature of the medium exceeds the Curie temperature. Above this temperature, there is no energy shift between the 3d$^+$ and 3d$^-$ sub-bands. The two sub-bands are equally populated, and the F metal exhibits no net magnetization.

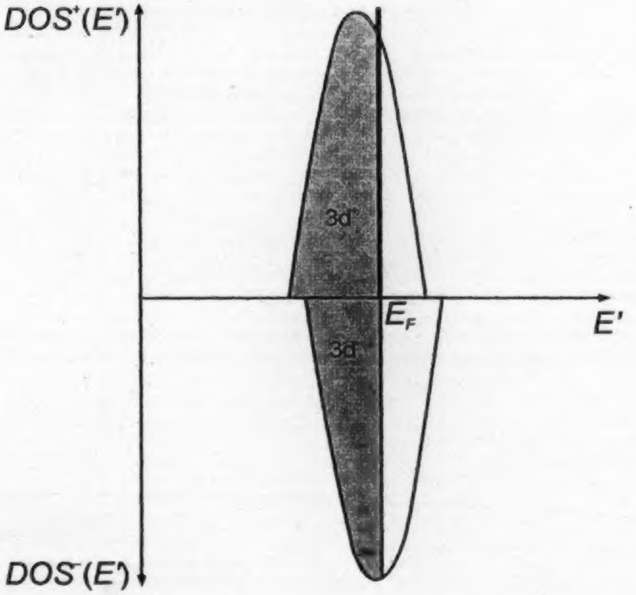

Figure 5.3. Density of states diagram and the occupation of two spin sub-bands 3d$^+$ and 3d$^-$ below the Curie temperature.

In a large, macroscopic F sample below the Curie temperature, the F metal is composed of many magnetic domains. These are regions in the sample in which the alignment of magnetic dipole moments are along the same direction. For the sample as a whole, the magnetic domains are randomly oriented such that the magnetizations due to the individual domains largely cancel. When the F sample is immersed in an external magnetic field, the domains preferentially align along the magnetic field direction, and the sample exhibits a net magnetization. The increase in the gross magnetic moment of an F medium in an applied magnetic field takes place by two processes. In a weak magnetic field the volume of domains oriented along the magnetic field increases at the expense unaligned domains. In strong magnetic fields the domain magnetization rotates toward the direction of the magnetic field [2].

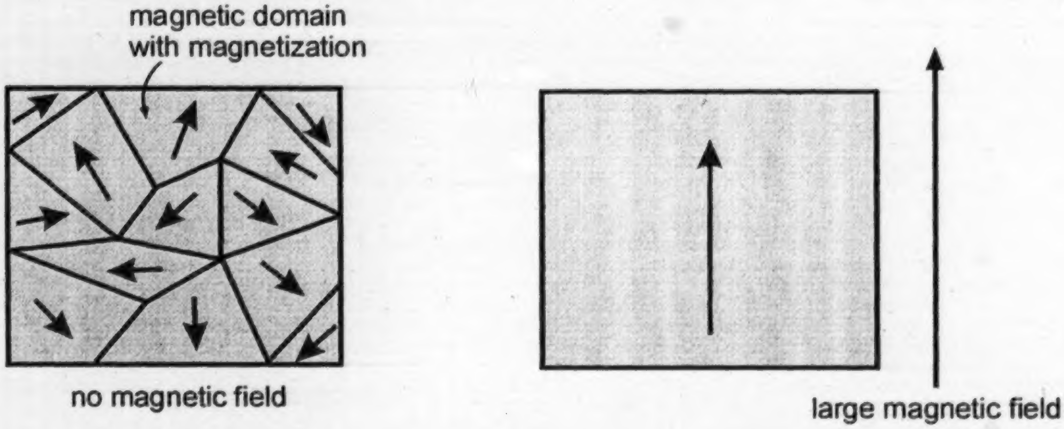

Figure 5.4. (left) Ferromagnetic metal with no applied magnetic field composed of many magnetic domains with randomly oriented magnetizations. (right) Ferromagnetic metal immersed in a large magnetic field. The magnetic domains boundaries have been erased and the magnetization of the sample points along the direction of the applied field.

Another unique feature of F metals is their anisotropic resistivity when immersed in a magnetic field. The anisotropic magnetoresistance (AMR) effect in F media is a technologically vital phenomenon and forms the backbone of advanced technologies such as magnetic sensors, recording heads and memories [3-6]. Anisotropic magnetoresistance in F metals arises due to spin orbit coupling between 3d electrons. To understand the origin of this effect, consider a current flowing in a F metal that has been immersed in a magnetic field, as shown in Figure 5.5. Both 4s and 3d electrons can contribute to the conduction current; however, the conduction current is primarily composed of 4s electrons since the 3d electrons are more localized near their parent nucleus. The resistivity of the metal is largely governed by conduction electron scattering from other electrons. Since the densities of states of the 3d electrons are much greater than the density of states for the 4s elections, the conduction electrons scatter more significantly from the 3d electrons. The scattering cross-section of the 3d electrons is determined by their spin angular momentum. As the magnetization direction rotates in response to an applied magnetic field, the 3d electron cloud deforms, which changes the amount of conduction electron scattering. This is depicted in Figure 5.5. When the magnetization direction is perpendicular to the current direction, the scattering cross-section of the 3d electrons is reduced compared to the zero field case. However, when the magnetization direction is parallel to the current direction, the scattering cross-section is increased. Thus, the resistivity of the ferromagnetic metal depends on the relative orientation of the current direction and the external magnetic field. It has been shown that this anisotropic magnetoresistivity effect exhibits a form of [7]

$$\rho_{AMR}(\theta) = \rho_{\perp} + (\rho_{\parallel} - \rho_{\perp})\cos^2\theta \qquad (5.2.1)$$

where $\rho_{\perp}$ and $\rho_{\parallel}$ are the resistivities when the magnetization is perpendicular and parallel to the current direction, respectively, and θ is the angular separation between the current direction and the external magnetic field. This anisotropic magnetoresistance effect differs from the magnetoresistance inherent to all metals that arises from Lorentz force acting on the conduction electrons. For Lorentz magnetoresistance, the resistance is high (low) when the magnetic field is perpendicular (parallel) to the current direction.

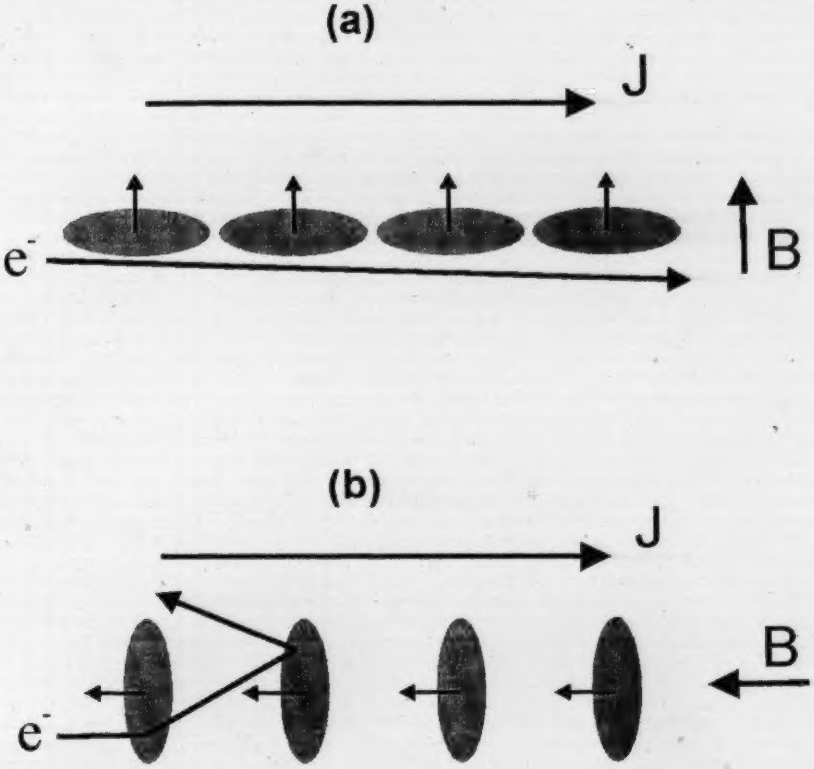

Figure 5.5. Conceptual illustration of the origin of anisotropic magnetoresistance in ferromagnetic metals. When a magnetic field is aligned perpendicular to the current direction (a), the spin-orbits of the 3d electrons have minimal electron scattering cross-section. In the parallel case (b), the spin-orbits of the 3d electrons have maximal electron scattering cross-section.

5.3 Spintronic Devices

Ferromagnetic metals are one of the key building blocks of spintronic devices. Spintronic devices are commonly composed of an F metal which acts as a source of spins in conjunction with a N medium that acts as a collector of spins. One of the simplest spintronic structures is an F metal placed in direct contact with a nonmagnetic (N) metal, as depicted in Figure 5.6. There are two cases that can occur: 1) the F metal can be fully magnetized such that the magnetization is uniform and 2) the F metal is completely demagnetized, consisting of many domains with random orientation. For case 1), the transport between the F and N metals can be represented by density of states diagrams, which represent the 3d-4s band of the transition metals such as Ni, Fe, or Co. Here, the F metal is represented using an electron band model where the one of the 3d spin sub-bands is entirely below the Fermi level. The N metal is modeled as an ideal gas of free electrons obeying the Pauli Exclusion Principle. When there is no voltage applied across the interface, the Fermi levels of the two metals align, as shown in Figure 5.6.

When a voltage is applied across the F/N interface, there is electric current driven from the F metal into the N metal. As shown in Figure 5.7, the down-spin electron sub-band is below the Fermi level, so only the up-spin electron sub-band is available to carry current. Since the electrons that constitute the current carry charge and spin angular momentum, the electric current, I_e, can also be viewed as a current carrying magnetic dipoles. Effectively, there is a current of magnetization, I_m, transported from F to N which is represented by

$$I_m = Q\,\beta_m\, I_e/e \tag{5.3.1}$$

where β_m is the Bohr magnetron and $Q = (j^+ - j^-)/(j^+ + j^-)$ is a parameter which describes the efficiency of the spin transport process. Here, $j^{+,-}$ represent the current densities of the two spin sub-bands. In the simple model depicted by Figure 5.7, $Q = 1$, but in general, $Q < 1$ due to contributions to the conduction current by other spin sub-bands.

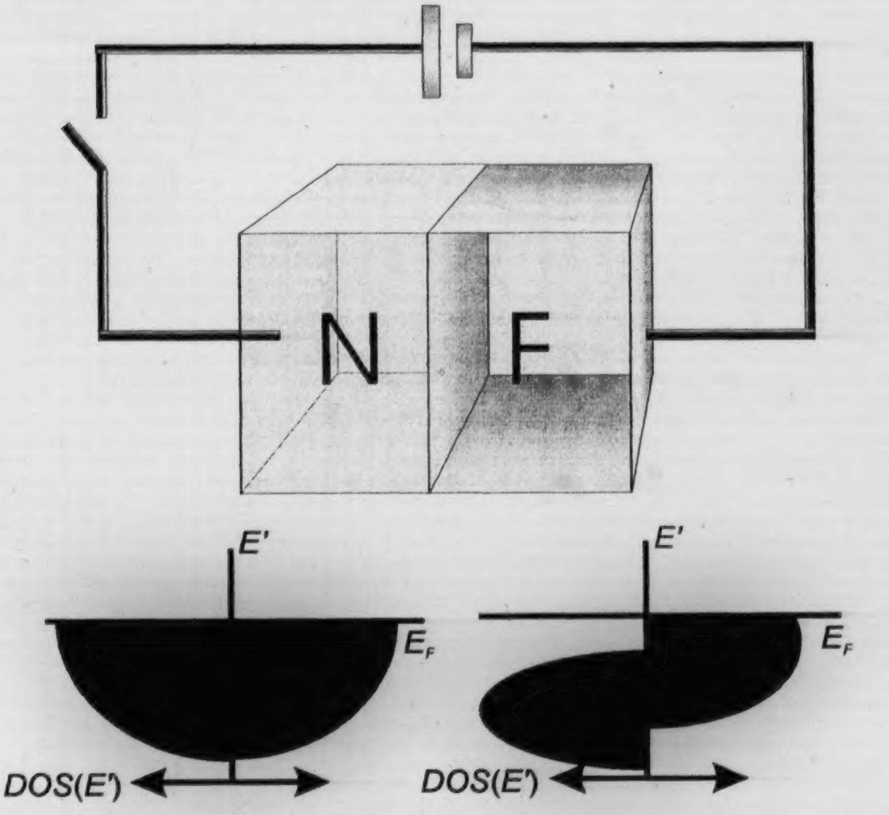

Figure 5.6. Illustration of a ferromagnetic metal in contact with a nonmagnetic metal. The density of states diagram for the 3d electron bands of the nonmagnetic and ferromagnetic metal are shown below.

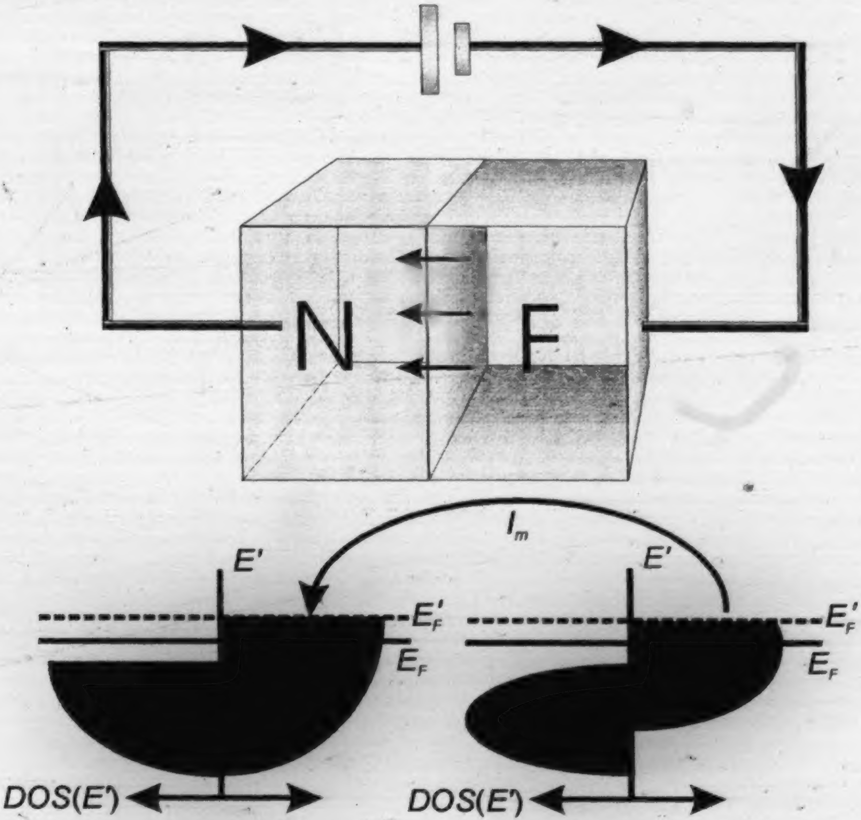

Figure 5.7. Illustration of a ferromagnetic metal in contact with a nonmagnetic metal with a voltage applied across the interface. The density of states diagram for the 3d electron bands of the nonmagnetic and ferromagnetic metal are shown below. A spin-polarized current, I_m, is driven from the ferromagnetic metal into the nonmagnetic metal.

Near the F/N interface at steady state, spin polarized electrons are added to N at a rate of I_m, and the spin polarization is lost due to random scattering at a rate $1/T_2$, where T_2 is the spin relaxation time. A non-equilibrium population of electron spin builds up in N, given approximately by

$$M_{spin} = I_m T_2 / (V_{spin}) \tag{5.3.2}$$

where V_{spin} is the volume in which the non-equilibrium population of electron spins occupy the N metal. As the spin-polarized electrons accumulate in the N metal, the chemical potential of F must rise so that the Fermi level of its up-spin sub-band (as shown in Figure 5.7) aligns with the Fermi level of N. This creates a potential difference across the interface that acts to impede the entrance of spins into the N metal. The mechanism can be pictured as a "spin bottleneck", in which the buildup of spins acts to impede the continued flow of spins across the F/N interface. This spin-dependent resistance arising from the spin bottleneck is known as the spin accumulation effect [8-10].

5.4 Active Plasmonics

Plasmonics is a field whose central theme involves the study of electromagnetic surface waves confined to a metallic-dielectric interface. One of the key features of surface plasmons is the ability to confine electromagnetic energy over subwavelength scale volumes. The ability of surface plasmons to confine electromagnetic energy over subwavelength extents is one of the central motivations behind the development of photonic devices based on surface plasmons. Currently, a key challenge facing the field of plasmonics is the development of active surface plasmon-based devices, which can be switched or modulated via an external stimulus [11].

Fundamentally, a surface plasmon wave is confined between the interface of a metal and a dielectric, characterized by permittivities of $\varepsilon_{metal}(\omega)$ and $\varepsilon_d(\omega)$, respectively. Because the surface plasmon wave exists in both media, it can be modulated by actively changing the permittivity of the dielectric or the permittivity of the metal. For instance, manipulation of the SPP signal propagated on a thin silver film was recently demonstrated [12]. The active component of the device consisted of the two polymer layers sandwiching the thin silver film, where one layer contains donor chromophore molecules and the other contains acceptor fluorophore molecules. The SPP wave on the silver film provides efficient energy transfer from the donor molecules on one side of the film to the fluorophore molecules on the other side of the film. The results provide demonstration of the control of surface plasmon waves by manipulating the flow of electromagnetic energy across thin metallic films via radiative transfer between donor and acceptor molecules placed near the metallic surface. Moreover, there are continuing research efforts to develop active surface plasmon devices where the permittivity of the surrounding dielectric medium can be changed via electro-optic, all-optical, and piezoelectric modulation [13]. A more direct way to manipulate surface plasmon waves is to actively change the electromagnetic properties of the metal, $\varepsilon_{metal}(\omega)$. For instance, in a metal-on-dielectric waveguide containing a section composed of gallium metal that is several microns long, the SPP signal can controlled by switching the structural phase of gallium [14]. The signal modulation depth can exceed 80%, and switching time scales are expected to be on the picosecond scale.

Another method to actively modulate the propagation of surface plasmon waves is to affect the density of states of the metal. While this is difficult to achieve with N metals such as Cu, Au, and Ag, the density of states of F metals can be strongly affected with the application of relatively weak external magnetic fields. Surface plasmon waves on F metals, therefore, are a potential candidate for the development of active plasmonic media. Several investigations have explored SPP wave propagation on ferromagnetic surfaces. In the work by Newman et al. [15], it was shown that the transport properties of SPP waves on F media is sensitive to the magnetization of the surface on which they traveled. Their results showed that the far-field re-radiation from SPPs on a F surface is linearly dependent on the sample magnetization when an applied magnetic field drives the magnetization perpendicular to the SPP propagation direction. In similar work, Duchs et al. [16] demonstrated that SPPs propagated on continuous silver films decorated with 60 nm diameter Co scatterers showed anisotropic SPP scattered when a magnetic field was applied normal to the surface of the film. While SPP wave interaction with F surfaces has been studied, localized particle plasmon interaction with F particles has yet to be explored. Since the surface field associated with particle plasmons interacts with a greater metallic surface area to volume ratio than the surface field associated with SPPs, particle plasmon interaction with F particles is expected to give rise to more pronounced magnetically dependent phenomena.

Using a rudimentary plasmonic circuit, namely, a dense ensemble of microparticles, this Chapter demonstrates that the THz particle-plasmon mediated conduction across the particles can be actively modulated via electron-spin-dependent phenomena. Two unique manifestations of electron-spin-dependent effects are observed using samples of F particles and F/N composite particles. In samples of F particles immersed in an external magnetic field, the THz electric field transmission through the particles shows anisotropic amplitude and delay dependent on the relative orientation of the magnetic field and the THz polarization. This magnetically anisotropic THz electric field transmission phenomenon is shown to arise from the AMR effect inherent to the F medium. The dependence of the THz electric field transmission anisotropy on the ferromagnetic particle morphology is explored in Section 5.6. Comparative studies of highly porous and smooth ferromagnetic particles immersed in a magnetic field show that the particle morphology can give rise to strikingly disparate THz electromagnetic responses. It is further shown that THz electric field transmission through F particles that have been coated with thin N nano-layers exhibits large, magnetically dependent attenuation present neither in pure N particles nor in pure F particles. The enhanced magnetic attenuation associated with the thin N nano-layer is modeled as non-equilibrium, spin-dependent interface resistance that inhibits THz charge density fluctuations at the F/N interface. A quantitative measurement of the dependence of the THz electric field attenuation on the thickness of the nonmagnetic layer is in very good agreement with the spin diffusion length predicted by the spin accumulation model, as well as with other experimental measurements of this length. The results of this Chapter have been published in the manuscripts *Physical Review Letters*, vol. 96, 033903 (2006); *Applied Physics Letters*, vol. 90, 121122 (2007); and *Physical Review Letters*, vol. 98, 133901 (2007).

5.5 Magnetically Anisotropic Terahertz Particle-Plasmon-Mediated Transmission

Anisotropy is the quality of being directionally dependent. Electromagnetic anisotropy is characterized by a dependence of the properties of a medium on the polarization direction of an incident electromagnetic wave. A common example is a birefringent crystal, such as calcite (Figure 5.8). This medium is anisotropic, or birefringent, because depending on the directionality of the wave polarization with respect to the optical axis, the wave propagates with two distinctive velocities. Another fundamental form of anisotropy is the AMR inherent to F metals, such as Co, Ni, and Fe. These metals exhibit anisotropic resistance depending on the directionality of an applied magnetic field, B, with respect to the current direction. When B is aligned perpendicular (parallel) to the current direction, the spin-orbits that constitute the magnetization of the metal have a relatively small (large) electron scattering cross section, giving rise to a relative small (large) magnetoresistance.

When a THz electromagnetic wave is coupled into non-resonant particle plasmons on *ferromagnetic* particles, the non-radiative decay of the particle plasmons can be influenced via the magnetoresistance of the particles. As was shown in Chapter 1, the non-radiative decay of the THz non-resonant particle plasmons is governed by the effective resistivity of the particles at the surface. For ferromagnetic Co particles, the effective resistivity is given by

$$\rho_{eff}(B,\theta) = \rho_o + \rho_{Lorentz}(B,\theta) + \rho_{AMR}(B,\theta) \tag{5.5.1}$$

where ρ_o is the nonmagnetic background resistivity, $\rho_{Lorentz}(B,\theta)$ is the magnetoresistivity arising from Lorentz force, $\rho_{AMR}(B,\theta)$ is the magnetoresistivity due to the AMR effect, and θ is the angle between the current and the magnetization direction. In all metals, $\rho_{Lorentz}(B,\theta)$ is present as a small magnetoresistivity modulation proportional to the Lorentz force, $-e\boldsymbol{v}\times\boldsymbol{B}$, where $\boldsymbol{v}$ is the electron velocity. In ferromagnetic metals, $\rho_{AMR}(B,\theta)$ is a significantly larger magnetoresistivity effect where the resistivity is maximum (minimum) when the electron velocity is parallel (perpendicular) to the magnetization. The dependence of $\rho_{AMR}(B,\theta)$ on θ is given by $\rho_{AMR}(\theta) \propto \cos^2\theta$ [7]. Since the non-radiative decay is largely governed by the AMR effect in the F medium [17-19], THz particle plasmons on F particles are inherently magnetically anisotropic.

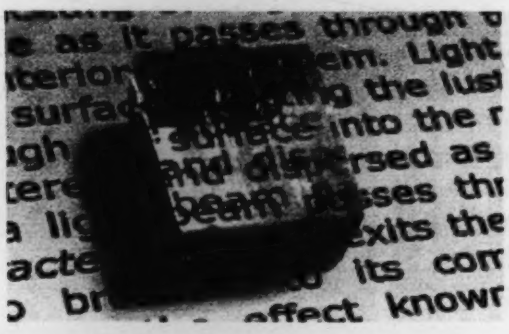

Figure 5.8. Image seen through a calcite crystal. The inherent birefringence of calcite causes the double image of the text seen through the crystal.

To study the magnetic anisotropy associated with non-resonant particle plasmons on F particles, the THz electromagnetic properties of F particle ensembles immersed in a magnetic field is examined. In particular, THz time-domain spectroscopy (with a setup similar to that described in Chapter 2) is used to measure the THz electric field transmission through a ferromagnetic particle sample consisting of > 99.7% pure Co. The particles are randomly shaped and poly-disperse, with a mean dimension of $\delta = 74 \pm 5$ μm and a measured volume packing fraction of 0.51 ± 0.02. The THz electric field transmission through the particles is studied as a function of the strength and orientation of an applied magnetic field B, which magnetizes the particles. The biasing B field is supplied from permanent magnets.

By magnetically varying the resistivity of the Co particles, THz electromagnetic transmission through the ensembles is influenced through $\rho_{Lorentz}(B,\theta)$, $\rho_{AMR}(B,\theta)$, or both. As shown in Figure 5.9, the time-domain characteristics of the experimental THz electric field transmission through the Co sample reveal several magnetically dependent effects. The most remarkable observation is that the THz electric field pulse arrival time, T_A, (measured at the first peak of the transmitted pulse) depends on the orientation of the biasing B field (B = 0.18 T) relative to the incident pulse polarization. When B is aligned perpendicular (parallel) to the incident THz electric field polarization, there is minimal (maximal) delay with respect to the transmission in the absence of B. This observation is accompanied by simultaneous transmission attenuation exhibiting a similar B-orientation dependence. Evidently, the THz electromagnetic properties of the Co sample are highly dependent on θ. The increased temporal delay and attenuation when a $B_{||}$ field is applied indicate increased non-radiative decay, which can be equivalently interpreted as an increase in $\rho_{AMR}(B,\theta)$ of the medium. In contrast, the insignificant attenuation and delay observed in a $B_{\perp}$ field show that $\rho_{Lorentz}(B,\theta)$ arising from Lorentz force is negligible.

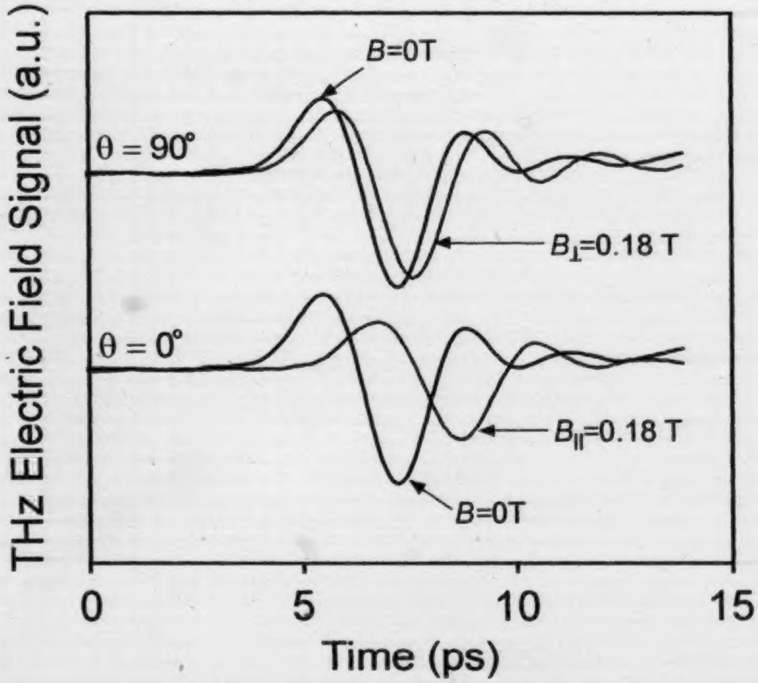

Figure 5.9. Time-domain THz pulses (gray traces) transmitted through a 2 mm thick ensemble of Co particles when a 0.18 T magnetic field is applied perpendicular (top) and parallel (bottom) to the incident THz polarization. Also shown is the transmitted pulse in the absence of a magnetic field (black traces).

The attenuation and delay of the transmitted THz electric field pulses have a similar B-orientation dependence as AMR inherent to bulk ferromagnetic metals [19]. Shown in Figure 5.10 is a plot of the transmission amplitude (normalized to the transmission amplitude for $B = 0$) as a function of the relative orientation between the biasing field and the incident polarization for a biasing field of 180 mT. Remarkably, the THz electric field transmission amplitude for the Co ensemble shows a $\cos^2\theta$ dependence, matching the $\cos^2\theta$ dependence of AMR. The results provide strong evidence that the F particle ensemble's THz electric field transmission anisotropy is a direct manifestation of AMR inherent to the F medium.

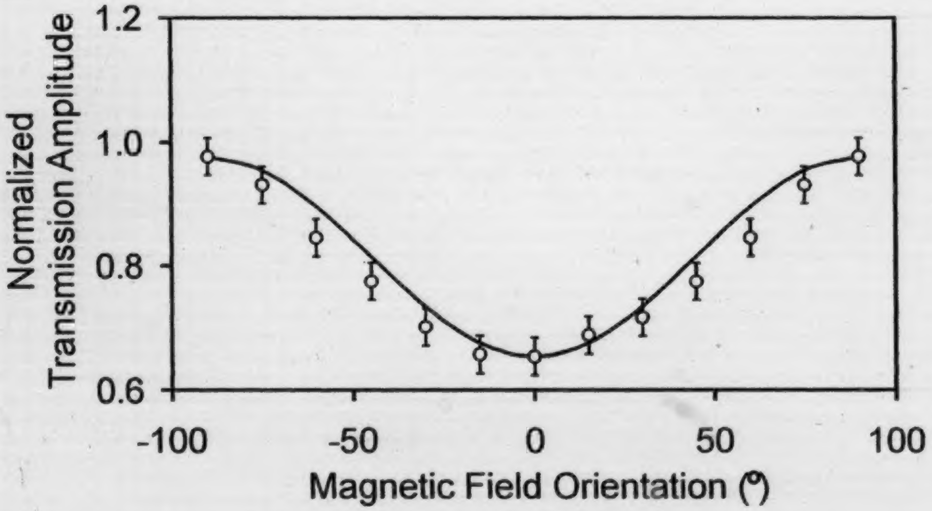

Figure 5.10. Normalized transmission amplitude through 3 mm thick Co particle samples versus the B orientation relative to the incident polarization where $|B| = 160$ mT. The transmission amplitudes have been normalized to the zero-field transmission values. The data have been fitted to $\cos^2\theta$ functions shown by the solid line.

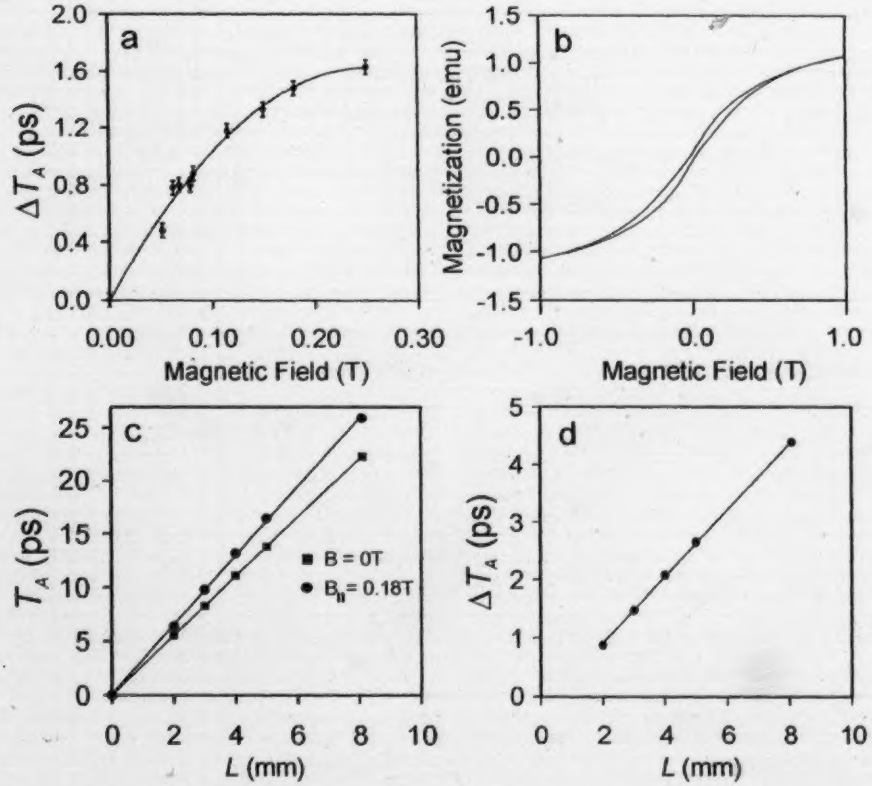

Figure 5.11. (a) Relative arrival delay (between the parallel and perpendicular magnetic field configurations) of the transmitted pulse through a 2 mm thick Co particle ensemble versus magnetic field strength. (b) depicts magnetization measurements of the Co particles versus magnetic field strength. The arrival delay is plotted in (c) versus sample thickness for an applied magnetic field of 0.18 T and 0 T. The relative arrival delay (between the parallel and perpendicular magnetic field configurations) in (d) is shown versus sample length for an applied magnetic field of 0.18 T.

To further investigate this phenomenon, the *B* and *L* dependences of the effect are studied. By varying the $B_{||}$ field from 0 T to 0.15 T, the magnetically-induced delay for a *L* = 3 mm sample grows linearly from 0 to 1.2 ps, and in the range of 0.15 T to 0.25 T, the delay begins to saturate [Figure 5.11 (a)]. This behaviour accords with independent measurements of the magnetization response of the Co particles. As seen in Figure 5.11 (b), the magnetization of the Co particles increases linearly for $|B| < 0.20$ T, and for $|B| >$

0.20 T, begins to saturate. Employing $B_{||} = 0.18$ T (corresponding to the onset of delay saturation), it is shown in Figure 5.11 (c) that the arrival delay of the transmitted pulse increases linearly with respect to L. Figure 5.11 (d) plots the relative arrival delay of the transmission between the perpendicular and parallel B configurations, ΔT_A. As seen in the Figure, ΔT_A increases linearly with L with a retardation coefficient of $\Delta T_A / L = 0.57 \pm 0.01$ ps/mm, indicating that the anisotropic delay accrued by the transmission is a cumulative effect proportional to the number of Co particles across the sample.

To ensure that the magnetically anisotropic THz electric field transmission does not arising from a deflection of the transmitted THz beam, the spatial distribution of the transmitted THz beam is characterized with and without the applied B. The electric field distribution of the THz wave-front in the plane perpendicular to the B direction is measured by a knife-edge technique, where the THz field is sampled as an opaque metallic edge is scanned across the wave-front. As shown in Figure 5.12 (a), the application of the magnetic field does not alter the spatial distribution of the on-axis transmitted wave. Based on this experimental evidence, it is concluded that magnetically induced deflection of the transmitted THz beam through the Co particles is negligible. Further evidence of the magnetic origin of this effect is drawn from comparative transmission measurements through an ensemble of ~ 70 μm Cu particles with the application of $B_{||} = 0.18$ T. As Cu is non-magnetic, the relatively weak spin-orbit coupling results in no measurable magnetically dependent delay, evident in Figure 5.12 (b).

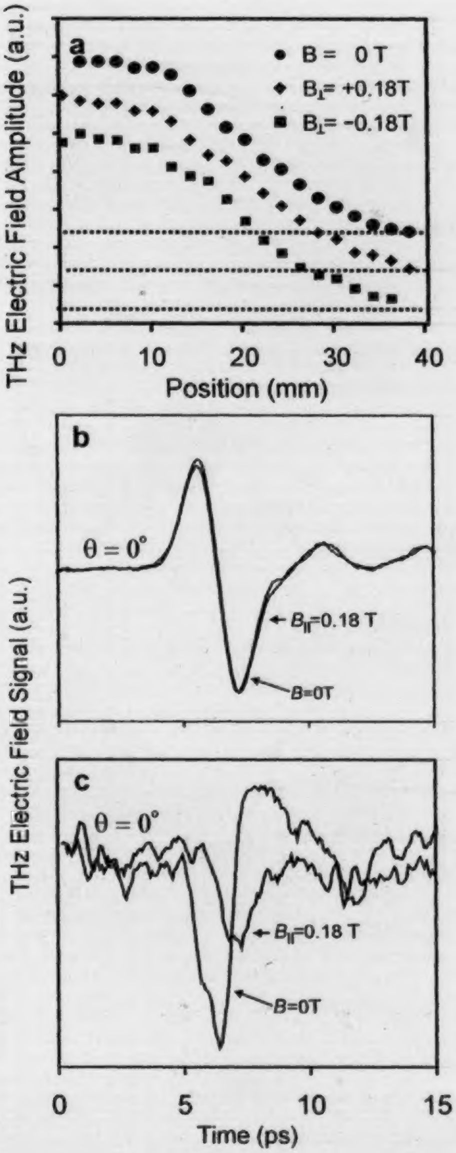

Figure 5.12. (a) The integrated spatial profile of the THz transmission (along the direction perpendicular to the applied magnetic field) through a 2 mm thick Co sample for a field of 0 T, +0.18 T, and −0.18 T. The curves have been off-set for clarity; the offsets are shown by the dashed lines. Time-domain transmission measured through a 3 mm thick sample of Cu particles is illustrated in (b) for a magnetic field of 0 T and 0.18 T applied parallel to the THz polarization. (c) shows the time-domain transmission measured through a 2 mm thick Co/wax ensemble for a magnetic field of 0 T and 0.18 T applied parallel to the THz polarization.

Another factor which may affect the transmissivity of the F particle ensemble is spurious mechanical motion and rearrangement of the particles in an external B. To study the influence of mechanical motion, additional experiments are performed using Co particles immersed in a solidified wax matrix. Shown in Figure 5.12 (c) are experimental results where the on-axis transmission is measured through 3 mm thick Co/wax ensembles without and with an applied $B_{||} = 0.18$ T. As seen in the Figure, the application of $B_{||}$ results in attenuation and delay of the transmitted THz waveform. Since mechanical motion of the particles is precluded in the Co/wax composite, the magnetically induced attenuation and delay must arise directly from the Co particles. It is also interesting to note that the transmitted waveforms through the Co/wax composite are significantly attenuated relative to that transmitted through the Co/air composites. Due to the higher index of refraction of wax (~1.5 at 1 THz) relative to air, the electromagnetic interparticle separation is increased by a factor of ~ 1.5. As a result, near-field interaction, which is governed by near fields exhibiting a r^{-3} dependence, is reduced by a factor of $1.5^3 \approx 3.4$.

Anisotropic transmission modulation in the metallic particles arises directly from the θ-dependent magnetoresistivity of the F metal. This can be understood by describing the vector plasmonic response of a single Co particle. As the size scale of the particles' roughness (~1 μm) relative to the central wavelength obey Rayleigh's criterion for smooth surfaces, the particle is approximated to be a smooth sphere [20]. For $\delta << \lambda$, the incident THz pulse can be described as a homogeneous electric field oriented along the z-axis. It has been shown in Chapter 1 that the vector electric fields associated with the THz particle plasmon are given by

$$\boldsymbol{E}_{total} = \boldsymbol{E}_s + \boldsymbol{E}_{ind} = E_{in} \cos \theta_z \, \hat{r} \tag{5.5.2}$$

where θ_z is the angular coordinate from the z-axis, $\boldsymbol{E}_{total}$ is the total electric field, $\boldsymbol{E}_s$ is the electric field of the incident THz pulse, and $\boldsymbol{E}_{ind}$ is the electric field associated with the dipolar induced charge on the particle. Due to cancellation of the tangential electric field components at the particle surface, the total electric field is oriented normal to the particle surface. Note that $\boldsymbol{E}_{total}$ is strongest along the direction of the incident field ($\theta_z = 0°$) and approaches zero in the orthogonal direction ($\theta_z = 90°$). Accordingly, current density driven by the total electric field,

$$\boldsymbol{j}_p = \frac{\boldsymbol{E}_{total}}{\rho_{eff}(B,\theta)} = \frac{E_s \cos\theta_z}{\rho_{eff}(B,\theta)} \hat{r} \tag{5.5.3}$$

is also polarized along the incident field direction. Polarization of the mediating surface currents along the incident field gives rise to the observed anisotropy, as conceptually illustrated in Figure 5.13. The characteristic $\rho_{eff}(B,\theta)$ of the ferromagnetic particles depends strongly on the angle between the incident field polarization (coinciding with the orientation of the surface currents) relative to the magnetic field direction. Attenuation of $\boldsymbol{j}_p$ via $\rho_{AMR}(B,\theta) >> \rho_{Lorentz}(B,\theta)$ directly results in transmission amplitude reduction and delay in a $B_{||}$ field relative to a $B_{\perp}$ field. Since Cu exhibits negligible magnetoresistivity, no magnetically-induced transmission modulation is observed in the Cu particles.

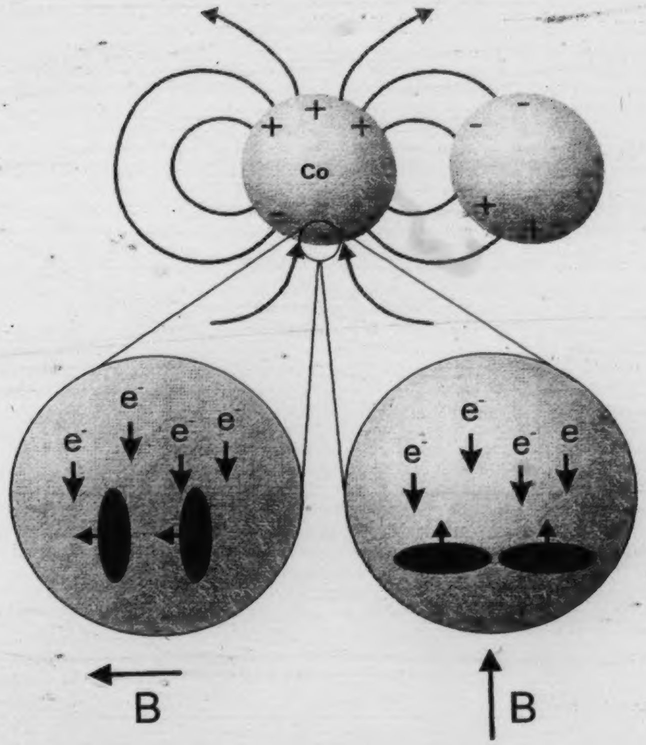

Figure 5.13. Cartoon illustrating the physical origin of THz plasmonic magnetoresistance. The incident THz pulse polarizes the individual particles by inducing finite charge motion at the surface of the particles. The resistivity at the particle surface depends on the orientation of the magnetic field relative to the polarization direction of the incident THz pulse. The particle plasmon losses are determined by the magnetoresistivity of the particles, which is sensitive to the *B* orientation. For high resistivity, the re-radiated THz pulse is attenuated and delayed.

Polarization characterization of the experimental THz electric field transmission enables further understanding of the magnetic anisotropy associated with the THz particle plasmon response of the F particles. Figure 5.14 maps the experimentally measured electric field trajectory of the transmitted electric field (through a 3 mm thick sample) as a function of the angle of the applied magnetic field with respect to the incident THz pulse polarization. For $B = 0$, coherent coupling across the F particle collection preserves the incident linear polarization. When the applied magnetic field is aligned 0°, 90°, and

180° with respect to the incident polarization, the transmitted electric field also preserves the incident polarization state. However, when B is aligned at $\theta = 30°, 60°, 120°$ and $150°$, the transmitted electric field polarization no longer preserves the incident polarization but is rather elliptically polarized. Hence, the experiments show that the magnetized ferromagnetic medium effectively behaves like a birefringent crystal where the principal axes are when the incident polarization is aligned parallel and perpendicular to the magnetic field orientation.

Figure 5.14. (top) Illustration of the relative orientations of the external magnetic field and the polarization of a THz electric field incident on a Co particle. The incident electric field induces current density components parallel and perpendicular to the magnetic field orientation. (bottom) Electric field trajectory of the transmitted THz pulses through 2 mm thick ensemble of magnetized Co particles. The trajectories are shown as the orientation of the magnetic field (0.18 T) is varied over 180°. The relative orientation of the incident THz polarization and the magnetic field are shown above the electric field trajectory plots.

The polarization response of the F particle ensemble in a magnetic field can be understood by considering the nature of THz wave propagation through the medium. When $B_{\|}$ and $B_{\perp}$ are applied (Figure 5.14), the THz electromagnetic wave propagates isotropically (via nearest neighbor coupling) at velocities $v_{g,\|}$ and $v_{g,\perp} = v_{g,0}$, respectively. However, when a B field oriented at $0^{\circ} < |\theta| < 90^{\circ}$ is applied, the incident THz electric field pulse simultaneously excites charge density oscillations on the individual particles oriented both parallel and perpendicular the applied B, as shown in Figure 5.14. The parallel and perpendicular particle plasmon oscillations propagate across the sample at velocities of $v_{g,\|} = 0.51\ c$ and $v_{g,\perp} = 0.55\ c$, respectively. The electromagnetic fields associated with the parallel and perpendicular particle plasmons accrue a phase difference as they propagate across the ensemble. The superposition of the two orthogonal electric field components at the exit face of the sample causes the observed polarization ellipticity. Hence, due to ferromagnetic anisotropy inherent to the F medium, the magnetized F particle ensemble is magnetically birefringent at THz frequencies.

5.6 Isotropic Magnetoresistance Signatures in the Terahertz Transmission through Porous Ferromagnetic Particles

As shown in the previous section, the inherent anisotropic $\cos^2\theta$ magnetic field dependence associated with AMR can be observed in the THz electric field transmission through subwavelength ferromagnetic microparticle ensembles [21]. In this manner, AMR is mapped onto an effective magnetic birefringence of the metallic particle medium. However, unlike conventional AMR present in the *electrical transport* in ferromagnetic metal, the THz transmission counterpart is a more pronounced effect exhibiting greater sensitivity to extrinsic parameters such as the morphology and the size of the constituent ferromagnetic particles. This section investigates unique AMR signatures in the THz electric field transmission through highly porous, "cauliflower" shaped ferromagnetic, Ni particles. The sample consists of 99.8 % pure, highly porous spheroid particles having a nominal dimension of $\delta = 320$ μm. The morphology of the particles is characterized by large, randomly distributed columnar pillars with a typical height ≈ $\delta/3$ and a subwavelength width. Interestingly, the overall particle shape resembles a cauliflower structure [Figure 5.15 (a) and 5.15 (b)]. Large inter-columnar voids, characterized by a mean aspect ratio of 11.3 ± 4.6, account for an overall ensemble volume packing fraction of only 0.39 ± 0.02. The THz beam is focused onto a polystyrene sample cell housing a 1.9 mm thick collection of particles. To examine the magnetically dependent THz transmissivity of the particles, the ensemble is immersed in an external biasing B tunable from 0 mT to 120 mT where the beam samples the same random configuration of the particle ensemble.

The dominant polarization mode of a metallic particle excited by THz electromagnetic radiation is strongly dependent on the particle size relative to λ. Whereas particles having $\delta < \lambda$ show dipolar polarizability, particles having $\delta \sim \lambda$ exhibit polarizability of higher orders [22] as illustrated in Figure 5.15 (c) and 5.15 (d). As discussed in Chapter 1, non-resonant particle plasmons at THz frequencies decay via non-radiative losses governed by the metal resistivity (i.e. Ohmic losses) [23]. In ferromagnetic metals, such non-radiative losses are strongly dependent on the magnitude and orientation of the external magnetic field via a magnetoresistivity given by $\rho(B, \theta) =$

$\rho_o + \rho_{Lorentz}(B, \theta) + \rho_{AMR}(B, \theta)$. Generally, $\rho_{AMR}(B, \theta) >> \rho_{Lorentz}(B, \theta)$ [19], and $\rho(B, \theta) \propto \cos^2\theta$. Resistive losses from $\rho_{AMR}(B, \theta)$ result in THz electric field attenuation and propagation strongly dependent on the magnetic field strength and direction.

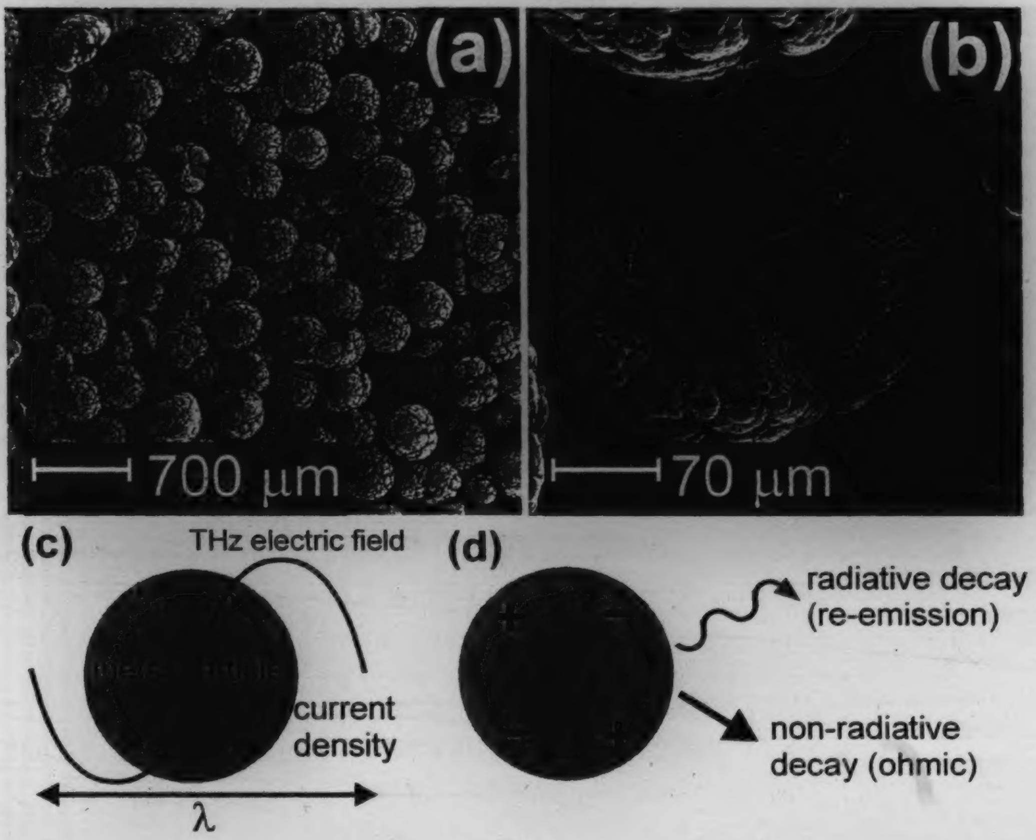

Figure 5.15. (a) Scanning electron microscope image of a collection of porous Ni particles of nominal size δ. (b) A magnified image of a typical Ni particle highlighting an overall spheroid shape and subwavelength columnar microstructure. (c) A conceptual illustration of the excitation of a THz particle plasmon on a metallic microsphere. The incident electric field induces a surface current density, which polarizes the microparticle. The dominant polarization mode for the particle ($\delta \sim \lambda$) is a quadrupolar mode. (d) After excitation, the particle plasmon decays via radiation re-emission or non-radiative decay in the metallic sphere. The non-radiative losses are dictated by the resistivity of the sphere within a skin depth of the surface.

Shown in Figure 5.16 (a) and 5.16 (b) are the on-axis THz electromagnetic transmission through the porous Ni particle ensemble with B applied parallel ($B_{\parallel}$) and perpendicular ($B_{\perp}$) to the incident polarization. The broad (~15 ps) pulses, for identical $B_{\parallel}$ and $B_{\perp}$ magnitudes, display similar electric field amplitude attenuation. A detailed study of this B-dependence reveals a striking near-identical power, $<E_{tr} E_{tr}^{*}>$, decrease of 50% for the two B orientations throughout the entire range 0 mT < B < 120 mT [Figure 5.16 (c)]. Thus, the results show that the non-radiative losses in the porous particle ensemble are independent of the B orientation. This isotropic behaviour is contrary to the anisotropic characteristics of ferromagnetic materials, observed using solid ferromagnetic particles.

While magnetic anisotropy eludes detection in the power measurements, its signature can be exposed via the pulse arrival delay [Figure 5.16 (a) and 5.16 (b)]. Here, the arrival delay is defined as the time that corresponds to the arrival of the pulse energy centroid. As the resistivity of the particle increases (decreases), the radiation propagation velocity decreases (increases). Referring to Figure 5.16 (d), as $B_{\parallel}$ is varied from 0 mT to 60 mT, there is a strong non-linear dependence of the arrival delay on B, reaching maximum value of 0.8 ps. Above $B_{\parallel} = 60$ mT, the arrival delay linearly increases at 2.7 ± 0.4 fs/mT. On the contrary, over the entire range of 0 mT to 120 mT an equivalent 3.0 ± 0.2 fs/mT linear trend in the arrival delay is observed for the $B_{\perp}$ configuration. Overall, the arrival delay results suggest increased particle resistivity in a $B_{\parallel}$ field relative to a $B_{\perp}$ field. The anisotropy in the arrival delay is consistent with AMR characteristic of the ferromagnetic medium.

Figure 5.16. Time-domain transmitted THz electric field waveforms through porous Ni particles for various B field magnitudes, with B (a) parallel and (b) perpendicular to the incident THz polarization. The inset in (a) portrays the reference waveform transmitted through an empty polystyrene sample cell. (c) Power and (d) arrival delay of the transmitted THz pulse versus applied external magnetic field strength for the parallel and perpendicular configurations. (e) Power and (f) arrival delay of the transmitted pulse through solid Ni spheroids versus applied external magnetic field strength for the parallel and perpendicular configurations.

To explore whether morphological irregularities cause the isotropic B-dependent transmission attenuation, control experiments are performed using solid Ni spheroids that lack the columnar structures featured in the porous Ni particles [inset Figure 5.16 (e)]. Interestingly, by varying $B_{\parallel}$ and $B_{\perp}$ over the range between 0 to 120 mT and measuring the transmitted power, there is large anisotropy (~ 20%) as illustrated in Figure 5.16 (e).

Moreover, as shown in Figure 5.16 (f), the time-domain behaviour of the transmitted electric field also shows an anisotropic *B* dependence. Since the solid Ni particles exhibit anisotropic signatures in both the attenuation and arrival delay, it is evident that the isotropic attenuation must be artificially induced by the morphology of the porous particles.

The experimental results suggest that the unique *B*-dependent THz properties of the porous particles arise from their surface morphology. When the THz electric field is incident on the porous, "cauliflower" shaped particle, plasmonic surface currents are excited throughout the particle surface area. To elucidate the origins of the isotropic power attenuation in the porous particles, the plasmon oscillations on the exterior particle surface (exterior surface plasmons) are distinguished from those on the interior surface within the particle voids (interior surface plasmons). These two contributions to the total surface current influence the *B*-dependent properties of the particle in different manners. Since the surface area within the voids is significantly greater than the surface area of the particle exterior, overall Ohmic losses (causing amplitude attenuation of the re-emitted fields from the particle) are largely determined by losses associated with the interior plasmonic currents. These currents are driven by the near-field electric field within the voids. It should be noted that for a good conductor, the THz electric field lines meet normal to the metal surface. Due to the morphology of the particle voids, the interior electric fields (and their associated plasmonic currents) are randomly oriented and have *no preferred directionality* with respect to the applied *B* field. Thus, the cauliflower-shaped particles exhibit, on average, *B*-induced attenuation independent of θ, giving rise to isotropic photonic magnetoresistance.

The *B*-dependent transmission arrival delay exhibits a different morphological sensitivity than the attenuation. The THz radiation propagates through the particle ensembles via near-field coupling of the radiative field associated with the polarized particle. On the individual porous particles, interior plasmons within the voids are highly confined (since the inter-columnar spacing $< \lambda$) and cannot radiate efficiently. Therefore, radiation propagation is predominantly mediated by the radiative field originating from surface plasmons on the particle's exterior. Unlike the randomly oriented interior plasmons, exterior plasmons retain an overall directionality along the incident polarization. As a result, exterior plasmonic currents are more sensitive to $\rho(B, \theta) \propto \cos^2\theta$. This sensitivity is mapped onto the experimentally observed anisotropic *B*-dependent arrival delay (or propagation velocity).

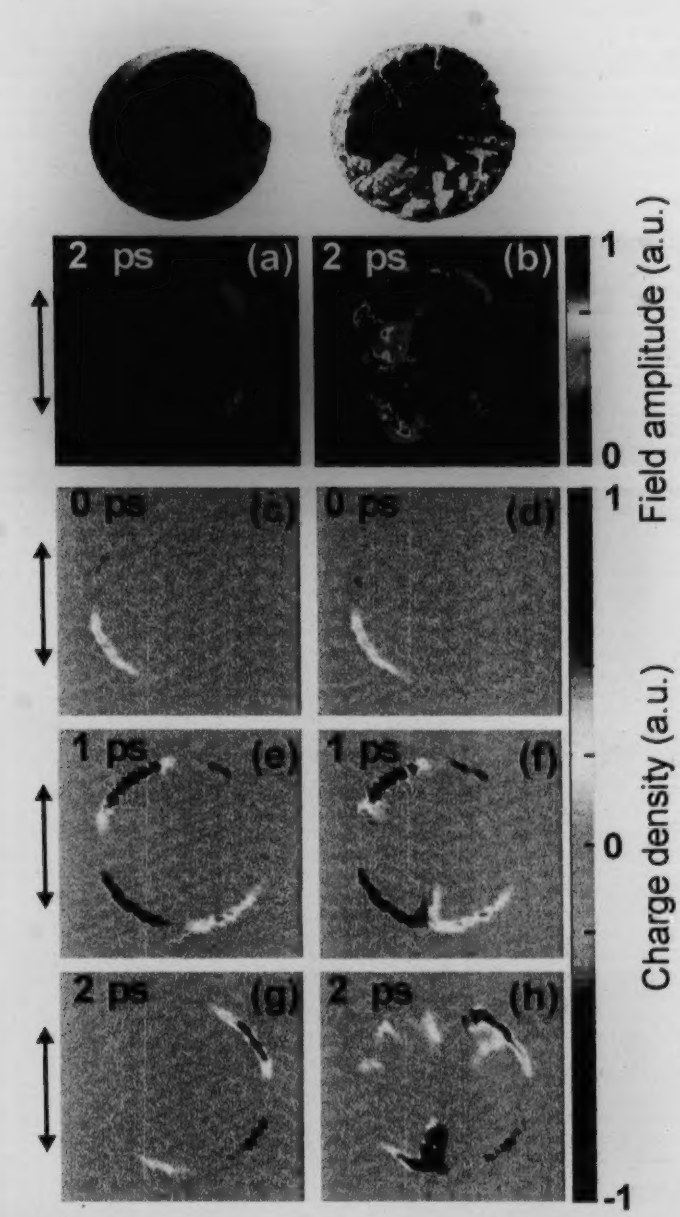

Figure 5.17. The top panels illustrate the solid (left) and porous (right) structures employed in three-dimensional FDTD, which use spatial and temporal resolutions of 5 μm and 5 fs, respectively. A quadrant of the particles is removed for illustrative purposes to highlight the internal structures. Electric field amplitude images of single-cycle THz pulse excitation of (a) a solid Ni spheroid and (b) a porous Ni spheroid 2 ps after the arrival of the THz pulse. Corresponding charge density images for a solid Ni spheroid [(c),(e),(g)] and a porous Ni spheroid [(d),(f),(h)] at various times. The arrows depict the polarization orientation of the incident electric field.

To further explore the effect of particle morphology and to visualize the interior surface plasmons within the porous particles, comparative three-dimensional FDTD analyses are performed of the THz electromagnetic responses of a solid and a porous spherical particle having morphology and size matching those used in the experiments. Figure 5.17 (a) and 5.17 (b) show the electric field amplitude spatial distribution for both Ni particles taken 2 ps after 1 ps wide THz pulse excitation. For the spherical particle, the electric field near the outer surface is weak and symmetrically distributed. In contrast, the porous particle shows spatial field confinement at the voids. To map and to visualize the spatial distribution of the surface currents on both particles, the electromagnetically induced surface charge is plotted. For representative illustration, the surface charge distribution is shown along the mid-plane of the particles parallel to the incident field polarization. It should be noted that due to the large volume of simulation data, the plots in Figure 5.17 are based on electric field data from every second point, and hence have a minimum resolution of 10 μm. Since the charge distribution is obtained from the spatial derivative of the field data, the resolution of the charge distribution maps is 20 μm. As shown in Figure 5.17 (c) and 5.17 (d), the incident pulse at time $t = 0$ ps induces similar bipolar charge distributions at the surfaces of both solid and porous particles. Later, at time $t = 1$ ps, [Figure 5.17 (e) and 5.17 (f)] a quadrupole charge distribution is evident in the particles where two halves of the outer particle surfaces oscillate at opposite polarity. The frames at $t = 2$ ps [Figure 5.17 (g) and 5.17 (h)] clearly illustrate high surface charge accumulation within the columnar structures of the porous particle. Over the excitation interval, the porous spheroid exhibits similar quadrupolar exterior charge accumulation as the solid spheroid, albeit with additional isotropically distributed interior charge accumulation. Thus, whereas the THz electric field interacts with only the exterior of the solid particle, the porous particle exhibits significant charge accumulation and electric field confinement within the particle voids. These simulations provide evidence of the existence of electromagnetically induced charge motion within the particle voids (giving rise to interior surface plasmons), which has been experimentally and phenomenologically shown to be the origin of the observed isotropic photonic magnetoresistance effect in the porous particles.

5.7 Electron-Spin-Dependent Terahertz Particle-Plasmon-Mediated Transmission

A composite medium consisting of F/N metallic nano-layers may show enhanced magnetoresistance relative to a purely F medium. The enhancement arises due to the transport of spin-polarized electrons from the F metal into the N metal, giving rise to a spin-dependent interface resistance. This can be most easily accomplished by simply applying a voltage across an F/N interface, as shown in Figure 5.18 (a). Another method to drive conduction electron current across an F/N interface is by an electromagnetic wave. Consider an F/N composite particle with dimensions much smaller than the incident electromagnetic wavelength. When the electromagnetic wave impinges on the particle, the electric field associated with the wave can coherently induce conduction electron current flow from the F medium to the N medium, as shown in Figure 5.18 (b). Spin-polarized electrons will accumulate in the N medium over the duration of a half-cycle of the electromagnetic wave, and spin polarization is lost due to random scattering at a rate $1/T_2$. So long as the spin-polarized charge driven by the incident electromagnetic field across an F/N interface occurs over time scales comparable to T_2, non-equilibrium accumulation of spins will give rise to a spin-dependent interface resistance analogous to the DC case. As spin relaxation times are typically on the order of picoseconds [1, 9, 10], observation of this *electromagnetically driven* spin accumulation effect requires electromagnetic wave excitation of a subwavelength F/N structure at THz frequencies or below.

To observe electromagnetically driven spin accumulation, subwavelength F/N spinplasmonic structures are fabricated consisting of Co microparticles partially coated with several Au nano-layers, as shown in Figure 5.19. The 45 ± 2 nm thick Au layers are sputter deposited on Co particles ensembles having dimensions ranging from 40 μm to 140 μm and an average dimension of 74 ± 23 μm. A single deposition coats the exposed regions of the Co particles with a thin Au layer. The distributed Au coverage is increased by re-orienting the particle collections after each deposition to expose fresh, uncovered Co particles and re-depositing another 45 ± 2 nm thick Au layer. This procedure is repeated to achieve the desired Au coverage of the particle ensemble. X-ray photoelectron spectroscopy analysis reveals that the percentage Au surface compositions of the three samples are 35 ± 2 %, 42 ± 2 % and 77 ± 2 %.

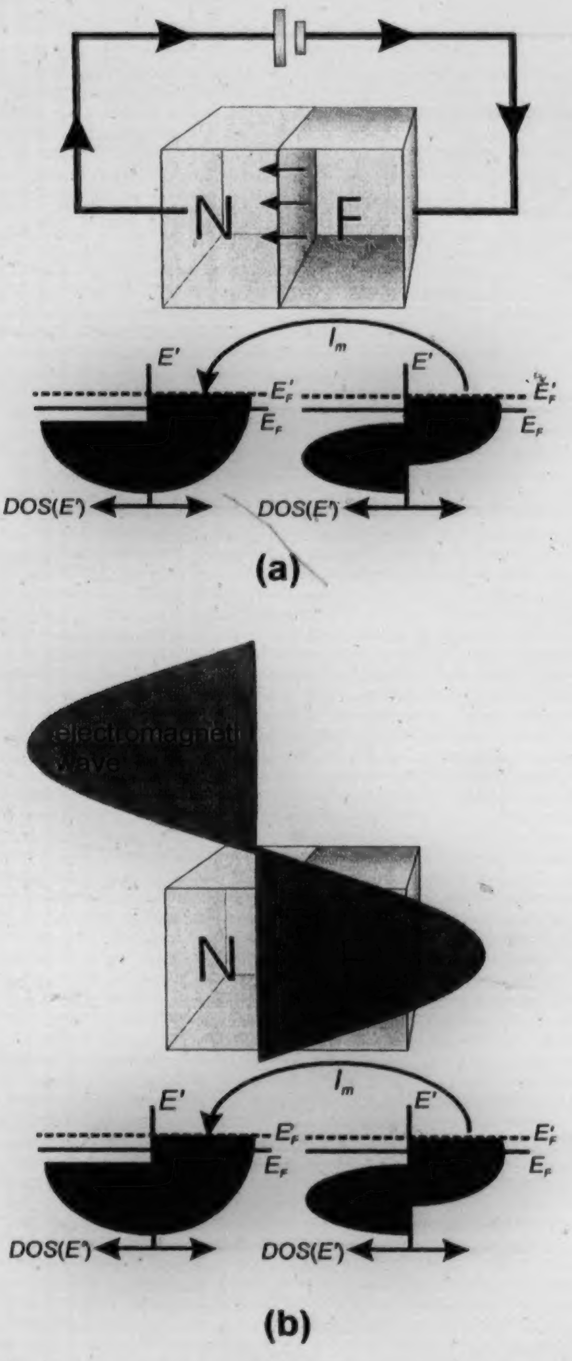
N
F
I_m
E'
E'
E_F'
E_F
E_F'
E_F
DOS(E')
DOS(E')
(a)
electromagnetic wave
N
I_m
E'
E'
E_F
E_F
E_F'
E_F
DOS(E')
DOS(E')
(b)

Figure 5.18. (a) Illustration of a ferromagnetic metal in contact with a nonmagnetic metal with a voltage applied across the interface. (b) Illustration of a ferromagnetic metal in contact with a nonmagnetic metal where spin-polarized current is driven by an incident electromagnetic wave.

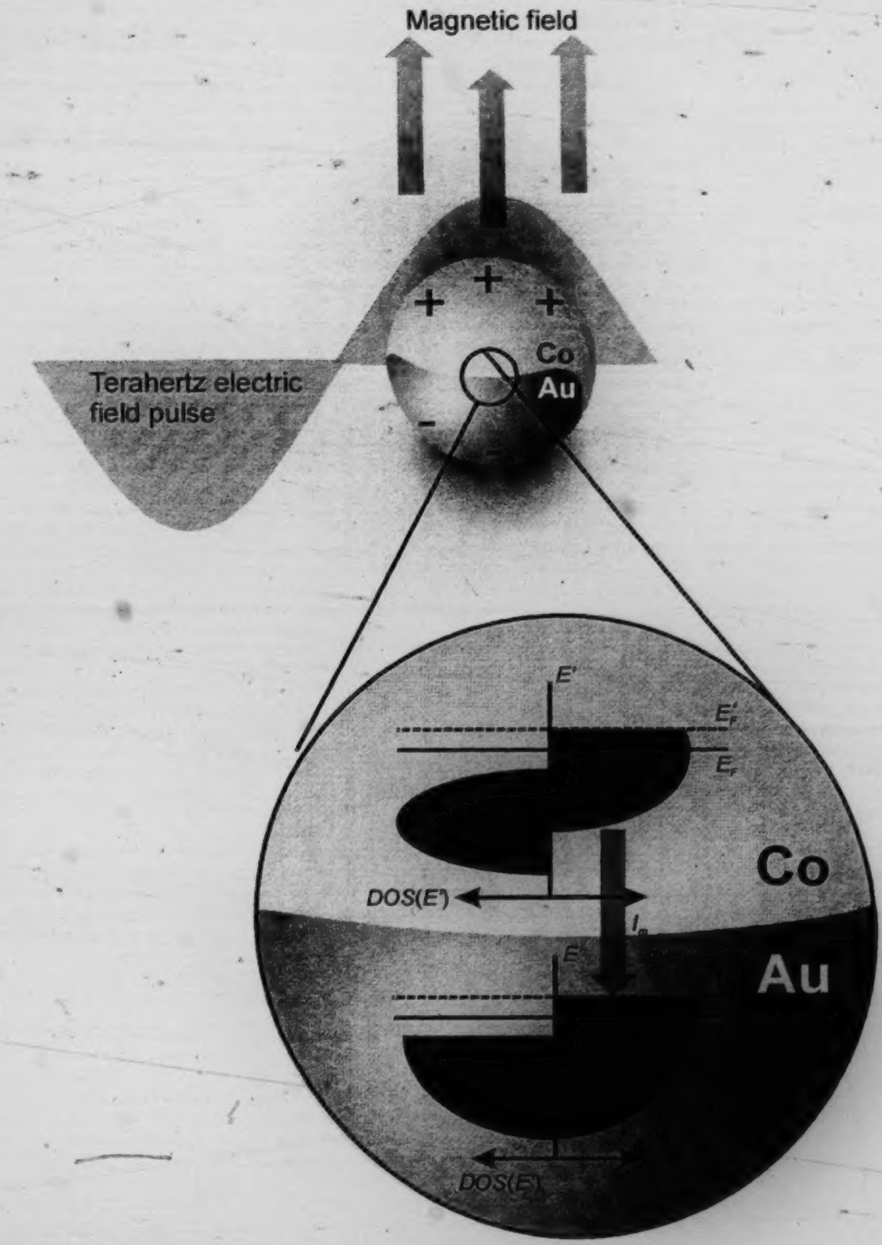
Magnetic field
+
+
+
Co
Au
Terahertz electric field pulse
-
E'
E'F
EF
Co
DOS(E')
Is
E'
Au
DOS(E')

Figure 5.19. Illustration of a subwavelength spinplasmonic structure consisting of a Co particle coated with Au nano-layers excited with a THz electromagnetic field pulse. The spintronic structure is immersed in a magnetic field so as to align the magnetic domains of the Co particle. The incident electromagnetic pulse induces spin-polarized current from the Co particle to the Au layer, creating a spin-dependent interface resistance.

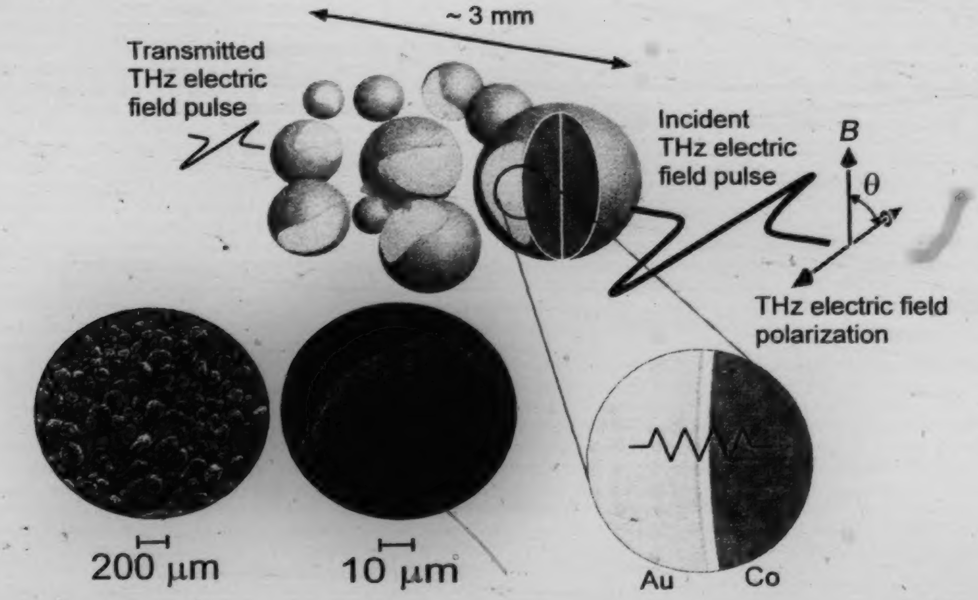
~ 3 mm
Transmitted THz electric field pulse
Incident THz electric field pulse
B
θ
THz electric field polarization
200 μm
10 μm
Au
Co

Figure 5.20. Illustration of near-field particle plasmon coupled transport across a collection of Co/Au bimetallic particles. Spin accumulation at the F/N bimetallic interfaces gives rise to a magnetically modulated interface resistance. The insets depict scanning electron microscope images of the Co particles used in the experiments.

The experimental configuration is introduced in the conceptual illustration in Figure 5.20. A single-cycle 1 ps THz pulse that is incident on a collection of subwavelength sized spinplasmonic Co/Au particles is transported across a length of 3 mm because of near-field dipole-dipole coupling. Electron spin accumulation effects in the Co/Au particles are manifest in the dynamic, temporal characteristics of the transmitted electric field, which are accessed using time-domain spectroscopy (as described in Chapter 2). A 3 mm thick polystyrene sample cell houses the randomly oriented Co/Au particles. The particles are packed into the sample cell to achieve a filling fraction of 0.50 ± 0.05. A plunger lightly depresses on the particle collection in the sample cell to ensure that the fill fraction remains constant during the experimentation period. As shown in Figure 5.19 and Figure 5.20, the spinplasmonic Co/Au structures are immersed in a biasing magnetic field, which is aligned at an angle θ with respect to the incident THz polarization. Since a single Co particle consists of many magnetic domains, an externally applied magnetic field is required to align the magnetic domains to enable non-equilibrium spin effects. When no magnetic field is applied, the magnetizations of the magnetic domains are randomly aligned and the electrons in the Co metal are not spin-polarized. However, when an external magnetic field is applied to the spintronic structure, the magnetic domains, and thus the electron spins, in the Co particle become aligned. In this case, the incident THz electromagnetic wave induces spin-polarized current from the Co particle into the Au layer which causes a spin-dependent interface resistance.

The interface resistance arising from electron spin accumulation directly influences the THz electric field transmission through the ensemble of F/N particles. The current density associated with the THz non-resonant particle plasmon on an individual particle crosses the F/N interface of area A_i and responds to the total resistance within a volume $\sim\alpha A_i$ via Ohm's law $j(t) \propto E_{in}(t)\ /\ [\mathrm{R}_{\mathrm{tot}}(B)\ A_i]$, where $\mathrm{R}_{\mathrm{tot}}(B)$ is the sum of several contributions:

$$\mathrm{R}_{\mathrm{tot}}\,(B) = \mathrm{R}_{\mathrm{Au}} + \mathrm{R}_{\mathrm{Co}}\,(B) + \mathrm{R}_{\mathrm{i}} + \mathrm{R}_{\mathrm{spin}}\,(B) \tag{5.7.1}$$

where R_{Au} is the resistance of Au, $\mathrm{R}_{\mathrm{Co}}\,(B)$ is the resistance of Co incorporating the magnetic field dependent resistance due to AMR, R_{i} is the intrinsic nonmagnetic interface resistance between the metals, and $\mathrm{R}_{\mathrm{spin}}\,(B)$ is the spin-dependent interface resistance. By means of near-field dipole-dipole coupling, resistivity changes within the skin depth of the particle surface influence the THz electromagnetic field propagation through the sample.

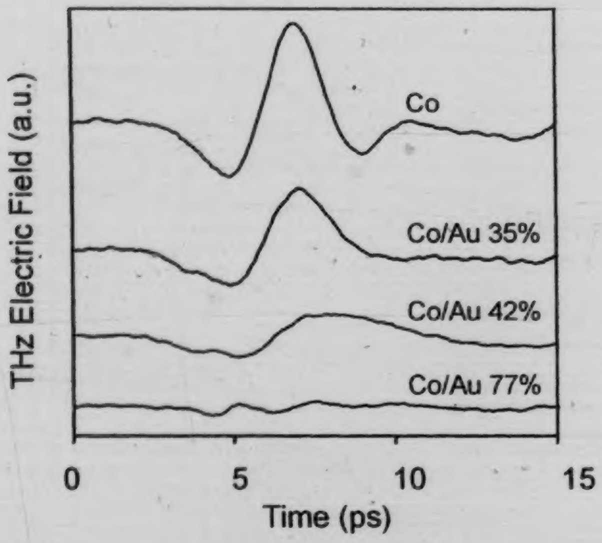

Figure 5.21. Time-domain THz transmission signals through 3 mm thick particle ensembles having varying Au coverage, in zero field.

The role of the bimetallic F/N interface on the transmission through the Co/Au particles in zero field is examined. The field $E_{tr}(t)$ transmitted through Co particle samples having 0 %, 35 %, 42 % and 77 % Au surface coverages (Figure 5.21) indicates that the Au layer causes drastic reduction of the transmissivity independent of magnetic field or electron-spin effects. As Au coverage increases from 0 to 77 %, the amplitude is attenuated by 91 ± 3 %. The attenuation cannot arise from the inherent resistivity of the Au layer, which is much less than that of Co. The marked attenuation that increases with increasing Au coverage is attributed instead to the introduction of an interface resistance at the Co/Au boundary, R_i, which is proportional to the coverage area [24]. This effect has been previously observed and studied in Section 3.9.

The effects of *B* on the THz waveforms transmitted through the composite F/N particles are examined next. Analogous to electrically-driven current in multilayer F/N systems, the electromagnetically driven surface charge on the F/N particles exist in a medium where the resistivity is magnetically influenced via AMR through $R_{Co}(B)$, spin accumulation effects through $R_{spin}(B)$, or both. These contributions can be discriminated by varying the orientation of B. Figure 5.22 (a) and 5.22 (b) show that the transmission through the Co (0% Au) sample exhibits attenuation and delay due to AMR. In a field $B_{\perp}$ perpendicular to the electric field polarization [Figure 5.22 (a)] negligible attenuation and negligible pulse re-shaping are observed whereas both substantial amplitude reduction and pulse re-shaping are observed in a parallel field $B_{\parallel}$ [Figure 5.22 (b)].

The THz pulse transmission is studied through Co and Co/Au particles in $B_{\parallel}$ where both AMR and spin accumulation effects may occur. Figure 5.22 (d) and 5.22(f) show $E_{tr}(t)$ in the presence of a dc magnetic field $B_{\parallel} = 150$ mT (yellow traces) in comparison with $E_{tr}(t)$ in the absence of a magnetic field (blue traces). Pulses transmitted through the Co/Au 35% sample, depicted in Figure 5.22 (d), show increased magnetically induced attenuation and delay relative to the Co (0% Au) sample [Figure 5.22 (b)] when $B_{\parallel}$ is applied. Similar behaviour with greater magnetically induced attenuation and delay is seen in the data for the Co/Au 42% sample [Figure 5.22 (f)]. These B-dependent trends of transmission amplitude and delay for $B_{\parallel}$ are quantified in Figure 5.23 (a) and 5.23 (b). Referring to Figure 5.23 (a), for an increase in $B_{\parallel}$ from 0 mT to 150 mT, $|E_{tr}(t)|$ decreases by 28 ± 3 %, 54 ± 3%, and 73 ± 3% for the Co (0% Au), Co/Au 35%, and Co/Au 42% samples, respectively. The B-dependent electric field attenuation in the Co/Au 42 % sample is about 3 times greater than that in uncoated Co particles or, equivalently, the intensity attenuation is about an order of magnitude greater. Such marked attenuations are accompanied by large temporal delays (relative to their zero-field transmissions) as shown in Figure 5.23 (b). Remarkably, magnetically induced attenuation and delay increase with greater *nonmagnetic* Au coverage of the Co particles. These effects are caused by enhanced magnetoresistance in the Co / Au particles.

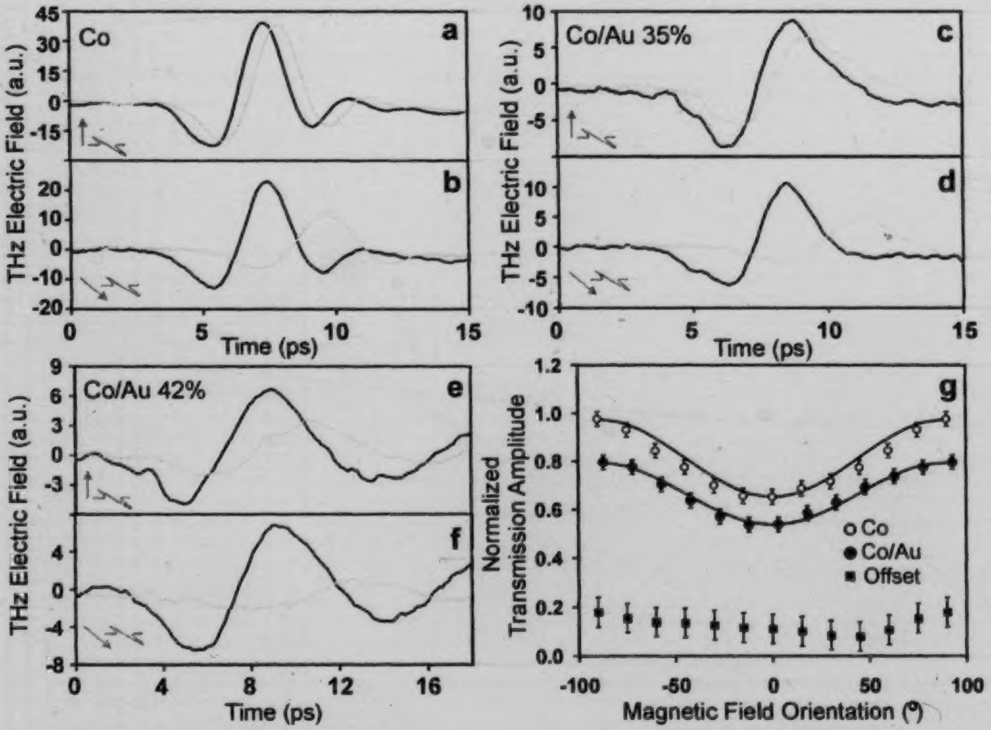

Figure 5.22. Time-domain THz transmission through (a) Co (0 % Au) (perpendicular), (b) Co (0 % Au) (parallel), (c) Co/Au 35 % (perpendicular), (d) Co/Au 35 % (parallel), (e) Co/Au 42 % (perpendicular) and (f) Co/Au 42 % (parallel) particle ensembles for $|B|$ = 0 T (blue traces) and $|B|$ = 150 mT (yellow traces). The diagrams depict the orientation of the B field (arrow) relative to the electric field polarization. (g) Normalized transmission amplitude through 3 mm thick Co (filled circle) and Co/Au (empty circle) particle samples versus the field angle relative to the incident polarization, where $|B|$ = 160 mT. The transmission amplitudes for both samples have been normalized to their respective zero-field amplitudes, and the data have been fitted with $\cos^2\theta$ functions shown by the solid lines. Filled squares represent the offset between the curves for the Co and Co/Au samples. Within error, the offset is independent of the B orientation.

Spin accumulation occurs in the F/N microparticles when the surface domains of the Co particles are much larger than the spin diffusion length in the Au film. This requires the magnetization to be uniform in any direction and is therefore isotropic with respect to field angle. To demonstrate this property of the Co/Au samples, Figure 5.22 (g) shows the transmission amplitude for 3 mm thick Co and Co/Au samples versus the field angle, θ, with respect to the electric field polarization. Both curves have been normalized to their $B = 0$ mT amplitudes, respectively. As seen in Figure 5.22 (g), the transmission amplitude for the Co ensemble exhibits a $\cos^2\theta$ dependence, providing direct evidence that the magnetically induced attenuation in the Co ensemble is a direct manifestation of AMR. The curve for the Co/Au sample also shows a $\cos^2\theta$ dependence but is offset from the curve for the Co sample by a constant amount that is independent of θ within experimental error. This offset indicates isotropically enhanced B-dependent losses in the Co/Au particles and corresponds to the θ- independent spin contribution to the magnetic attenuation in the coated particles. It is noteworthy that at $\theta = 90°$, the normalized transmission through the Co sample is nearly unity, since AMR is negligible. Thus, spin accumulation effects in the Co/Au samples can be studied with minimal AMR effects by simply re-orienting B to 90° with respect to the electric field polarization vector. As shown in Figure 5.22 (a), the field $E_{tr}(t)$ transmitted through Co (0% Au) particles in $B_\perp$ shows insignificant attenuation (< 2 %). In comparison, $E_{tr}(t)$ transmitted through the Co/Au 35 % and Co/Au 42 % samples [Figure 5.22 (c) and 5.22 (e)] exhibit large magnetically-induced attenuation in a $B_\perp$ field. This behaviour is shown quantitatively in Figure 5.23 (c). As illustrated in this plot, $|E_{tr}(t)|$ is substantially attenuated by 25 ± 3 % and 52 ± 3 % for the Co/Au 35 % and Co/Au 42 % samples, respectively, at a field $B_\perp = 150$ mT. Furthermore, in contrast with the temporal behaviour of $E_{tr}(t)$ in a $B_\parallel$ field, $E_{tr}(t)$ in a $B_\perp$ field is characterized by a much shorter magnetically induced temporal delay. This is evidence that the origin of the B-dependent pulse attenuation, and therefore of the magnetoresistance, in a $B_\perp$ field is different from the B-dependent effects observed in $B_\parallel$, which include both spin accumulation and AMR mechanisms.

An essential characteristic of spin-dependent effects in spintronic devices is the hysteretic behaviour of the magnetoresistance under magnetic field cycling. As shown in Figure 5.23 (d) and 5.23 (e), by cycling $B_\perp$ from zero to 250 mT and then back to zero, there is magnetoresistance hysteresis and remanence in the Co/Au samples. At the return of the B cycle, the zero field amplitudes are reduced by 25 ± 3% and 45 ± 3% for the Co/Au 35 % and Co/Au 42 % samples, respectively. The hysteresis and remanence of the THz transmission is consistent with magnetization measurements of the Co particles shown in the inset of Figure 5.23 (e) that indicate an inflection point in the magnetization at 300 mT, saturation at ~ 1 T, and hysteresis upon magnetic field cycling.

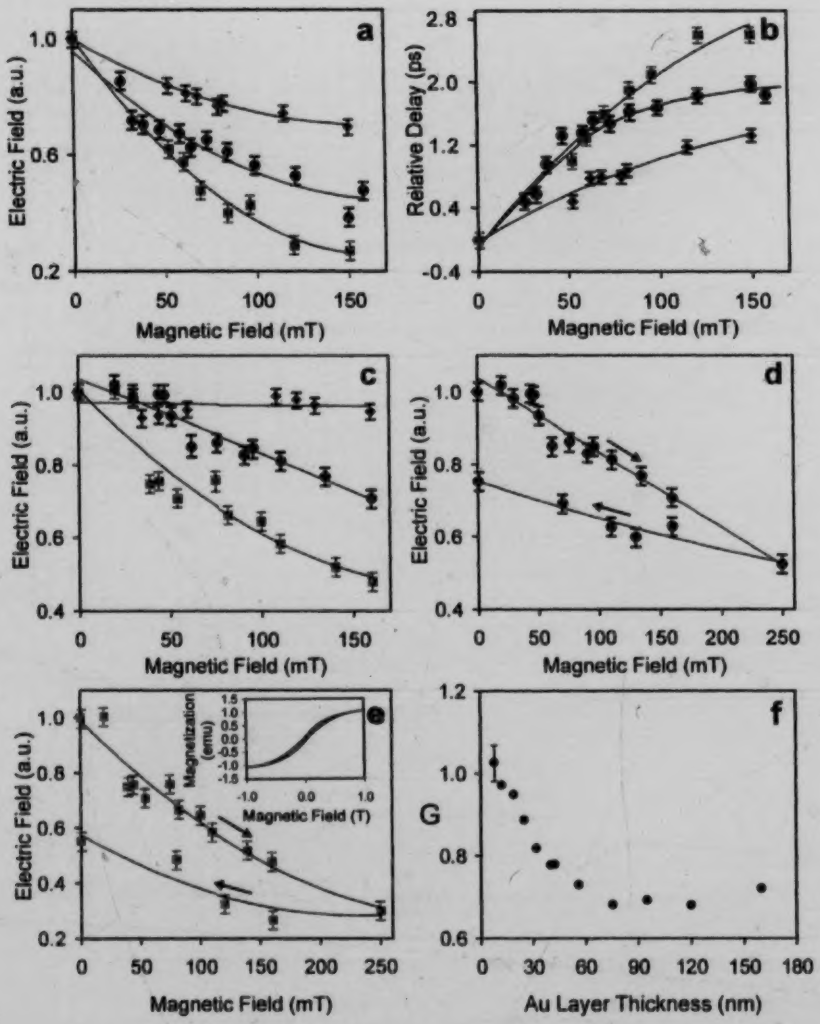

Figure 5.23. (a) THz electric field amplitude transmitted through Co (0% Au) (diamonds), Co/Au 35 % (circles) and Co/Au 42 % (squares) particle ensembles versus magnetic field strength in the parallel configuration. (b) Delay of the transmitted THz pulse through Co (0% Au) (diamonds), Co/Au 35 % (circles) and Co/Au 42 % (squares) particle ensembles versus magnetic field strength for the parallel configuration. (c) THz electric field amplitude transmitted through Co (0% Au) (diamonds), Co/Au 35 % (circles) and Co/Au 42 % (squares) particle ensembles versus magnetic field strength in the perpendicular configuration. The transmitted electric field amplitude versus the magnetic field strength for the Co/Au 35 % and Co/Au 42 % particle ensembles are shown in (d) and (e), respectively. The inset in (e) shows magnetization measurements of the Co particles up to ±1.0 T. (f) Normalized, time-averaged electric field amplitude (in an applied field of B = 160 mT) transmitted through 3 mm thick samples of Co/Au particles versus the Au film thickness in the perpendicular configuration.

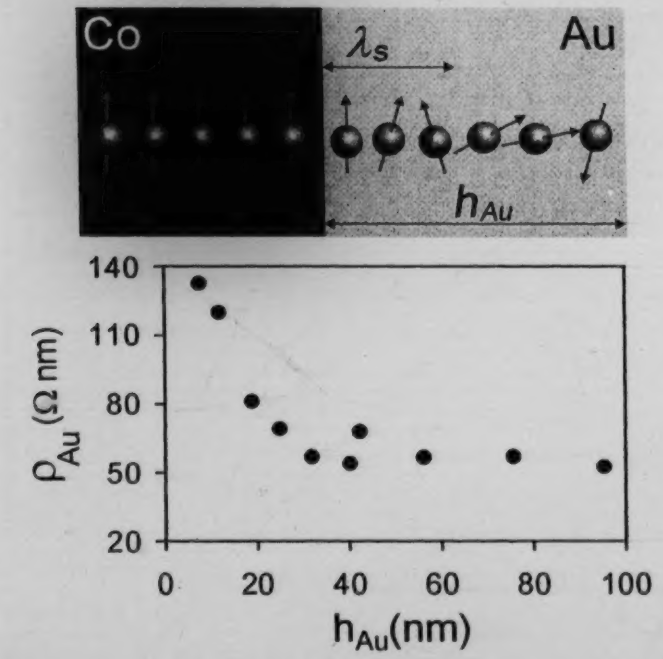

Figure 5.24. The upper image depicts an illustration of spin accumulation in the Au layer. The lower image shows the measured resistivity of the Au layer versus the film thickness. The resistivities are measured using a four-point probe technique on witness Au films deposited on glass slides.

A fundamental quantitative parameter that governs spin accumulation in Au is the spin diffusion length, λ_s, (Figure 5.24) which determines the spatial extent of non-equilibrium spin injection into the nonmagnet [1]. To support the model and to investigate the relationship between the Au film thickness, h_{Au}, and λ_s, additional experiments are performed in a field $B_{\perp}$ with thirteen Co/Au samples having identical Au surface coverages but variable Au layer thicknesses ranging from 0 to 160 nm. In discussing the semi-quantitative model, the single-cycle THz pulse drives spin-polarized conduction electrons across the F/N interface for a time ~ 1 ps. Effects that arise from dynamics on a time scale > 1 ps can have no effect on the attenuation of the transient pulse. The diffusion length for the limiting time of τ_i = 1 ps is $\lambda_i = \sqrt{D_e \tau_i}$ = 85 nm, where D_e is the electron diffusivity and is deduced using an Einstein relation and the resistivity ρ_{Au} of the Au film (refer to inset of Figure 5.24 and note that ρ_{Au} is approximately constant for h_{Au} > 40 nm). In this transient experiment, the interface resistance from spin accumulation is not expected to change for samples with $h_{Au} > \lambda_i$ because diffusing carriers cannot reach portions of any film thicker than λ_i. The diffusive spin accumulation model is not valid for h_{Au} comparable with the electron mean free path, on the order of tens of nm. The resistivity, mean scattering time and spin relaxation time are all very sensitive to film morphology, and data in this range of h_{Au} do not merit a rigorous fit. However, a valid prediction of the model is that the interface resistance will be determined by spin accumulation within a spin depth $\lambda_s = \sqrt{D_e \tau_S}$, where τ_s is the spin relaxation time in the Au film, for any sample with $h_{Au} > \lambda_s$ [25]. The spin-dependent interface resistance is

$$R_{\text{spin}}\,(h_{Au} > \lambda_s) = Q^2\, \rho_{Au}\, \lambda_s \,/\, A_i \tag{5.7.2}$$

where Q is the fractional spin polarization of electrons crossing the interface.

As shown in Figure 5.23 (f), the normalized, time-averaged, field dependent transmission, G = $< E_{tr}\,(160\ \text{mT}) > / < E_{tr}\,(0\ \text{mT}) >$, is very sensitive to small values of h_{Au} but changes little for h_{Au} > 75 nm. These data are consistent with our prediction that R_{spin} should not change for $h_{Au} > \lambda_i$. The asymptotic approach to a constant value also permits us to identify a lower bound for the spin diffusion length, $\lambda_s \geq 75$ nm.

Using this value of λ_s, a measured value $\rho_{Au} = 5.5 \times 10^{-8}\ \Omega$ m, and a typical value of Q in the range 20 % to 40 %, an estimate of the interface resistance contribution arising from spin accumulation from Equation (5.7.2) is found to be in the range $R_{\text{spin}}\, A_i = 2 \times 10^{-16}\ \Omega\ \text{m}^2$ to $7 \times 10^{-16}\ \Omega\ \text{m}^2$. As discussed above, the nonmagnetic, spin-independent attenuation effects that are reported are believed to be entirely dominated by interface resistance. For Q in the range between 20 % to 40 %, the calculated contribution to interface resistance from spin accumulation is between 8 % to 29 % of the field independent contribution from interface resistance, which has been estimated to be $R_i A_i = 2.4 \times 10^{-15}\ \Omega\ \mathrm{m}^2$ [26]. There is reasonable agreement, given the limitations of the semi-quantitative model, between the calculation and the 30% attenuation observed in Figure 5.23 (f) for $h_{Au} > 75$ nm.

A lower bound for the spin relaxation time T_2 that corresponds with $\lambda_s = 75$ nm is $T_2 = \tau_s = \lambda_s^2 / D_e \approx 1$ ps. Using a Drude scattering time of $\tau = 12$ fs (derived from $\rho_{Au} = 5.5 \times 10^{-8}\ \Omega$ m), a spin flip probability of $a = \tau / T_2 = 1 \times 10^{-2}$ is obtained, as an upper bound. This is in good agreement with a previously measured value for Ag films of $a = 4.0 \pm 0.5 \times 10^{-3}$ [27].

5.8 Conclusion

In this Chapter, two manifestations of electron-spin-dependent phenomena have been demonstrated in the THz particle plasmon mediated transmission through ensembles of F particles and F/N composite particles. Using ensembles of subwavelength size F particles, it has been experimentally shown that the amplitude and arrival time of the THz electromagnetic wave transmission are strongly dependent on the orientation of an externally applied magnetic field. The B orientation dependence of the transmission has the same magnetic field orientation dependence as the electrical AMR inherent to bulk F metals. Thus, the experiments demonstrate a THz plasmonic manifestation of the AMR effect, a phenomenon conventionally associated with electronic transport. Moreover, the dependence of the THz electric field transmission anisotropy on the ferromagnetic particle morphology is explored. Comparative studies of highly porous and smooth ferromagnetic particles immersed in a magnetic field show that the porous particle geometry can effectively erase the magnetic anisotropy in the THz electric field transmission amplitude. The discovery of a plasmonic AMR effect paves the way for the development of THz plasmonic magnetoresistive devices where modulation is achieved via an externally applied magnetic field.

Furthermore, using ensembles of subwavelength size bimetallic F/N microparticles, it has been shown that the electron spin accumulation effect can influence the THz electric field transmission through the particles. Ferromagnetic particles coated with N metal nano-layers exhibit an enhanced magnetic field sensitive attenuation of the THz electromagnetic field propagated through the sample. The magnetic effect for the coated F particles differs because the dependence on the magnetic field angle is unique and the magnitude of the THz electric field attenuation is *an order of magnitude larger*. The mechanism in the F/N particles is related to dynamic, electromagnetically induced spin accumulation in the N medium. The experimental results, presented with a semi-quantitative model of non-equilibrium spin accumulation in the N layer, represent a unique manifestation of electron-spin-dependent phenomena in the THz electromagnetic interaction with metallic microparticles. Now that a spinplasmonic transport phenomenon has been shown, a novel avenue has been opened in both the fields of spintronics and plasmonics. The ability to magnetically manipulate near-field mediated light transport through metallic particles via electron spin promises another degree of freedom in the development of light-based information devices.

Chapter 5 References

[1] I. Zutic, J. Fabian, and S. Das Sarma, "Spintronics: Fundamentals and applications," *Reviews of Modern Physics*, vol. 76, pp. 323-410, 2004.

[2] C. Kittel, *Introduction to Solid State Physics*, 7th ed. New York: John Wiley & Sons, 1996.

[3] D. Jiles, *Introduction to Magnetism and Magnetic Materials*, 2nd ed. Boca Raton, Florida: CRC Press, 2000.

[4] G. A. Prinz, "Device physics - Magnetoelectronics," *Science*, vol. 282, pp. 1660-1993, 1998.

[5] N. Spaldin, *Magnetic Materials: Fundamental and Device Applications*. Cambridge: University Press, 2003.

[6] S. A. Wolf, D. D. Awschalom, R. A. Buhrman, J. M. Daughton, S. von Molnar, M. L. Roukes, A. Y. Chtchelkanova, and D. M. Treger, "Spintronics: A spin-based electronics vision for the future," *Science*, vol. 294, pp. 1488-1495, 2001.

[7] J. Velev, R. F. Sabirianov, S. S. Jaswal, and E. Y. Tsymbal, "Ballistic anisotropic magnetoresistance," *Physical Review Letters*, vol. 94, pp. 127203, 2005.

[8] M. Johnson, "Bilayer embodiment of the bipolar spin switch," *Applied Physics Letters*, vol. 63, pp. 1435-1437, 1993.

[9] M. Johnson, "Spin Accumulation in Gold Films," *Physical Review Letters*, vol. 70, pp. 2142-2145, 1993.

[10] M. Johnson, "Spin polarization of gold films via transport," *Journal of Applied Physics*, vol. 75, pp. 6714-6719, 1994.

[11] W. L. Barnes, A. Dereux, and T. W. Ebbesen, "Surface plasmon subwavelength optics," *Nature*, vol. 424, pp. 824-830, 2003.

[12] P. Andrew and W. L. Barnes, "Energy transfer across a metal film mediated by surface plasmon polaritons," *Science*, vol. 306, pp. 1002-1005, 2004.

[13] E. Ozbay, "Plasmonics: Merging Photonics and Electronics at Nanoscale Dimensions," *Science*, vol. 311, pp. 189-193, 2006.

[14] A. V. Krasavin, A. V. Zayats, and N. I. Zheludev, "Active control of surface plasmon-polaritons," *Journal of Optics A - Pure and Applied Optics*, vol. 7, pp. S85-S89, 2005.

[15] D. M. Newman, M. L. Wears, and R. J. Matelon, "Plasmon transport phenomena on a continuous ferromagnetic surface," *Europhysics Letters*, vol. 68, pp. 692-698, 2004.

[16] G. Duchs, G. L. J. A. Rikken, T. Grenet, and P. Wyder, "Magnetotransverse scattering of surface plasmon polaritons," *Physical Review Letters*, vol. 87, pp. 127402, 2001.

[17] A. Gerber, A. Milner, B. Groisman, M. Karpovsky, A. Gladkikh, and A. Sulpice, "Magnetoresistance of granular ferromagnets," *Physical Review B*, vol. 55, pp. 6446-6452, 1997.

[18] J. Kondo, "Anomalous Hall Effect and Magnetoresistance of Ferromagnetic Metals," *Progress of Theoretical Physics*, vol. 27, pp. 772-792, 1962.

[19] T. R. McGuire and R. I. Potter, "Anisotropic Magnetoresistance in Ferromagnetic 3d Alloys," *IEEE Transactions on Magnetics*, vol. 11, pp. 1018-1038, 1975.

[20] P. Beckmann and A. Spizzichino, *The Scattering of Electromagnetic Waves from Rough Surfaces*. New York: Pergamom Press, 1963.

[21] K. J. Chau and A. Y. Elezzabi, "Photonic Anisotropic Magnetoresistance in Dense Co Particle Ensembles," *Physical Review Letters*, vol. 96, pp. 033903, 2006.

[22] B. J. Messinger, K. Ulrich von Raben, R. K. Chang, and P. W. Barber, "Local fields at the surface of noble-metal microspheres," *Physical Review B*, vol. 24, pp. 649-657, 1981.

[23] K. J. Chau and A. Y. Elezzabi, "Terahertz transmission through ensembles of subwavelength-size metallic particles," *Physical Review B*, vol. 72, pp. 075110, 2005.

[24] K. J. Chau and A. Y. Elezzabi, "Effect of interface resistance on terahertz pulses in bimetallic microparticles," *Physical Review B*, vol. 73, pp. 085419, 2006.

[25] M. Johnson and R. H. Silsbee, "Thermodynamic analysis of interfacial transport and of the thermomagnetoelectric system," *Physical Review B*, vol. 35, pp. 4959-4972, 1987.

[26] R. Godfrey and M. Johnson, "Spin injection in mesoscopic silver wires: Experimental test of resistance mismatch," *Physical Review Letters*, vol. 96, pp. 136601, 2006.

[27] A. Y. Elezzabi, M. R. Freeman, and M. Johnson, "Direct Measurement of the Conduction Electron Spin-Lattice Relaxation Time T1 in Gold," *Physical Review Letters*, vol. 77, pp. 3220-3223, 1996.

Chapter 6:

Terahertz Electromagnetic Wave Propagation in Mesoscopic Chiral Materials

6.1 Background

Throughout this thesis, it has been shown that structures with subwavelength scale features can possess electromagnetic properties departing from those of the constituent material. An additional, important class of such materials is chiral media. In the most general sense, a medium is chiral if its structure is mirror-asymmetric. A common example of a chiral medium is a human hand, as shown in Figure 6.1. A human hand is mirror-asymmetric since a left hand cannot be superimposed on a right hand without taking it out of plane. Moreover, since the mirror image of a left hand is a right hand, left and right hands are enantiomers of each other. In the case when a structure's subwavelength micro-, nano-, or atomic-scale molecular arrangement is chiral, electromagnetic interaction with the structure may lead to a unique phenomenon known as optical activity. Optical activity occurs when a medium preferentially interacts with either the left- or right- circularly polarized electromagnetic wave components, causing a polarization circularization and/or polarization rotation of the interacting radiation. In this manner, a medium's subwavelength scale structural chirality is mapped onto a polarization transformation of incident electromagnetic waves.

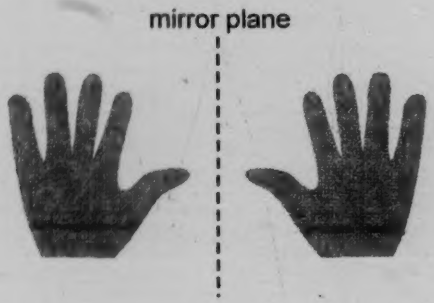

Figure 6.1. A human hand is a common example of a chiral medium.

The study of chiral media and its associated optical activity has had a long history in science. Since Arago's first observation of light polarization rotation in a chiral quartz crystal in 1811, the study of chiral light-matter interaction has been an impetus for progress in chemistry [1], biology [2], optics [3], and the study of fundamental symmetries in particle physics [4, 5]. This wide influence is due to the sheer diversity of chiral manifestations. At different levels, seashells, bacteria, amino-acids, and even elementary particle interactions all show different proportions of left- and right- handed occurrences. Of the many manifestations of chirality, the helical conformation is widely considered the most universally significant. The significance of the helical shape in affecting light polarization was demonstrated over a century ago [6, 7] in experiments showing polarization rotation of radiation transmitted through helices, which qualitatively established the structural similarities between macroscopic helices and microscopic optically active molecules [8, 9]. Since then, extensive theoretical and experimental work has been performed on the electromagnetic properties of helices. Theoretical frequency-domain calculations [10-18] and experimental work in the visible and microwave range [19-25] have revealed that the optical activity of helices fundamentally arises from the anisotropic scattering of left- and right- circularly polarized light from the geometrical shape of the helix. Owing to the inherent complexity of the helical geometry, analytical descriptions of light scattering in helices have proven to be formidable [26], and to date, all theoretical models have employed simplifying approximations. In some approximations light interaction with a helix is described by multiple-scattering theory [27] where the helix is modeled as a collection of point-polarizable scatterers arranged along a helical path. Bustamante et al. [10] described the radiation scattered from a helix using the Born approximation, which neglects the retarded interaction between point scatterers on the helix. Furthermore, Jaggard et al. [8] proposed a quasi-static approximation wherein scattering from a helical element is modeled by re-radiation from coupled magnetic and electric dipoles. In this particular formalism, a single helix turn is decomposed into an effective loop and stem [28], and electromagnetically induced current in the loop and the stem gives rise to inter-coupled magnetic and electric dipoles, respectively. While these theoretical works have greatly contributed to current understanding of radiation scattering from a helix, they do not capture the full complexity of the phenomenon.

Indeed, physical insights into the optical activity associated with a helix may require new experimental methods both to probe and to comprehend polarization rotation in helical structures. To date, experimental investigations of helices have been restricted to irradiance-based experiments where the helix is excited by continuous electromagnetic radiation [19-25]. While such continuous wave experiments have enabled the extraction of the complex material parameters of helices (see, for instance, Ref. [25]), they do not permit investigation of the transient scattering mechanism which gives rise to optical rotation and polarization circularization. An alternative method to study optical activity from a helix is to excite the structure with an ultrashort electromagnetic pulse and examine the time-domain scattering response. Such time-domain, transient investigations permit a more direct study of optical activity since scattering mechanisms within the helix can be ascertained from the arrival time and the instantaneous polarization state of the scattered radiation. Moreover, transmitted waveforms can be parsed to separate the complex interactions occurring in the helix.

This chapter explores the THz optical activity of a helical structure by studying its time-domain response to THz electromagnetic pulse excitation. By dynamically accessing the THz electric fields scattered from a helix, optical activity signatures are correlated with the arrival time and polarization state of the scattered radiation. To fully characterize the properties of the helix, the helix is studied in two unique configurations where the THz electromagnetic wave is incident 1) parallel to the helical axis and 2) transverse to the helical axis, as shown in Figure 6.2. In Section 6.2, it is shown that for axial THz electromagnetic wave propagation, polarization circularization of the transmission arises from multiply scattered electromagnetic waves forming resonant, helical propagation modes. In contrast, for transverse illumination of the helix, it is demonstrated in Section 6.3 that polarization rotation of the forward scattered transmission results from non-resonant, singly scattered electromagnetic waves from the helical structure. The work in this Chapter has been published in *Optics Express*, vol. 15, 3557-3567 (2007).

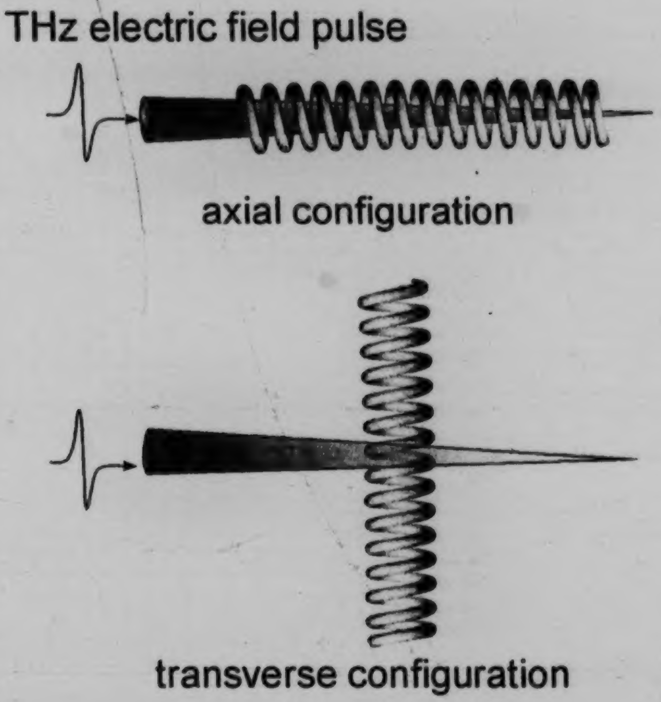

Figure 6.2. THz electromagnetic wave interaction with a helical element in the (top) axial configuration and (bottom) transverse configuration. In these experiments, the THz pulse is focused onto the helix is maximize the amount of electromagnetic signal that interacts with the structure.

6.2 Axial Terahertz Electromagnetic Wave Propagation in a Helical Structure

This section reports on the time-resolved experimental and numerical investigations of few-cycle THz pulse propagation along the axis of a subwavelength size helix. For the measurements, broadband THz electric field excitation (with wavelengths ranging from 3 mm to 200 μm) is employed together with synchronized, polarization-sensitive detection. The model chiral structure studied is an Au-coated Cu helix consisting of m right-handed circular revolutions having a pitch $K = 120 \pm 10$ μm, a wire diameter $b = 60 \pm 2$ μm and a helical centre-to-centre diameter $\delta_h = 295 \pm 10$ μm, as shown in Figure 6.3. The helix is fabricated by carefully winding the thin Cu wire into helical conformation. In this work, a metallic structure is studied (as opposed to a dielectric structure) because optical activity signatures in the metallic structure must arise from scattering (reflection) from the helix. At THz frequencies, metals are perfectly opaque to the radiation due to their large negative permittivity. Thus, THz electromagnetic waves incident on metallic structures are almost completely reflected. The situation is more complicated in a dielectric helical structure, where light can 1) pass directly through the structure, 2) be absorbed within the dielectric, and/or 3) scatter from the surface of the structure. Moreover, broadband excitation is ideal for probing the electromagnetic response of the helix in regimes where $\pi\ \delta_h > \lambda$, $\pi\ \delta_h \sim \lambda$, and $\pi\ \delta_h < \lambda$; in particular, the helix diameter is chosen such that over the wavelength range $0.32 < \pi\delta_h/\lambda < 4.79$ and $K < \lambda$. As shown in Figure 6.4, the THz pulse and the femtosecond probe pulse are co-focused by a 2.5 cm focal length gold-coated parabolic mirror along the axis of the helix. To preclude THz radiation leakage around the helical structure, a 300 μm diameter metallic aperture is placed directly in front of the helix entrance. Since the aperture size is comparable to the wavelength, the aperture strongly diffracts the incident radiation (in Figure 6.4, the THz beam is shown to propagate directly through the helix for illustrative purposes only). That is, the THz radiation will spread out at large angles into the region beyond the aperture, and the aperture effectively behaves like a point source of THz radiation. In our experiments, this "point source" is located in the immediate vicinity of the helix, centred on the helical axis. It should be noted that near-field coupling between the aperture and the exterior of the helix may influence the measured transmission. It will be shown in simulations, however, that this effect is negligible.

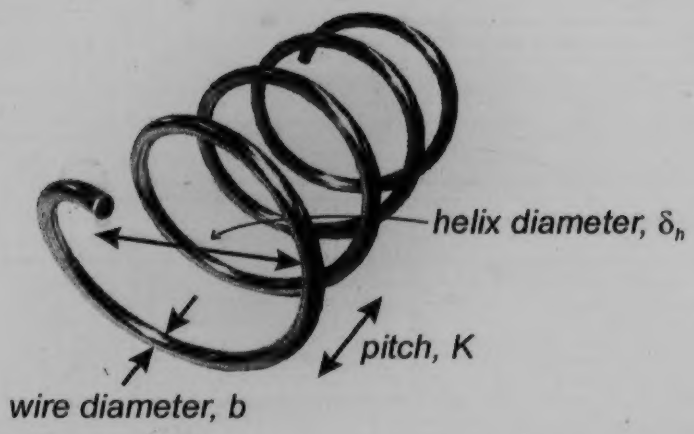
helix diameter, δ_h
pitch, K
wire diameter, b

Figure 6.3. Diagram depicting a helical conformation that is characterized by a wire diameter, pitch, and helix diameter.

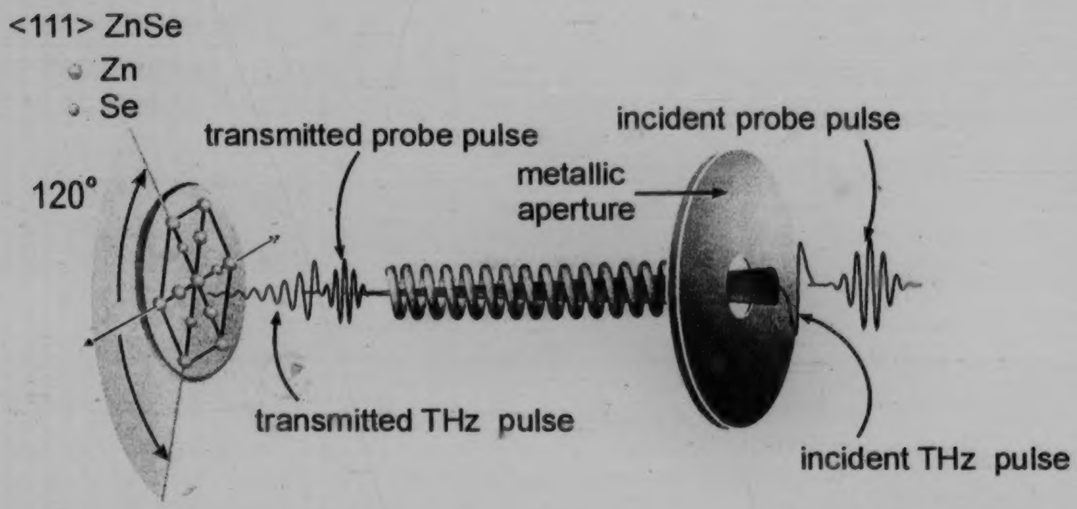
<111> ZnSe
Zn
Se
120°
transmitted probe pulse
incident probe pulse
metallic aperture
transmitted THz pulse
incident THz pulse

Figure 6.4. A diagram of the setup used to characterize the THz on-axis transmission through a subwavelength helix.

Optical activity in bulk media manifests as polarization rotation (tilt in the polarization plane) and/or polarization circularization (transformation from linear polarization to elliptical polarization) of the scattered light. In the experiments, the scattering mechanisms responsible for optical activity are probed by measuring the temporal THz electric field pulse transmitted via axial propagation along helices having various numbers of turns, m. In the experiments, the co-polarized, $E_{\|}(t)$ (parallel to incident polarization), and cross-polarized, $E_{\perp}(t)$ (perpendicular to incident polarization), components of the pulses are measured emerging from helical structures having lengths, L, ranging from 0.50 ± 0.05 mm (m = 4) to 1.52 ± 0.05 mm (m = 12). To explore the optical activity associated with the helix, the transmitted electric field vector is decomposed into orthogonal left-handed (LH) and right-handed (RH) circularly polarized components. The LH [i.e. $E_l(t)$] and RH [i.e. $E_r(t)$] circular components are determined from the linearly polarized field components via the relations $E_l(t)=1/\sqrt{2}[E_{\|}(t)+iE_{\perp}(t)]$ and $E_r(t)=1/\sqrt{2}[E_{\|}(t)-iE_{\perp}(t)]$. Here, $E_{\|}(t)$ and $E_{\perp}(t)$ are aligned with respect to the x- and y-axes, respectively. When facing the direction of wave propagation, right- (left-) circularly polarized radiation rotates in the clock-wise (counter-clockwise) direction. In Figure 6.5, the time-domain left- and right- circular electric field pulses are shown after they emerge from the helical structure. Optical activity manifests as a difference in the propagation time and/or the transmitted amplitude of the left- and right- circularly polarized fields. The transmitted pulse through the aperture does not show optical activity, since the left- and right- circular pulses arrive at similar times and with identical amplitudes. The circularly polarized components of the electric field pulse transmitted through the helices, however, show markedly different behaviour. For helices with m = 4 up to m = 15, there is distinctive, preferential transmission of $E_r(t)$ relative to $E_l(t)$. The difference in the amplitudes of the RH and LH circularly polarized pulses increases as the helix length increases, showing that this effect is cumulative over the length of the helix. Due to the greater transparency of the helix to RH light relative to LH light, the electric field vector, $\mathbf{E}_{tr}(t) = \mathbf{E}_{\parallel}(t) + \mathbf{E}_{\perp}(t)$, transmitted through the helix shows significant polarization circularization, as shown in Figure 6.6. In addition to the preferential attenuation of $E_l(t)$ relative to $E_r(t)$, the helical structure also introduces significant temporal dispersion in both the $E_l(t)$ and $E_r(t)$ waveforms. As m increases, the $E_l(t)$ and $E_r(t)$ waveform durations are progressively broadened, and the waveforms acquire more subsidiary oscillations. Such pronounced, resonating waveforms indicate a geometrically enhanced frequency selectivity of the structure with increasing length.

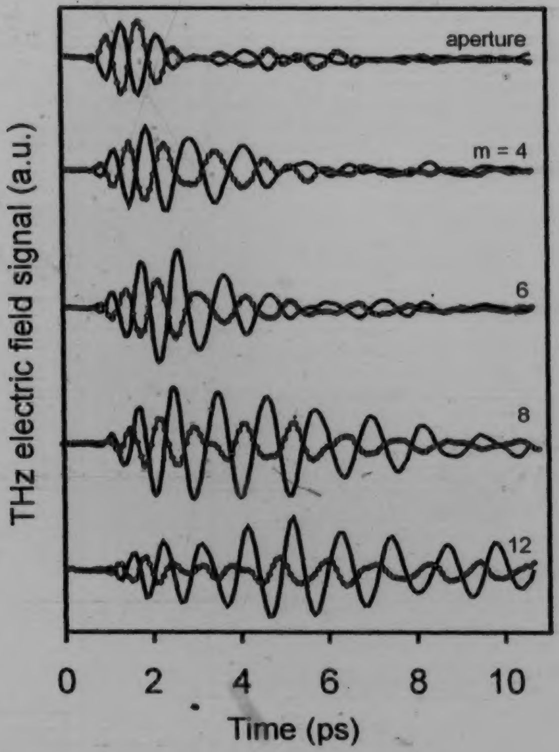

Figure 6.5. The measured right circular $E_r(t)$ (solid line) and left circular $E_l(t)$, (empty circles) electric field pulses through helices of various lengths, along with a reference pulse transmitted through the screening aperture.

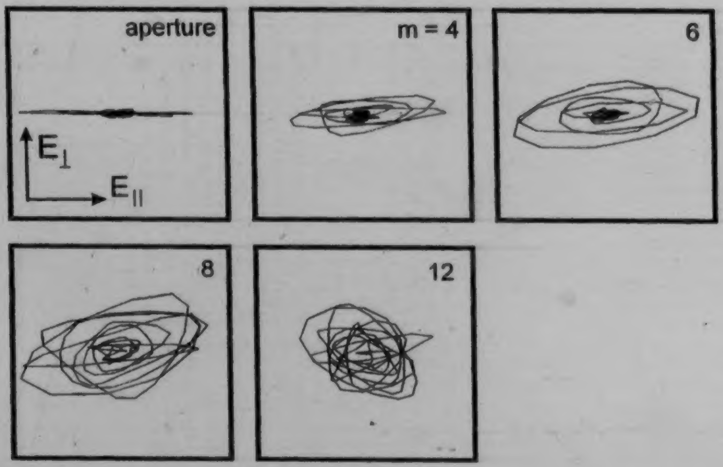

Figure 6.6. Trajectories of the tip of the electric field vector for the transmission through the aperture and helices having m = 4, 6, 8, 10, and 12.

In contrast to irradiance polarization-state measurements, experimental access to the time-domain response of the helix enables direct characterization of the helix's transient optical activity. The helix's transient optical activity is quantified by calculating the instantaneous degree of polarization circularization, $\beta(t) = [I_l(t) - I_r(t)] / [I_l(t) + I_r(t)]$, where $I_{r,l}(t) = E^*_{r,l}(t)E_{r,l}(t)$ are the instantaneous intensities of the RH and LH circularly polarized components. Shown in Figure 6.7 (a) is $\beta(t)$ for various helix lengths (m = 4, 6, 8, and 12) along with $\beta(t)$ for the bare circular aperture. As expected for the aperture transmission, $\beta(t) \approx 0$ over the duration of the transmitted pulse. There is a small offset in $\beta(t)$ from 0 due to the slight ellipticity of the pulse emitted from the THz photoconductive source. By inserting a 4-turn helical structure into the THz beam path, $|\beta(t)|$ increases dramatically from ~ 0 up to 0.5 over the pulse duration, indicating that the helical conformation introduces significant polarization transformation. Interestingly, the magnitude of the degree of polarization circularization, $|\beta(t)|$, is not constant, but increases approximately linearly with time over the pulse duration. This suggests that manifestations of optical activity in the transient scattered field are not instantaneous, but rather build up over several electric field cycles. The degree of circularization for m = 6 shows similar behaviour as that observed for m = 4. The parameter $|\beta(t)|$ linearly increases over the duration of the pulse and peaks at a value of 0.6 at 3.5 ps. As shown in Figure 6.7 (a), polarization circularization for the 8- and 12-turn helices reveals interesting dynamics for temporal durations exceeding $t \approx 3.5$ ps. For both m = 8 and m = 12, $|\beta(t)|$ increases linearly from 0 to ~ 0.8 between $t = 0$ and $t = 3.7$ ps, consistent with the observed trends for m = 4 and m = 6. However, for $t > 3.7$ ps, the degree of polarization circularization reaches steady state values and remains approximately constant. Based on this data, $\tau_p \approx 3.7$ ps is identified as the time required for sustained polarization circularization to develop in the transmission through the subwavelength helical structure. This result shows that the transient optical activity of a helix involves two regimes; an initial regime where polarization circularization increases over several electric field cycles and a latter regime of sustained polarization circularization.

To correlate the spectral selectivity of the helical structure to the temporal evolution of polarization circularization, the time-dependent spectral contents of the pulse are determined via time-partitioned Fourier transform of $E_t(t)$. Here, the Fourier transform is taken of the time-domain pulse after it has been multiplied by a square window with a width of 3.2 ps. The window is time-shifted to obtain the time-dependent frequency contents of the transmitted electric field pulse. As shown in Figure 6.7 (b), the scattered pulse arriving before τ_p is centered at approximately 1.4 ± 0.1 THz. In contrast, the spectral components of the pulse arriving at $t > \tau_p$ are narrowband and centered about $\nu_l = 0.85 \pm 0.07$ THz. To quantify the frequency-dependent optically active response of the helix in these two regimes, the effective imaginary refractive index difference between the LH and RH circular pulses propagated through the helix (i.e. circular index difference), $\Delta(\omega) = \ln[E_l(\omega) / E_r(\omega)] / kL$ [23], is calculated. It should be noted that the refractive index generally applies to continuous, linear, and homogeneous media. However, the optical properties of media having subwavelength scale heterogeneity can often be described by an effective medium that is continuous, linear, and homogeneous, but possesses an effective refractive index which accounts for the electromagnetic response of the heterogeneous structure. As shown in Figure 6.7 (c), $\Delta(\omega)$ for an m = 12 helix is determined from the scattered electric field pulse arriving at $0 < t < \tau_p$ (labelled "transient") and at $t > \tau_p$ (labelled "steady state"). As seen in Figure 6.7 (c), the effective index difference calculated from the initial portion of the transmitted pulse varies from −0.03 to −0.01 over spectral range from 0.9 THz up to 1.6 THz. The magnitude of $\Delta(\omega)$ increases with decreasing frequency due to stronger scattering of the lower frequency pulse components where $\pi\delta_h/\lambda$ approaches unity. The effective refractive index difference calculated from the scattered field arriving at $t > \tau_p$ shows significantly greater optical activity. Over the spectral range of the later arriving fields, $\Delta(\omega)$ is between the range of −0.05 to −0.07. The scattered fields arriving at times $t > \tau_p$ show nearly double the optical activity relative to the initial portion of the scattered waveform where polarization circularization begins to develop. Interestingly, Figure 6.7 (c) reveals that over a frequency range from 0.9 THz to 1.1 THz, the effective index difference of the helix abruptly changes from approximately −0.03 to approximately −0.06. This "gap" reflects different scattering mechanisms operating within the helical structure in the transient and steady state regimes.

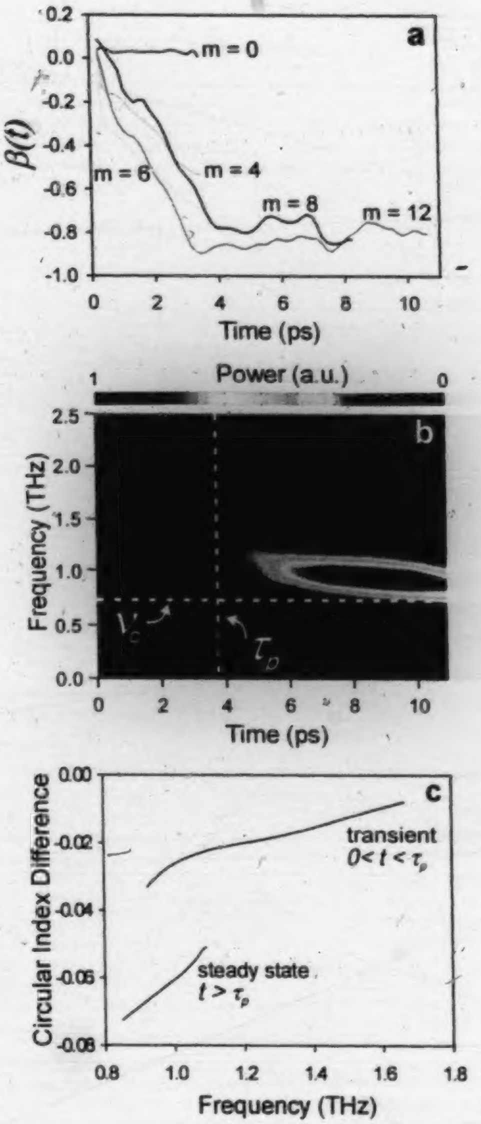

Figure 6.7. (a) Degree of polarization circularization for the transmitted pulse through the aperture and helices having m = 4, 6, 8, and 12. (b) depicts the normalized time-partitioned Fourier spectra of the right-circularly polarized transmission through the 12 turn helix, using a Fourier window of 3.2 ps. The experimental transmission spectra show a cut off frequency at 0.74 ± 0.05 THz. This cut off behaviour can be understood by considering the guided modes in the helix. Approximating the helix as an infinite cylindrical waveguide, the helix has a cut off frequency of 0.75 THz, in excellent agreement with the experimental data. (c) The frequency-dependent imaginary refractive index difference between the RH and LH fields propagated through the helix calculated over the transient regime and over the steady state regime.

A three-dimensional FDTD technique is employed to model the propagation of a linearly polarized, 1 ps THz pulse through the helical structure. The Cu helix used in the calculations physically matches that employed in the experiments. For the simulations, the THz response of the Cu metal is described by the Drude model where the plasma and collision frequencies are given by $\omega_p = 1.2 \times 10^{16}$ s^{-1} and $\Gamma = 1.38 \times 10^{13}$ s^{-1}, respectively, and the surrounding medium is vacuum. A 300 μm metallic aperture is placed in front of the helix to emulate the experimental conditions. Figure 6.8 shows snapshots of the calculated vector electric field at the centre of the helix at various times ranging from $t = 0$ ps to 20 ps. As the electric field pulse is guided along the helical axis, it develops rotational sense evident by the cycling electric field vector and emerges with a right-handed sense of rotation matching that of the helix.

To confirm that the calculations offer a true representation of the electric field and polarization dynamics, the simulated time-domain behaviour of the transmitted fields is compared with the experiments. As depicted in Figure 6.9 (a), the three-dimensional FDTD model determines that the helical structure introduces a group delay of 0.38 ± 0.05 ps/revolution, which is in good agreement with the measured value of 0.30 ± 0.05 ps/revolution. The calculated time-domain electric field pulse transmitted through an m = 12 helix is shown in Figure 6.9 (b), along with the experimentally measured pulse. In accord with the experiments, the calculations show that $E_r(t)$ is preferentially transmitted through the helix relative to $E_l(t)$. In addition, $E_l(t)$ and $E_r(t)$ consist of several temporal electric field oscillations. Polarization circularization is evident in the calculated time-domain evolution of the electric field vector [inset of Figure 6.9 (c)], which demonstrates polarization transformation of the pulse transmitted through a 12 turn helix that is strikingly similar to the experimental plot for m = 12 in Figure 6.6.

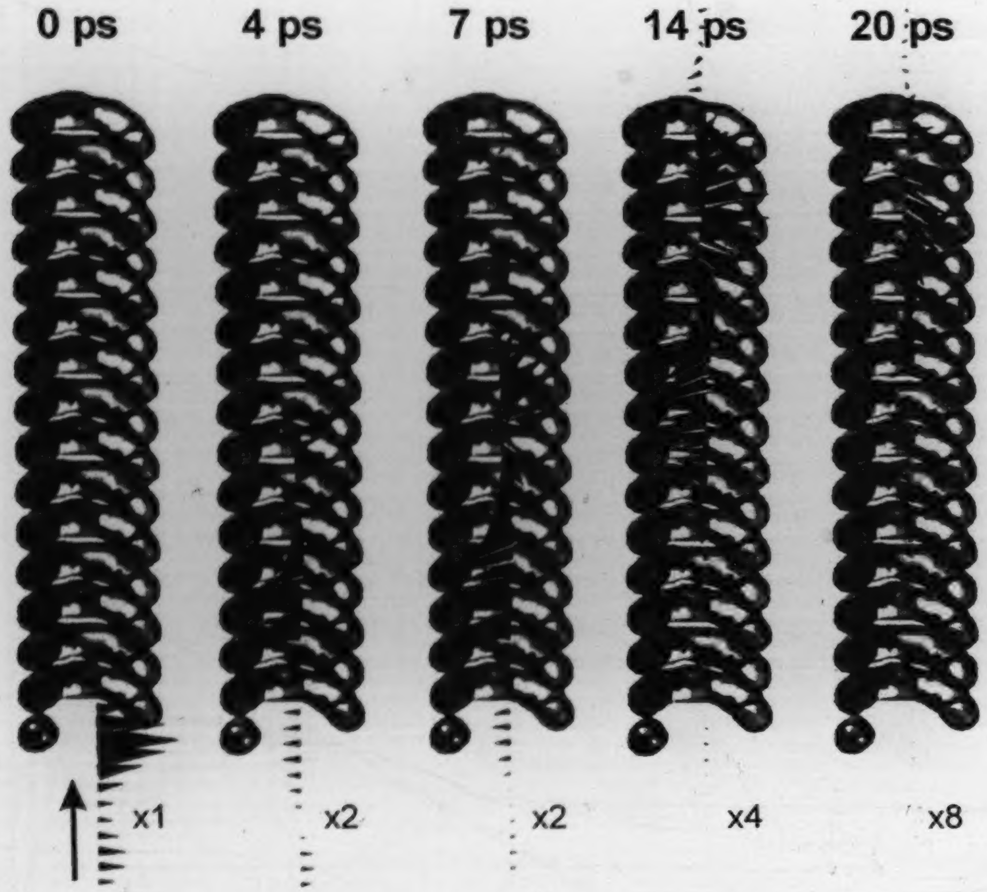

Figure 6.8. A vector plot of the three-dimensional FDTD-calculated electric field vector along the helical axis at times 0 ps, 4 ps, 7 ps, 14 ps, and 20 ps. The images include a cross-sectional view of the 15 turn helical structure employed in the simulation. The size parameters of the helix used in the simulations physically match those of the helix used in the experiments. The arrow indicates the direction of propagation of the incident THz electric field pulse.

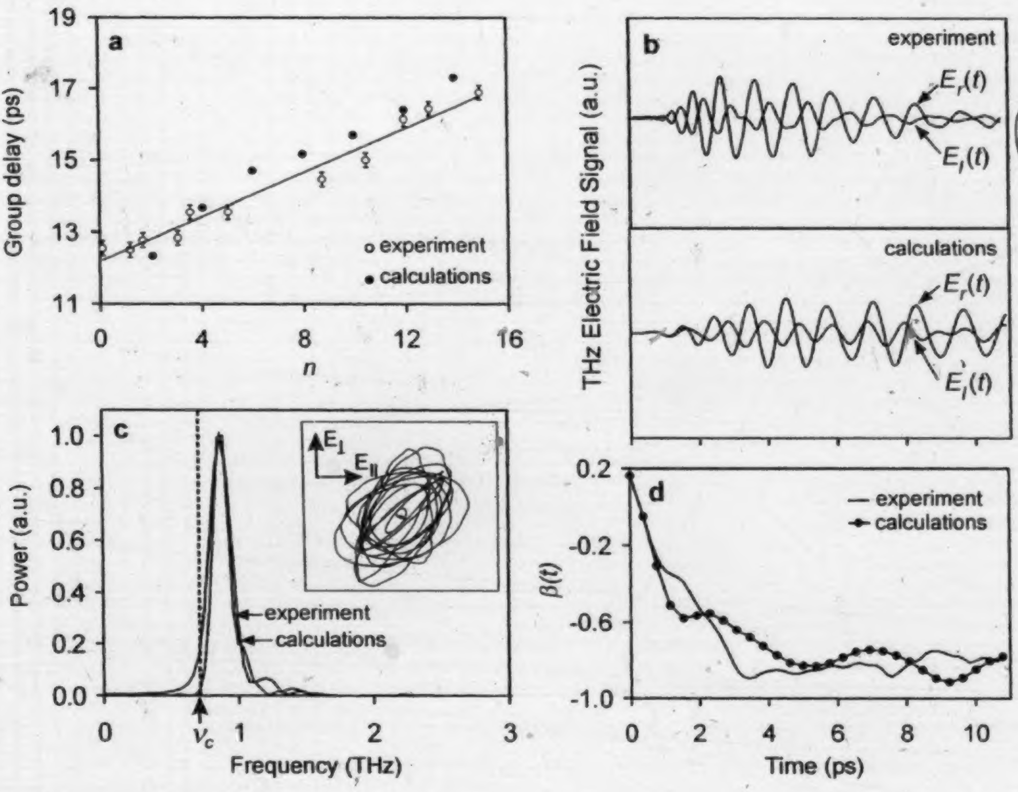

Figure 6.9. (a) The experimental and FDTD-calculated group delay is plotted versus m. (b) displays the experimental and calculated right-circular and left-circular electric field pulses transmitted through an m = 12 helix. (c) The experimentally measured and three-dimensional FDTD-calculated transmission power spectra for m = 12 are compared. The inset in (c) shows the calculated trajectory of the tip of the electric field vector for m = 12. (d) Calculated and experimental degree of polarization circularization for an m = 12 helix.

The model also predicts the experimentally observed spectral response of the helix associated the pulse components arriving at $t > \tau_p$. The calculated peak at ν_{1calc} = 0.85 THz agrees well with the sharp spectral peak experimentally measured at $\nu_l = 0.86 \pm 0.07$ THz for an m = 12 helical structure. In addition, the calculation results show cutoff behaviour for $\nu < 0.75$ THz similar to the experiments. Figure 6.9 (d) charts the parameter $\beta(t)$ over the pulse duration of the experimental and calculated pulses shown in Figure 6.9 (b). The calculated $\beta(t)$ shows similar trends as the experiment; the magnitude of the degree of polarization circularization increases rapidly for the first ~ 3 ps of the pulse arrival. Afterward, $\beta(t)$ saturates and remains approximately constant over the pulse duration. Thus, the three-dimensional FDTD model concurrently predicts, with accuracy, the group delays, the resonance frequency, the cut off behaviour ($v_c = 0.74 \pm 0.05$ THz), and the transient polarization circularization of the measured pulses.

To visualize the dynamical fields within the helical structure, a snapshot of the electric field intensity within the helical structure is shown after the passage of the initial pulse wave-front (corresponding to the regime of sustained polarization circularization) in Figure 6.10. The most pronounced effect evident in Figure 6.10 is the spiralling behaviour of the electric field intensity along the helical structure. Over four helical turns (m = 8 to m = 11), the electric field vector progressively re-orients and completes a single electric field rotation. The representative Poynting vector distribution (yellow arrows) shown at the 12th turn reveals that the field has acquired a non-zero Poynting vector component perpendicular to the propagation axis. In contrast to purely circularly polarized light that has a Poynting vector parallel to the propagation direction, the electromagnetic field emerging through a macroscopic helix not only carries intrinsic spin momentum (circular polarization), but also carries extrinsic orbital angular momentum evident by the gyrating Poynting vector. This trend is further illustrated in Figure 6.11 depicting Poynting vector distributions perpendicular to the propagation axis over four helical turns (m = 8 to m = 11). At the helix centre located at (300 μm, 300 μm), there is minimal electromagnetic energy flow within the plane perpendicular to the propagation direction. Near the inner walls of the helical structure, the Poynting vector distributions are characterized by circuitous pattern with a right-handed sense matching the handedness of the helix. The calculation results suggest that electromagnetic energy does not propagate in a straight-line path through the helical structure. Rather, electromagnetic energy is scattered and re-directed between points in the helix. It is also noteworthy that there is negligible energy outside of the helix, suggesting that electromagnetic coupling between the aperture and the outside of the helical structure is insignificant.

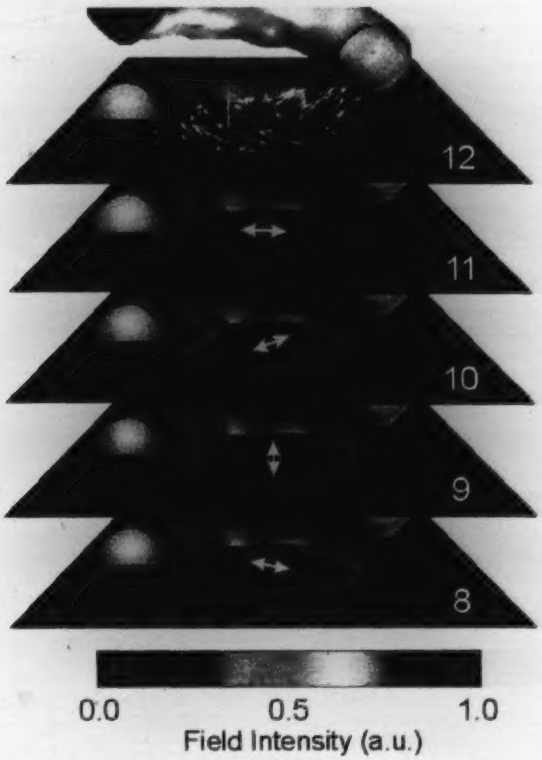

Figure 6.10. A plot of the electric field intensity at t = 14 ps along planes cutting through turn number 8, 9, 10, 11, and 12. The white arrows superimposed on the intensity plots indicate the orientation of the electric field vector on a plane. A representative plot of the Poynting vector at the plane cutting through turn number 12 shows the cycling behaviour of the electromagnetic energy flow in the helix.

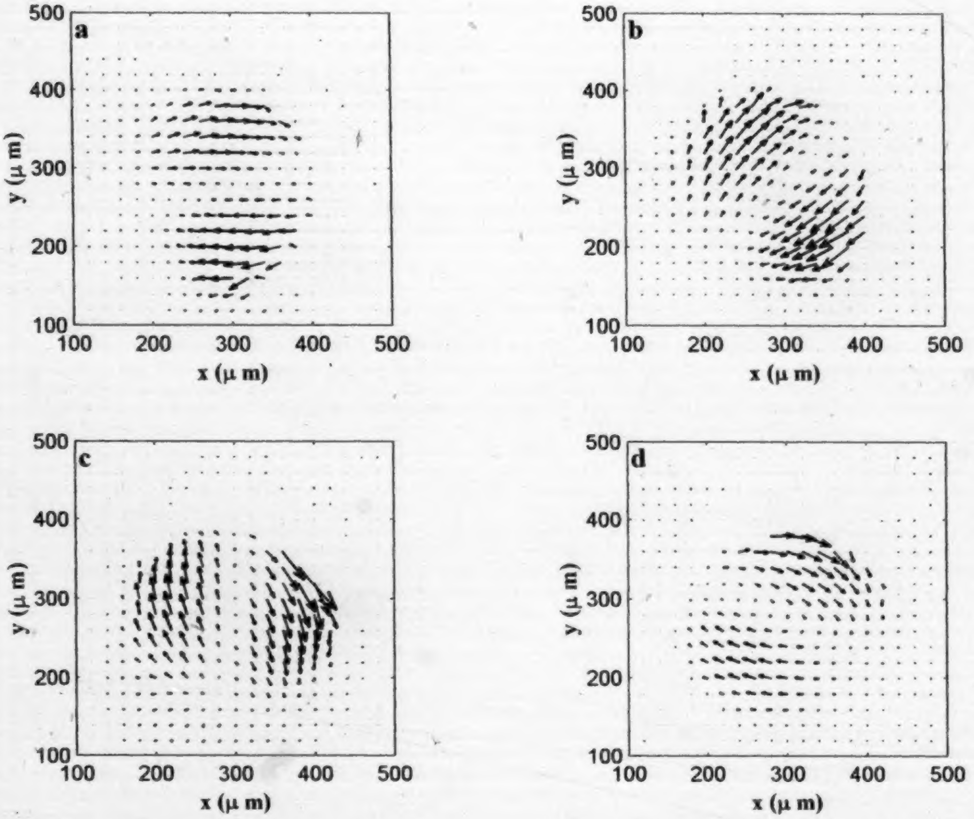

Figure 6.11. The calculated Poynting vector distributions within four planes perpendicular to the helical axis intersecting turns (a) 8, (b) 9, (c) 10, and (d) 11 of the helix at time t = 8.6 ps.. The helix is centred at (300 μm, 300 μm). The distributions are depicted from a viewpoint of an observer facing the wave propagation direction.

Although the three-dimensional FDTD calculations provide good agreement with experiments, it is our premise that a description of polarization circularization based on the electromagnetic energy flow in the subwavelength helix can give a more physical picture of optical activity. A graphical illustration in Figure 6.12 (a) shows the Poynting vector evolution spanning m = 1 to m = 7 captured at a time t = 10.6 ps, after the passage of the initial pulse wave-front. As seen in the Figure 6.12 (a), the Poynting vector streamlines, which describe the spatial orientation of the instantaneous energy flow, show that electromagnetic energy is erratically scattered near the helix entrance and most of the electromagnetic energy escapes from the helix. When viewed along the axis [Figure 6.12 (b)], the Poynting vectors show random scattering of the electromagnetic energy from the inner helix walls where the electromagnetic energy flow abruptly changes direction. In comparison, four representative Poynting vector streamlines spanning m = 8 to m = 12 are captured at a similar time of t = 10.6 ps. The calculated Poynting vectors near the exit end of the helix show that most of the electromagnetic wave gyrates through the helical structure via successive scattering from the inner helix walls. The intricate scattering patterns in Figure 6.12 (c) show complex energy flow where the Poynting vector streamlines interweave along the helical axis. Physically, these streamlines represent the propagation path of the delayed, resonant pulse component characterized by sustained polarization circularization. Interestingly, when viewed along the helical axis as shown in Figure 6.12 (d), the streamlines show a well-defined right-handed helical pattern. These streamlines describe a distinctive propagation mode where a significant portion of the electromagnetic energy is confined in and propagates along the helical structure via successive scattering from the inner helical walls. The enantiometric LH helical pattern is not supported in the RH helix and cannot propagate, which is the origin of the polarization circularization arising from the helix. From the calculated Poynting vector streamlines, a three-dimensional propagation mode is constructed consisting of three points A, B, and C defining the locations where the Poynting vector associated with the mode is scattered [the blue streamline in Figure 6.12 (c)] and changes direction [Figure 6.12 (e)]. A, B, and C are extracted from the Poynting vector representations and correspond to spatial locations where the Poynting vector streamlines form apexes of the helical pattern. Geometrically, A, B, and C are displaced along the helical axis by 1.33 turns and azimuthally translated relative to each other by approximately 120°, forming the triangular pattern. Given point D, which corresponds to point A displaced 4 turns away, ABCD defines the fundamental propagation mode of the helix and has an optical path length, $\eta = 760$ μm. Interestingly, for the criterion $\eta = q\lambda$, where q is an integer, the electromagnetic wave completes an integer number of oscillations upon propagating via ABCD = η. To ascertain the geometrical interpretation of this eigenmode, the resonance frequencies are compared to those observed in the experiment ($\nu_l = 0.86 \pm 0.07$ THz) and calculations ($\nu_{lcalc} = 0.85$ THz) with the criterion $\nu = qc/\eta$. Given $\eta = 760$ μm and $q = 2$, it is found that $\nu = 0.8$ THz, reasonably agreeing with both the experimental and three-dimensional FDTD-calculated values. It should be noted that the $q = 1$ mode is not present since it is below the cut-off of the helical structure, while higher order $q > 2$ modes are above the bandwidth of the experimental pulse. Furthermore, the geometrical interpretation of the optically active mode in the structure is valid for only a subwavelength helix.

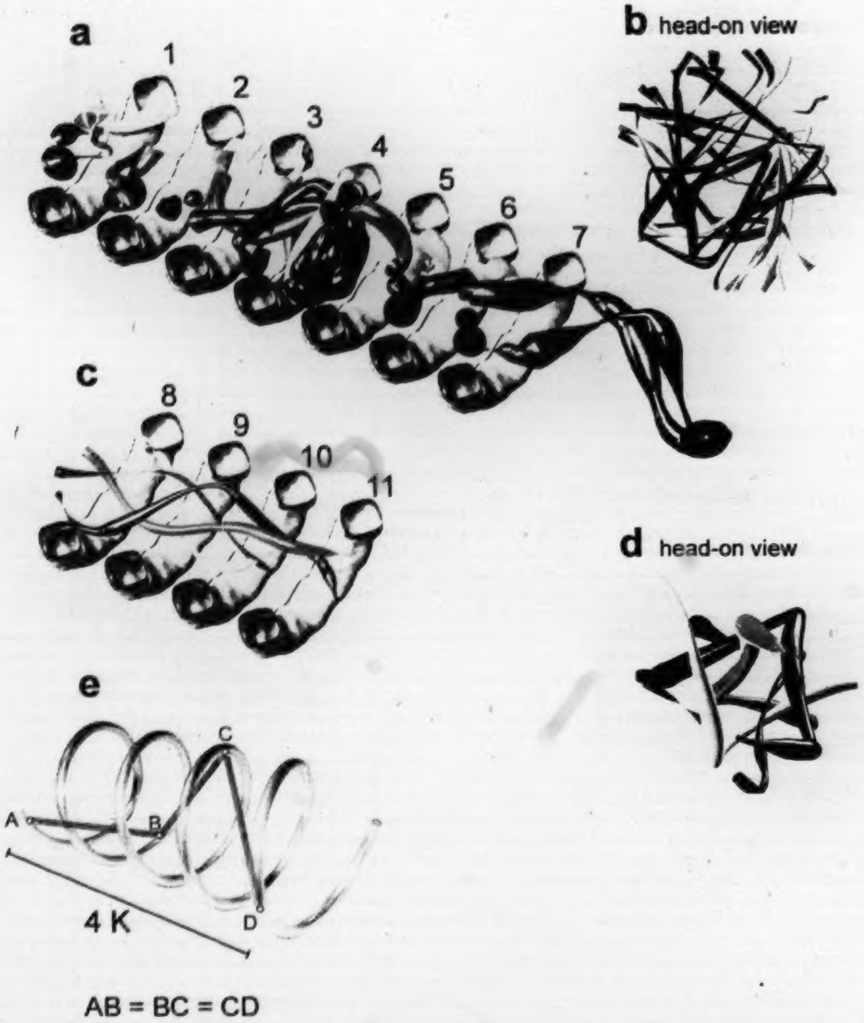

Figure 6.12. (a) Several representative Poynting vector streamlines spanning m = 1 to m = 7 captured at an arbitrary time t = 10.6 ps calculated from the three-dimensional FDTD simulations. Nearly all of the streamlines are scattered outside the helix. The width of the streamlines is proportional to the time rate of change of the energy density. The streamlines are depicted with a cross sectional view of the helical structure employed in the simulations. (b) A head-on perspective of the same vector streamlines shown in (a). (c) shows four representative Poynting vector streamlines spanning m = 8 to m = 12 captured at t = 10.6 ps calculated from the three-dimensional FDTD simulations. The yellow and red Poynting vector streamlines are scattered outside the helix after the third turn, while the green and blue streamlines are confined within the helix throughout the 4 turns. (d) shows a head-on perspective of the same vector streamlines shown in (c). (e) Based on the spatial locations where energy flow abruptly changes direction, the fundamental mode consisting of four points A, B, C, and D is constructed, coinciding with the locations where the Poynting vector changes direction.

6.3 Transverse Terahertz Electromagnetic Wave Propagation in a Helical Structure

Optical activity associated with the helical conformation is inherently sensitive to the configuration of electromagnetic wave excitation. In the axial case, electromagnetic waves are guided along the axis of the helix and scattering from the inner helical walls establishes resonant propagation modes that cause polarization circularization of the transmitted electromagnetic wave. In contrast, for transverse electromagnetic wave excitation, radiation is not confined by the helix and the interaction distance is limited to the helical diameter. Hence, it is expected that optical activity arising from the helix in the transverse configuration show different signatures than for the axial case.

In this section, THz optical activity of a sub-wavelength helix is studied using transverse electromagnetic wave excitation. Optical activity signatures in the forward scattered electric fields are directly measured in the time-domain using THz time-domain spectroscopy. The chiral element used in the experiments is a Cu wire helix consisting of m right-handed circular revolutions having a pitch $K = 120 \pm 10$ μm, a wire diameter $b = 60 \pm 2$ μm and a helical centre-to-centre diameter $\delta_h = 295 \pm 10$ μm. The helix is mounted in a photopolymer adhesive (Norland Optical Adhesive 68), which is transparent to THz radiation. The helix is excited by a 1 ps single-cycle pulse, and polarization transformation is captured in the forward-scattered radiation. Electric field components parallel, $E_{\parallel}(t)$, and perpendicular, $E_{\perp}(t)$, to the incident polarization are measured to characterize the total vector electric fields transmitted through the helix. To isolate optical activity signatures from native anisotropic absorption associated with the structure, the THz electric field transmission is measured as a function of the angle, θ, between the helical axis and the incident THz pulse polarization.

The ratio K/λ strongly influences the scattering characteristics of the helical structure. For $K > \lambda$, the structure interacts with electromagnetic waves like a periodic three-dimensional diffraction grating, which introduces spurious depolarisation independent of electromagnetic activity. However, since the pitch distance, K, of our experimental geometry lies in the range $0.04 < K/\lambda < 0.5$, far-field depolarizing diffraction effects are negligible.

From the $E_{||}(t)$ and $E_{\perp}(t)$ components of the measured THz pulses, the left-circularly polarized, $E_l(t)$, and right-circularly polarized, $E_r(t)$, electric field components are obtained via $E_l(t) = 1/\sqrt{2}[E_{||}(t) + iE_{\perp}(t)]$ and $E_r(t) = 1/\sqrt{2}[E_{||}(t) - iE_{\perp}(t)]$, respectively. Here, $E_{||}(t)$ and $E_{\perp}(t)$ are aligned with respect to the x- and y-axes, respectively. Shown in Figure 6.13 are representative time-domain $E_r(t)$ signals transmitted through the helix for $\theta = 0°$ and $\theta = 90°$, corresponding to the configurations where the incident THz polarization is aligned parallel and perpendicular to the helical axis, respectively. Similar to the reference pulse (shown in the inset of Figure 6.13), the pulses scattered from the helix for the two configurations consist of bipolar waveforms with temporal durations of ~2.5 ps. The radiation scattered from the helical element shows negligible dispersion relative to the reference pulse. To extract the dynamic polarization rotation from the forward scattered temporal waveforms, the time-dependent phase difference, $\Delta\Phi(t) = \Phi_r(t) - \Phi_l(t)$ accrued between the left- and right- circularly polarized components of the pulse is calculated, where $\Phi_{r,l}(t)$ is the temporal phase of the right and left-circularly polarized pulse components, respectively. As shown in Figure

6.13, the reference pulse transmitted through the photopolymer matrix shows $\Delta\Phi\ (t) = 0$ over the pulse duration, indicating an absence of polarization rotation effects. Interestingly, the electric field pulses forward scattered from the single helical element show marked, positive phase difference between the right- and left-circularly polarized pulse components for both the $\theta = 0°$ and $\theta = 90°$ configurations. This phase difference suggests that the right-circularly polarized pulse component scattered from the single helical element is effectively delayed relative to its left-circularly polarized counterpart. The magnitude of $\Delta\Phi(t)$ in the two configurations is commensurate, although in the later regime of the pulse duration ($t > 2.5$ ps), $\Delta\Phi(t)$ is approximately ~0.08 radians larger for $\theta = 0°$ relative to $\theta = 90°$. Differences in the dynamic magnitudes of $\Delta\Phi(t)$ for $\theta = 0°$ and $\theta = 90°$ may arise from the inherent linear anisotropy of the helical element and will be discussed further.

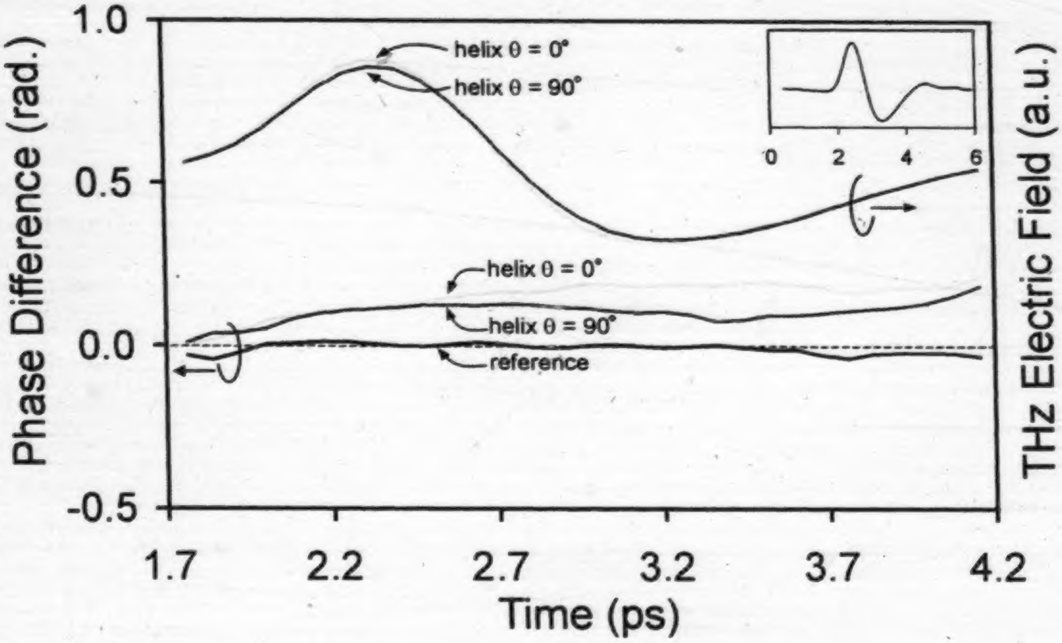

Figure 6.13. (left axis) The time-dependent phase difference between the right-circularly polarized and left-circularly polarized pulse components transmitted through the reference (blue), the helix in the parallel configuration (yellow), and the helix in the perpendicular configuration (green). (right axis) The temporal right-circularly polarized waveforms transmitted through the helix are shown for the parallel and perpendicular configurations. The inset shows the reference pulse transmitted through the photopolymer matrix without a helix.

The time-domain behaviour of $\Delta\Phi(t)$ provides insight into the underlying mechanisms responsible for the polarization rotation in the single helical element for transverse electromagnetic wave excitation. As seen in Figure 6.13, polarization rotation effects are first observed in the scattered pulse within 300 fs of the pulse arrival time at $t = 1.7$ ps (the pulse arrival time is characterized by the time where the signal to noise ratio exceeds 10:1), indicating that polarization rotation within the helix arises from near-instantaneous scattering occurring over time scales < 300 fs.

To elucidate the relationship between the chiral geometry of the helix and its associated optical activity, the polarization transformation imparted by *sub-helical* structures is examined. These sub-helical structures are parametrically identical to the full helix (having the same pitch, radius of curvature, and handedness), but portions of the structure have been selectively removed, as shown in Figure 6.14. Using this methodology, the helix's effective chirality can be arbitrarily reduced by decreasing its interaction length, enabling systematic characterization the influence of the helical geometry (chirality) on its inherent electromagnetic activity.

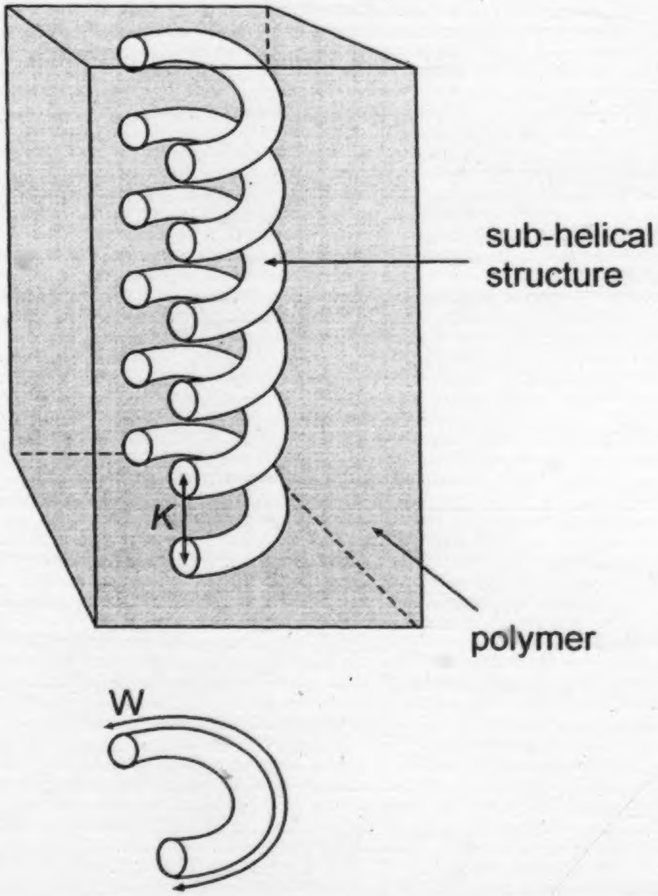

Figure 6.14. Illustration of the sub-helical structures used in the experiments. The sub-helical structures are characterized by a wire length per revolution.

Sub-helical structures are fabricated by mounting a full helix in a photopolymer matrix. The mounted helix is then mechanically ground along a plane parallel to the helical axis to selectively remove sections of the helical structure (see Figure 6.14). The resulting sub-helical structures consist of an array of disconnected, partially complete helical revolutions spaced by the pitch distance, *K*. Seven sub-helical structures are fabricated where the wire length per revolution, W, ranges from 189 μm to 739 μm.

Figure 6.15 (a) illustrates the Fourier spectra of the $E_r(t)$ waveforms transmitted through the helical structure (W = 739 μm) and sub-helical structures (W = 189 μm and 408 μm). As seen in the Figure, the partial, sub-helical structures show enhanced transmission power relative to the full helix; however, the sub-helical and helical structures exhibit the similar transmission bandwidth and spectral content. To further examine the electromagnetic properties of the helical and sub-helical elements, the polarization rotation in the forward scattered pulses is analyzed versus the relative angle between the helical axis and the incident THz polarization, θ. Polarization rotation in the structures can independently arise from optical activity or linear dichroism associated with native anisotropic absorption. The latter arises from differential absorption by the helix depending on the relative orientation of the incident THz electric field vector with respect to the helical axis. When the incident electric field vector is perpendicular to the helical axis, there is maximum absorption since a large portion of the electric field vector is aligned along the wire surface. However, when the incident electric field vector is parallel to the helical axis, there is minimum absorption. Optical activity and anisotropic absorption can be distinguished by examining the polarization rotation as a function of the relative orientation of the incident polarization and the helical axis. Shown in Figure

6.15 (b) is the effective circular birefringence versus θ for helical and sub-helical inclusions having W = 739 μm, 408 μm, and 189 μm. The effective circular birefringence of the helical and sub-helical elements is obtained using the relation $\Delta n_{circ} = n_{right} - n_{left} = [\Phi_r(\omega) - \Phi_l(\omega)]/kL$, where $n_{right,left}$ are the effective refractive indices for the right and left circular components, $\Phi_{r,l}(\omega)$ is the frequency-dependent phase of the right- and left- circularly polarized pulse components, and L is the thickness of the helical/sub-helical inclusion. Polarization rotation due to native anisotropic absorption gives rise to the $\cos\theta$ dependence in Δn_{circ} since anisotropic absorption by the helix is dependent on the projection of the incident electric field vector onto the helical wire. Chirality-induced polarization rotation, on the other hand, is not dependent on the relative orientation of the incident electric field vector and the helical axis and manifests as a constant offset in Δn_{circ} from zero.

As seen in Figure 6.15 (b), the chirality-induced Δn_{circ} offset of ~ 0.6 for the full helix corresponds to a specific rotation of 16°/mm at the central frequency of 0.45 THz. Interestingly, the sub-helical structures show increased anisotropy relative to the full helix, evident by the larger oscillations in Δn_{circ} versus θ. This increased anisotropy arises because the sub-helical structures are geometrically similar to an array of parallel wires, and exhibit anisotropic transmission properties akin to a wire grid polarizer. Along with increased anisotropy, the chirality-induced polarization rotation for the sub-helical elements is reduced relative to that for the full helix. For the sub-helical structure where W = 408 μm, the chirality-induced offset in Δn is reduced by 45% relative to that for the full helix. The sub-helical element having W = 189 μm is strongly anisotropic and shows almost no optical activity (no offset). Thus, as W of the helical/sub-helical structure is reduced, the effective chirality of the structure is also reduced, resulting in diminished polarization rotation of the transmitted pulse.

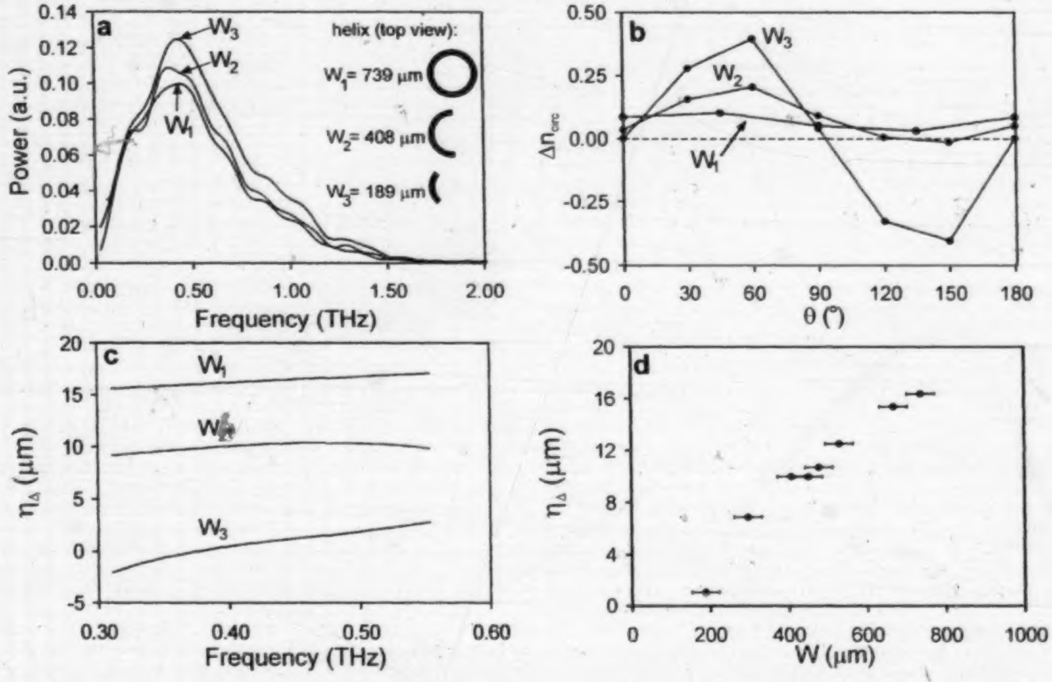

Figure 6.15. (a) Fourier spectra of the right-circularly polarized pulse transmitted through the helix and sub-helical structures where the wire length/revolution is 408 μm and 189 μm. (b) shows the circular birefringence (the difference in the effective left and right refractive indices) for the helical and sub-helical structures. (c) depicts the frequency-dependent chirality-induced optical path length difference between the right-circularly polarized and left-circularly polarized pulse components for the helical and sub-helical structures. (d) charts the chirality-induced optical path length difference at a central frequency of 0.45 THz versus the wire length/revolution.

Broadband excitation of the structures enables further examination of the frequency-dependent chirality-induced polarization rotation associated with the helical and sub-helical elements. Chirality causes optical activity, which is characterized by an optical path length difference for the left- and right-circularly polarized electric fields interacted with the chiral structure. The chirality-induced optical path length difference,

$\eta_\Delta = <\Delta n_{circ} L>_\theta = <[\Phi_r(\omega) - \Phi_l(\omega)]/k>_\theta$, for the helical and sub-helical elements is measured. Here, η_Δ is configurationally averaged over all θ to eliminate θ-dependent polarization rotation effects due to anisotropic absorption in the chiral structures. Figure 6.15 (c) plots η_Δ for the helical and sub-helical structures where W = 739 μm, 408 μm, and 189 μm. Over the transmission bandwidth from 0.30 THz to 0.55 THz, the chirality-induced polarization rotation for the three structures show negligible frequency dependence, suggesting an absence of resonant electromagnetic phenomenon in the transverse configuration (refer to Appendix E for supplementary data). This contrasts with the axial case, where resonant polarization was shown in Section 6.2. The full helix shows the largest chirality-induced optical path length difference, where the right-circularly polarized pulse component propagates a distance between 15.6 μm to 17.1 μm greater than the left-circularly polarized counterpart over the frequency range from 0.30 THz to 0.55 THz. The sub-helical element having W = 408 μm show significantly decreased η_Δ due to the decreased interaction distance. The chirality-induced optical path length difference for the W = 189 μm sub-helical element is nearly zero, indicating that the two circularly polarized components of the scattered pulse propagate nearly identical distances. To further examine the influence of the sub-helical geometry on its electromagnetic activity, Figure 6.15 (d) shows η_Δ as a function of the wire length/revolution measured at a central frequency of 0.4 THz. Interestingly, the results show that chirality-induced polarization rotation in the helical and sub-helical structures accrues linearly over the wire length/revolution, and in the limit where W approaches zero, the chirality-induced polarization rotation also approaches zero. The linear relationship between the chirality-induced polarization rotation and W also shows that the electromagnetic activity of a helix is directly proportional to its chirality (geometrical parameters), and is not significantly affected by the continuity of the structure or electromagnetic interaction between points of a helix. This further suggests that in the experimental regime, the Born approximation is an adequate approximation in describing radiation interaction with the helix in the transverse configuration, since mutual interaction between points of the helix can be ignored.

6.4 Conclusion

In summary, the THz electromagnetic properties of a subwavelength size helix have been studied in two configurations where the THz electromagnetic wave is incident parallel to the helical axis and transverse to the helical axis. These two configurations give rise to strikingly different optical activity phenomena. For axial electromagnetic wave propagation, it is shown that dynamic optical activity signatures in the transmitted THz electric field are not instantaneous; rather, circularization of the transmitted electric field polarization gradually increases over several picoseconds until reaching sustained values. A three-dimensional FDTD model is employed to visualize the internal electric field and Poynting vector dynamics that lead to the steady state polarization circularization of light exiting from the helix. In particular, it is shown that steady state polarization circulation is associated with the formation of helical propagation modes within the helical structure. The results not only affirm the established picture that optical activity arises from multiple scattering in the helix, but also show that this process requires several electric field cycles to fully establish.

In contrast, the optical activity signatures of a subwavelength helix for electromagnetic wave excitation transverse to the helical axis are non-resonant and nearly instantaneous. Systematic measurements of THz electric field pulses transmitted through helical and sub-helical elements shows that polarization rotation accumulates linearly within the chiral structure, revealing a direct relationship between optical activity of a helix and its geometrical chirality. The results are important for the development of theoretical descriptions of electromagnetic wave interaction with helices and may find applicability in the design and characterization of chiral artificial materials.

Chapter 6 References

[1] L. D. Barron, *Molecular Light Scattering and Optical Activity*. Cambridge: Cambridge University Press, 1982.

[2] S. F. Mason, *Molecular Optical Activity and the Chiral Discriminations* Cambridge: Cambridge University Press, 1982.

[3] M. Born and E. Wolf, *Principles of Optics*, 5th ed. Oxford: Pergamon Press, 1975.

[4] M. Bouchiat and L. Pottier, "Optical experiments and weak interactions," *Science*, vol. 234, pp. 1203-1210, 1986.

[5] R. A. Hegstrom, J. P. Chamberlain, K. Seto, and R. G. Watson, "Mapping the weak chirality in atoms," *American Journal of Physics*, vol. 56, pp. 1086-1092, 1988.

[6] J. C. Bose, "On the rotation of plane of polarisation of electric waves by a twisted structure," *Proceedings of the Royal Society of London A*, vol. 63, pp. 146-152, 1898.

[7] K. F. Lindman, "Über eine durch ein isotropes System von spiralförmigen Resonatoren erzeugte Rotationspolarization der elektromagnetische Wellen," *Annalen der Physik*, vol. 63, pp. 621-644, 1920.

[8] D. L. Jaggard, A. R. Mickelson, and C. H. Papas, "On Electromagnetic Waves in Chiral Media," *Applied Physics*, vol. 18, pp. 211-216, 1979.

[9] S. F. Mason, "Optical Activity and Molecular Dissymmetry," *Contemporary Physics*, vol. 9, pp. 239-256, 1968.

[10] C. Bustamante, M. F. Maestre, and I. Tinoco Jr., "Circular intensity differential scattering of light by helical structures. I. Theory," *Journal of Chemical Physics*, vol. 73, pp. 4273-4281, 1980.

[11] C. Bustamante, M. F. Maestre, and I. Tinoco Jr., "Circular intensity differential scattering of light by helical structures. II. Applications," *Journal of Chemical Physics*, vol. 73, pp. 6046-6055, 1980.

[12] C. Bustamante, I. Tinoco Jr., and M. F. Maestre, "Circular intensity differential scattering of light by helical structures. III. A general polarizability tensor and anomalous scattering," *Journal of Chemical Physics*, vol. 74, pp. 4839-4850, 1981.

[13] P. Chiappetta and B. Torresani, "Electromagnetic scattering from a dielectric helix," *Applied Optics*, vol. 27, pp. 4856-4860, 1988.

[14] F. Guerin, P. Bannelier, and M. Labeyrie, "Scattering of electromagnetic waves by helices and application of the modelling of chiral composites. I: simple effective-medium theories," *Journal of Physics D*, vol. 28, pp. 623-642, 1995.

[15] F. Guerin, P. Bannelier, M. Labeyrie, J.-P. Ganne, and P. Guillon, "Scattering of electromagnetic waves by helices and applications to the modelling of chiral composites. II. Maxwell Garnett treatment," *Journal of Physics D*, vol. 28, pp. 643-656, 1995.

[16] W. M. McClain, J. A. Schauerte, and R. A. Harris, "Model calculations of intramolecular interference effects in Rayleigh scattering from solutions of macromolecules," *Journal of Chemical Physics*, vol. 80, pp. 606-616, 1984.

[17] F. Perrin, "Polarization of Light Scattered by Isotropic Opalescent Media," *Journal of Chemical Physics*, vol. 10, pp. 415-427, 1942.

[18] P. G. Zablocky and N. Engheta, "Transients in chiral media with single-resonance dispersion," *Journal of the Optical Society of America A*, vol. 10, pp. 740-758, 1993.

[19] A. G. Cha, "Wave Propagation on Helical Antennas," *IEEE Transactions on Antennas and Propagation*, vol. 20, pp. 556-560, 1972.

[20] J. D. Kraus, *Antennas*, 2nd ed. New York: McGraw-Hill, 1988.

[21] M. Kuwata-Gonokami, N. Saito, Y. Ino, M. Kauranen, K. Jefimovs, T. Vallius, J. Turunen, and Y. Svirko, "Giant Optical Activity in Quasi-Two-Dimensional Planar Nanostructures," *Physical Review Letters*, vol. 95, pp. 227401, 2005.

[22] A. Papkostas, A. Potts, D. M. Bagnall, S. L. Prosvirnin, H. J. Coles, and N. I. Zheludev, "Optical Manifestations of Planar Chirality," *Physical Review Letters*, vol. 90, pp. 107404, 2003.

[23] I. Tinoco Jr. and M. P. Freeman, "The optical activity of oriented copper helices. I. Experimental," *Journal of Physical Chemistry*, vol. 61, pp. 1196-1200, 1957.

[24] T. Vallius, K. Jefimovs, J. Turunen, P. Vahimaa, and Y. Svirko, "Optical activity in subwavelength-period arrays of chiral metallic particles," *Applied Physics Letters*, vol. 83, pp. 234-236, 2003.

[25] V. V. Varadan, R. Ro, and V. K. Varadan, "Measurement of the electromagnetic properties of chiral composite materials in the 8-40 GHz range," *Radio Science*, vol. 29, pp. 9-22, 1994.

[26] I. V. Lindell, A. H. Sihvola, S. A. Tretyakov, and A. J. Viitanen, *Electromagnetic Waves in Chiral and Bi-Isotropic Media*. Boston: Artech House, 1994.

[27] V. V. Varadan, A. Lakhtakia, and V. K. Varadan, "Equivalent dipole moments of helical arrangements of small, isotropic point-polarizable scatters: Application to chiral polymer design," *Journal of Applied Physics*, vol. 63, pp. 280-284, 1988.

[28] S. A. Tretyakov, F. Mariotte, C. R. Simovski, T. G. Kharina, and J.-P. Heliot, "Analytical Antenna Model for Chiral Scatterers: Comparison with Numerical and Experimental Data," *IEEE Transactions on Antennas and Propagation*, vol. 44, pp. 1006-1014, 1996.

Chapter 7:

Conclusions and Outlook

7.1 Summary

Subwavelength scale heterogeneous media constitute a rich regime of light-matter interaction because the subwavelength structure of the medium can lead to electromagnetic properties not inherent to the constituent medium. In this thesis, it has been shown using several types of mesoscopic systems that this simple principle opens the door to the exploration of a wide range of interesting electromagnetic phenomena.

In Chapter 2, THz electromagnetic wave propagation in a strongly scattering system composed of subwavelength dielectric particles was explored. In the regime where the heterogeneity scale of the dielectric medium was less than the wavelength, it was found that the effective medium approximation became invalid, indicating the onset of diffusive THz photon transport through the sample.

Unlike dielectric media, metallic media are nearly opaque at THz frequencies. However, it was shown in Chapter 3 that for a dense ensemble of metallic particles individually smaller than the radiation wavelength, the ensemble can exhibit surprisingly large amplitude, polarized THz electric field transmission. The enhanced, polarized THz transmission arises from coherent near-field particle plasmon coupling between nearest neighbor particles. Further investigations of the transmission phenomenon showed a striking sensitivity of the transmitted THz electric field waveform on the particle size, shape, and conductivity of the metallic medium. Moreover, it was demonstrated that a marked attenuation of the transmitted THz waveform can be achieved by simply coating the metallic particles with a nano-scale layer of a different metal. This attenuation originates from Ohmic losses associated with interface resistance at the junction of the two dissimilar metals. Exploiting the interface resistance effect in multilayered particles, the THz charge induction distance within the surface of the metallic particles was mapped. Experimental evidence demonstrated that THz particle plasmon formation within the particles occurs within a skin depth of the particle surface. In further investigations, a novel amorphous metamaterial at THz frequencies was proposed consisting of ensembles of subwavelength sized dielectric and metallic particles. It was shown that the effective electromagnetic properties of the amorphous metamaterial exhibit a nonlinear dependence on the relative volume fraction of the metallic and dielectric inclusions. This behaviour was resolved by considering the particle-plasmon interactions between the metallic inclusions.

The enhanced THz transmission through metallic particle ensembles opened the door to novel THz spectroscopic investigations of metallic media. In Chapter 4, a phase transition phenomenon was studied in ensembles of Ga particles when the ensemble temperature is raised above the melting temperature. The results showed frequency-independent phase modulation of the THz electric field transmission at the melting point temperature, and frequency-dependent phase and amplitude modulation as the temperature exceeded the melting temperature.

In Chapter 4, two novel manifestations of electron spin-dependent phenomena were demonstrated in the THz particle plasmon mediated transmission through ensembles of F particles and F/N composite particles. In one manifestation, magnetized ferromagnetic particle ensembles were shown to exhibit an effective THz birefringence due to AMR inherent to the ferromagnetic medium. In another manifestation, an ensemble of ferromagnetic particles coated with nonmagnetic nano-layers was demonstrated to exhibit enhanced magnetic attenuation, delay and pulse-re-shaping of the transmitted THz waveform relative to an ensemble of uncoated ferromagnetic particles. The enhanced magnetic effect in the particles that were coated with a nonmagnetic layer is attributed to electron spin accumulation from the ferromagnetic particle into the nonmagnetic layer. The findings of Chapter 5 represent a unique marriage of plasmonic and spintronic phenomena and open a novel avenue of research. The ability to magnetically manipulate near-field mediated light transport through metallic particles via electron spin promises another degree of freedom in the development of light-based information devices.

Electromagnetic wave interaction with a subwavelength sized particle that is asymmetric, or chiral, may lead to an electromagnetic effect known as optical activity. To explore the connection between chirality and optical activity, Chapter 6 examined the THz electromagnetic properties of a subwavelength size helix. For radiation incident along the helical axis, it was shown that the transmitted radiation exhibits polarization circularization due to resonant propagation modes established along the helical axis. On the other hand, in the configuration where radiation is incident transverse to the helical axis, non-resonant polarization rotation of the forward scattered radiation was observed. In contrast to the axial configuration, polarization rotation in the transverse case arises from singly scattered radiation from the helical structure. The detailed investigation of the dynamic electromagnetic response of a subwavelength helix provided insights into the interrelationship between chirality and optical activity and a framework for the investigation of other chiral manifestations.

7.2 Future Outlook

This thesis has presented a range of exciting findings of THz electromagnetic wave interaction with mesoscopic media which may pave the way for further explorations of interesting electromagnetic phenomena. Here, a brief overview is provided of open research questions arising from this thesis and future directions that this work may motivate.

Multiple Scattering in Random Dielectric Media

In Chapter 2, on-axis THz transmission through strongly scattering dielectric media was studied in the time-domain, revealing ballistic and singly scattered components of the transmission. An important property of strongly scattering dielectric media is their ability to trap electromagnetic energy via multiple scattering. The most direct method to characterize the multiple scattering in a disordered system is by measuring the backscattered radiation from the sample. Hence, future studies of multiple scattering in a strongly scattering sample may include the examination of the time-resolved backscattered THz radiation from the sample. Measurement of the time-domain backscattered THz electromagnetic waves will reveal the temporal dynamics of the electromagnetic waves escaping from the scattering medium and also enable a direct measurement of the photon dwell time in the medium.

Electromagnetic Properties of Metallic Nano-particle Ensembles

The experimental and numerical work on THz electromagnetic wave interaction with subwavelength size metallic media provided a plethora of insight into the microscopic mechanisms of non-resonant THz particle plasmon formation and coupling between neighboring particles. Of immediate interest would be the miniaturization of these three-dimensional particle systems into the nano-scale regime, where the resonant particle plasmon response of the individual metallic particles is accessible via optical excitation. Ensembles of nano-scale metallic particles resonantly excited with optical radiation would exhibit a much stronger electromagnetic response than their micro-scale counterpart excited with THz radiation. Much like microparticles at THz frequencies, ensembles of nano-particles could transport visible electromagnetic energy via particle plasmon excitation and nearest neighbor coupling. Hence, ensembles of metallic nano-particles may hold promise for the development of nano-photonic optical information devices.

Spinplasmonics

Perhaps one of the most exciting outcomes of this work is the observations of electron-spin dependent phenomena in the THz plasmonic transmission through ferromagnetic and ferromagnetic/nonmagnetic particles. By applying relatively weak magnetic fields to the particle ensembles, large modulation of the plasmonic-mediated THz electric field transmission was observed. These finding, therefore, represent a marriage of spintronic and plasmonic technologies and a significant step forward in the development of active plasmonic devices. Future work into this exciting research avenue would include further study of electron spin-dependent effects using different plasmonic geometries (such as metallic wire waveguides, films, or particle chains) composed of ferromagnetic and ferromagnetic/nonmagnetic composite media. Moreover, it would be of immediate interest to explore THz plasmonic manifestations of other spintronic, or electron-spin-dependent effects. For instance, systems composed of alternating ferromagnetic/nonmagnetic nano-layers show a pronounced spin-dependent effect known as the "spin valve effect", in which the scattering of spin-polarized electrons is controlled by varying the magnetization orientation of adjacent ferromagnetic layers. These spin valve structures could be grown on the surface of the metallic microparticles; by varying the relative magnetization orientation of adjacent ferromagnetic layers, the THz electromagnetic properties of the particles can be modulated with relatively weak magnetic fields.

Optical Activity Arising from Other Chiral Manifestations

The exploration of transient optical activity associated with the helical structure in Chapter 6 provided a glimpse of the interrelationship between chiral structure and electromagnetic activity. The studies presented in this thesis, however, were limited to the case of a helical structure. Future work in this area of research may include the investigation of transient optical activity associated with other chiral manifestations, such as spirals and gammadions. These investigations will provide a more complete picture of the general interrelationship between chirality and optical activity.

7.3 Conclusion

Interesting physics occurs when the size scale of a medium is less than the wavelength of an electromagnetic wave. In this mesoscopic regime, the medium's electromagnetic properties depart from their bulk values and acquire a strong extrinsic dependence on the subwavelength scale structure of the medium. Throughout this thesis, it has been shown using several mesoscopic systems that this simple fact opens the door to the exploration of electromagnetic phenomena not otherwise present in the constituent medium. Using THz time-domain spectroscopy, THz electromagnetic interactions have been studied in dielectric, metallic, ferromagnetic, and chiral media where the relevant dimensions of the media are on a subwavelength regime. Equally important to the discovery of these THz electromagnetic effects is the understanding of their microscopic origins. Rooted in classical electromagnetics and solid state theory, this thesis provides simple and intuitive discussions of the origins of THz electromagnetic phenomena in mesoscopic media. With the thorough and comprehensive study of mesoscopic electromagnetic phenomenon as the goal of this thesis, it is envisioned that the work will spawn future studies of mesoscale phenomena in other frequency regimes (in particular the visible regime) and find applicability in the development of light-based information devices.

Appendices

Appendix A: Model of Magnetic Field Enhanced Terahertz Emission from Semiconductor Surfaces

The generation of ultrashort high power free space THz radiation pulses has become increasingly important for spectroscopic [1] and imaging applications [2]. The optical excitation of bare semiconductor surfaces provides a compact source of THz radiation that does not require micro-fabrication and can be easily integrated into large area emitters. Experimental studies have demonstrated that the THz emission power from photo-excited semiconductor surfaces can be enhanced by applying an external magnetic field. Investigations by Corchia et al. [3] into THz emission from femtosecond irradiated n-type GaAs surfaces have shown that emission strength increases with magnetic field to a plateau at 6 T. In undoped InAs samples, McLaughlin et al. [4] have reported a quadratic dependence of THz emission on the magnetic field up to 3 T. Beyond 3 T, Ohtake et. al. [5] have demonstrated that the radiated THz power saturates at 4 T, decreases to a minimum at 6 T, and increases again at 14 T. Experimental works have also studied enhancement in InAs for various excitation regimes and doping levels. Heyman et al. [6] have reported a lower emission power from n-doped InAs as opposed to undoped InAs, but no explanation of the observed phenomenon was reported. When a magnetic field of 3 T was applied, the emission power from doped InAs was approximately half of that from the undoped sample. In studies by H. Takahashi et al. [7], the THz emission enhancement factor from undoped InAs was observed to decrease rapidly as the excitation fluence is increased above 0.06 μJ/cm^2. For excitations fluences exceeding 0.2 μJ/cm^2, the THz power enhancement saturates completely.

Understanding enhancement mechanisms and their dependence on excitation fluence, doping, and magnetic field are crucial to the development of highly efficient THz emitters. To describe magnetic field enhanced emission from InAs and n-GaAs surfaces several models, based on a semi-classical prescription, have been used. Shan et al. [8] attributed enhancement to increased out-coupling of THz radiation from the air-semiconductor interface. Their single particle model, however, does not provide insight into complicated photo-Dember mechanisms and space charge screening effects that are important in high mobility semiconductors such as InAs. To explain THz emission from InAs surfaces, Heyman et al. [6] described the THz emission in terms of classical dynamics of both the electrons accumulated at the surface and in the bulk of the semiconductor. Their picture of electron motion in InAs provides a physical understanding of the enhancement mechanism for a narrow range of magnetic fields below 1.0 T; however, their model breaks down for magnetic field values >|1.0 T|. More recently, Johnston et al. have developed a three-dimensional Monte Carlo model [9] of THz emission enhancement based on semi-classical electron motion. The model describes emission from GaAs, but for InAs their treatment does not explain the anomalous decrease in THz emission strength near 3 T and fails to predict the dependence of emission on doping concentrations. Moreover, the simulations are computationally intensive and require the accurate input of a large number of parameters related to band structure and scattering rates that are not well known at high magnetic fields.

This appendix presents a two-dimensional drift-diffusion model to describe THz emission from n-GaAs and InAs surfaces in a magnetic field. Carrier transport is described in two dimensions to accommodate acceleration induced by the magnetic field. In contrast to single particle semi-classical descriptions, the study provides a consolidated picture of collective carrier behavior during optical excitation, and includes the effects of extrinsic and photo-generated carriers, charge screening effects, and photo-Dember mechanisms. The effects of optical excitation intensity, magnetic field orientation, and magnetic field strength on the far field THz emission are accurately reproduced and in accordance with previously reported experimental observations.

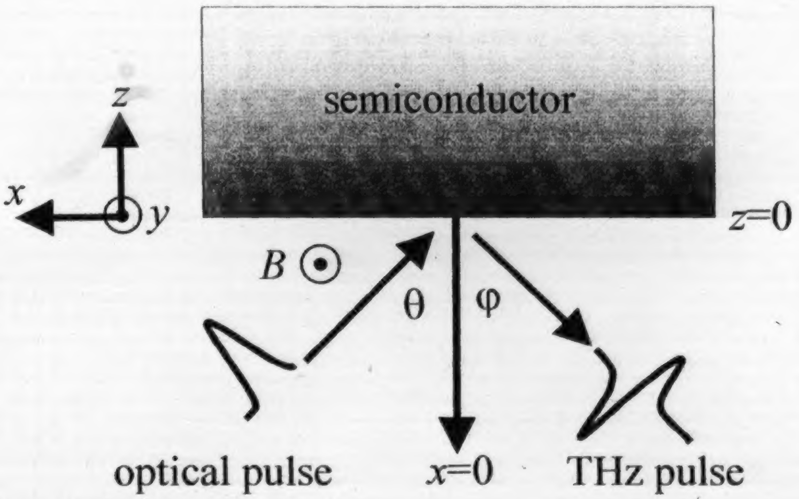

Figure A.1. Configuration of the laser pulse and THz emission with respect to the semiconductor surface.

The geometrical layout of the surface THz emitter used in the analysis is depicted in Figure A.1. An optical pulse is incident on the semiconductor surface at $\theta = 45^\circ$ and the THz emission is detected at $\varphi = 45^\circ$. The magnetic field is oriented along the y-axis. Such a configuration has been shown to produce the optimum THz power [10].

In order to accurately describe the carrier dynamics, one must consider the fields existing at the surface of GaAs and InAs prior to photo-excitation. Electron trapping at boundary states near the GaAs surface causes a surface depletion layer whose electric field, $E_{surf}(z)$, acts on photo-excited carriers. Here, a Schottky model is used to describe such unperturbed surface field. In this formalism, the electric field is taken to be maximum at the surface ($z = 0$) and decreases linearly away from the surface to zero within the depletion length w. The electric field at the surface $E_{surf}(z)$ and the depletion width w are given by

$$E_{surf}(z) = \left(\frac{2eN_d \Phi_b}{\varepsilon_o \varepsilon_2} \right)^{1/2} (1 - \frac{z}{w}), \quad \text{for } 0 \leq z \leq w \tag{A.1}$$

and

$$w = \left(\frac{2\varepsilon_o \varepsilon_2 \Phi_b}{eN_d} \right)^{1/2} \tag{A.2}$$

where N_d is the doping density, e is the electron charge, ε_2 is the relative permittivity of the semiconductor, ε_o is the permittivity of free space, and Φ_b is the band bending at the surface. In contrast, the origin of the surface field in InAs is due to a different mechanism. In InAs, donor-like surface states and Fermi pinning to the conduction band at the surface results in the accumulation of electrons near the surface [11]. As there is no depletion field to drive the photo-excited electrons, diffusion processes govern the dynamics of photo-excited electrons. The spatial distribution of the steady state carrier density, n_a, beneath the interface is estimated from experimental data using $n_a = n_o e^{-\beta z}$ where $\beta = 30$ nm and n_o is the equilibrium electron concentration [12, 13].

In semiconductors at high carrier densities ($> 10^{15}$ cm^{-3}) and in the time scales of interest (~100 fs) where carrier-carrier, carrier-phonon, and carrier-impurity scattering rates are high, the Boltzmann transport picture describes photo-excited carrier motion accurately. In this formalism, the holes are taken to be stationary and electron acceleration is governed by an electrostatic potential, $\zeta(x,z,t)$. This electrostatic potential incorporates the potential due to the surface field and the potential due to space charge separation. The current density, $\vec{j}(x,z,t)$, is obtained from the momentum conservation equations under relaxation

$$\frac{\partial \vec{j}(x,z,t)}{\partial t} = \frac{e}{m*}(en(x,z,t)\vec{\nabla}\zeta(x,z,t) + \vec{j}(x,z,t)\times B + \frac{eD_e}{\mu}\vec{\nabla}n(x,z,t)) - \frac{\vec{j}(x,z,t)}{\tau} \qquad \text{(A.3)}$$

where B is the static magnetic field, D_e is the electron diffusion coefficient, μ is the electron mobility, and τ is the steady state momentum relaxation time due to carrier collisions.

To satisfy conservation of charge flux, the current density is related to the carrier density through the continuity equations

$$\frac{\partial n(x,z,t)}{\partial t} = \frac{\alpha\ (1-R)}{\eta\omega}\ I(x,z,t) + \frac{1}{e}\vec{\nabla}\cdot\vec{j}(x,z,t) - \frac{n(x,z,t)}{\gamma} \qquad \text{(A.4)}$$

and

$$\frac{\partial p(x,z,t)}{\partial t} = \frac{\alpha\ (1-R)}{\eta\omega}\ I(x,z,t) - \frac{p(x,z,t)}{\gamma} \qquad \text{(A.5)}$$

where $p(x,z,t)$ is the hole density, η is Planck's constant, and ω is the frequency of the laser pulse, R is the reflectivity of the semiconductor, γ is the carrier lifetime, and α is the semiconductor absorption depth. The time dependent intensity, $I(x,z,t)$, of the excitation pulse is given by

$$I(x,z,t) = I(t)\exp(-\frac{(x\cos\theta_l - z\sin\theta_l)^2}{\sigma_p^2} - (x\sin\theta_l + z\cos\theta_l)\alpha) \qquad \text{(A.6)}$$

where *I*(*t*) is the Gaussian temporal envelope of the pulse intensity, θ_l is the angle of incidence of the laser pulse with respect to the surface, and σ_p is the effective pulse spot diameter. Through the application of Poisson's equation,

$$\nabla^2 \zeta(x,z,t) = \frac{e}{\varepsilon_2 \varepsilon_o}\left(n(x,z,t) - p(x,z,t) + N_d\right) \tag{A.7}$$

charge separation effects induced by carrier transport are coupled self-consistently to the electrostatic potential.

The system of coupled partial differential Equations (A.3) to (A.5) and (A.7) are solved for all time using a predictor corrector method where at each step, $n(x,z,t)$ is determined. An over-relaxed Gauss-Sidel method is utilized to evaluate $\zeta(x,z,t)$ and solve self-consistently for $\overset{\omega}{j}(x,z,t)$. At $z = 0$, Neumann boundary conditions are imposed on $\overset{\omega}{j}(x,z,t)$ and at $|x| > |\sigma|$ and $z > \alpha^{-1}$, $\overset{\omega}{j}(x,z,t)$ is set to zero. The emitted THz electric field components originating from the focal volume is given by

$$E_{x,z}(t) = \frac{t_{x,z}(\varphi)\sigma_{p,y}}{4\pi\varepsilon_2\varepsilon_o c^2}\frac{d}{dt}\int \frac{j_{x,z}(x',z',t)}{|L_d - r'|}\,dV \tag{A.8}$$

where L_d is the distance of the detector from the origin, *c* is the speed of light, $\sigma_{p,y}$ is the pulse spot size in the *y*-direction, and $t_{x,z}(\varphi)$ incorporates the transmission coefficient due to refraction at the air-semiconductor interface. The transmission coefficients for the THz field components parallel $E_x(t)$ and perpendicular $E_z(t)$ to the surface are expressed as [8]

$$t_x(\varphi) = \frac{(\varepsilon_2 - \sin^2\varphi)^{1/2}}{(\varepsilon_2 \cos\varphi + (\varepsilon_2 - \sin^2\varphi)^{1/2})} \tag{A.9}$$

and

$$t_z(\varphi) = \frac{\sin\varphi}{\varepsilon_2 \cos\varphi + (\varepsilon_2 - \sin^2\varphi)^{1/2}} \tag{A.10}$$

respectively.

The two-dimensional drift-diffusion model is then used to investigate the carrier dynamics in n-doped GaAs and undoped InAs for varying magnetic field strengths and excitation regimes. The results are compared with previously reported experimental data. The parameters used in the simulation are listed in Table A.1.

	GaAs	InAs
ε_2	12.8	14.6
α^{-1}	500nm	143nm
D_e	200 cm^2/s	1000 cm^2/s
m*	0.067m$_o$	0.023m$_o$
μ	4600 cm^2/Vs	25000 cm^2/Vs
γ^{-1}	1000 fs	1000 fs
τ	50 fs	150 fs
R_I	0.3	0.3
n_o	1x10^{15}cm^{-3}	1x10^{15}cm^{-3}

Table A.1. List of parameters used in the numerical simulations.

To explain the complex carrier dynamics, both the current density and electrostatic potential must be considered simultaneously. Figure A.2 depicts the sequence of events of the spatio-temporal evolution of the current density, $\overset{\omega}{j}(x,z,t)$, in n-GaAs for B = 0 T at times $t = -100$ fs, 300 fs, and 700 fs after photo excitation with a 100 fs, 800 nm laser pulse. The corresponding electric potential is plotted in Figure A.3.

Prior to the arrival of the pulse at $t = -100$ fs, the steady state carrier dynamics govern the potential distribution. The equilibrated steady state carrier population sets up a depletion field extending 500 nm into the n-GaAs surface with a peak value of 7.6 kV/cm. At $t = 0$ fs a high density of carriers within the depletion region has been photo-excited by the laser pulse. At $t = 300$ fs, the depletion field within 100 nm of the surface has been almost entirely screened by the photo-generated carriers as evidenced by the zero gradient of the electrostatic potential in Figure A.3. Coupled drift and diffusion forces govern the dynamics of photo-generated carriers. As a result, electron diffusion from the high carrier concentration region causes a small current density component parallel to the surface, $j_x(x,z,t)$. Meanwhile, the current density component perpendicular to the surface $j_z(x,z,t)$ is driven by the strong surface depletion field and exceeds $j_x(x,z,t)$ by a factor of 12, as shown in Figure A.2. Evidently, diffusion currents play a minor role in the current density evolution in n-GaAs. This prediction is consistent with observations by Johnston et al. [9]. At longer times, $t = 700$ fs, carrier scattering and carrier recombination reduce current densities to equilibrium values.

When the magnetic field is non-zero, the carrier dynamics are significantly modified. Figure A.4 illustrates the evolution of the current density in n-GaAs when a magnetic field of $B = 6$ T is applied. In contrast to the $B = 0$ T case, when a magnetic field is applied $j_x(x,z,t)$ does not exhibit a bipolar distribution at $t = 300$ fs. Instead, carriers that are initially driven perpendicular to the surface by the depletion field are accelerated into the parallel direction by the magnetic field, enhancing the current density component parallel to the surface. In this situation, the current density perpendicular to the surface, $j_z(x,z,t)$, is only a factor of 2 larger than $j_x(x,z,t)$. As $j_x(x,z,t)$ is enhanced, the coupling efficiency of the THz emission increases due to polarization sensitive refraction at the semiconductor-air interface.

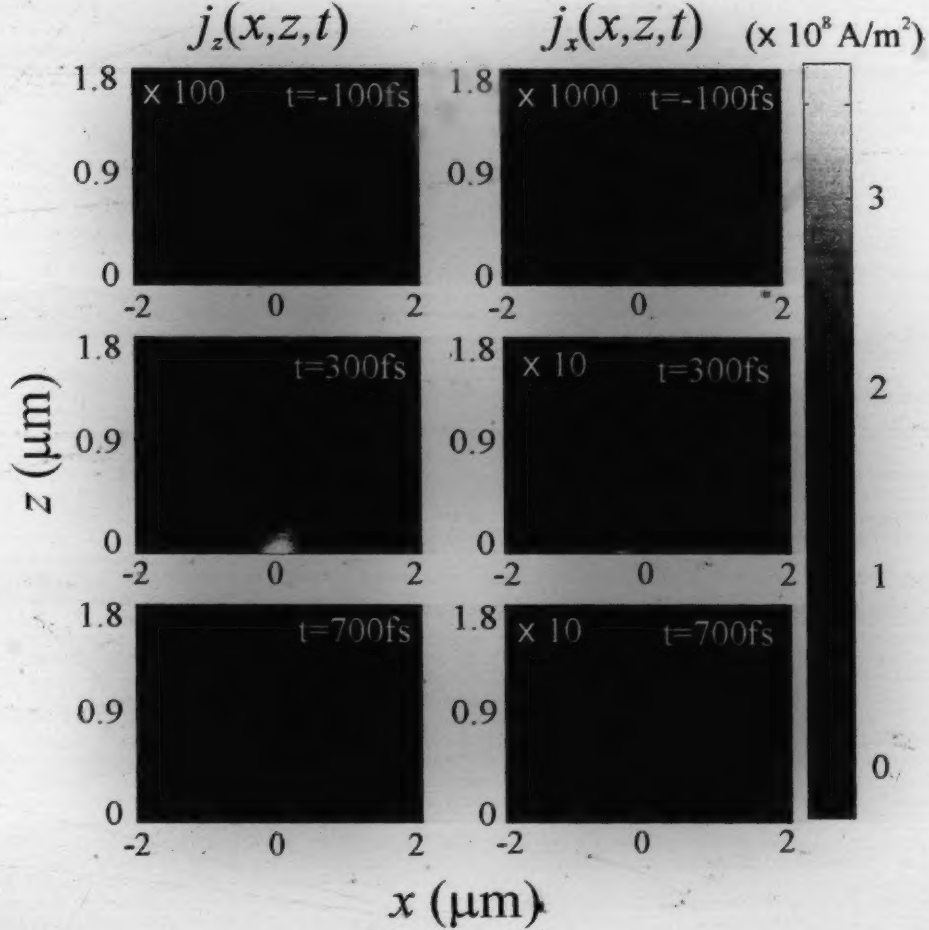

Figure A.2. Spatio-temporal evolution of the perpendicular (left) and parallel (right) current densities within n-GaAs at different times for B = 0 T. Note that the laser is illuminating the semiconductor surface at $z = 0$ from below at an angle of 45°.

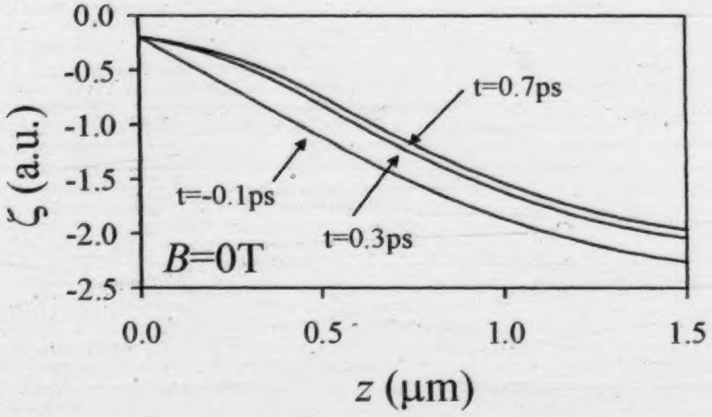

Figure A.3. Electrostatic potential as a function of depth in n-GaAs at various times for $B = 0$ T.

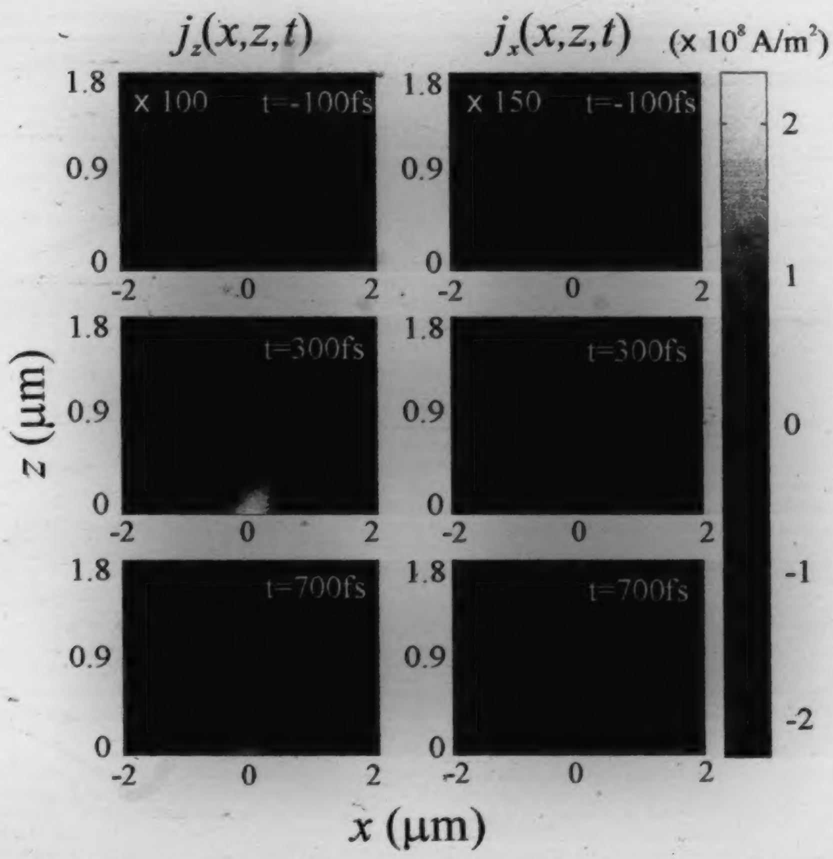

Figure A.4. Spatio-temporal evolution of the perpendicular (left) and parallel (right) current densities within n-GaAs at different times for $B = 6$ T. Note that the laser is illuminating the semiconductor surface at $z = 0$ from below at an angle of 45°.

On the other hand, carrier dynamics are drastically different in InAs due to the higher electron diffusivity and the absence of a surface depletion field. Again, to illustrate the carrier dynamics, both the current density and electrostatic potential are considered. Figure A.5 depicts the spatial dependence of the electrostatic potential beneath the InAs surface at various times for $B = 0$ T. Prior to excitation at $t = -100$ fs, the constant potential within the semiconductor describes the absence of a surface field. Upon the photo-excitation of electron-hole pairs at $t = 0$ fs, diffusion of high mobility electrons will cause charge separation and the establishment of a built in photo-Dember field (2 kV/cm). This can be illustrated later at $t = 300$ fs, where a large photo-Dember potential is established within 50 nm of the surface. At $t = 700$ fs, the photo-Dember field penetrates a maximum depth of ~100 nm into the InAs surface. The photo-Dember field vanishes for times greater than the carrier lifetime. While the photo-Dember field is established, ultrafast electron diffusion drives large currents within the semiconductor. Figure A.6 depicts the current density components in undoped InAs at times $t = -100$ fs, 300 fs, and 700 fs for a zero magnetic field strength. At $t = -100$ fs, few carriers are excited by the weak wing of the Gaussian pulse, resulting in insignificant, but finite, current densities in both the x- and z- directions. At the peak of the pulse, $t = 0$ fs, large carrier populations have been created by the absorption of the laser pulse within 143 nm of the InAs surface. As shown for $t = 300$ fs in Figure A.6, carrier diffusion, which is proportional to the carrier density gradient in the photoexcited region, results in the unipolar and bipolar spatial distributions of $j_z(x,z,t)$ and $j_x(x,z,t)$, respectively. At a later time at $t = 700$ fs, carrier scattering and recombination drive the current densities to equilibrium values.

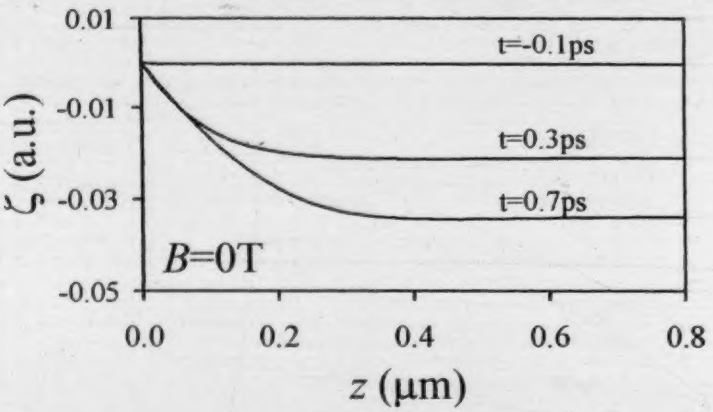

Figure A.5. Electrostatic potential versus depth in InAs at various times for B = 0 T.

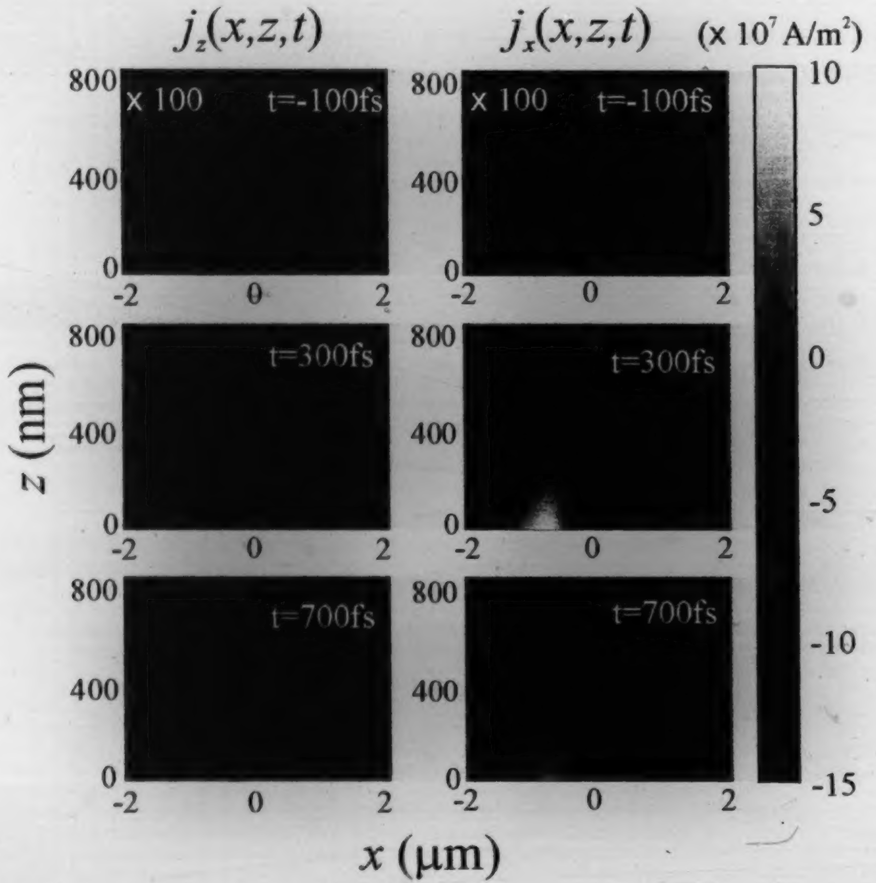

Figure A.6. Spatio-temporal evolution of the perpendicular (left) and parallel (right) current densities within InAs at different times for B = 0 T. Note that the laser is illuminating the semiconductor surface at z = 0 from below at an angle of 45°.

When a high magnetic field is applied, the Lorentz force alters the carrier trajectories and thus the spatial distribution of the current densities. This is illustrated in Figure A.7 by following the current density spatio-temporal evolution for B = 3 T. In contrast to the B = 0 T case, at t = 300 fs, the application of the magnetic field has altered the current density distributions such that $j_z(x,z,t)$ is now bipolar whereas $j_x(x,z,t)$ is unipolar. This is equivalent to the reorientation of the electrical dipole by 90°. When compared to n-GaAs, the magnitude of $j_x(x,z,t)$ relative to $j_z(x,z,t)$ in InAs has not been significantly enhanced with the application of a magnetic field. Instead, the experimentally observed THz radiation emission enhancement in InAs can be attributed to the modified current density spatial distributions. That is, for B = 0 T, the bi-directional nature of $j_x(x,z,t)$ results in far field cancellation of the THz emission component parallel to the surface. However, when B = 3 T, $j_x(x,z,t)$ is uni-directional, resulting in the coherent addition of the emitted THz radiation in the far-field. This suggests that the observed THz radiation enhancement in InAs is primarily ascribed to the spatial re-orientation of the current densities.

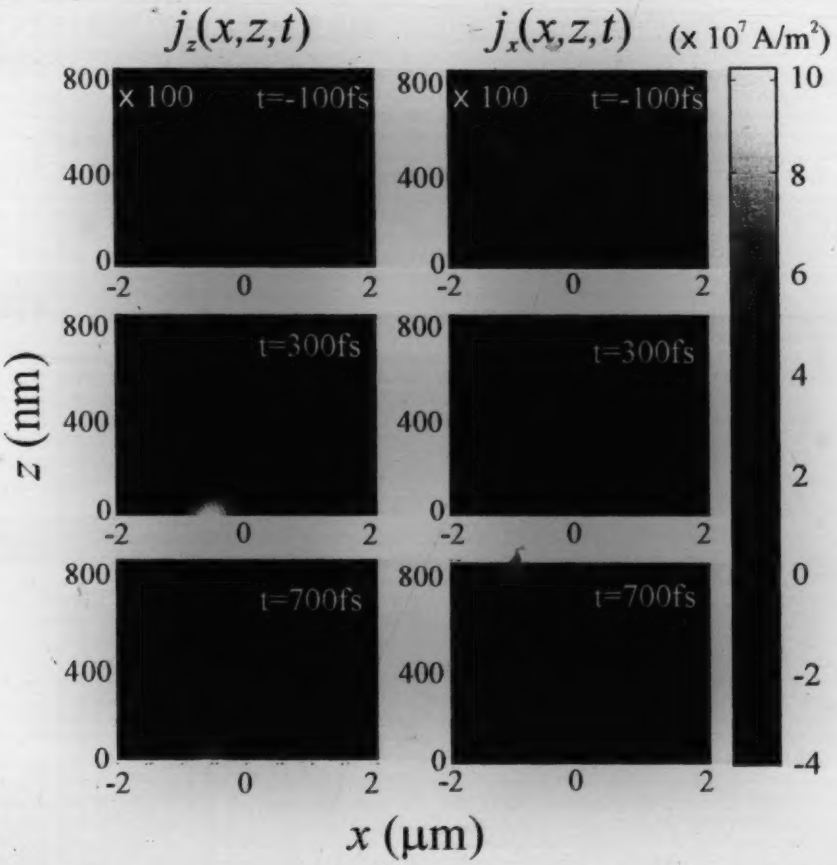

Figure A.7. Spatio-temporal evolution of the perpendicular (left) and parallel (right) current densities within InAs at different times for B = 3 T. Note that the laser is illuminating the semiconductor surface at z = 0 from below at an angle of 45°.

The THz radiation emission from the surface of n-GaAs is shown in Figure A.8 for various magnetic field strengths. For B = 0 T, the THz pulse component polarized along the x-axis is lower by a factor of ~250 and is relatively broader than the z-polarized field component. This is due to the fact that $j_x(x,z,t)$ is driven by slow diffusion processes while $j_z(x,z,t)$ originates from rapid carrier acceleration by the surface field. When the applied magnetic field is increased, the amplitude of $E_x(t)$ increases significantly while $E_z(t)$ slightly decreases. This results in an overall enhancement of the THz emission amplitude. In addition, it is observed that the electric field components, $E_x(t)$ and $E_z(t)$, evolve from a predominantly unipolar pulse envelope at low magnetic field into a pronounced bi-polar pulse shape as the field increases. In the spectral domain, this behaviour manifests itself through spectral broadening and shifting. The emission spectra at $B = 3$ T and $B = 6$ T are depicted in Figure A.9 (a). At $B = 3$ T, the spectrum consists of a single broad peak centred at 0.6 THz. As the magnetic field reaches 6 T, the spectrum broadens and the spectral peak shifts towards 1 THz. This behaviour is in excellent agreement with experimental results demonstrated by Corchia et al. [3] for n-GaAs using similar experimental parameters. In their experiment, similar spectral broadening and shifting is observed as the magnetic field is increased from 2 T to 4 T.

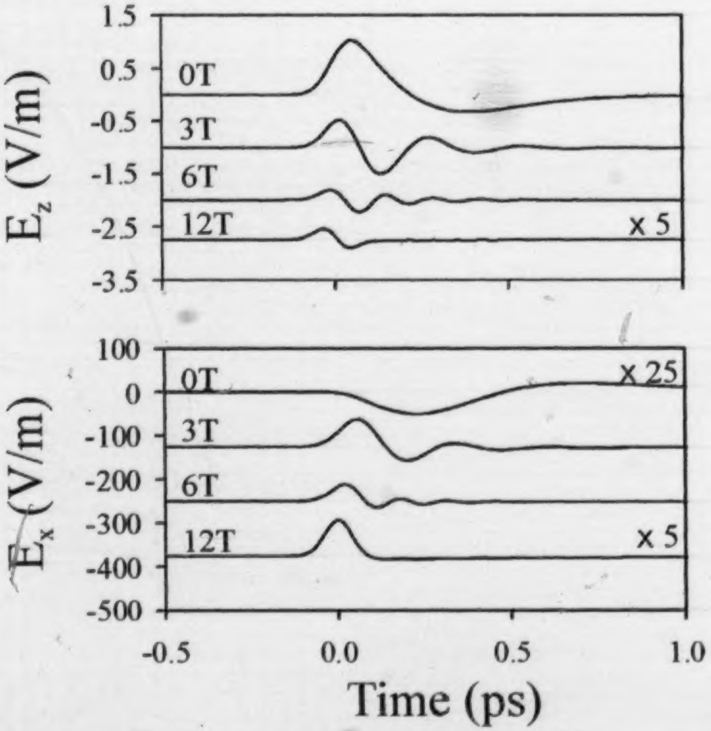

Figure A.8. The *z*-polarized (top) and *x*-polarized (bottom) temporal waveforms of THz emission from n-GaAs at various magnetic field strengths.

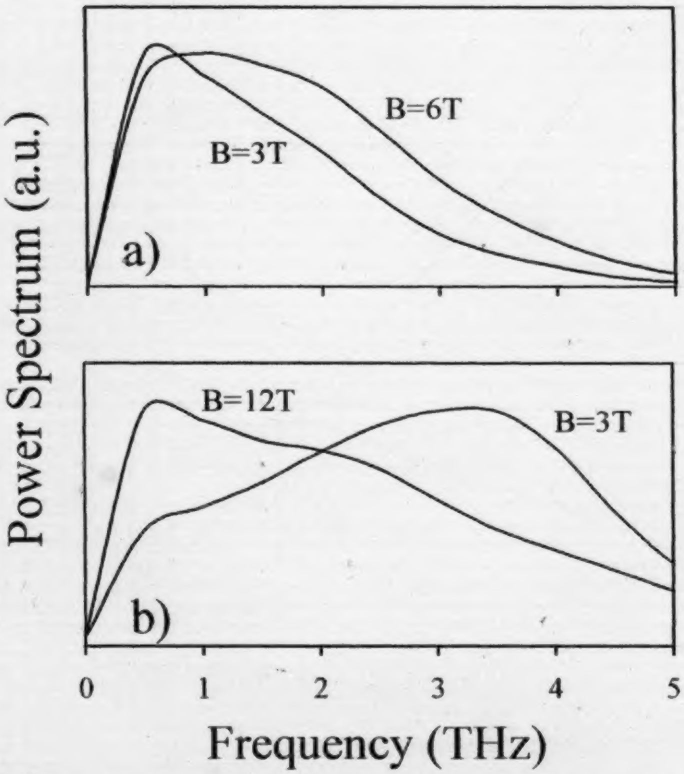

Figure A.9. (a) Normalized THz emission spectra from n-GaAs at $B = 3$ T and $B = 6$ T. (b) Normalized THz emission spectra from InAs at $B = 3$ T and $B = 12$ T.

The temporal and spectral behaviour of the THz emission from InAs are also analyzed as a function of the applied magnetic field. The components $E_x(t)$ and $E_z(t)$ from undoped InAs are presented in Figure A.10 for varying magnetic fields. At $B = 0$ T, both *x*- and *z*-polarized components have broad, bipolar pulse shapes due to diffusion-driven current densities. As the magnetic field is increased to 3 T, the THz pulse exhibits temporal narrowing and significant post-peak oscillations following photo-excitation. Further increase in the magnetic field up to 12 T results in overdamped emission with reduced amplitude. Interestingly, these temporal characteristics are similar to what was experimentally observed by McLaughlin et al. [4]. The emission spectra at $B = 3$ T and B

= 12 T are illustrated in Figure A.9 (b). At B = 3 T, the spectrum is broad and centred at 3.25 THz. When the magnetic field is increased to 12 T, the spectrum shifts toward lower frequencies and peaks at approximately 0.75 THz. Although the locations of the peaks reported in [5] occur at lower frequencies, the overall predicted behaviour agrees with the experimental emission spectra. In their work, a marked shift in the THz spectrum toward lower frequencies is observed as the field is increased from 3 T to 14 T.

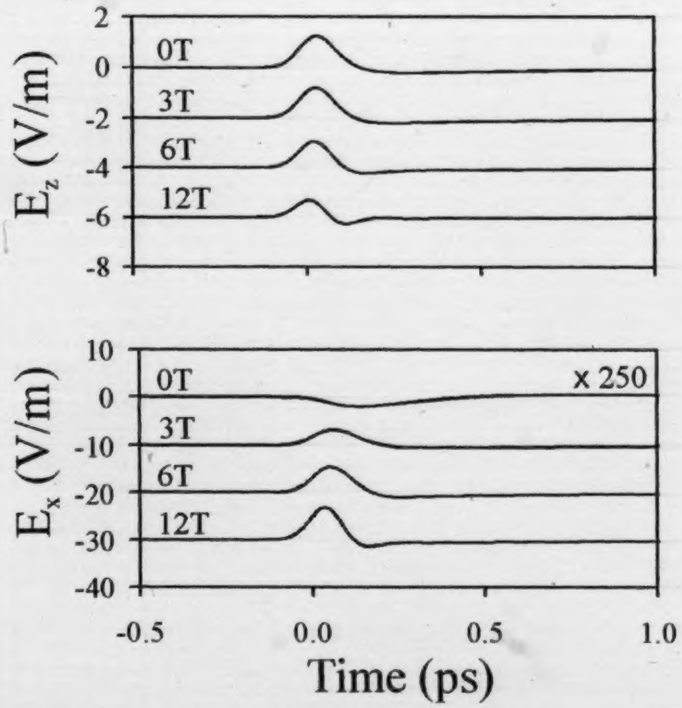

Figure A.10. The z-polarized (top) and x-polarized (bottom) temporal waveforms of THz emission from InAs at various magnetic field strengths.

An important prediction from the model is the THz radiation power dependence on the applied magnetic field. Figure A.11 illustrates the power of the THz emission from n-doped GaAs as a function of the magnetic field strength at a fluence of 0.22 μJ/cm^2.

Interestingly, the magnetic field dependence of the THz emission power is asymmetric about 0 T with a minimum THz power emission occurring at approximately 0.3 T. Experimentally, Heyman et al. [6] have measured a similar trend where an offset in the minimum THz power was observed at 0.9 T. The discrepancy between the experiment and the model are likely due to small differences in the optical pulse fluence and the doping concentrations of the sample. From our model, the offset in the minimum is attributed to off-normal illumination of the surface. As there are significant diffusion currents along the x-direction at $B = 0$ T, the minimum THz emission does not occur at $B = 0$ T. Instead, when a slight magnetic field of 0.3 T is applied, re-direction of a small amount of $j_z(x,z,t)$ to the x-direction results in minimum THz radiation power due to cancellation of the emission along $\pm x$. Beyond a magnetic field magnitude of |1 T|, the THz emission increases linearly and then saturates at ~ |5.5 T|. Such a behavior is also in accordance with experimental studies reported by Heyman et al. [6].

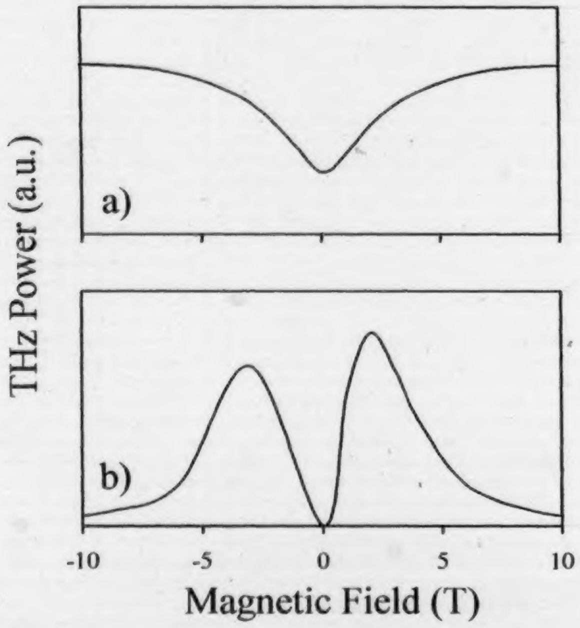

Figure A.11. THz emission power for a) n-GaAs and b) InAs as a function of the magnetic field strength.

The magnetic field dependence of the THz emission power from n-InAs at a fluence of 0.04 μJ/cm^2 is illustrated in Figure A.11. The emission power increases rapidly from 0 T and peaks at approximately 3 T. The peak power at +3 T exceeds that at –3 T, consistent with several experimental studies [5, 6, 14]. The asymmetric power dependence on the magnetic field can again be explained from our model by considering the effect of off-normal photo-excitation. In such a configuration, the diffusion forces adjacent to the photo-excited region are not symmetric. As a result, the amount of dipole rotation induced by the magnetic field will depend on the direction of rotation and consequently, the direction of the magnetic field. Unlike previous Monte-Carlo simulations, our analysis accurately models the decrease in the emission power beyond 3 T in InAs. However, the model is unable to reproduce the recovery in the THz emission reported above B = 6 T [5].

The optical excitation fluence is a crucial factor in the magnetic field-induced enhancement of THz emission. Figure A.12 (a) illustrates the THz emission power versus excitation fluence up to 2.2 μJ/cm^2. For fluences from 40 nJ/cm^2 to 0.5 μJ/cm^2, the power enhancement is approximately 25. This enhancement value predicted in the model agrees well the reported experimental enhancement factors (10 to 35) using n-GaAs [6, 15]. This behaviour is in accordance with studies by Corchia et al. [3], where the enhancement is nearly constant for fluences from 10 to 200 nJ/cm^2. Interestingly, as the fluence is increased above 0.5 μJ/cm^2, carrier screening of the surface field results in a decrease in the emission enhancement factor. The screening, which is directly proportional to the energy fluence, causes a linear decrease in the THz emission power as the energy fluence increases. Figure A.12 (b) depicts the enhancement factor in InAs versus optical excitation fluence. For a fluence of 0.25 μJ/cm^2, an enhancement factor of 84 is predicted. This is in good agreement with the enhancement factor of 74 measured in experiments by Heyman et al. [6], where 60 nJ/cm^2 pulses and an identical geometry are used. As the excitation fluence increases above 0.5 μJ/cm^2 the maximum power enhancement decreases markedly, saturating above 0.9 μJ/cm^2. The decreased enhancement with increasing fluence is attributed to charge screening of the photo-Dember field, limiting the dipole rotation induced by the magnetic field. A much sharper decrease is observed in InAs as opposed to n-GaAs since diffusion and photo-Dember effects more responsive to the carrier densities than drift effects. The predicted fluence dependence is found to be in excellent agreement with experimental data by Takahashi et al. [7] plotted as an inset of Figure A.12 (b). To study the effects of doping on THz emission from InAs, doped InAs is modeled by simply increasing the background concentration of electrons in InAs while keeping all other parameters constant. For the doped sample (n_o = 1×10^{16} cm^{-3}), the maximum THz emission power is predicted to decrease by a factor of 1.4. This value is in good agreement with [6] where the emission from the doped InAs sample (n_o = 7.5×10^{16} cm^{-3}) was 2 times weaker than the nominally undoped InAs (n_o = 1.8×10^{16} cm^{-3}). The decreased emission power from the doped sample is attributed to the increased charge screening due to the increased steady state electron accumulation layer.

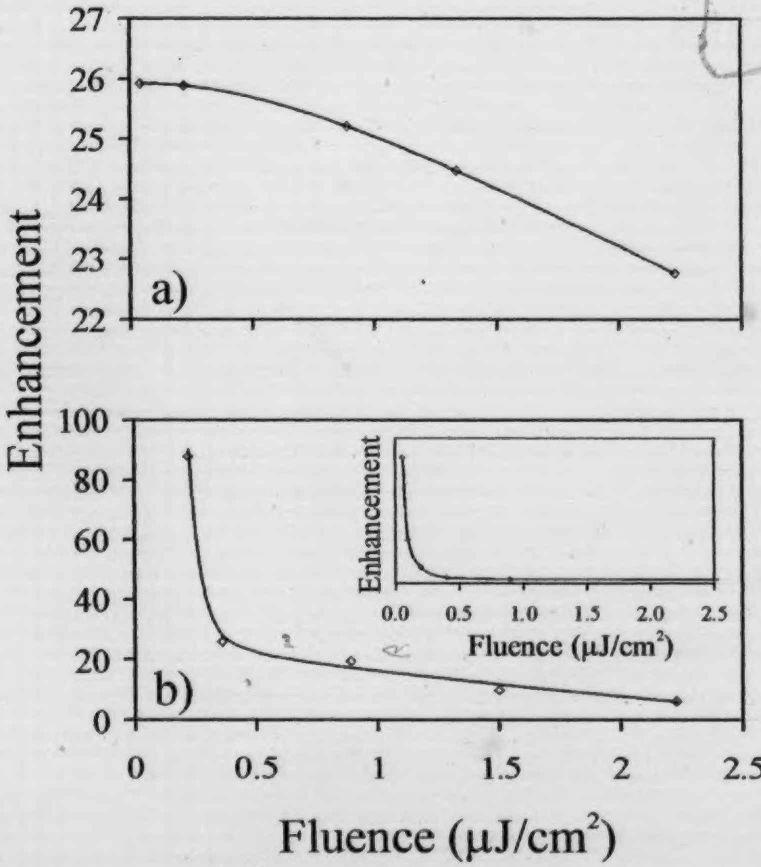

Figure A.12. Enhancement factor for (a) n-GaAs and (b) InAs as a function of the optical fluence. For n-GaAs, the enhancement is the ratio between the THz emission power at 6 T and 0 T. The enhancement for InAs is the ratio of the THz power at 3 T and 0 T. The inset in (b) is taken from Ref. [7].

In conclusion, THz emission for n-GaAs and InAs surfaces based on drift-diffusion transport model has been investigated. Unlike previous semi-classical and Monte Carlo simulations, the current analysis provides a complete two-dimensional picture of current densities and carrier population evolution and includes charge screening, photo-Dember, and THz refraction effects. The work clearly demonstrates that diffusion and photo-Dember driven current densities are responsible for THz emission from InAs whereas drift currents dominate in n-GaAs. Terahertz power enhancement and spectra for n-GaAs are well described for magnetic fields up to 10 T. Anomalous decrease in the THz emission power from InAs surfaces above 3 T is accurately reproduced. In addition, experimentally observed asymmetric power dependences on the magnetic field in InAs and n-GaAs have been explained and in both cases, are ascribed to off-normal surface illumination. For fluences up to 2.2 μJ/cm^2, the enhancement as a function of fluence for n-GaAs and InAs is in excellent agreement with previously reported experimental data. The analysis provides a physical picture and a novel theoretical understanding of enhancement of THz emission from semiconductor surfaces. The application of this model will certainly be used in the design and optimization of THz surface emitters.

Appendix A References

[1] D. Grischkowsky, S. Keiding, M. v. Exter, and C. Fattinger, "Far-infrared time-domain spectroscopy with terahertz beams of dielectrics and semiconductors," *Journal of the Optical Society of America B*, vol. 7, pp. 2006-2015, 1990.

[2] B. B. Hu and M. C. Nuss, "Imaging with terahertz waves," *Optics Letters*, vol. 20, pp. 1716-1718, 1995.

[3] A. Corchia, R. McLaughlin, M. B. Johnston, D. M. Whittaker, D. D. Arnone, E. H. Linfield, A. G. Davies, and M. Pepper, "Effects of magnetic field and optical fluence on terahertz emission in gallium arsenide," *Physical Review B*, vol. 64, pp. 205204, 2001.

[4] R. McLaughlin, A. Corchia, M. B. Johnston, Q. Chen, C. M. Ciesta, D. D. Arnone, G. A. C. Jones, E. H. Linfield, A. G. Davies, and M. Pepper, "Enhanced coherent terahertz emission from indium arsenide in the presence of a magnetic field," *Applied Physics Letters*, vol. 76, pp. 2038-2040, 2000.

[5] H. Ohtake, H. Murakami, T. Yano, S. Ono, N. Sarukura, H. Takahashi, Y. Suzuki, G. Nishijima, and K. Watanabe, "Anomalous power and spectrum dependence of terahertz radiation from femtosecond-laser-irradiated indium arsenide in high magnetic fields up to 14 T," *Applied Physics Letters*, vol. 82, pp. 1162-1164, 2003.

[6] J. N. Heyman, P. Neocleous, D. Hebert, P. A. Crowell, T. Muller, and K. Unterrainer, "Terahertz emission from GaAs and InAs in a magnetic field," *Physical Review B*, vol. 64, pp. 085202, 2001.

[7] H. Takahashi, A. Quema, R. Yoshioka, S. Ono, and N. Sarukura, "Excitation fluence dependence of terahertz radiation mechanism from femtosecond-laser-irradiated InAs under magnetic field," *Applied Physics Letters*, vol. 83, pp. 1068-1070, 2003.

[8] J. Shan, C. Weiss, R. Wallenstein, R. Beigang, and T. F. Heinz, "Origin of magnetic field enhancement in the generation of terahertz radiation from semiconductor surfaces," *Optics Letters*, vol. 26, pp. 849-851, 2001.

[9] M. B. Johnston, D. M. Whittaker, A. Corchia, A. G. Davies, and E. H. Linfield, "Simulation of terahertz generation at semiconductor surfaces," *Physical Review B*, vol. 65, pp. 165301, 2002.

[10] H. Ohtake, S. Ono, M. Sakai, Z. Liu, T. Tsukamoto, and N. Sarukura, "Saturation of THz radiation power from femtosecond-laser-irradiated InAs in a high magnetic field," *Applied Physics Letters*, vol. 76, pp. 1398-1400, 2000.

[11] L. O. Olsson, C. B. M. Andersson, M. C. Hakansson, J. Kanski, L. Ilver, and U. O. Karlsson, "Charge accumulation at InAs surfaces," *Physical Review Letters*, vol. 76, pp. 3626-3629, 1996.

[12] G. R. Bell, C. F. McConville, and T. S. Jones, "Plasmon excitations and accumulation leyers in heavily doped InAs(001)," *Physical Review B*, vol. 54, pp. 2654-2661, 1996.

[13] T. D. Veal and C. F. McConville, "Profiling of electron accumulation layers in the near-surface region of InAs (110)," *Physical Review B*, vol. 64, pp. 085311, 2001.

[14] H. Takahashi, M. Sakai, A. Quema, S. Ono, N. Sarukura, G. Nishijima, and K. Watanabe, "Terahertz radiation from InAs with various surface orientations under magnetic field irradiated with femtosecond optical pulses at different wavelengths," *Journal of Applied Physics*, vol. 95, pp. 4545-4550, 2004.

[15] M. B. Johnston, D. M. Whittaker, A. Corchia, A. G. Davies, and E. H. Linfield, "Theory of magnetic-field enhancement of suerface-field terahertz emission," *Journal of Applied Physics*, vol. 91, pp. 2104-2106, 2002.

Appendix B: Nonlinear Response of <111> ZnSe

Electro-optic detection of the THz pulse is achieved in a <111> ZnSe crystal. The scheme for this detection is shown in Figure B.1. In this configuration, both the probe and the THz pulse co-propagate into the crystal along the [111] direction. The probe and the THz pulse are polarized at angles θ_{probe} and θ_{THz} from the z_o basis vector of the laboratory coordinate system (x_o, y_o, z_o). The incoming probe can be expressed as

$$\vec{E}_{probe} = E_{probe} \sin\theta_{probe}\, \hat{y}_o + E_{probe} \cos\theta_{probe}\, \hat{z}_o \qquad \text{(B.1).}$$

It can be shown that a coordinate transformation of $\hat{y}_o = \hat{y}_2 \cos\theta_{THz}/2 - \hat{z}_2 \sin\theta_{THz}/2$ and $\hat{z}_o = \hat{y}_2 \sin\theta_{THz}/2 + \hat{z}_2 \cos\theta_{THz}/2$ is required to eliminate the cross terms in the index ellipsoid. This transformation corresponds to a rotation of $\theta_{THz}/2$ about the x_o axis. Applying this transformation, the probe pulse expressed in the coordinate system (x_2, y_2, z_2) is

$$\begin{aligned}\vec{E}_{probe} = E_{probe}\, [(&\sin\theta_{probe} \cos\theta_{THz}/2 + \cos\theta_{probe} \sin\theta_{THz}/2)\hat{y}_2 + \\ (&\cos\theta_{probe} \cos\theta_{THz}/2 - \sin\theta_{probe} \sin\theta_{THz}/2)\hat{z}_2\end{aligned} \qquad \text{(B.2).}$$

Including the spatio-temporal dependence of the probe pulse, the electric field that exits the electro-optic crystal is expressed as

$$\begin{aligned}\vec{E}_{probe} = E_{probe} &\sin(\theta_{probe} + \theta_{THz}/2)e^{i(\omega t - kn_{y2}L)}\hat{y}_2 + \\ E_{probe} &\cos(\theta_{probe} + \theta_{THz}/2)e^{i(\omega t - kn_{z2}L)}\hat{z}_2\end{aligned} \qquad \text{(B.3)}$$

where L is the thickness of the electro-optic crystal, k is the wavevector, n_{y2} is the refractive index along $\hat{y}_2$ and n_{z2} is the refractive index along $\hat{z}_2$. The phase retardation introduced by THz pulse is experimentally resolved using a quarter wave-plate and Wollaston prism. For maximum phase retardation, the slow and fast axes of the quarter wave-plate are aligned as 45° with respect to the probe polarization. To account for this effect, a coordinate transformation is applied where

$$\hat{y}_2 = \cos(3\theta_{THz}/2 - \pi/4)\hat{y}_3 + \sin(3\theta_{THz}/2 - \pi/4)\hat{z}_3 \tag{B.4}$$

and

$$\hat{z}_2 = -\sin(3\theta_{THz}/2 - \pi/4)\hat{y}_3 + \cos(3\theta_{THz}/2 - \pi/4)\hat{z}_3 \tag{B.5}$$

to Equation B.3 and introducing a π/2 phase shift, the probe electric field exiting the electro-optic crystal is

$$\begin{aligned}
&\overset{\omega}{E}_{probe} = \\
&E_{probe}\,[\sin(\theta_{probe} + \theta_{THz}/2)\cos(3\theta_{THz}/2 - \pi/4)e^{i(\omega t - kn_{y2}L + \pi/4)} - \\
&\cos(\theta_{probe} + \theta_{THz}/2)\sin(3\theta_{THz}/2 - \pi/4)e^{i(\omega t - kn_{z2}L + \pi/4)}]\hat{y}_3 + \qquad \text{(B.6).}\\
&E_{probe}\,[\sin(\theta_{probe} + \theta_{THz}/2)\sin(3\theta_{THz}/2 - \pi/4)e^{i(\omega t - kn_{y2}L - \pi/4)} + \\
&\cos(\theta_{probe} + \theta_{THz}/2)\cos(3\theta_{THz}/2 - \pi/4)e^{i(\omega t - kn_{z2}L - \pi/4)}]\hat{z}_3
\end{aligned}$$

The Wollaston prism splits the probe beam into two components that are parallel to the incident probe polarization and perpendicular to the incident probe polarization. The electric field components are

$$\begin{aligned}
&\overset{\omega}{E}_{probe\ 1} = E_{probe}/\sqrt{2} \times \\
&[\sin(\theta_{probe} + \theta_{THz}/2)\cos(3\theta_{THz}/2 - \pi/4)e^{i(\omega t - kn_{y2}L + \pi/4)} - \\
&\cos(\theta_{probe} + \theta_{THz}/2)\sin(3\theta_{THz}/2 - \pi/4)e^{i(\omega t - kn_{z2}L + \pi/4)} - \qquad \text{(B.7)}\\
&\sin(\theta_{probe} + \theta_{THz}/2)\sin(3\theta_{THz}/2 - \pi/4)e^{i(\omega t - kn_{y2}L - \pi/4)} - \\
&\cos(\theta_{probe} + \theta_{THz}/2)\cos(3\theta_{THz}/2 - \pi/4)e^{i(\omega t - kn_{z2}L - \pi/4)}]
\end{aligned}$$

and

$$\begin{aligned}
&\overset{\omega}{E}_{probe\ 2} = E_{probe} / \sqrt{2} \times \\
&[\sin(\theta_{probe} + \theta_{THz}/2)\cos(3\theta_{THz}/2 - \pi/4)e^{i(\omega t - kn_{y2}L + \pi/4)} - \\
&\cos(\theta_{probe} + \theta_{THz}/2)\sin(3\theta_{THz}/2 - \pi/4)e^{i(\omega t - kn_{z2}L + \pi/4)} + \qquad \text{(B.8).} \\
&\sin(\theta_{probe} + \theta_{THz}/2)\sin(3\theta_{THz}/2 - \pi/4)e^{i(\omega t - kn_{y2}L - \pi/4)} + \\
&\cos(\theta_{probe} + \theta_{THz}/2)\cos(3\theta_{THz}/2 - \pi/4)e^{i(\omega t - kn_{z2}L - \pi/4)}]
\end{aligned}$$

The power difference between the two probe components produces a differential signal proportional to the THz electric field given by

$$\Delta P = P_{probe}\sin[k(n_{y2} - n_{z2})L]\sin(2\theta_{probe} + \theta_{THz}) \qquad \text{(B.9).}$$

The electro-optic response of the <111> ZnSe crystal enables the independent measurement of orthogonal THz pulse components. For orthogonal THz pulse components aligned along $\theta_{THz} = \theta_{probe}$ and $\theta_{THz} = \theta_{probe} + 90^\circ$, the electro-optic responses of the <111> ZnSe crystal to the two THz pulse components are

$$\Delta P_{\theta_{THz} = \theta_{probe}} \propto \sin(3\theta_{probe}) \qquad \text{(B.10)}$$

and

$$\Delta P_{\theta_{THz} = \theta_{probe} + 90^{0}} \propto \cos(3\theta_{probe}) \qquad \text{(B.11).}$$

The 120° rotational symmetry of the ZnSe crystal along the [111] direction causes the three-fold symmetric electro-optic response as a function of the crystal orientation, θ_{probe}. Since perpendicular THz pulse components produce mutually orthogonal electro-optic responses, the two components of the THz pulse can be measured by simply re-orienting the electro-optic crystal by 30° in the laboratory frame.

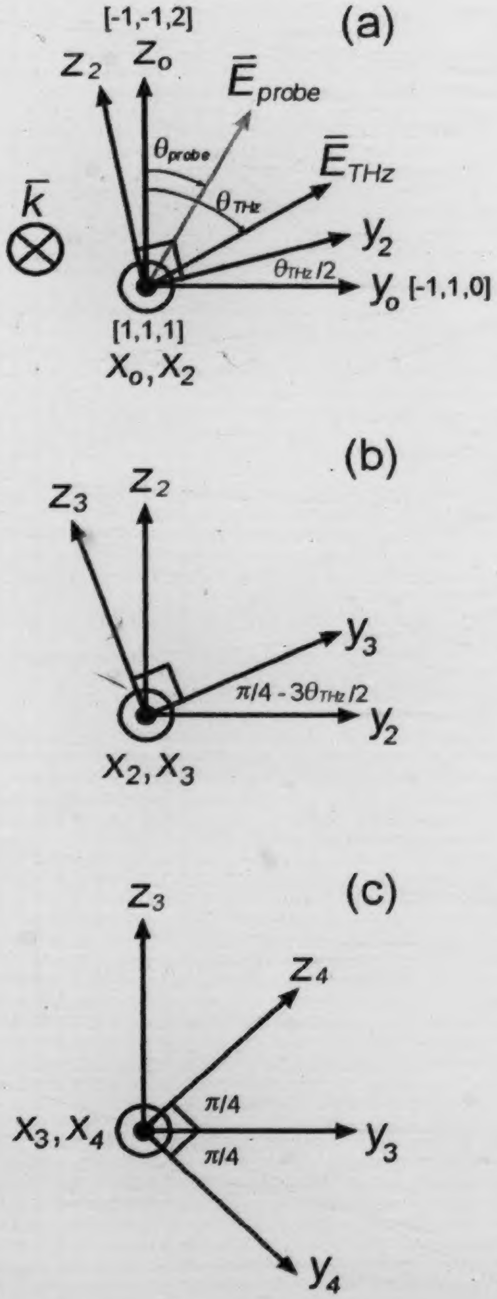
(a)
[-1,-1,2]
z_2
z_o
$\bar{E}_{probe}$
θ_{probe}
$\bar{E}_{THz}$
θ_{THz}
$\bar{k}$
y_2
$\theta_{THz}/2$
y_o [-1,1,0]
[1,1,1]
x_o, x_2
(b)
z_3
z_2
y_3
$\pi/4 - 3\theta_{THz}/2$
y_2
x_2, x_3
(c)
z_3
z_4
$\pi/4$
x_3, x_4
y_3
$\pi/4$
y_4

Figure B.1. (a) The THz electric field and probe electric field are shown in the laboratory coordinate system (x_o, y_o, z_o) and the rotated coordinate system (x_2, y_2, z_2). The laboratory coordinate system is aligned with the [−1,−1,2], [−1,1,0], and [1,1,1] directions. (b) The rotated coordinate system (x_2, y_2, z_2) is shown with the quarter wave-plate coordinate system (x_3, y_3, z_3). (c) The coordinate systems for the quarter wave-plate (x_3, y_3, z_3) and Wollaston prism polarizers (x_4, y_4, z_4) are shown.

Appendix C: Finite Difference Time-Domain Calculations

To describe electromagnetic wave interaction with dielectric and metallic media, Maxwell's equations are employed to describe the spatial and temporal distribution of the electric and magnetic fields in the presence of (unmagnetized) matter.

$$-\frac{\partial \boldsymbol{H}}{\partial t}=\frac{1}{\mu_o}\nabla\times\boldsymbol{E} \tag{C.1}$$

$$\frac{\partial \boldsymbol{D}}{\partial t}=\nabla\times\boldsymbol{H} \tag{C.2}$$

where ***H*** is the magnetic flux density, ***D*** is the displacement field, ***E*** is the electric field, and μ_o is the free space permeability. To solve these equations, many numerical methods can be employed. One of the most widely used techniques is the Finite Difference Time-Domain (FDTD) method. The FDTD method is advantageous due to its relative simplicity and ease of use. Because the material properties of each pixel of the simulation space can be specified, many linear and nonlinear materials can be modeled in a wide range of geometries. The time-domain nature of the FDTD technique implied that the response of a system to broadband electromagnetic pulse excitation over a wide range of frequencies can be obtained with a single simulation. Moreover, the FDTD solves the complete spatial and temporal electric and magnetic fields, which permits animated displays of the electromagnetic field progression through a system.

In the two-dimensional simulations used in this thesis, transverse magnetic (TM) polarized THz electromagnetic pulse excitation is employed. Equations (C.1) and (C.2) can be written in terms of the field components E_x, E_y, D_x, D_y, and H_z to yield

$$-\partial H_z/\partial t = (\partial E_x/\partial y - \partial E_y/\partial x)/\mu_o \tag{C.3}$$

$$\partial D_x/\partial t = \partial H_z/\partial y \tag{C.4}$$

$$\partial D_y / \partial t = -\partial H_z / \partial x \tag{C.5}.$$

These equations, in conjunction with the constitutive relation, $\boldsymbol{D} = \varepsilon \boldsymbol{E}$, where ε is the permittivity, are employed to describe electromagnetic wave interaction with media. To numerically solve these equations, Equations (C.3)-(C.5) are discretized to yield

$$\frac{H_z\big|_{i,j}^{n+1} - H_z\big|_{i,j}^{n}}{\Delta t} = \frac{1}{\mu_o}\left(\frac{E_x\big|_{i,j+1/2}^{n+1/2} - E_x\big|_{i,j-1/2}^{n+1/2}}{\Delta y} - \frac{E_x\big|_{i+1/2,j}^{n+1/2} - E_x\big|_{i-1/2,j}^{n+1/2}}{\Delta x}\right) \tag{C.6}$$

$$\frac{D_x\big|_{i,j}^{n+1/2} - D_x\big|_{i,j}^{n-1/2}}{\Delta t} = \frac{H_z\big|_{i,j+1/2}^{n} - H_z\big|_{i,j-1/2}^{n}}{\Delta y} \tag{C.7}$$

$$\frac{D_y\big|_{i,j}^{n+1/2} - D_y\big|_{i,j}^{n-1/2}}{\Delta t} = -\frac{H_z\big|_{i+1/2,j}^{n} - H_z\big|_{i-1/2,j}^{n}}{\Delta x} \tag{C.8}$$

where Δx and Δy are the spatial step size along the x- and y- directions and Δt is the temporal step size. The index n describes the temporal step number, while the indices i and j describe the spatial step number in the x- and y-directions. In these simulations, the maximum grid size is approximately one-tenth the extent of the spatial variation of the fields. For simulations where the fields interact with a mesoscopic structure, the maximum grid size corresponds to one-tenth of the minimum feature size of the structure. As the grid size decreases further, the FDTD algorithm provides a more accurate representation of the spatial distribution of the fields. Once the grid size is selected, the temporal step size must satisfy the condition

$$\Delta t \le c^{-1}\left[(\Delta x)^{-2} + (\Delta y)^{-2}\right]^{-1/2} \tag{C.9}$$

to ensure stability of the FDTD algorithm. To solve Equations (C.6)-(C.9), the equations are re-arranged such that the most forward time step is equated to an expression containing elements from previous time steps

$$H_z\Big|_{i,j}^{n+1} = H_z\Big|_{i,j}^{n} + \frac{\Delta t}{\mu_o}\left(\frac{E_x\Big|_{i,j+1/2}^{n+1/2} - E_x\Big|_{i,j-1/2}^{n+1/2}}{\Delta y} - \frac{E_x\Big|_{i+1/2,j}^{n+1/2} - E_x\Big|_{i-1/2,j}^{n+1/2}}{\Delta x}\right) \tag{C.10}$$

$$D_x\Big|_{i,j}^{n+1/2} = D_x\Big|_{i,j}^{n-1/2} + \Delta t\,\frac{H_z\Big|_{i,j+1/2}^{n} - H_z\Big|_{i,j-1/2}^{n}}{\Delta y} \tag{C.11}$$

$$D_y\Big|_{i,j}^{n+1/2} = D_y\Big|_{i,j}^{n-1/2} - \Delta t\,\frac{H_z\Big|_{i+1/2,j}^{n} - H_z\Big|_{i-1/2,j}^{n}}{\Delta x} \tag{C.12}$$

Given initial conditions for the field components at previous times, the field components at the time step $n + 1$ can be determined. By this process, the entire spatial and temporal evolution of electromagnetic interaction can be calculated.

To model metallic media, the FDTD algorithm employed a Drude model. The permittivity of the metal is incorporated into the FDTD method via the auxiliary differential equation, which related ***E*** and ***D*** via

$$\Gamma\frac{\partial \boldsymbol{D}}{\partial t}+\frac{\partial^2 \boldsymbol{D}}{\partial t^2}=\omega_p^2\varepsilon_o\boldsymbol{E}+\Gamma\varepsilon_o\frac{\partial \boldsymbol{E}}{\partial t}+\varepsilon_o\frac{\partial^2 \boldsymbol{E}}{\partial t^2} \tag{C.13}$$

where ε_o is the permittivity of free space, ω_p and Γ are the plasma and damping frequencies of the material, respectively. Equation (C.13) can be discretized and re-arranged to yield:

$$E_x^{n+1} = \frac{(\Gamma\Delta t - 2)D_x^{n+1} + 4D_x^{n} - (\Gamma\Delta t + 2)D_x^{n-1}}{\varepsilon_o\left(-2 + \Gamma\Delta t - \omega_p^2(\Delta t)^2\right)} \tag{C.14}$$

$$E_y^{n+1} = \frac{(\Gamma\Delta t - 2)D_y^{n+1} + 4D_y^{n} - (\Gamma\Delta t + 2)D_y^{n-1}}{\varepsilon_o\left(-2 + \Gamma\Delta t - \omega_p^2(\Delta t)^2\right)} \tag{C.15}$$

Thus, the Equations (C.10)-(C.12) can be solved numerically for the components of the ***E***, ***D***, and ***H*** vector fields. The material response at each point in the simulation space is determined by the permittivity value at that location. When the point is a dielectric, the ***D*** and ***E*** fields are related via $\boldsymbol{D} = \varepsilon \boldsymbol{E}$. When the point is a metal, ***E*** and ***D*** are related via Equations (C.14) and (C.15).

The computer program used to implement the FDTD algorithm is divided into 4 main parts: 1) the main program (main.h and main.cpp), 2) a program to input and output bitmap files (bitmap.h and bitmap.cpp), 3) a program to calculate the dielectric response of the materials (material.h and material.cpp), and 4) a program to numerically solve Maxwell's equations given the material response (two_dim.h and two_dim.cpp). The computer program used in the simulations was written largely by Graeme Dice with contributions from Kenneth Chau. A simplified version of the program which solves for the case of the electric field in the plane is shown below:

```
////////////////////////////////////////////////////////////////////////////////////////////////////////////////
// 2D FDTD Simulations                                                                                        //
//                                                                                                            //
// Graeme Dice and Kenneth Chau                                                                               //
// Ultrafast Photonics and Nano-Optics Laboratory                                                             //
// Electrical and Computer Engineering Department                                                             //
// University of Alberta                                                                                      //
//                                                                                                            //
//        Solves Maxwell's equations using a central differencing scheme.  Assumes                            //
//        that the third dimension is infinite.  The following is a simplified version                        //
//        which solves for only TM polarization (electric field in the plane)                                 //
////////////////////////////////////////////////////////////////////////////////////////////////////////////////
//                                                                                                            //
// main.h : defines the constants used in the main program                                                    //
//                                                                                                            //
////////////////////////////////////////////////////////////////////////////////////////////////////////////////
#ifndef MAIN_H
#define MAIN_H
#include "util.h"
#include <limits.h>
const float cnaught = 3e8;                        // speed of light in m/s
const float enaught = 8.85e-12;                   // permittivity of free space
const float pi = 3.14159265359;                   // pi
const float munaught = 4*pi*1e-7;                 // permeability of free space
const float grid_size = 5e-6;                     // feature_size/10 in m;
const float delta_time = 5e-15;                     // grid_size/(2*cnaught) in s;
const int time_steps = 8000;                        // number of time steps
const int x_size = 1000;                            // number of space steps in x
const int y_size = 1000;                            // number of space steps in y
const int PML_width = 20;                           // boundary width
const int PML_cond = 1000;                          // conductivity of outside layer
const bool single_cycle = true;                     // true for THz pulse
const bool gaussian = true;                         // Gaussian profile
const float beam_FWHM = 0.3e-3;                     // beam FWHM in m
const bool pulsed = false;                          // true for optical
const float pulse_FWHM = .7e-12;                    // parameter to get THz pulse from Gauusian
const float pulse_start = 1.5*pulse_FWHM;           // location of centre of pulse, 1.5 for THz
const bool load_geometry = true;                    // load file called geom.bmp
const bool bitmap_output = true;                    // output bitmap files
const bool text_output = false;                     // output text files
const float wavelength = 5e-4;                      // central wavelength of radiation in m
const int file_spacing = 200;                       // spacing of the output files
const int source_x = x_size/2;                      // horizontal centre of the beam
const int source_y = 25;                            // vertical beam position > boundary layer
const int first_line_y = source_y+PML_width;        // where to measure first output
const int second_line_y = y_size-2*PML_width;// where to measure second output
const float bitmap_max = 0.5;                       // related to color scale of bitmap output
const float epsilon_medium = 1;                     // relative permittivity of medium
#endif
//////////////////////////////////////////////////////////////////////////////////////////////
//
// main.cpp : main program
//
//////////////////////////////////////////////////////////////////////////////////////////////
#include <math.h>
#include <iostream.h>
#include "main.h"
#include "two_dim.h"
#include <stdio.h>
#include "util.h"

int main(int argc, char * argv)
{
        two_dim solver;
        solver.TM_solve();
        return 0;
}
//////////////////////////////////////////////////////////////////////////////////////////////
//                                                                                          //
// bitmap.h                                                                                 //
//      -Implements a bitmap reader and writer for output of data and input of             //
//      geometry information                                                                //
//      -Implements the text file output for data so that it can be moved out of the       //
//      FDTD section                                                                        //
//////////////////////////////////////////////////////////////////////////////////////////////
```

```
#ifndef BITMAP_H
#define BITMAP_H
#include "material.h"
#define Bitmap_File_Header BITMAPFILEHEADER
#define Bitmap_Info_Header BITMAPINFOHEADER
class bitmap
{
public:
        static int write(char * filename, float ** field_data, float max);
        static int output_geometry(char * filename, material ** media_data);
        static int read_geometry(char * filename, material ** media_data);
        static int read_data(char * filename, float ** field_data);
        static int read_old_geometry(char * filename, material ** media_data);
};
#endif
////////////////////////////////////////////////////////////////////////////////////////////////////////////////////////
//                                                                                  //
// bitmap.cpp                                                                       //
//      -Reads the geometries in the bitmaps and outputs the FDTD calculations      //
//      onto bitmap files                                                           //
//      - writes the FDTD calculations onto a bitmap file with appropriate color scale //
////////////////////////////////////////////////////////////////////////////////////////////////////////////////////////
#include "bitmap.h"
#include <windows.h>
#include <stdio.h>
#include "main.h"
#include <math.h>
int bitmap::write(char * filename, float ** field_data, float max)
{
        Bitmap_Info_Header bih;
        Bitmap_File_Header bfh;
        char textfilename[512], BMP_filename[512];
        FILE * textfile, * BMP_file;
        int err = 0;
        bfh.bfType = 19778;
        bfh.bfReserved1 = 0;
        bfh.bfReserved2 = 0;
        bfh.bfOffBits = sizeof(bfh) + sizeof(bih);
        bfh.bfSize = bfh.bfOffBits + x_size*y_size*3;
        bih.biSize = sizeof(bih);
        bih.biWidth = x_size;
        bih.biHeight = y_size;
        bih.biPlanes = 1;
        bih.biBitCount = 24;
        bih.biCompression = BI_RGB;
        bih.biSizeImage = x_size*y_size*3;
        bih.biXPelsPerMeter = bih.biYPelsPerMeter = 0;
        bih.biClrUsed = 0;
        bih.biClrImportant = 0;
        sprintf(BMP_filename, "%s.bmp", filename);
```

```
BMP_file = fopen(BMP_filename, "wb");
fwrite(&bfh,sizeof(bfh),1,BMP_file);
fwrite(&bih,sizeof(bih),1,BMP_file);
float min = 0;
for (int j = 0; j < y_size; j++)
{
        for (int i = 0; i < x_size; i++)
        {
                unsigned char bgr[3];
                int colorRange = (5*256);
                double percent = (fabs(min) + field_data[i][j]) / (fabs(max) +
                fabs(min));
                int color = (int)(percent*colorRange);
                if (color < 256)
                {
                        bgr[0] = color;
                }
                else if (color <= 2*256)
                {
                        bgr[0] = 255;
                }
                else if (color < 3*256)
                {
                        bgr[0] = 3*256-color;
                }
        else
                {
                        bgr[0] = 0;
                }

                if (color < 256)
                {
                        bgr[1] = 0;
                }
                else if (color < 2*256)
                {
                        bgr[1] = color-256;
                }
                else if (color <= 3*256)
                {
                        bgr[1] = 255;
                }
        else if (color < 4*256)
                {
                        bgr[1] = 4*256-color;
                }
        else
                {
                        bgr[1] = 0;
                }
                if (color < 3*256/2)
```

```
                        {
                                bgr[2] = 0;
                        }
                        else if (color < 5*256/2)
                        {
                        bgr[2] = color-3*256/2;
                        }
                        else
                        {
                                bgr[2] = 255;
                        }
                        fwrite(bgr,sizeof(unsigned char),3,BMP_file);
                }
                if( i % 4 != 0)
                {
                        unsigned char space = 0;
                        int n = 0;
                        for( n=0; n<i%4 ; n ++ )
                                fwrite(&space,sizeof(unsigned char),1,BMP_file);
                }
        }
        if( BMP_file != NULL )
                fclose(BMP_file);
        return err;
}
////////////////////////////////////////////////////////////////////////////////////////////////////
// Outputs the bitmap files                                                                      //
////////////////////////////////////////////////////////////////////////////////////////////////////
int bitmap::output_geometry(char * filename, material ** media_data)
{
        Bitmap_Info_Header bih;
        Bitmap_File_Header bfh;
        char textfilename[512], BMP_filename[512];
        FILE * textfile, * BMP_file;
        int err = 0;
        bfh.bfType = 19778;
        bfh.bfReserved1 = 0;
        bfh.bfReserved2 = 0;
        bfh.bfOffBits = sizeof(bfh) + sizeof(bih);
        bfh.bfSize = bfh.bfOffBits + x_size*y_size*3;
        bih.biSize = sizeof(bih);
        bih.biWidth = x_size;
        bih.biHeight = y_size;
        bih.biPlanes = 1;
        bih.biBitCount = 24;
        bih.biCompression = BI_RGB;
        bih.biSizeImage = x_size*y_size*3;
        bih.biXPelsPerMeter = bih.biYPelsPerMeter = 0;
        bih.biClrUsed = 0;
        bih.biClrImportant = 0;
```

```
sprintf(BMP_filename, "%s.bmp", filename);
BMP_file = fopen(BMP_filename, "wb");
int i,j;
fwrite(&bfh,sizeof(bfh),1,BMP_file);
fwrite(&bih,sizeof(bih),1,BMP_file);
for (j = 0; j < y_size; j++)
{
        for (i = 0; i < x_size; i++)
        {
                unsigned char bgr[3];
                int colorRange = (5*256);
                bgr[0] = 0;
                bgr[1] = 0;
                bgr[2] = 0;
                if (media_data[i][j].get_permittivity() >= 2.5 &&
                media_data[i][j].get_permittivity() <= 2.6)
                {
                        bgr[0] = 0;
                        bgr[1] = 0;
                        bgr[2] = 255;
                }
                if (media_data[i][j].is_metal())
                {
                        bgr[0] = 0;
                        bgr[1] = 255;
                        bgr[2] = 255;
                }
                if (j == source_y)
                {
                        bgr[0] = 0;
                        bgr[1] = 255;
                        bgr[2] = 0;
                }
                if (i < PML_width || j < PML_width || i >= x_size-PML_width || j
                >= y_size-PML_width)
                {
                        bgr[0] = 255;
                        bgr[1] = 255;
                        bgr[2] = 255;
                }
                fwrite(bgr,sizeof(unsigned char),3,BMP_file);
        }
        if( i % 4 != 0)
        {
                unsigned char space = 0;
                int n = 0;
                for( n=0; n<i%4 ; n ++ )
                        fwrite(&space,sizeof(unsigned char),1,BMP_file);
        }
}
```

```
    if( BMP_file != NULL )
        fclose(BMP_file);
    return err;
}
//////////////////////////////////////////////////////////////////////////////////////////////////////////
// Correlating the color of the pixels in the bitmap file with material parameters              //
//////////////////////////////////////////////////////////////////////////////////////////////////////////
int bitmap::read_geometry(char * filename, material ** media_data)
{
    Bitmap_Info_Header bih;
    Bitmap_File_Header bfh;
    char BMP_filename[512];
    FILE * BMP_file;
    int err = 0;
    sprintf(BMP_filename, "%s.bmp", filename);
    BMP_file = fopen(BMP_filename, "rb");
    fread(&bfh,sizeof(bfh),1,BMP_file);
    fread(&bih,sizeof(bih),1,BMP_file);
    for (int j = 0; j < y_size; j++)
    {
        for (int i = 0; i < x_size; i++)
        {
            unsigned char bgr[3];
            fread(bgr,sizeof(unsigned char),3,BMP_file);
            if (bgr[0] == 0 && bgr[1] == 255 && bgr[2] == 255) //(blue &&
            green && red) yellow=green + red
            {
        //Copper material parameters below
                media_data[i][j].set_material(1,1,0,0,true,
                true,0,0,0,0,0,0,1.91E15,8.34E12);
            }
            else
            {
        //Free space material parameters below
                media_data[i][j].set_material(epsilon_medium,
                1,0,0,false,false,0,0,0,0,0,0,0,0);
            }
        }
        if( i % 4 != 0)
        {
            unsigned char space = 0;
            int n = 0;
            for( n=0; n<i%4 ; n ++ )
                fread(&space,sizeof(unsigned char),1,BMP_file);
        }
    }
    if( BMP_file != NULL )
        fclose(BMP_file);
    return err;
}
```

```
////////////////////////////////////////////////////////////////////////////////////////////////////
//                                                                                              //
// material.h :                                                                                 //
//        -Defines constants and functions used to determine the dielectric                     //
//        response of the materials used in the simulations                                     //
////////////////////////////////////////////////////////////////////////////////////////////////////
#ifndef MATERIAL_H
#define MATERIAL_H
#include "main.h"
class material
{
public:
        material(float permittivity, float permeability, float conductivity, float mag_cond,
                bool dispersive, bool metallic, float reson_1, float reson_2, float reson_3,
                float B1, float B2, float B3, float freq_plasma, float freq_scatter);
        material();
        inline void set_material(float permittivity, float permeability, float conductivity,
                float mag_cond, bool dispersive, bool metallic, float B1, float B2, float
                B3, float reson_1, float reson_2, float reson_3, float freq_plasma, float
                freq_scatter)
        {
                epsilon = permittivity;
                mu = permeability;
                e_cond = conductivity;
                h_cond = mag_cond;
                dispersion = dispersive;
                metal = metallic;
                omega1 = reson_1 == 0 ? 0:2*pi*cnaught/reson_1;
                omega2 = reson_2 == 0 ? 0:2*pi*cnaught/reson_2;
                omega3 = reson_3 == 0 ? 0:2*pi*cnaught/reson_3;
                b1 = B1;
                b2 = B2;
                b3 = B3;
                plasma_freq = freq_plasma;
                scatter_freq = freq_scatter;

        // Recalculates the constants to be used for the polarization dependent dispersion
                a1 = 2 + omega1*omega1*delta_time*delta_time*(1+b1);
                a2 = 2 + omega2*omega2*delta_time*delta_time*(1+b2);
                a3 = 2 + omega3*omega3*delta_time*delta_time*(1+b3);
                c1 = omega1*omega1*b1*delta_time*delta_time;
                c2 = omega2*omega2*b2*delta_time*delta_time;
                c3 = omega3*omega3*b3*delta_time*delta_time;
                g1 = -2 - omega1*omega1*delta_time*delta_time*(1+b1);
                g2 = -2 - omega2*omega2*delta_time*delta_time*(1+b2);
                g3 = -2 - omega3*omega3*delta_time*delta_time*(1+b3);
                m1 = 2 + scatter_freq*delta_time;
                m2 = 2 - scatter_freq*delta_time;
                m3 = plasma_freq*plasma_freq*enaught*delta_time*delta_time
                        - scatter_freq*enaught*epsilon*delta_time + 2*enaught*epsilon;
        m4 = plasma_freq*plasma_freq*enaught*delta_time*delta_time
            + scatter_freq*enaught*epsilon*delta_time + 2*enaught*epsilon;
}

inline float H_Hcoeff()
{
        return (1-h_cond*delta_time/(2*mu*munaught))/
        (1+h_cond*delta_time/(2*mu*munaught));
}
inline float H_Ecoeff()
{
        return (delta_time/(mu*munaught*grid_size))/
        (1+h_cond*delta_time/(2*mu*munaught));
}
inline float E_Ecoeff()
{
        return (1-e_cond*delta_time/(2*epsilon*enaught))/
        (1+e_cond*delta_time/(2*epsilon*enaught));
}
inline float E_Hcoeff()
{
        return (delta_time/(epsilon*enaught*grid_size))/
        (1+e_cond*delta_time/(2*epsilon*enaught));
}
inline float get_permittivity()
{
        return epsilon;
}
inline bool is_dispersive()
{
        return dispersion;
}
inline bool is_metal()
{
        return metal;
}
inline float get_a1()
{
        return a1;
}
inline float get_a2()
{
        return a2;
}
inline float get_a3()
{
        return a3;
}
inline float get_c1()
{
        return c1;
        }
        inline float get_c2()
        {
                return c2;
        }
        inline float get_c3()
        {
                return c3;
        }
        inline float get_g1()
        {
                return g1;
        }
        inline float get_g2()
        {
                return g2;
        }
        inline float get_g3()
        {
                return g3;
        }
        inline float get_m1()
        {
                return m1;
        }
        inline float get_m2()
        {
                return m2;
        }
        inline float get_m3()
        {
                return m3;
        }
        inline float get_m4()
        {
                return m4;
        }
private:
        float epsilon, mu, e_cond, h_cond;
        bool dispersion;
        bool metal;

//Sellmeier dispersion coefficients
        float omega1, omega2, omega3;
        float b1, b2, b3;
        float a1, a2, a3, c1, c2, c3, g1, g2, g3;

//Drude Model Coefficients
        float m1, m2, m3, m4;
        float plasma_freq, scatter_freq;
```

```
};
#endif
////////////////////////////////////////////////////////////////////////////////////////////////////////////
//                                                                                                      //
// material.cpp : determines the dielectric response of the materials in the simulation       //
////////////////////////////////////////////////////////////////////////////////////////////////////////////
#include "material.h"
#include "main.h"
material::material()
{
}
material::material(float permittivity, float permeability, float conductivity, float
mag_cond, bool dispersive, bool metallic, float reson_1, float reson_2, float reson_3,
float B1, float B2, float B3, float freq_plasma, float freq_scatter)
{
        epsilon = permittivity;
        mu = permeability;
        e_cond = conductivity;
        h_cond = mag_cond;
        dispersion = dispersive;
        metal = metallic;
        omega1 = reson_1 == 0 ? 0:2*pi*cnaught/reson_1;
        omega2 = reson_2 == 0 ? 0:2*pi*cnaught/reson_2;
        omega3 = reson_3 == 0 ? 0:2*pi*cnaught/reson_3;
        b1 = B1;
        b2 = B2;
        b3 = B3;
        plasma_freq = freq_plasma;
        scatter_freq = freq_scatter;
//Recalculate the constants to be used for the polarization dependent dispersion
        a1 = 2 + omega1*omega1*delta_time*delta_time*(1+b1);
        a2 = 2 + omega2*omega2*delta_time*delta_time*(1+b2);
        a3 = 2 + omega3*omega3*delta_time*delta_time*(1+b3);
        c1 = omega1*omega1*b1*delta_time*delta_time;
        c2 = omega2*omega2*b2*delta_time*delta_time;
        c3 = omega3*omega3*b3*delta_time*delta_time;
        g1 = -2 - omega1*omega1*delta_time*delta_time*(1+b1);
        g2 = -2 - omega2*omega2*delta_time*delta_time*(1+b2);
        g3 = -2 - omega3*omega3*delta_time*delta_time*(1+b3);
        m1 = 2.0 + scatter_freq*delta_time;
        m2 = 2.0 - scatter_freq*delta_time;
        m3 = plasma_freq*plasma_freq*enaught*delta_time*delta_time
                - scatter_freq*enaught*epsilon*delta_time + 2*enaught*epsilon;
        m4 = plasma_freq*plasma_freq*enaught*delta_time*delta_time
                + scatter_freq*enaught*epsilon*delta_time + 2*enaught*epsilon;
}
```

```
////////////////////////////////////////////////////////////////////////////////////////////////////////////
//                                                                                                         //
// two_dim.h :                                                                                             //
//        -Defines the constants and functions used to solve Maxwell's equations in                        //
//        two dimensions.                                                                                  //
////////////////////////////////////////////////////////////////////////////////////////////////////////////
#ifndef TWO_DIM_H
#define TWO_DIM_H
#include "main.h"
#include "material.h"
class two_dim
{
public:
        two_dim();
        ~two_dim();
        void TM_solve();
private:
        float ** Ex;
        float ** Ex_prev;
        float ** Ey;
        float ** Ey_prev;
        float ** Et;//The total EM field for TM mode
        float ** Dx, ** Dx_prev, ** Dx_prev_prev;
        float ** Dy, ** Dy_prev, ** Dy_prev_prev;
        float ** Dz, ** Dz_prev, ** Dz_prev_prev;
        float ** Hx, ** Hy, ** Hz, ** Ht;
        float ** Hzx, ** Hzy;
        float ** P1X_prev, ** P2X_prev, ** P3X_prev;
        float ** P1X_prev_prev, ** P2X_prev_prev, ** P3X_prev_prev;
        float ** P1Y_prev, ** P2Y_prev, ** P3Y_prev;
        float ** P1Y_prev_prev, ** P2Y_prev_prev, ** P3Y_prev_prev;
        material ** media; //material is a homemade class
        float Econd(int position);
        float Hcond(int position);
        float source_Ex(float x, float y, float time_step);
        float source_Hz(float x, float y, float time_step);
        float H_Hcoeffs[PML_width], H_Ecoeffs[PML_width], E_Hcoeffs[PML_width],
        E_Ecoeffs[PML_width];
        float ref_index(int x, int y);
        int write_data(char * filename, float ** field_data);
        float integrate(int line_y, float ** field_data);
};
#endif
////////////////////////////////////////////////////////////////////////////////////////////////////////////
//                                                                                                         //
// two_dim.cpp :                                                                                           //
//        -Program used to solve Maxwell's equations in two dimensions                                     //
////////////////////////////////////////////////////////////////////////////////////////////////////////////
#include "two_dim.h"
#include "main.h"
```

```
#include <math.h>
#include <stdio.h>
#include <iostream.h>
#include "bitmap.h"
two_dim::two_dim()
{
}
two_dim::~two_dim()
{
}
float two_dim::Econd(int position)
{
        return PML_cond*((float)(position+0.5)/(float)PML_width);
}
float two_dim::Hcond(int position)
{
        return (PML_cond*munaught/enaught)*((float)position/(float)PML_width);
}
float two_dim::source_Hz(float x, float y, float time_step)
{
        float wz, wo, Zo, Hfield, scaling, wave, x_offset, y_offset;
        float pulse_scaling, time_factor, time_offset, THz_scaling;
        wo = beam_FWHM;
        Zo = pi * ref_index((int)x,(int)y)*wo*wo/wavelength;
        x_offset = (x-source_x)*grid_size;
        y_offset = (y-source_y)*grid_size;
        wz = wo * sqrt(1 + (y_offset*y_offset/(Zo*Zo)));
        scaling = wo/wz * exp(- (x_offset*x_offset)/(wz*wz));
        time_factor = 2*log(sqrt(2)+1)/pulse_FWHM;
        time_offset = time_step*delta_time-pulse_start;
        pulse_scaling = 2/(exp(time_offset*time_factor) +
        exp(-time_offset*time_factor));
        wave = cos(+ 2*pi*cnaught/wavelength*delta_time*time_step);
        pulse_scaling = pulsed ? pulse_scaling:1.0;
        scaling = gaussian ? scaling:1.0;
        Hfield = pulse_scaling*scaling*wave*sqrt(enaught/munaught);
        if (single_cycle)
        {
                double sigma = beam_FWHM / (2*sqrt(2*log(2)));
                double pulse_sigma = pulse_FWHM / (2*sqrt(2*log(2)));
                double scaling_factor = 2*exp(-0.5);
                double offset = grid_size * sqrt((x - source_x) * (x - source_x));
                Hfield = sqrt(enaught/munaught)*exp(-0.5*offset*offset/sigma/sigma);
                Hfield*=-2/scaling_factor*(time_offset)/pulse_sigma*
                exp(-(time_offset)*(time_offset) / (2*pulse_sigma*pulse_sigma));
                if (Hfield < 0)
                {
                        scaling = 0.688;
                }
                else
                {
                        scaling = 1.0;
                }
                return -Hfield*scaling;
        }
        return Hfield;
}
float two_dim::source_Ex(float x, float y, float time_step)
{
        float wz, wo, Zo, Efield, scaling, wave, x_offset, y_offset;
        float pulse_scaling, time_factor,time_offset;
        wo = beam_FWHM;
        Zo = pi * ref_index((int)x,(int)y)*wo*wo/wavelength;
        x_offset = (x-source_x)*grid_size;
        y_offset = (y-source_y)*grid_size;
        wz = wo * sqrt(1 + (y_offset*y_offset/(Zo*Zo)));
        scaling = wo/wz * exp(- (x_offset*x_offset)/(wz*wz));
        time_factor = 2*log(sqrt(2)+1)/pulse_FWHM;
        time_offset = time_step*delta_time-pulse_start;
        pulse_scaling = 2/(exp(time_offset*time_factor) +
        exp(-time_offset*time_factor));
        wave = cos(-pi/wavelength*grid_size +
        2*pi*cnaught/wavelength*delta_time*(time_step+0.5));
        pulse_scaling = pulsed ? pulse_scaling:1.0;
        scaling = gaussian ? scaling:1.0;
        Efield = pulse_scaling*scaling*wave;
        if (single_cycle)
        {
                double sigma = beam_FWHM / (2*sqrt(2*log(2)));
                double pulse_sigma = pulse_FWHM/(2*sqrt(2*log(2)));
                double scaling_factor = 2*exp(-0.5);
                double offset = grid_size * sqrt((x - source_x)*(x - source_x));
                Efield = exp(-0.5*offset*offset/sigma/sigma);
                Efield *= -2/scaling_factor*(time_offset+0.5*grid_size/
                cnaught)/pulse_sigma*exp( -(time_offset+0.5*grid_size/cnaught)*
                (time_offset+0.5*grid_size/cnaught)/(2*pulse_sigma*pulse_sigma));
                if (Efield < 0)
                {
                        scaling = 0.688;
                }
                else
                {
                        scaling = 1.0;
                }
                return Efield*scaling;
        }
        return -Efield;
}
float two_dim::ref_index(int x, int y)
{
        return sqrt(media[x][y].get_permittivity());
}
```

```
int two_dim::write_data(char * filename, float ** field_data)
{
        char textfilename[512], BMP_filename[512];
        FILE * textfile, * BMP_file;
        int err = 0;
        sprintf(textfilename, "%s.txt", filename);
        textfile = fopen(textfilename, "wb");
        for (int i = 0; i < x_size; i++)
        {
                for (int j = 0; j < y_size; j++)
                {
                        fwrite(&field_data[i][j],sizeof(field_data[i][j]),1,textfile);
                }
        }

        if( textfile != NULL )
                fclose(textfile);
        return err;
}
float two_dim::integrate(int line_y, float ** field_data)
{
        float cur_total = 0.0;
        for (int i = PML_width; i < x_size-PML_width; i++)
        {
                cur_total += field_data[i][line_y];
        }
        return cur_total;
}
void two_dim::TM_solve()
{
        FILE * ezdatafile;
        char * filename1;
        char * filename2;
        char * filename3;
        float P1X, P1Y, P2X, P2Y, P3X, P3Y;
        filename1 = new char[200];
        filename2 = new char[200];
        filename3 = new char[200];
// Determines the coefficients of the PML layer such that E and H fields die out
// exponentially : J P Berenger IEEE paper on PML
        for (int p = 0; p < PML_width; p++)
        {
                H_Hcoeffs[p] = exp(-Hcond(p)*delta_time/munaught);
                E_Ecoeffs[p] = exp(-Econd(p)*delta_time/enaught);
                H_Ecoeffs[p] = (1-exp(-Hcond(p)*delta_time/
                munaught))/Hcond(p)/grid_size;
                E_Hcoeffs[p] = (1-exp(-Econd(p)*delta_time/
                enaught))/Econd(p)/grid_size;
        }
        H_Ecoeffs[0] = delta_time/munaught/grid_size;
```

```
// media stores material parameters at each point of bitmap
        media = new material * [x_size];
        for (int x = 0; x < x_size; x++)
        {
                media[x] = new material [y_size];
        }
// First creates a media space that has properties of epsilon_medium
        for (x = 0; x < x_size; x++)
        {
                for (int y = 0; y < y_size; y++)
                {
                //Free Space
                        media[x][y].set_material(epsilon_medium,
                        1,0,0,false,false,0,0,0,0,0,0,0);
                }
        }
        bitmap::read_geometry("./data/geom", media);
        bitmap::output_geometry("./data/geomout", media);
// Allocating memory -- creating arrays and variables to point to the arrays
        Ex = new float *[x_size];
        Ey = new float *[x_size];
        Et = new float *[x_size];
        Ex_prev = new float *[x_size];
        Ey_prev = new float *[x_size];
        Dx = new float *[x_size];
        Dx_prev = new float *[x_size];
        Dx_prev_prev = new float *[x_size];
        Dy = new float *[x_size];
        Dy_prev = new float *[x_size];
        Dy_prev_prev = new float *[x_size];
        Hz = new float *[x_size];
        Hzx = new float *[x_size];
        Hzy = new float *[x_size];
        P1X_prev = new float * [x_size];
        P1Y_prev = new float * [x_size];
        P2X_prev = new float * [x_size];
        P2Y_prev = new float * [x_size];
        P3X_prev = new float * [x_size];
        P3Y_prev = new float * [x_size];
        P1X_prev_prev = new float * [x_size];
        P1Y_prev_prev = new float * [x_size];
        P2X_prev_prev = new float * [x_size];
        P2Y_prev_prev = new float * [x_size];
        P3X_prev_prev = new float * [x_size];
        P3Y_prev_prev = new float * [x_size];
        for (x = 0; x < x_size; x++)
        {
                Ex[x] = new float [y_size];
                Ex_prev[x] = new float [y_size];
                Ey[x] = new float [y_size];
                Ey_prev[x] = new float [y_size];
                Et[x] = new float [y_size];
                Dx[x] = new float [y_size];
                Dx_prev[x] = new float [y_size];
                Dx_prev_prev[x] = new float [y_size];
                Dy[x] = new float [y_size];
                Dy_prev[x] = new float [y_size];
                Dy_prev_prev[x] = new float [y_size];
                Hz[x] = new float [y_size];
                Hzx[x] = new float [y_size];
                Hzy[x] = new float [y_size];
                P1X_prev[x] = new float [y_size];
                P1Y_prev[x] = new float [y_size];
                P2X_prev[x] = new float [y_size];
                P2Y_prev[x] = new float [y_size];
                P3X_prev[x] = new float [y_size];
                P3Y_prev[x] = new float [y_size];
                P1X_prev_prev[x] = new float [y_size];
                P1Y_prev_prev[x] = new float [y_size];
                P2X_prev_prev[x] = new float [y_size];
                P2Y_prev_prev[x] = new float [y_size];
                P3X_prev_prev[x] = new float [y_size];
                P3Y_prev_prev[x] = new float [y_size];
        }
// Initial conditions for all the fields
        for (x = 0; x < x_size; x++)
        {
                for (int y = 0; y < y_size; y++)
                {
                        Ex[x][y] = 0;
                        Ey[x][y] = 0;
                        Et[x][y] = 0;
                        Ex_prev[x][y] = 0;
                        Ey_prev[x][y] = 0;

                        Dx[x][y] = 0;
                        Dx_prev[x][y] = 0;
                        Dx_prev_prev[x][y] = 0;
                        Dy[x][y] = 0;
                        Dy_prev[x][y] = 0;
                        Dy_prev_prev[x][y] = 0;

                        Hz[x][y] = 0;
                        Hzx[x][y] = 0;
                        Hzy[x][y] = 0;

                        P1X_prev[x][y] = 0;
                        P1Y_prev[x][y] = 0;
                        P2X_prev[x][y] = 0;
                        P2Y_prev[x][y] = 0;
                        P3X_prev[x][y] = 0;
```

```
            P3Y_prev[x][y] = 0;

            P1X_prev_prev[x][y] = 0;
            P1X_prev_prev[x][y] = 0;
            P2X_prev_prev[x][y] = 0;
            P2Y_prev_prev[x][y] = 0;
            P3X_prev_prev[x][y] = 0;
            P3Y_prev_prev[x][y] = 0;
        }
    }
    FILE * fieldoutput, * integrate_output;
    fieldoutput = fopen("./data/output_point.txt","w+");
    integrate_output = fopen("./data/output_line.txt","w+");
// Solve for the temporal evolutions of the fields
    for (int n = 0; n < time_steps; n++)
    {
        float tot_Ex_start, tot_Ey_start, tot_Et_start, tot_Hz_start,
            tot_Ex_end, tot_Ey_end, tot_Et_end, tot_Hz_end;

        tot_Ex_start = integrate(first_line_y, Ex);
        tot_Ey_start = integrate(first_line_y, Ey);
        tot_Et_start = integrate(first_line_y, Et);
        tot_Hz_start = integrate(first_line_y, Hz);
        tot_Ex_end = integrate(second_line_y, Ex);
        tot_Ey_end = integrate(second_line_y, Ey);
        tot_Et_end = integrate(second_line_y, Et);
        tot_Hz_end = integrate(second_line_y, Hz);
    // Outputing the field data into text and bitmap files
        fprintf(integrate_output,"%e %e %e %e %e %e %e %e
            %e\n",n*delta_time, tot_Ex_start, tot_Ey_start, tot_Et_start,
            tot_Hz_start, tot_Ex_end, tot_Ey_end, tot_Et_end, tot_Hz_end);
        fprintf(fieldoutput,"%e %e %e %e %e %e
            %e\n",n*delta_time,Ex[x_size/2][first_line_y],
            Ey[x_size/2][first_line_y],Hz[x_size/2][first_line_y],
            Ex[x_size/2][second_line_y],Ey[x_size/2][second_line_y],
            Hz[x_size/2][second_line_y]);
        if (n % file_spacing == 0)
        {
            sprintf(filename1, "./data/%6.0d_dataEx", n);
            sprintf(filename2, "./data/%6.0d_dataEy", n);
            sprintf(filename3, "./data/%6.0d_dataEt", n);

            if (bitmap_output)
            {
                bitmap::write(filename3, Et,bitmap_max);
            }
            if (text_output)
            {
                write_data(filename1, Ex);
                write_data(filename2, Ey);
            }
```

```
}
for (int x = 0; x < x_size; x++)
{
        for (int y = 0; y < y_size; y++)
        {
                if (x < PML_width || y < PML_width || x >= x_size-
                PML_width || y >= y_size-PML_width)
                {
                        float H_Hcoeff_Y, H_Ecoeff_Y, H_Hcoeff_X,
                        H_Ecoeff_X, E_Ecoeff_X, E_Hcoeff_X,
                        E_Ecoeff_Y, E_Hcoeff_Y;
                        H_Hcoeff_X = media[x][y].H_Hcoeff();
                        H_Ecoeff_X = media[x][y].H_Ecoeff();
                        E_Hcoeff_X = media[x][y].E_Hcoeff();
                        E_Ecoeff_X = media[x][y].E_Ecoeff();
                        H_Hcoeff_Y = H_Hcoeff_X;
                        H_Ecoeff_Y = H_Ecoeff_X;
                        E_Hcoeff_Y = E_Hcoeff_X;
                        E_Ecoeff_Y = E_Ecoeff_X;
                        int temp = 0;
                        if (x < PML_width)
                        {
                                //In the left edge
                                temp = PML_width - x - 1;
                                H_Hcoeff_X = H_Hcoeffs[temp];
                                H_Ecoeff_X = H_Ecoeffs[temp];
                                E_Hcoeff_Y = E_Hcoeffs[temp];
                                E_Ecoeff_Y = E_Ecoeffs[temp];
                        }
                        if (y < PML_width)
                        {
                                //In the bottom edge
                                temp = PML_width - y - 1;
                                H_Hcoeff_Y = H_Hcoeffs[temp];
                                H_Ecoeff_Y = H_Ecoeffs[temp];
                                E_Hcoeff_X = E_Hcoeffs[temp];
                                E_Ecoeff_X = E_Ecoeffs[temp];
                        }
                        if (x >= x_size-PML_width)
                        {
                                //In the right edge
                                temp = x - x_size + PML_width;
                                H_Hcoeff_X = H_Hcoeffs[temp];
                                H_Ecoeff_X = H_Ecoeffs[temp];
                                E_Hcoeff_Y = E_Hcoeffs[temp];
                                E_Ecoeff_Y = E_Ecoeffs[temp];
                        }
                        if (y >= y_size-PML_width)
                        {
                                //In the top edge
                                temp = y - y_size + PML_width;
                H_Hcoeff_Y = H_Hcoeffs[temp];
                H_Ecoeff_Y = H_Ecoeffs[temp];
                E_Hcoeff_X = E_Hcoeffs[temp];
                E_Ecoeff_X = E_Ecoeffs[temp];
        }
//EM field calculations
//The FDTD equations for the PML are below
        float temp_Hz;
        temp_Hz = y == y_size-1 ? 0.0:Hz[x][y+1];

        Ex[x][y] = E_Ecoeff_X*Ex[x][y]
                - E_Hcoeff_X * (Hz[x][y] - temp_Hz);

        temp_Hz = x == x_size-1 ? 0.0:Hz[x+1][y];

        Ey[x][y] = E_Ecoeff_Y*Ey[x][y]
                - E_Hcoeff_Y * (temp_Hz - Hz[x][y]);

        float temp_Ex, temp_Ey;

        temp_Ey = x == 0 ? 0.0:Ey[x-1][y];
        temp_Ex = y == 0 ? 0.0:Ex[x][y-1];

        Hzx[x][y] = H_Hcoeff_X*Hzx[x][y]
                - H_Ecoeff_X * (Ey[x][y] - temp_Ey);

        Hzy[x][y] = H_Hcoeff_Y*Hzy[x][y]
                - H_Ecoeff_Y * (temp_Ex - Ex[x][y]);

        Hz[x][y] = Hzx[x][y] + Hzy[x][y];
}
else
{
        float H_Hcoeff, H_Ecoeff, E_Ecoeff, E_Hcoeff;
        float temp_Ex = Ex[x][y];
        float temp_Ey = Ey[x][y];

        float Exinc = 0.0;
        float Hzinc = 0.0;

        float denominator = 0.0;
        float a1, a2, a3, c1, c2, c3, g1, g2, g3;
        float K1X, K2X, K3X;
        float K1Y, K2Y, K3Y;
        float m1, m2, m3, m4;
        a1 = 0;
        a2 = 0;
        a3 = 0;
        c1 = 0;
        c2 = 0;
```

```
c3 = 0;
g1 = 0;
g2 = 0;
g3 = 0;
m1 = 0;
m2 = 0;
m3 = 0;
m4 = 0;
Exinc = 0.0;
Hzinc = 0.0;
if (y == source_y)
{
        Exinc = source_Ex(x,y,n);
        Hzinc = source_Hz(x,y,n);
}

Dx[x][y] = Dx[x][y] + delta_time/grid_size*
(Hz[x][y+1] - Hz[x][y] - Hzinc);

Dy[x][y] = Dy[x][y]     + delta_time/grid_size*
(Hz[x][y] - Hz[x+1][y]);

if (media[x][y].is_dispersive())
{
        if (media[x][y].is_metal())
        {
                m1 = media[x][y].get_m1();
                m2 = media[x][y].get_m2();
                m3 = media[x][y].get_m3();
                m4 = media[x][y].get_m4();

                Ex[x][y] = (m1*Dx[x][y] -
                4*Dx_prev[x][y] +
                m2*Dx_prev_prev[x][y]
                + 4*enaught*
                media[x][y].get_permittivity()*
                Ex[x][y]- m3*Ex_prev[x][y]) / m4;

                Ey[x][y] = (m1*Dy[x][y] - 4*
                Dy_prev[x][y] + m2*
                Dy_prev_prev[x][y] + 4*enaught*
                media[x][y].get_permittivity()*
                Ey[x][y]- m3*Ey_prev[x][y]) / m4;
        }
        else
        {
                a1 = media[x][y].get_a1();
                a2 = media[x][y].get_a2();
                a3 = media[x][y].get_a3();
                c1 = media[x][y].get_c1();
                c2 = media[x][y].get_c2();
```

```
c3 = media[x][y].get_c3();
g1 = media[x][y].get_g1();
g2 = media[x][y].get_g2();
g3 = media[x][y].get_g3();

denominator = -a1*a2*a3 +
a1*c2*c3 + c2*c1*a3 - 2*c2*c1*
c3 + c3*c1*a2;

K1X = c1*(Dx[x][y] +
Dx_prev_prev[x][y] -
P2X_prev_prev[x][y] –
P3X_prev_prev[x][y]) +
4*P1X_prev[x][y] +
g1*P1X_prev_prev[x][y];
K2X = c2*(Dx[x][y] +
Dx_prev_prev[x][y] –
P1X_prev_prev[x][y] –
P3X_prev_prev[x][y]) +
4*P2X_prev[x][y] +
g2*P2X_prev_prev[x][y];
K3X = c3*(Dx[x][y] +
Dx_prev_prev[x][y] –
P1X_prev_prev[x][y] –
P2X_prev_prev[x][y]) +
4*P3X_prev[x][y] +
g3*P3X_prev_prev[x][y];
K1Y = c1*(Dy[x][y] +
Dy_prev_prev[x][y] –
P2Y_prev_prev[x][y] –
P3Y_prev_prev[x][y]) +
4*P1Y_prev[x][y] +
 g1*P1Y_prev_prev[x][y];
K2Y = c2*(Dy[x][y] +
Dy_prev_prev[x][y] –
P1Y_prev_prev[x][y] –
P3Y_prev_prev[x][y]) +
4*P2Y_prev[x][y] +
g2*P2Y_prev_prev[x][y];
K3Y = c3*(Dy[x][y] +
Dy_prev_prev[x][y] –
P1Y_prev_prev[x][y] –
P2Y_prev_prev[x][y]) +
4*P3Y_prev[x][y] +
g3*P3Y_prev_prev[x][y];

P1X = (-a2*a3+c2*c3)/
denominator*K1X-c1*(-a3+c3)/
denominator*K2X-c1*(c2-a2)/
denominator*K3X;
P2X = -c2*(-a3+c3)/
```

```
                                denominator*K1X-(a1*a3-c1*c3)/
                                denominator*K2X+c2*(a1-c1)/
                                denominator*K3X;
                                P3X = -c3*(c2-a2)/
                                denominator*K1X+c3*(a1-c1)/
                                denominator*K2X-(a1*a2-c1*c2)/
                                denominator*K3X;
                                P1Y = (-a2*a3+c2*c3)/
                                denominator*K1Y-c1*(-a3+c3)/
                                denominator*K2Y-c1*(c2-a2)/
                                denominator*K3Y;
                                P2Y = -c2*(-a3+c3)/
                                denominator*K1Y-(a1*a3-c1*c3)/
                                denominator*K2Y+c2*(a1-c1)/
                                denominator*K3Y;
                                P3Y = -c3*(c2-a2)/
                                denominator*K1Y+c3*(a1-c1)/
                                denominator*K2Y-(a1*a2-c1*c2)/
                                denominator*K3Y;

                                Ex[x][y] = (1.0/enaught)*(Dx[x][y]-
                                P1X - P2X - P3X);
                                Ey[x][y] = (1.0/enaught)*(Dy[x][y] -
                                P1Y - P2Y - P3Y);
                        }
                }
                else
                {
                        E_Ecoeff = media[x][y].E_Ecoeff();
                        E_Hcoeff = media[x][y].E_Hcoeff();
                        P1X = 0;
                        P2X = 0;
                        P3X = 0;
                        P1Y = 0;
                        P2Y = 0;
                        P3Y = 0;
                        Ex[x][y] = E_Ecoeff*Ex[x][y]
                        + E_Hcoeff*(Hz[x][y+1] - Hz[x][y]
                        - Hzinc);
                        Ey[x][y] = E_Ecoeff*Ey[x][y]
                        + E_Hcoeff*(Hz[x][y] –
                        Hz[x+1][y]);
                }
                Ex_prev[x][y] = temp_Ex;
                Ey_prev[x][y] = temp_Ey;

                Dx_prev_prev[x][y] = Dx_prev[x][y];
                Dx_prev[x][y] = Dx[x][y];
                Dy_prev_prev[x][y] = Dy_prev[x][y];
                Dy_prev[x][y] = Dy[x][y];
```

```
                        P1X_prev_prev[x][y] = P1X_prev[x][y];
                        P2X_prev_prev[x][y] = P2X_prev[x][y];
                        P3X_prev_prev[x][y] = P3X_prev[x][y];

                        P1X_prev[x][y] = P1X;
                        P2X_prev[x][y] = P2X;
                        P3X_prev[x][y] = P3X;

                        P1Y_prev_prev[x][y] = P1Y_prev[x][y];
                        P2Y_prev_prev[x][y] = P2Y_prev[x][y];
                        P3Y_prev_prev[x][y] = P3Y_prev[x][y];

                        P1Y_prev[x][y] = P1Y;
                        P2Y_prev[x][y] = P2Y;
                        P3Y_prev[x][y] = P3Y;

                        H_Hcoeff = media[x][y].H_Hcoeff();
                        H_Ecoeff = media[x][y].H_Ecoeff();

                        Hz[x][y] = H_Hcoeff*Hz[x][y]
                        + H_Ecoeff*(Ex[x][y] - Ex[x][y-1] –
                        Ey[x][y] + Ey[x-1][y] - Exinc);
                    }
                    Et[x][y] = sqrt(Ex[x][y]*Ex[x][y] + Ey[x][y]*Ey[x][y]);
                }
            }
        }
}
/////////////////////////////////////////////////////////////////////////////////////////////////////////////////////
```

Appendix D: Analysis Techniques

Frequency-Dependent Effective Refractive Index:

To extract the frequency-dependent refractive index of a sample, two measurements are made: 1) the reference time-domain electric field, $E_o(t)$, transmitted through a medium with a known refractive index, n_{ref} (usually this is free-space, where $n_{ref} = 1$) and 2) the time-domain electric field, $E_1(t)$, transmitted through a sample of effective refractive index $n_{eff}(\omega)$ and sample thickness L. To obtain frequency-domain information, $E_o(t)$ and $E_1(t)$ are Fourier transformed to yield frequency-domain representations of the fields $\widetilde{E}_o(\omega) = |E_o(\omega)| e^{i\Phi_o(\omega)}$ and $\widetilde{E}_1(\omega) = |E_1(\omega)| e^{i\Phi_1(\omega)}$. Here, $|E_1(\omega)|$, $|E_o(\omega)|$ and $\Phi_1(\omega)$, $\Phi_o(\omega)$ are the amplitude and phase spectra of the measured electric fields, respectively. The phase spectrum of the reference pulse is related to the index, $n_{ref} = 1$, via $\Phi_o(\omega) = k_oL + C$, where k_o is the free space wavevector and C is an arbitrary constant equal to the phase accumulation of the electric field pulse as it propagates through the experimental setup. On the other hand, the relationship between the phase spectrum, $\Phi_1(\omega)$, and the refractive index (real part) of the sample is given by $\Phi_1(\omega) = n_{eff}(\omega) = k_oL + C$. Thus, $n_{eff}(\omega)$ is obtained through the relation

$$n_{eff}(\omega) = \frac{\Phi_1(\omega) - \Phi_o(\omega)}{k_oL} + 1 \qquad \text{(D.1).}$$

Relative Effective Absorption Coefficient:

Assuming that attenuation of the electric fields $E_o(t)$ and $E_1(t)$ are governed by absorption in the region occupied by the sample, the amplitude spectra of the transmitted electric fields $E_o(t)$ and $E_1(t)$ can be written in terms of effective absorption coefficients $|E_o(\omega)|=|E_{o,i}(\omega)|e^{-\kappa_o(\omega)L}$ and $|E_1(\omega)|=|E_{1,i}(\omega)|e^{-\kappa_1(\omega)L}$. Here, $|E_{o,i}(\omega)|$ and $|E_{1,i}(\omega)|$ are the incident electric field amplitudes and $\kappa_o(\omega)$ and $\kappa_1(\omega)$ are the frequency-dependent absorption coefficients of the reference and the sample. When $|E_{o,i}(\omega)| = |E_{1,i}(\omega)|$, the effective absorption coefficient change caused by the sample relative to the reference, $\Delta\kappa(\omega)$, can be expressed as

$$\kappa_1(\omega)-\kappa_o(\omega)=\Delta\kappa(\omega)=-\frac{1}{L}\ln\left(\frac{|E_1(\omega)|}{|E_o(\omega)|}\right) \qquad \text{(D.2).}$$

The absorption coefficient can be also written in terms of the change in the imaginary part of the effective refractive index, $\Delta\mathrm{Im}[n_{eff}(\omega)]$ via $\Delta\mathrm{Im}[n_{eff}(\omega)] = \Delta\kappa(\omega)/k_o$. It should be noted that when reflection from the surfaces of the sample are appreciable such that $E_{o,i}(\omega) \neq E_{1,i}(\omega)$, the relation for $\Delta\kappa(\omega)$ must account for reflection losses.

Effective Electromagnetic Group Velocity:

One can estimate the group velocity, v_g, through a sample from the relative temporal delay of $E_1(t)$ relative to $E_o(t)$. Here, the relative delay, ΔT, is defined as the time difference between peaks of the time-dependent intensity profiles, $I_1(t)$ and $I_o(t)$. To obtain the time-dependent intensity profiles, the Hilbert transforms of the real signals $E_o(t)$ and $E_1(t)$ are taken to yield the imaginary parts of the signals, $E_o^i(t)$ and $E_1^i(t)$. From the complex electric fields $\widetilde{E}_o(t)=E_o(t)+iE_o^i(t)$ and $\widetilde{E}_1(t)=E_1(t)+iE_1^i(t)$, the time-dependent intensity profiles are obtained via $I_o(t)=\widetilde{E}_o(t)\widetilde{E}_o^*(t)$ and $I_1(t)=\widetilde{E}_1(t)\widetilde{E}_1^*(t)$, where $\widetilde{E}_o^*(t)$ and $\widetilde{E}_1^*(t)$ are the complex conjugates of

$\widetilde{E}_o(t)$ and $\widetilde{E}_1(t)$, respectively. From the relative delay, the effective electromagnetic group velocity is estimated from

$$v_g = \frac{L}{\Delta T + L/c} \tag{D.3}$$

where c is the speed of light.

Appendix E: Metallization Processes and Characterization

The bimetallic particle samples described within this thesis were prepared using sputter metallization processes. Prior to metallization, the metallic particles are chemically cleaned in both isopropanol and acetone solutions, and then physically cleaned in an ultrasonic bath for ~ 20 minutes. The sputter processes are briefly described here.

Metallization Processes:

Metal: Au
Sputter System: Kurt J. Lesker Magnetron Sputter System
Process Gas: Argon
Process Gas Pressure: 7 mtorr
Base Pressure: 10^{-7} torr
Sputter Gun Power: 75 mW
Sputter Gun Position: High

Metal: Cu
Sputter System: Kurt J. Lesker Magnetron Sputter System
Process Gas: Argon
Process Gas Pressure: 7 mtorr
Base Pressure: 10^{-7} torr
Sputter Gun Power: 300 mW
Sputter Gun Position: Low

Characterization Processes:

The resistivities of the metallic films were measured using a four-point probe technique, which eliminates deleterious contact resistance between the contact and the sample film. The measurements were made on witness metallic films deposited on cleaned glass substrates. The thickness of the metallic films was characterized using the Alphastep 200 Profilometer at the University of Alberta Nanofab. The scanning electron microscope images of the particles were obtained using the Scanning Electron Microscope LEO 1430 also at the University of Alberta Nanofab.

Appendix F: Microwave Transmission Spectra of the Helical Structure

For transverse THz electromagnetic wave excitation, it was shown in Chapter 6 that the subwavelength helical structure exhibits non-resonant optical activity. No measurable resonant effects were observed in the THz transmission spectra since the geometrical resonances associated with the helical structure lie in the gigahertz (GHz) range. To confirm that the geometrical resonances of the helix are beyond the bandwidth of the THz spectroscopic measurements, supplementary experiments are performed to measure the microwave transmission spectra of the helix. The helix is embedded in a photopolymer matrix (similar to the THz spectroscopic experiments) and mounted in a microwave wave-guide which supports frequencies ranging from 7 GHz to 12 GHz. The transmission spectrum of the helix is measured using an Agilent 8720ES 50MHz - 20 GHz S Parameter Network Analyzer. Shown in Figure F.1 (a) and F.1 (b) are the magnitude and phase spectra of the transmission through the helix where the helical axis is aligned parallel to the incident polarization of the microwave. Over the bandwidth of the measurement, there are no observable resonances within error of the measurement. In contrast, for the configuration where the helical axis is aligned perpendicular to the incident polarization, distinct resonance features are seen in both the amplitude and phase spectra [Figure F.1 (c) and F.1 (d)]. This resonance, which is peaked at 10.3 GHz, lies well below the bandwidth of the THz pulse and is not detected in the THz spectroscopic measurements in Chapter 6.

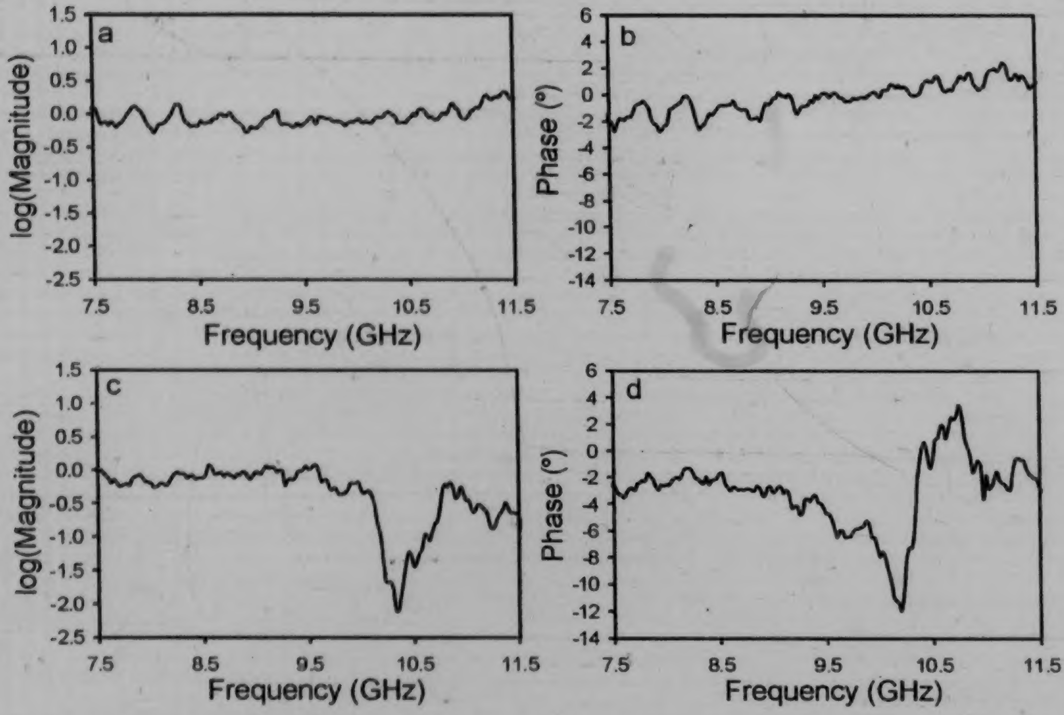

Figure F.1. (a) Magnitude and (b) phase spectra of the transmission through the helix (used in Chapter 6) where the helical axis is aligned parallel to the microwave polarization. (c) Magnitude and (d) phase spectra of the transmission through the helix where the helical axis is aligned perpendicular to the microwave polarization.